The role of Extremely Red Galaxies in the history of structure formation

KARINA I. CAPUTI

Institute for Astronomy

School of Physics

A thesis submitted to the University of Edinburgh
for the degree of Doctor of Philosophy

November 2004

Declaration

I hereby declare that no part of this thesis entitled *The role of Extremely Red Galaxies in the history of structure formation* has already been or is being concurrently submitted for any other degree, diploma or professional qualification. I also state that all the work presented here is my own, except where otherwise acknowledged in the text.
Parts of the work contained in this thesis have been published or are due to be published in refereed scientific journals:

- Most of the contents of Chapter 3 have been published in the paper *A deeper view of Extremely Red Galaxies: the redshift distribution in the GOODS/CDFS ISAAC field*, K.I. Caputi, J.S. Dunlop, R.J. McLure, N.D. Roche, MNRAS **353**, 30
- The contents of Chapter 4 are due to be published in the paper *The evolution of K_s-selected galaxies in the GOODS/CDFS deep ISAAC field*, K.I. Caputi, J.S. Dunlop, R.J. McLure, N.D. Roche, MNRAS submitted

Karina I. Caputi
Edinburgh
November 2004.

Abstract

In this thesis we investigate the redshift distribution and derived cosmological properties of Extremely Red Galaxies (ERGs), through the study of a sample selected with $K_s \leq 22$ and $(I_{775} - K_s) > 3.92$ (Vega) in 50.4 arcmin^2 of the GOODS/CDFS field. We also study the properties of the total parent sample of K_s-selected galaxies in the same field, with the aim of understanding their evolution and clarifying the role of ERGs within this population. We determine that the bright end of the K_s-band luminosity function, which is progressively well reproduced by the ERGs with increasing redshift, shows no sign of decline up to at least redshift $z \sim 2.5$. We also explore the evolution of massive systems present in our sample: $\sim 20\% - 25\%$ of the population of local galaxies with assembled stellar mass $M > 1 \times 10^{11} M_{\odot}$ were formed before redshift $z \sim 4$, and contain $\sim 45\%$ to 70% of the stellar mass density of the Universe at that redshift. Within our sample, the comoving number density of these massive systems is then essentially constant down to redshift $z \sim 1.5$. The remaining massive systems observed in the local Universe are assembled later, at redshifts $z < 1.5$. Thus, a two-fold assembly history for massive galaxies is suggested, in which galaxy/star formation proceeds very efficiently in high mass haloes at very high redshift. It is the massive ERGs at redshift $z > 1$ which contain the imprints of the most efficient period of galaxy formation. Finally, from the morphological study of our galaxies with estimated mass $M > 10^{11} M_{\odot}$ and redshifts $z < 2$, we explore the bridge between massive ERGs at $z > 1$ and local massive galaxies. $\sim 50\% - 60\%$ of all the massive galaxies at $0.5 \lesssim z \lesssim 2.0$ have surface brightness profiles close to a de Vaucouleurs law. All our results are consistent with a scenario in which the most massive ERGs are the progenitors of local cluster elliptical/S0 galaxies.

Acknowledgements

First of all, my most sincere acknowledgement to Jim Dunlop and Ross McLure, for being excellent supervisors without whose guide this work would never have been accomplished so effectively and in time. To both of you: thank you very much!

Also, to the other people who directly contributed to this work to different extents: Nathan Roche, Will Percival, Alan Heavens and Ben Panter.

To John Peacock, for his responsibility for providing quick and effective replies to postgraduate students' problems.

To my office mates and other people in the IfA who helped to make very friendly my days in Edinburgh.

To my teachers in the Instituto Balseiro, Argentina, in particular to Raúl Barrachina, for their continuous effort to provide first-quality education in spite of the many limitations of the third world.

To my friends, always prompt to pop up in my email box to demonstrate that long distances do not matter.

To mum and dad, and to my sister Vero, because their huge love can resist everything, including my nearly permanent absence.

And, of course and very especially, to Mariano. No words are sufficient to acknowledge all his love and support during these years.

...there are two paths you can
go by, but in the long run
There's still time to change
the road you're on.

J.Page/R.Plant. *Stairway to Heaven.*

Contents

1 Introduction **1**

1.1 Structure formation in the Universe 1

1.2 Constraints from galaxy populations 3

1.3 The purpose of this thesis 4

2 An overview of Extremely Red Galaxies **6**

2.1 Introduction 6

2.2 The nature of the extremely red colours 7

2.2.1 A few basic definitions 7

2.2.2 The evolution of stellar populations 7

2.2.3 A further complication: the presence of dust 9

2.2.4 The evolution of the (I – K) colours 12

2.3 In search of Extremely Red Galaxies 14

2.3.1 First identifications 14

2.3.2 The K20 survey 15

2.3.3 Other surveys 16

2.4 Properties of ERGs 17

2.4.1 Clustering 17

2.4.2 Morphology 19

2.4.3 Spectra 20

2.4.4 An attempt to solve the age and dust degeneracy 22

2.5 Assessment of galaxy formation theories 23

2.6 The relation between ERGs and other galaxy populations 26

2.6.1 Other red near-IR selected galaxies 26

2.6.2 Radio galaxies 27
2.6.3 Mid-to-Far-IR and submillimetre galaxies 28
2.6.4 X-ray sources 29
2.7 Summary and discussion 30

3 A deeper view of Extremely Red Galaxies **32**
3.1 Introduction 32
3.2 The GOODS project 33
3.2.1 General description 33
3.2.2 The GOODS/CDFS deep ISAAC field 34
3.2.3 HST/ACS optical/near-IR imaging 35
3.3 The ERG sample 35
3.3.1 Sample selection 35
3.3.2 Multiwavelength photometry 37
3.4 Redshift estimates 38
3.4.1 Photometric redshift algorithms 38
3.4.2 Caveats 41
3.4.3 Strategy for redshift estimations 42
3.5 Results 44
3.5.1 The redshift distribution 44
3.5.2 The Hubble diagram: K_s vs. z_{phot} 46
3.5.3 The red envelope of galaxy evolution 50
3.5.4 The evolving luminosity function of ERGs 53
3.5.5 Comoving densities of $L > L^*$ progenitors 56
3.5.6 Sources beyond redshift z = 4 - the ERG - Lyman-break connection 61
3.5.7 Review of the ERG cluster candidate at redshift $z \sim 1.5$ 67
3.6 Summary and discussion 68

4 The evolution of K_s-selected galaxies **71**
4.1 Introduction 71
4.2 The $K_s \leq 22$ galaxy sample 72
4.2.1 Sample selection and multiwavelength photometry 72
4.2.2 Completeness 74

4.2.3 The ERG sample 74
4.2.4 Star/galaxy separation 74
4.2.5 Number counts 76
4.3 Redshift estimates 76
4.3.1 Strategy for redshift estimations 76
4.3.2 Photometric redshift calibration 77
4.3.3 The ERG photometric redshifts 80
4.4 Results 81
4.4.1 The redshift distribution 81
4.4.2 The Hubble diagram 83
4.4.3 The evolution of the K_s-band/ERG luminosity functions 85
4.4.4 The evolution of massive galaxies 91
4.5 Predictions of Spitzer/IRAC magnitudes 100
4.6 Summary and discussion 104

5 The morphology of massive galaxies at high z 106
5.1 Introduction 106
5.2 The sample 108
5.3 Morphology modelling 108
5.3.1 The surface-brightness-profile fitting algorithm 108
5.3.2 The input images and point-spread functions (PSFs) 112
5.4 Results 113
5.4.1 The morphology of massive galaxies 113
5.4.2 Bulge-dominated objects 120
5.5 Summary and discussion 122

6 Conclusions 124
6.1 The role of ERGs in the history of structure formation 124
6.2 Prospects for the future 126

A Catalog of $K_s \leq 22$-selected galaxies 128

List of Figures

2.1 The contribution of different stellar groups to the integrated galaxy SED 8
2.2 The evolving observer-frame (I – K) colours 13
2.3 The comoving correlation lengths for different galaxy populations 18
2.4 Examples of average ERG spectra in the K20 survey 21
2.5 The (I – K) vs. (J – K) colour-colour plot for ERGs at redshifts $1 < z < 2$ 23
2.6 The cumulative redshift distribution of $K < 20$ galaxies 24

3.1 The GOODS/CDFS deep ISAAC field 34
3.2 Examples of spectral energy distributions and redshift probability density distributions 43
3.3 The redshift distribution of the ERGs in the deep ISAAC field 45
3.4 The Hubble diagram for the ERGs in the deep ISAAC field 47
3.5 $(J - K_s)$ and $(I_{775} - K_s)$ colours vs. photometric redshifts 50
3.6 Dust-corrected $(J - K_s)$ and $(I_{775} - K_s)$ colours vs. photometric redshifts 51
3.7 The median of the V-band extinction values vs. photometric redshifts . 52
3.8 The luminosity function of ERGs at different redshifts 54
3.9 Lower limits on the comoving densities of ERGs progenitors of local $L > L^*$ galaxies 58
3.10 The redshift probability density distributions of the accepted $z > 4$ candidates 63

4.1 Differential number counts for K_s-selected galaxies and ERGs 75
4.2 Photometric redshifts vs. spectroscopic redshifts for $K_s \leq 22$-selected galaxies 78

4.3 Photometric redshifts obtained using the J and K_s-band data from the GOODS/EIS v1.0 release 79
4.4 New versus old redshift estimates for the ERGs in the deep ISAAC field 81
4.5 The redshift distribution of the total $K_s \leq 22$ sample of galaxies 82
4.6 The Hubble diagram for K_s-selected galaxies in the deep ISAAC field . . 84
4.7 The rest-frame K_s-band luminosity function 86
4.8 The raw rest-frame K_s-band luminosity function 87
4.9 Compared evolution of the total K_s-band and the ERG LFs with redshift 89
4.10 The relative errors of the redshift estimates for the sources considered in the K_s-band LF 90
4.11 The comoving number density of galaxies with stellar mass $M > 5 \times 10^{10} M_\odot$ and $M > 1 \times 10^{11} M_\odot$ 93
4.12 The distribution of the stellar mass density as a function of redshift . . 97
4.13 The comparison of the total stellar mass densities with values previously obtained by other authors 99
4.14 Predicted IR colours of $K_s \leq 22$-selected sources versus estimated redshifts 101

5.1 K_s-band postage stamps of massive galaxies at $z_{phot} < 2$ in the GOODS/CDFS deep ISAAC field 109
5.2 ACS z-band counterparts of massive galaxies at $z_{phot} < 2$ in the GOODS/CDFS deep ISAAC field 110
5.3 The best-fit single-component $\beta = 1/n$ index for massive galaxies at redshifts $z_{phot} < 2$ 114
5.4 ACS z-band image of a merger in the GOODS/CDFS deep ISAAC field 115
5.5 The bulge fraction versus estimated redshifts for galaxies with mass $M > 10^{11} M_\odot$ at $z_{phot} < 2$ 117
5.6 Half-light radii versus estimated redshifts for galaxies with mass $M > 10^{11} M_\odot$ at $z_{phot} < 2$ 119
5.7 K_s-band bulge fraction versus photometric redshifts for bulge-dominated galaxies with mass $M > 10^{11} M_\odot$ 121
5.8 z-band bulge fraction versus photometric redshifts for bulge-dominated galaxies with mass $M > 10^{11} M_\odot$ 122

List of Tables

3.1 The effective wavelengths of the filters used in HYPERZ 42

3.2 List of ERGs with HYPERZ primary solutions $z_{phot} > 4$ 65

3.3 A complementary list of the $z > 4$ candidate objects selected by other authors, present in the R03 ERG sample 66

3.4 Redshift estimates for the ERGs in a cluster candidate at $z \sim 1.5$ 67

3.5 Redshift estimates for 2 ERGs associated to the Chandra source XID:149 68

4.1 $K_s \leq 22$-selected sources among IRAC extremely red objects 102

A.1 Full catalog of K_s-selected galaxies 129

Chapter 1

Introduction

1.1 Structure formation in the Universe

Structure formation is the consequence of the evolution of mass density fluctuations in the primordial Universe. In a stationary homogeneous and isotropic medium, instabilities can grow exponentially in regions with small fluctuations in the density and velocity fields, where the pressure cannot balance the inter-particle gravitational force (*Jeans instability*). In an expanding medium, gravitational collapse can also take place, but the perturbations only grow as a power-law with time [1]. Thus, to explain the formation of structures in the expanding early Universe, the existence of additional finite perturbations has to be assumed.

The observed abundances of light elements produced in primordial nucleosynthesis indicate that baryons (i.e. protons, neutrons, electrons) are not sufficient to explain the mass density of the Universe. In the context of a Universe dominated by non-baryonic matter, two main theories of formation of large-scale structures have been developed, assuming the existence of finite perturbations in the initial mass-energy density field [2] [3].

The first model corresponds to a *Hot Dark Matter (HDM)* scenario, in which the density field has point-to-point variations producing local perturbations to the curvature of space. In this model, the dark matter is supposed to be mainly constituted by neutrinos. The neutrino interactions maintain the equilibrium between neutrons and protons in the early Universe, until the temperature is sufficiently low as to make the typical times for those interactions become greater than the age of the Universe

(neutrino *decoupling*) and the abundance ratios of neutrons to protons reach a constant value. The term 'hot' dark matter refers to the fact that the neutrinos were still relativistic at the moment of decoupling, i.e. $3k_BT > mc^2$, where $3k_BT$ is the relativistic mean kinetic energy and m the mass of the neutrino. These high kinetic energies in the moment of decoupling allow the neutrinos to escape the self-gravitational field in the small density perturbations. This phenomenon, which is known as *free streaming*, produces the damping of the small-scale fluctuations, characteristic of the HDM models. As a consequence, in this scenario only large initial fluctuations survive and trace the large-scale structure observed in the Universe. Smaller substructures form much later, from the fragmentation and instabilities in the large high-density regions. This fact is recognised as a major problem for the HDM models: galaxies are predicted to form only at relatively low redshifts.

In the *Cold Dark Matter (CDM)* scenario, on the contrary, the total mass-energy density field is not spatially perturbed, but the individual components (i.e. baryons, non-baryons and radiation) can change the amplitude of their fluctuations. In this scenario, the dark matter is composed of *weakly interacting massive particles (WIMPS)*, which are non-relativistic at the moment of decoupling. As a consequence, free-streaming has little importance in this model and perturbations of different scales can survive the epoch of recombination. However, the amplitude of the terms in the power-spectrum of the initial fluctuations is assumed to decrease with increasing mass and, thus, the formation of structures is a 'bottom-up' process, with smaller units formed first and then assembled into larger systems. Different variations of the CDM models have been proposed. In the *standard CDM (SCDM)*, the cosmological parameters are fixed to $\Omega_m = 1$ and $h = 0.5$ and the power-spectrum of the initial fluctuations is assumed to be linear in the reciprocal of the spatial scale $P(k) \propto k$ (Harrison-Zel'dovich form). A direct test for this model has been the measurement of the power-spectrum of the primordial density fluctuations in the *Cosmic Microwave Background (CMB)*, as obtained with the *Cosmic Background Explorer (COBE)*. COBE results showed that the SCDM model was inconsistent with observed galaxy velocities and clustering [4]. The measured shape of the primordial power-spectrum, as well as other observational results based on e.g. distant supernovae [5], favoured a lower value for the density parameter Ω_m, and a non-zero cosmological constant Ω_Λ had to be proposed to preserve the

geometry of a flat Universe: $k = \Omega_m + \Omega_\Lambda = 1$. A cold dark matter model with a finite cosmological constant *(ΛCDM)* is currently the most accepted model for structure formation, able to explain most of the observational data (see, however, §2.5). In particular, the most recent CMB studies made with the *Wilkinson Microwave Anisotropy Probe (WMAP)* yield $\Omega_m = 0.27 \pm 0.04$ and $\Omega_\Lambda = 0.73 \pm 0.04$ [6].

1.2 Constraints from galaxy populations

In CDM models, galaxies and large-scale structures are formed in a hierarchical process. The analytic formalism which describes the formation of structures from primordial Gaussian fluctuations in the density field was developed by Press and Schechter (1974) [7]. The hierarchical clustering is the consequence of the dynamical evolution of the dark matter and, thus, the structures which are predicted to form are the so-called *dark matter haloes*. Galaxy formation proceeds from the condensation of gas within the potential wells of dark matter haloes [8] [9]. Thus, additional recipes for gas cooling, star formation, chemical enrichment, dust, etc. need to be added to the Press-Schechter formalism to predict the properties of galaxy populations at different redshifts. CDM models have been successful in reproducing different galaxy properties, such as the local luminosity functions (LF) or the Tully-Fisher relation for spiral galaxies. However, the explanation of other observables, such as the redshift distribution of near-infrared (IR) selected galaxies or the number counts of far-IR/submillimetre galaxies, is still a challenge. This issue will be further discussed in §2.5.

The study of galaxy populations can put strong constraints on galaxy formation theories. The little scatter observed in the colours of cluster spheroidal galaxies up to redshifts $z \approx 0.5$ [10], consistent with the passive evolution of their stellar populations, allowed to conclude that these galaxies must have been formed at very early epochs. Although CDM models allow for a minor fraction of massive systems to be formed at high redshifts, the hierarchical scenario predicts that the majority of the largest structures should be formed last, after the merging of smaller units. Thus, quantifying the number density of massive systems at high redshift provides a powerful test of the validity of current theories of galaxy formation. If local cluster elliptical galaxies were indeed formed at very high redshifts and evolved passively to the present day, stellar

synthesis models predict that they should have displayed extremely red optical/near-IR colours at redshifts $z \gtrsim 1$. The search for these progenitors of the local cluster spheroidal galaxies is thus a key experiment for understanding the formation of massive structures in the Universe.

1.3 The purpose of this thesis

In this thesis, we study galaxies selected from the deepest significant sample of Extremely Red Galaxies (ERGs) defined to date, with the aim of understanding the evolution of these objects and their role in the history of structure formation. The characteristics of our sample allow us to trace the ERG population up to very high redshifts, $z \sim 4$. We enhance our knowledge on ERG evolution by an unprecedented systematic comparison of the properties of the ERG population and the parent sample of near-IR galaxies selected in the same field. This allows us to reconstruct the evolutionary line followed by massive galaxies since early times. Finally, through the study of galaxy morphology, we explore the bridge between massive ERGs at redshift $z \gtrsim 1$ and massive local galaxies. As a result, a picture of the total history of ERG evolution is intended to be outlined.

The layout of this thesis is as follows. In Chapter 2, we review the characteristic properties of the ERGs as determined by the many studies which followed their serendipitous discovery, up until commencement of the present work. In Chapters 3,4 and 5, we present and discuss the results from our new study. In Chapter 3, we use multicolour photometry to compute the redshift distribution and model the derived cosmological properties of our deep sample of ERGs. We study the evolution of the $(I - K_s)$ colours, the ERG luminosity function (LF) and the existence of progenitors of local luminous $L > L^*$ galaxies within the ERG population. In Chapter 4, we determine the redshift distribution and similar cosmological properties of the parent sample of K_s-selected galaxies in the same field. We perform a systematic comparison of the evolution of the LFs and number densities of ERGs and other K_s-selected galaxies. The evolution of the stellar mass density of the Universe is traced up to redshift $z \sim 4$. In Chapter 5, we study the morphology of the most massive galaxies present in our samples of galaxies up to $z \sim 2$ and try to relate their structural parameters with the

properties determined in the previous chapters. Finally, in Chapter 6, we present our general conclusions and discuss the remaining open questions which can motivate future work on this subject. We adopt throughout a cosmology with $H_o = 70\,km\,s^{-1}Mpc^{-1}$, $\Omega_m = 0.3$ and $\Omega_\Lambda = 0.7$. All the magnitudes and colours are given in the Vega system, unless otherwise stated.

Chapter 2

An overview of Extremely Red Galaxies

2.1 Introduction

The advent of sensitive near-infrared (near-IR) detectors in the last two decades has allowed rapid progress in extragalactic surveys conducted beyond the optical bands. The importance of near-IR surveys in the search for high-redshift galaxies has been recognised, and such surveys also offer the possibility of discovering galaxy populations undetected in optical bands. In 1988, Elston, Rieke & Rieke [11] reported the discovery of a new population of galaxies selected in the K band ($\sim 2\mu$m), with no counterparts in the R band and colours $(R - K) > 5$. Although the nature of these objects was unknown at that time, it was suggested that they might be primeval galaxies at very high redshift ($z > 6$), or heavily reddened galaxies, with possibly significant asymptotic giant branch (AGB) stellar populations. These near-IR selected sources with extreme colours ($(R - K) > 5$, or similarly $(I - K) > 4$) have been later named *extremely red objects* (EROs) and this is the name commonly used in the literature to refer to these sources.

Our aim in this chapter is to present a review of the characteristic properties of the EROs, as they were determined by the multiple studies which followed their discovery. This description attempts to clarify the importance of the study of such objects to put constraints on galaxy formation theories. We postpone to Chapters 3 to 6 the presentation of our new results, and the discussion of the role of the EROs in the

history of galaxy evolution.

2.2 The nature of the extremely red colours

2.2.1 A few basic definitions

We mentioned in §2.1 that EROs are usually defined as sources selected in the near-IR K band which have extreme colours ($(R-K) > 5$ or $(I-K) > 4$). As we shall see later, most of these objects are extragalactic. However, some cool dwarf stars of spectral classes M, L or T are also EROs [12]. To refer exclusively to the EROs of extragalactic origin, the term *extremely red galaxies* (ERGs) is sometimes preferred and this is the name we shall mainly use hereafter. In all cases, we refer to ERGs as K-selected galaxies with $(I-K) > 4$, unless otherwise stated.

2.2.2 The evolution of stellar populations

The spectral energy distribution (SED) of a galaxy from ultraviolet (UV) to near-IR wavelengths is the consequence of the integrated emission of the radiation of its stellar populations. Stars at different evolutionary stages dominate different regions of the integrated spectra. During most of a galaxy's life, the main contribution to the SED is given by stars with mass $M \lesssim 2M_{\odot}$. More massive stars only have a relevant contribution during relatively short periods $\lesssim 1$Gyr [13]. The evolution of a $M \lesssim 2M_{\odot}$ star begins on the main sequence (MS) of the colour-magnitude (CM) diagram, where the star spends most of its life, i.e. $\sim$ 1Gyr to more than 10Gyr, depending on the initial mass. During the MS phase, the star consumes the hydrogen (H) available in its core and the resulting radiation contributes to different wavelength regimes of the galaxy SED, from the UV to the near-IR. After leaving the MS, the star moves upwards and to the right in the CM diagram following the red-giant branch (RGB) . In this stage, in which all the H in the core has already been consumed, the star burns H in a shell around the core to produce Helium (He). Subsequently, the star burns the He available in the core (He flash) and, then, carbon (C) and also He in the shell around the core. This last phase corresponds to the AGB in the CM diagram and is characterised by a significant instability and mass loss for the star. AGB stars have an important contribution to the near to far-IR SED by the re-emission of radiation due

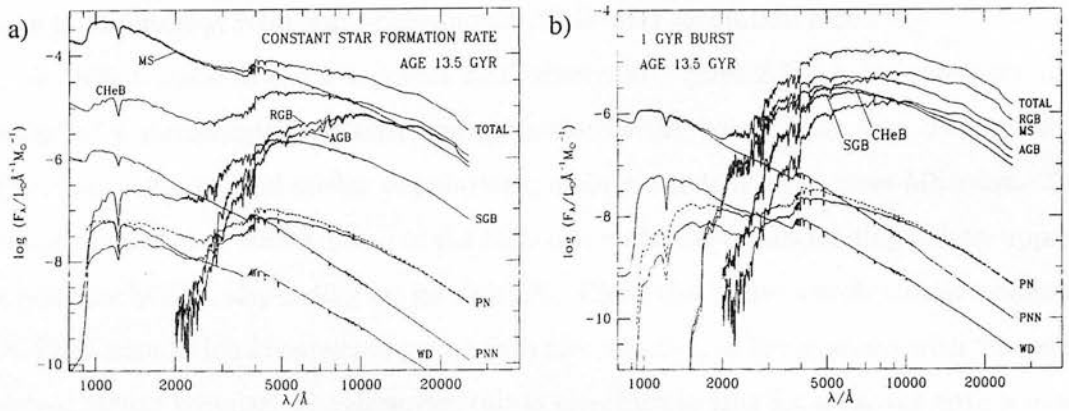

Figure 2.1: The contribution of different stellar groups to the integrated SED of a 13.5 Gyr-old galaxy: with constant star formation (a) and with a star formation history declining in a timescale of 1Gyr (b). The UV SED is dominated by MS stars while the star formation is active; the emission of WD and PN prevails afterwards. The red part of the spectrum has contributions of MS and post-MS (AGB, RGB) stars. Figures taken from Bruzual & Charlot (1993) [15].

to the envelope of dusty gas (H) that is expelled by the star [14]. The intense ionising radiation following the AGB phase brightens the H envelope producing a planetary nebula (PN). The star progressively runs out of fuel and starts to cool down, turning into a white dwarf (WD). PN and WD mainly contribute to the UV region of the galaxy SED. The contributions of stars in different stages of evolution to galaxy SEDs are illustrated in Figure 2.1, where we show the example of two galaxies of age 13.5 Gyr, one with constant star formation (a) and one formed on a timescale of 1Gyr (b).

The comparison of Figures 2.1a) and 2.1b) shows that the UV/optical galaxy SED is dominated by young MS stars while star formation is still active; afterwards, the main contribution to the UV spectrum is given by WD and PN. In the near-IR, MS and post-MS (AGB, RGB) stars contribute in similar amounts. These differential contributions in different regions of the integrated SED show that the UV/optical bands carry the information on the recent star formation activity, while the near-IR flux is a consequence of all the stars (i.e. mass) ever present in the galaxy, independently of when they were formed. In this way, the rest-frame near-IR magnitudes and, in particular the rest-frame K-band magnitude, constitute a direct estimator of the stellar

mass in the galaxy, relatively independent of the star formation history.

A clear feature in the integrated SED shown in Figure 2.1b) is the presence of a 'jump' at a wavelength $\sim$ 4000Å known as the 4000*Å break*. This is a characteristic of galaxies with evolved stellar populations, mainly constituted by post-MS stars. The presence of a strong 4000Å break in the SED can make the corresponding galaxy appear as 'extremely red', depending on its redshift. Thus, the colour cutoff characteristic of the ERG population is expected to produce the selection of the systems with the most evolved stellar populations. However, this is in principle true for a galaxy with a more or less coeval stellar population. As we shall discuss in Chapter 4, the simultaneous presence of younger stellar populations emitting additional amounts of UV flux might produce a less prominent 4000Å break in the integrated spectra and, in this case, the galaxy would not appear as extremely red (e.g. Figure 2.1a). The determination of the exact age of a galaxy is usually a difficult task. The uncertainties mainly come from the treatment of post-MS star evolution in different evolutionary synthesis models. In relatively young galaxies, however, this problem can be sometimes overcome by the use of UV spectra, which are dominated by the radiation of MS stars, whose evolution is much better understood [16] [17].

For a complete study of the galaxy SEDs, however, there is a further complication we have not mentioned so far: the presence of dust, which can increasingly attenuate the UV/optical rest-frame light to shorter wavelengths. In §2.2.3, we explain with some detail the usual methods to model the dust corrections in galaxy SEDs and discuss the impact of our limited knowledge on the treatment of this issue in the study of ERGs.

2.2.3 A further complication: the presence of dust

The presence of dust both in galaxies and along the line of sight modifies the observed SED resulting from the integrated stellar emission. Dust grains scatter and absorb the UV and optical light emitted by the stars, producing an overall dimming of the galaxy spectrum. The absorption of radiation heats the dust grains, which then re-emit this thermal energy at near-IR to millimetre wavelengths. The presence of dust is particularly important in galaxies with active star formation. Massive 'burst-like' star formation mainly occurs in dense molecular clouds, while 'quiescent' star formation is associated with diffuse dust present in the interstellar medium (ISM). The envelopes

of AGB stars also contribute to the dust content in normal galaxies. In local galaxies, more than one third of the bolometric luminosity is reprocessed by dust. Moreover, the significant contribution of the cosmic IR background [18] to the total extragalactic background indicates that dust is an important component in high-redshift galaxies.

The equation for the transfer of radiation through dust is a consequence of the conservation of energy applied to three coexisting processes: the emission of light from the source (e.g. the galaxy), and the absorption and scattering of light by the dust. This integro-differential equation reads:

$$\frac{dI_\lambda}{dr} = -\kappa_\lambda I_\lambda(r,\theta,\phi) + \epsilon_\lambda(r,\theta,\phi) + \kappa_\lambda \frac{\omega_\lambda}{4\pi} \int_\Omega I_\lambda(s,\theta',\phi')\, \Phi_\lambda(cos\Theta)\, d\Omega', \qquad (2.1)$$

where $I_\lambda(r,\theta,\phi)$ is the radiation intensity in each point of the space; Ω is the solid angle in the coordinate system of the dust grain; κ_λ is the opacity (absorption plus scattering) of the dust per unit of distance; $\epsilon_\lambda(r,\theta,\phi)$ is the emissivity of the source in the direction of the propagation of light; ω_λ is the fraction of the opacity due to scattering (albedo) and $\Phi_\lambda(cos\Theta)$ is a function giving the angular dependence of the cross-section for scattering by the dust [19] [20].

The solutions to eq.(2.1) depend on the geometry of both the emitting source and the dust distribution, and also on other properties such as, for example, the size of the dust grains. In the particular case of a pointlike source with a foreground screen of dust, eq.(2.1) has an exponentially-declining solution [20]:

$$I(\lambda) = I_0(\lambda)\, e^{-\tau(\lambda)} = I_0(\lambda)\, 10^{-0.4 A_\lambda} \qquad (2.2)$$

where $\tau(\lambda)$ is the optical depth of the dust screen as a function of wavelength λ; I_0 is the radiation intensity emitted by the source and I is the observed intensity. A_λ is called the *extinction*. The optical depth, which depends on the physics of the dust grains, usually increases to shorter wavelengths and determines the functional dependence of the so-called *reddening curve* $k(\lambda)$. The reddening curve and the extinction are related by the *colour excess* $E(B-V)$:

$$A_\lambda = k(\lambda) E(B-V) = \frac{k(\lambda)\, A_V}{R_V} \qquad (2.3)$$

$E(B-V)$ is defined as $E(B-V) = A_B - A_V$, in such a way that the reddening curve is normalised to $k(B) - k(V) = 1$. R_V, the value of $k(\lambda)$ at the effective wavelength of the V band, is a characteristic parameter of the reddening curve [22]. Thus, the apparent magnitude m of a source in a given band X is given by:

$$m_X = M_X + 5\,logd + 25 + A_X + K, \tag{2.4}$$

where M_X is the absolute magnitude in the band X, d is the luminosity distance in Mpc and K is the k-correction [14] (cf. §2).

In practice, two extinction corrections are usually applied to deredden magnitudes, one for Galactic absorption (and scattering) and another one for internal reddening. Several works have attempted to describe the Galactic extinction with a 'mean extinction curve', e.g. [21] [22]. However, it is known that the Galactic extinction is highly dependent on the environment surrounding the dust grains in different lines of sight. The advent of the Cosmic Background Explorer (COBE) and the Infrared Astronomical Satellite (IRAS) allowed for a detailed study of the dust emission in the whole sky. Schlegel, Finkbeiner & Davis [23] made a full-sky $100\,\mu m$ map which is generally used to measure the Galactic reddening of extragalactic sources in UV/optical wavelengths. The colour excess $E(B-V)$ is directly related to the intensity of the $100\,\mu m$ map normalised to a constant temperature D^T: $E(B-V) = p\,D^T$, where p is a constant calibrated using the correlation between the (B − V) colours and the magnesium Mg_2 index for a sample of nearby elliptical galaxies [24].

The study of the intrinsic reddening curves of extragalactic objects is a far more complicated issue. Measurements of the UV extinction have been made for the Large and Small Magellanic Clouds (LMC and SMC, respectively) [25] [26]. The resulting reddening curves display some important differences both with respect to the Milky Way (MW) curve and with respect to each other. For example, the MW and LMC curves are characterised by the presence of a bump at 2175Å produced by graphite absorption. In the SMC reddening curve, on the contrary, this feature is absent, probably indicating a smaller abundance of carbon in this galaxy. Thus, the shape of the reddening curve for each object depends on the metallicity and also on environmental effects, e.g. different distribution of dust grains in star-forming regions.

A reddening law for starbursts has been derived by Calzetti et al. (2000) [27], based

on the study of the far-IR emission of eight low-redshift star-forming galaxies:

$$k(\lambda) = \begin{cases} 2.659\left(-2.156 + \frac{1.509}{\lambda} - \frac{0.198}{\lambda^2} + \frac{0.011}{\lambda^3}\right) + R_V & 0.12\mu m \leq \lambda \leq 0.63\mu m \\ 2.659\left(-1.857 + \frac{1.040}{\lambda}\right) + R_V & 0.63\mu m \leq \lambda \leq 2.20\mu m, \end{cases} \tag{2.5}$$

where λ is the wavelength expressed in μm and $R_V = 4.05 \pm 0.80$. Some characteristics of the central regions of local starbursts are similar to those observed in high-redshift Lyman-break galaxies, e.g. the shape of the stellar continuum and the absorption features in the rest-frame UV spectra [28]. Thus, the Calzetti et al. reddening law has usually been considered a suitable way to describe the obscuration of high-redshift galaxies when only UV to near-IR data is available.

In the present work, we adopt the Calzetti et al. reddening law to describe the internal extinction of high-redshift galaxies, unless otherwise stated. All the properties we derive for high-redshift galaxies assume the validity of this reddening law. However, we should keep in mind that, for instance, the actual distribution of dust in galaxies might have much more complex geometries than a foreground screen. The validity of a very different reddening law could especially affect some of the derived properties of the most obscured ERGs.

2.2.4 The evolution of the (I − K) colours

From section 2.2.3, it is clear that, even in the case of active star formation yielding large amounts of UV and optical flux, the presence of sufficient quantities of dust might produce an intense reddening of a galaxy SED and, thus, that galaxy would be selected as an ERG. So, in summary, there are two main causes for the extremely red colours characteristic of the ERG population: the presence of evolved stellar populations and the presence of large amounts dust. This fact explains why the ERGs have traditionally been considered as a dichotomic population, either composed by old galaxies following a passive evolution (i.e. only suffering the ageing of their stellar populations) or by young starbursts heavily extincted by dust. We discuss the validity of this somewhat simplified picture throughout this work. The existence of these two possible causes for the reddening produces the so-called *age-dust degeneracy*, one of the main problems for understanding the nature of ERGs.

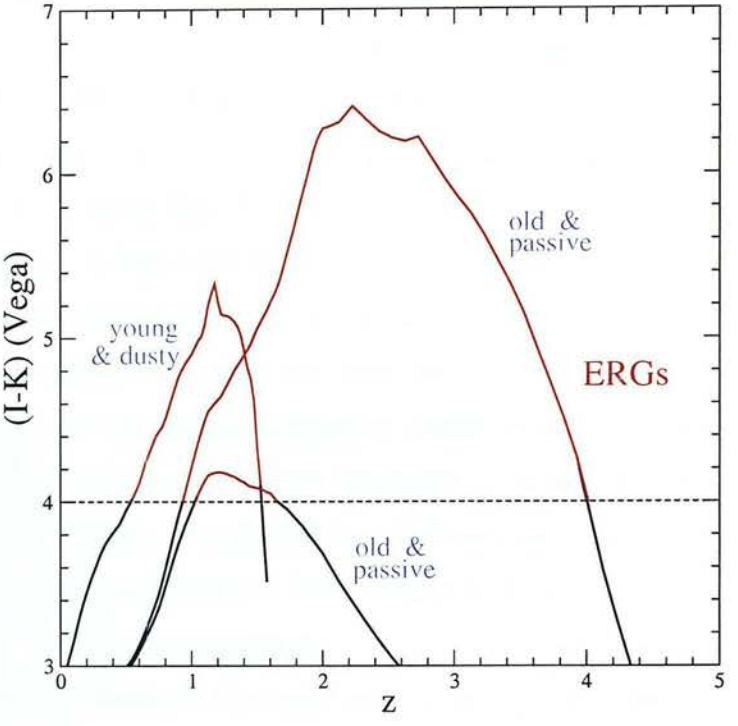

Figure 2.2: The evolving observer-frame (I−K) colours as a function of redshift for galaxies with different star formation histories. The curves flagged as 'old & passive' correspond to galaxies with no dust, formed at redshift $z_f = 5$ in an instantaneous burst (upper curve) and in a 1Gyr timescale (lower curve). The curve flagged as 'young & dusty' corresponds to a very dusty galaxy formed at $z_f = 1.6$. All three of them are ERGs during some period of their lives.

Figure 2.2 shows the evolution of the observed (I−K) colour for different galaxies as a function of redshift. The two curves flagged as 'old & passive' correspond to a galaxy formed in a single instantaneous burst at redshift $z_f = 5$ (upper curve), and to a galaxy formed at the same redshift with a 1Gyr exponentially-declining star-formation history (lower curve), both with no dust. We see that, while the first galaxy would be selected as an ERG from a very young age, the second one would only become an ERG much later, at redshifts $z \sim 1-2$. On the other hand, a galaxy formed at a lower redshift can also be an ERG, if sufficiently extincted by dust. The curve flagged as 'young & dusty' in Figure 2.2 corresponds to a very dusty galaxy formed in a single instantaneous burst at redshift $z_f = 1.6$. This galaxy would be an ERG during an extended period of its

life. We note that Figure 2.2 illustrates the selection effect intrinsically produced by the ERG colours: an $(I - K) > 4$ cut imposes the selection of exclusively high-redshift $z \gtrsim 0.5$ sources (without considering the stellar contaminants mentioned in §2.2.1).

Massive spheroidal galaxies have traditionally been thought to be formed in single bursts at very early times [29] [30]. However, the formation of massive galaxies in a 'monolithic collapse' at high redshifts appears to be at odds with the idea of hierarchical growth predicted by current cosmological models of structure formation, which suggests that the most massive systems form last, many at $z < 1$. However, several observations point to the existence of massive systems at higher redshifts. Bower, Lucey & Ellis (1992) [31] found the existence of very small scatter in the $(U - V)$ colours of local cluster spheroidal galaxies. This fact allowed to determine that most of the stellar mass present in these systems should have been assembled at redshifts $z \gtrsim 1$. Several other results indicate that a non-negligible fraction of all the massive systems present in the local Universe could have been formed at early times, e.g. the presence of radio galaxies or quasars at very high redshifts. If massive local early-type systems were formed at very high redshifts, from the evolution of the observed $(I - K)$ colours shown in Figure 2.2, we can conclude that they should probably have been extremely red objects at redshift $z \sim 1$. Thus, the existence of ERGs with evolved stellar populations could provide evidence in favour of very early galaxy formation and, thus, could potentially put strong constraints on galaxy formation theories. In the next section, we review the most important surveys conducted to date which searched for ERGs at high redshifts.

2.3 In search of Extremely Red Galaxies

2.3.1 First identifications

After their discovery by Elston, Rieke & Rieke [11], many surveys helped to shed light on the nature of the ERGs. Some of the first studies were linked to radio-galaxy surveys, but progressively the ERGs have become a matter of interest by themselves. In this section we summarise the results from some of the most important studies of this population.

A sample of ERGs was identified in a survey of radio sources at $z > 2$ by McCarthy, Persson and West (1992) [32]. Although the association could not be confirmed at

the time, the colours of the ERGs were consistent with them being part of a group containing the radio galaxies. The importance of this early study was to anticipate the property of clustering, which later was determined to be a distinctive characteristic of the ERG population (cf. §2.4.1).

In 1996, Dunlop et al. reported the existence of a 3.5 Gyr-old radio galaxy at redshift $z = 1.55$, characterised by a colour $(R - K) = 5.8$ [16]. The age of this galaxy was determined by fitting synthetic SEDs to the rest-frame UV spectrum, to avoid the uncertainties introduced by the treatment of post-MS stars in different models. The discovery of such an old object in the early Universe set strong constraints on the then current cosmological models. In particular, for a Hubble constant greater than $50\,\mathrm{km\,s^{-1}Mpc^{-1}}$, in a standard Einstein-de Sitter model (i.e. flat Universe with $\Omega_m = 1$ and $\Omega_\Lambda = 0$) the Universe was younger than 3.5 Gyr at redshift $z = 1.55$. Thus, the existence of such an old galaxy implied that an Einstein-de Sitter model should be discarded.

By the same time, Graham & Dey (1996) [33], studied another ERG at redshift $z = 1.44$. The strong $H\alpha$ + [NII] line found in its spectrum indicated important star formation or the presence of an active galactic nucleus (AGN). Also, the authors determined that the colours observed in the SED of this object could not be explained without the presence of dust. Consequently, the Dunlop et al. and Graham & Dey studies taken together provided evidence that the ERG population was composed of both old passively evolving galaxies and dusty star-forming (or active) galaxies. This mixture has since been confirmed by further spectroscopic studies [34].

2.3.2 The K20 survey

The K20 survey [35] was probably the most important comprehensive study of the properties of bright near-IR selected galaxies and, in particular, ERGs. Based on the (mostly spectroscopic) study of 550 objects with $K_s \leq 20$, distributed in two independent fields with a total area of $52\,\mathrm{arcmin}^2$, the K20 survey demonstrated the importance of near-IR suveys for understanding galaxy evolution. In particular, it was determined that the ERG population peaked at redshifts $z \sim 1 - 2$ and was composed of both old passive galaxies and dusty star-forming galaxies in approximately equal ratios. The spectra of the old red stellar systems implied a minimum formation redshift $z_f \approx 2.2$ [36]. The

two types of ERGs, however, appeared to have very different clustering properties. Old red galaxies displayed a strong positive correlation, supporting the idea that they could be the progenitors of local cluster elliptical galaxies. Dusty systems, on the contrary, appeared as very weakly correlated, in a similar way to local infrared galaxies [37], and in opposition to the clustering displayed by other dusty systems, e.g. high-redshift submillimetre galaxies [38] [39]. We discuss ERG clustering in §2.4.1.

Arguably, however, the most important achievement of the K20 survey was to re-open the debate on the ability of hierarchical models of galaxy formation to reproduce the observed properties of K_s-selected galaxies (see also [40]). After the work of Kauffmann & Charlot (1998) work [41], it was believed that hierarchical models were able to correctly predict the redshift distribution of bright K_s-selected galaxies. However, the new K20 data, coupled with changes in galaxy formation models, have re-opened this debate. We carry on the discussion and give further details of the present situation in §2.5.

2.3.3 Other surveys

Several studies of ERGs have been conducted since the K20 survey. On the one hand, they confirmed some of the already known properties of the ERG population. On the other hand, though, they have showed that the ERG population is perhaps more complex than has traditionally been considered.

Smail et al.(2002) [42] studied a sample of ERGs with $K \leq 20.5$ in an area slightly larger than the K20 survey. This work determined that between 30% and 60% of the ERGs present at redshift $z \gtrsim 1$ could not be explained without the presence of dust and, thus, should be galaxies with recent or still active star formation. Simultaneously, the existence of strong clustering for the ERG population was confirmed by Roche et al.(2002) [43], from the study of a $K \leq 21$ sample in a similar-size area. As in the K20 survey, the ERG number counts were greater than predicted by Λ-CDM hierarchical models.

Other more recent studies of K-selected galaxies have revealed some new properties of ERGs. For example, Miyazaki et al. (2003) [44] showed the existence of these extremely red sources up to redshifts $z \sim 4$. They found that 58% of their sample of $K_s < 20.3$ and $(R - K_s) \gtrsim 5$ ERGs was composed of galaxies with evolved stellar

populations. However, the colours of 24% of these old galaxies were best-fit by a composite model of evolved stellar populations with an additional component of star-formation. On the other hand, Yan et al. (2003) [45] determined that ERGs displayed a wide variety of morphologies, another clue against the idea of a simple dichotomy for the ERG population. In the next section, we review in more detail these and some other recent works and discuss the main characteristics of ERGs.

2.4 Properties of ERGs

2.4.1 Clustering

Galaxy clustering is usually computed using a two-point spatial correlation function $\xi(r)$, which gives the excess probability over a poissonian distribution of finding a galaxy at a distance r from another one. If n is the average number density of galaxies per unit volume (usually Mpc^3), then the probability of finding a galaxy by chance within a volume $\delta \mathrm{V}_1$ is simply $n\,\delta V_1$ (usually $n\,\delta V_1 \ll 1$ and, thus, this is a well-defined probability density). The joint probability of finding a galaxy within a volume δV_1 and another one within a volume δV_2, separated by a distance r, is given by:

$$\delta P = n^2\,[1 + \xi(r)]\,\delta V_1 \delta V_2. \tag{2.6}$$

In the case of a Poissonian distribution, $\xi(r) = 0$; an excess probability $\xi(r) > 0$ indicates that the galaxies are clustered [3]. In the range $0.1\,h^{-1}\,\mathrm{Mpc} \lesssim r \lesssim 10\,h^{-1}\,\mathrm{Mpc}$, the two-point spatial correlation function $\xi(r)$ is well described by a power-law $\xi(r) \propto (r/r_0)^{-\gamma}$, where $\gamma = 1.8$. The characteristic distance r_0 below which the excess probability $\xi(r)$ is significant (> 1) is known as the *correlation length*. Beyond the power-law regime, the correlation function $\xi(r)$ rapidly falls to zero. The correlation length r_0 is characteristic of each galaxy distribution: the larger r_0, the stronger the clustering [2].

Daddi et al.(2000) [46] measured for the first time the large-scale structure traced by ERGs at redshift $z \sim 1$. From the study of a sample of bright $\mathrm{K_s} \lesssim 19$ galaxies[1] in

[1]The differences between the K-band filter and the K-short-band filter $\mathrm{K_s}$ are negligible for most of the purposes of this work. The $\mathrm{K_s}$ filter is truncated at long wavelength such that the effective wavelength is $\lambda_{eff.} = 2.16\,\mu m$, slightly smaller than the effective wavelength of the K filter $\lambda_{eff.} = 2.19\,\mu m$.

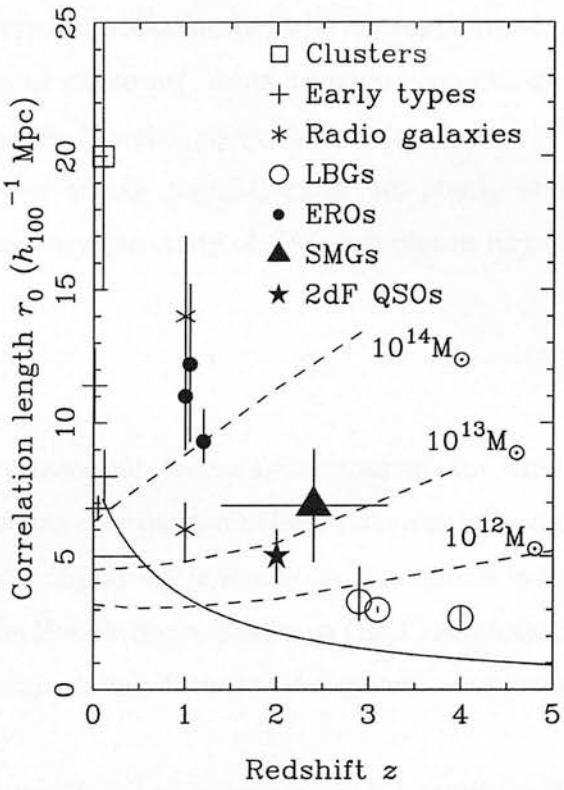

Figure 2.3: The comoving correlation lengths for different galaxy populations as a function of redshift. The dashed lines show the expected correlation length for dark matter haloes of different masses. Figure taken from Blain et al. (2004) [39] (cf. also [49]).

701 arcmin^2 of the sky, these authors determined that ERGs displayed a 2D-clustering signal about one order of magnitude larger than the clustering observed for all the K_s-selected galaxies of similar magnitudes. This important discovery suggested that ERGs could effectively be the progenitors of the elliptical galaxies present in local clusters. This result was confirmed by Daddi et al. in a later work [37], in which the 3D-clustering properties of ERGs have been studied using the complementary information provided by the spectroscopic redshifts available in the K20 survey. This new work gave a step forward by separately studying the clustering properties of old ERGs and dusty systems. The classification was based on the K20 survey spectra: objects with 4000Å break and CaII H&K absorption lines in the spectrum were considered as old galaxies, while objects with no 4000Å break and strong [OII]λ3727 emission were classified as dusty star-forming ERGs. The result was that the strongest clustering was displayed by the old ERGs rather than the dusty ones, indicating that only a subset of ERGs could potentially be the progenitors of the local cluster elliptical galaxies.

Strong clustering was later measured for ERGs up to fainter magnitudes [47] and for other high-redshift galaxy populations, such as $(J-K_s) > 1.7$ K_s-selected galaxies [48], submillimetre galaxies [39] and powerful FRII radio galaxies [49]. The correlation

lengths found for different galaxy types at different redshifts are summarised in Figure 2.3. Based on the similar degree of clustering, some possible connections between these populations have been suggested. However, as we shall discuss later, the possible connection between ERGs and other galaxy populations is still poorly understood. The clustering property makes necessary the study of ERG samples in large areas, to overcome the effects of cosmic variance[2].

2.4.2 Morphology

Another approach to studying the presence of evolved systems among the ERG population is morphology. Old passive systems are expected to look quite regular and compact, while burst-like star-forming systems display asymmetries and clumpiness in their morphology, e.g. [50]. The advent of the Hubble Space Telescope (HST) revolutionised this field, providing high-resolution images from which detailed galaxy morphology could be studied.

The surface brightness distribution $I(r)$ of an axisymmetric galaxy can be described by the following law:

$$I(r) = I_0 \, exp\left[\left(-\frac{r}{r_0}\right)^{1/n}\right], \tag{2.7}$$

where I_0 is the central surface brightness, r_0 is the characteristic scalelength and n is the so-called *Sérsic index* [51]. The brightness profiles of some elliptical galaxies are empirically found to be fitted by a Sérsic index $n = 4$ (de Vaucouleurs law [52]), while pure discs are characterised by exponential profiles with $n = 1$ (cf. Chapter 5).

The first significant studies of ERG morphology were made by Stiavelli & Treu (2000) [53] and Moriondo, Cimatti & Daddi (2000) [54]. The former work was based on a visual classification, while the latter used an algorithm to make a 2-dimensional (2D) modelling of the surface brightness distribution of the objects. On average, both works determined that $\sim 60\% - 80\%$ of the ERGs at redshift $z \sim 1$ had an elliptical shape, while the remaining objects were discy or irregular. However, these works already noticed that the morphological classification of ERGs suggested a more complex population than would be expected from the dichotomic scenario previously proposed.

[2]Although the term *sample variance* is more appropriate to refer to the errors introduced by the field-to-field variations, in this work we use *cosmic variance*, as it is usually referred to in the literature.

For instance, some compact objects appeared to have pure exponential (i.e. discy) brightness profiles. These objects could not be formally considered either as ellipticals, or as heavily-reddened starbursts given the regularity of their shapes.

This variety of morphologies in the ERG population was confirmed by later works. Yan & Thompson (2003) [45] studied a sample of 115 EROs and determined, both by visual inspection and using a profile fitting algorithm, that only $\sim 30\% - 37\%$ of the sample was composed of bulge-dominated objects. The majority of the ERGs appeared as disc-dominated and, some of them, as edge-on galaxies presumably at redshifts $z < 1$. Moustakas et al. (2004) [55] studied another sample of 275 ERGs with $K_s < 20.16$ and found, by visual classification, a similar proportion of elliptical galaxies. These authors noticed that the different ERG colours could be fitted by a relatively narrow range of SED templates, in spite of the rich variety displayed in the morphology. Thus, broad-band optical/near-IR magnitudes appeared as insufficient to reflect the diversity in the ERG morphological types.

No general consensus has yet been achieved regarding the morphology of ERGs and, in particular, the fraction of elliptical galaxies within the ERG population. The different conclusions obtained by different works were in part due to selection effects, such as incompleteness of the samples, different colour cuts, or the use of images taken at different wavelengths to study morphology. A systematic study of ERG morphology performed in conjunction with other complementary properties (e.g. redshifts, luminosities, masses) is still lacking. We continue the discussion of this issue in Chapter 5 and present the results of our morphological studies.

2.4.3 Spectra

ERGs are, by definition, relatively faint sources in optical bands and, thus, obtaining optical spectra for these objects is a very challenging task. The absence of near-IR multi-object spectrographs further complicates the situation, making it only possible to obtain near-IR spectra for a limited number of objects. Finally, the lack of prominent features in the observer-frame optical bands for sources at redshifts $1.5 \lesssim z \lesssim 2$ (the so-called *redshift desert)* makes spectroscopic observations particularly difficult for these high-redshift objects.

The K20 [35] survey provided the first significant sample (45 objects) of ERG

spectra [36]. The objects were classified into two groups: one characterised by spectra with no emission lines, a prominent 4000Å break and CaII H&K absorption lines, and the other one with spectra with no 4000Å break and strong [OII]λ3727 emission. Examples of the ERG spectra obtained in the K20 survey are shown in Figure 2.4. The two groups, which appeared equally populated, were identified with old passively evolving ellipticals and dusty star-forming systems, respectively. However, as it was noted by Yan, Thompson & Soifer (2004) [148], the direct association of the presence of old stellar populations with elliptical galaxies relied on the implicit assumption that galaxy spectral classes directly corresponded to morphology classes. Also, this reflected the traditional concept that the ERG population should necessarily be dichotomic.

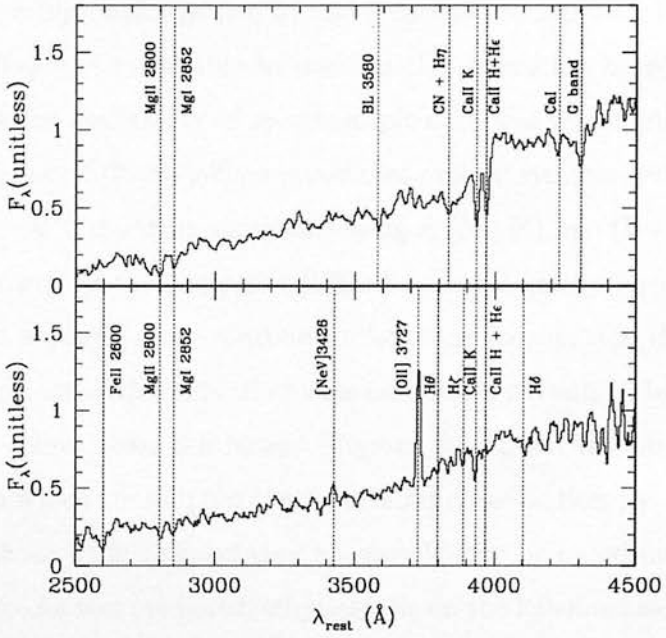

Figure 2.4: Examples of average ERG spectra in the K20 survey. The upper panel shows the spectrum of an old system at redshift $\langle z \rangle = 1.000$, where the rest-frame 4000Å break and characteristic absorption lines are clearly seen. The lower panel corresponds to a star-forming galaxy at $\langle z \rangle = 1.096$, characterised by a prominent [OII]λ3727 emission line. Figure taken from Cimatti et al. (2002) [36].

Yan et al.(2004) [148] obtained spectra for another sample of 24 bright ERGs. They found that 86% of the spectra presented absorption features from evolved stellar populations. On the other hand, 50% of the spectra had emission lines characteristic

of recent star formation. This showed that, for a significant fraction of ERGs, old and young stellar populations coexist. Moreover, these authors found that there were the same ratio of discy and bulge galaxies in the systems with emission lines in the spectra as in the systems with pure absorption lines. The conclusion was, then, that morphological and spectral classes do not necessarily correspond. The morphology of a galaxy might directly be conditioned by multiple factors other than its star-formation history, e.g. environment.

2.4.4 An attempt to solve the age and dust degeneracy

Under the dichotomic picture for ERGs of being either old elliptical galaxies or young dusty starbursts, a big challenge was to find a method to separate these two populations. This method had to be able to perform the separation based on photometric measurements, as the availability of spectroscopic data was very limited for ERGs.

Pozzetti & Mannucci (2000) [57] proposed that evolved systems and dusty starbursts at redshifts $1 < z < 2$ could be separated using a $(J - K)$ vs. $(I - K)$ colour-colour plot. The comparison of the respective SEDs for an old galaxy formed in a burst at high redshift and a young dusty starburst allows one to conclude that, even though the $(I - K)$ colours for both kinds of objects can be very similar, the former displays a bluer $(J - K)$ colour than the latter. Figure 2.5 shows the original Pozzetti & Mannucci plot, in which the elliptical and starburst classification has been made using independent methods such as spectroscopy, morphology or based on the presence of submillimetre flux. As was predicted, ellipticals lie on the left-hand side of the diagram while starbursts lie on the right-hand side.

However, it can be noted from Figure 2.5 that, in addition to the small statistics, some objects lie near the division line, which means that the applicability of the Pozzetti & Mannucci plot should be treated with some caution. As we have seen before, several recent studies conclude that the nature of ERGs appears as more complex than is expected in the traditional dichotomic elliptical/dusty-starburst picture. Actually, further attempts to use the Pozzetti & Mannucci criterion showed that $\sim 20\% - 30\%$ of both morphologically classified E/S0 and spiral/irregular galaxies usually lie on the wrong side of the diagram [58] (also [42]). This could be due to, for instance, the existence of mixed systems, in which underlying evolved stellar populations coexist with

recent or even still active star formation [58].

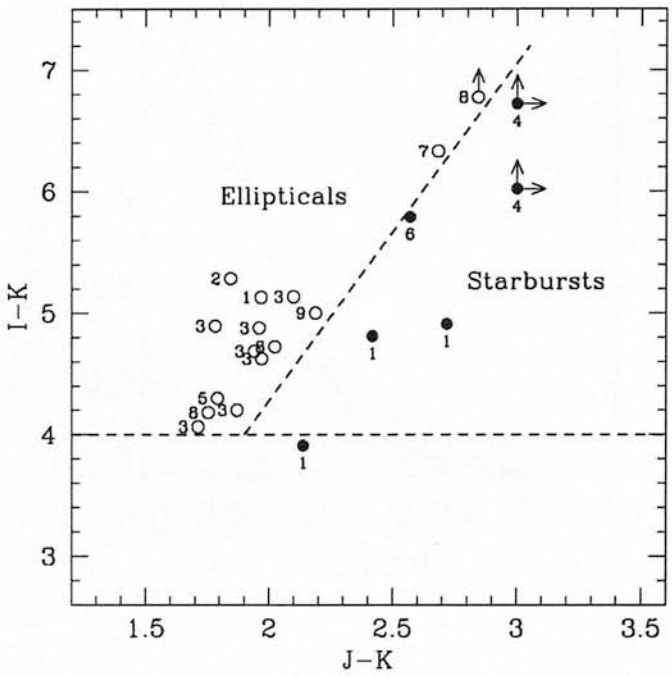

Figure 2.5: The (I − K) vs. (J − K) colour-colour plot for ERGs at redshifts $1 < z < 2$ (usually known as 'the Pozzetti & Mannucci plot'). Galaxies with evolved stellar populations are expected to lie on the left-hand side of the diagram, while dusty star-forming galaxies lie on the right-hand side. Recent studies have found a non-negligible fraction of objects lying on the wrong side of the diagram, probably due to the more complex nature of the ERG population. Figure taken from Pozzetti & Mannucci (2000) [57].

2.5 Assessment of galaxy formation theories

The determination of the presence of massive systems and systems with evolved stellar populations at high redshifts puts strong constraints on galaxy formation theories. As we have seen in §2.2.2, the rest-frame K band is the most suitable photometric tracer of stellar mass, as it is the region of the galaxy SED dominated by stellar light less affected by the galaxy star-formation history or dust extinction. K-band selected galaxy samples are expected to contain all of the most massive systems up to at least redshifts $z \sim 1 - 2$. Consequently, to reproduce the observed redshift distribution of K-selected galaxies has usually been a simple and powerful test for different paradigms of galaxy

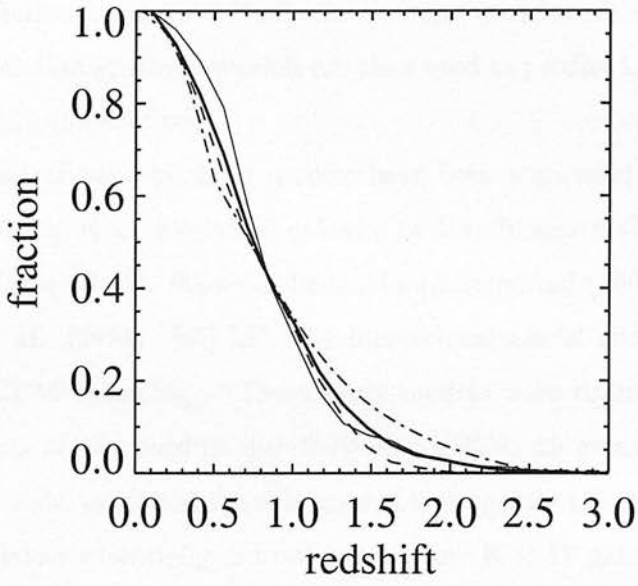

Figure 2.6: The cumulative redshift distribution of K < 20 (Vega) galaxies: GOODS/CDFS [70] (thick solid line); K20 survey [67] (thin solid line); PLE model (dotted-dashed); hierarchical model (dashed). Figure taken from Somerville et al. (2004) [69].

formation.

Traditional pure luminosity evolution (PLE) models of galaxy formation [59] [60] [61] are based on a phenomenological 'backwards-in-time' approach. They assume that all the galaxies observed in the local Universe have been formed at the same high redshift in a monolithic collapse and evolved as close-box systems. Some models also allow for the generation of new starbursts at every redshift, to account for local younger galaxies. The evolution of galaxies with different morphological types is usually parametrised using mean star formation histories which reproduce the observed SEDs. The ratios of the number counts of these different galaxy types, which are assumed to be constant in time, are normalised using the local type-dependent luminosity function (LF). The evolution of the LF and predictions for the number counts and redshift or colour distributions are computed using stellar population synthesis models.

In CDM models, on the contrary, the formation of galaxies occurs via the merging of small initial units in a hierarchical process [7] [8] [9] [62] [63] [64]. The evolu-

tion of galaxies is modelled consistently with different physical processes such as gas cooling, star formation, supernova feedback, chemical enrichment and the presence of dust. Stellar population synthesis models are then used to predict LFs, number counts, colours and redshift distributions.

The predictions of both kinds of models have been compared with the observed redshift distribution of $K < 19$-selected galaxies by Kauffmann & Charlot (1998) [41]. They used the PLE model by Pozzetti, Bruzual and Zamorani (1996) [61] normalised to the Marzke et al. (1994) [65] LF. The hierarchical model adopted corresponded to a $\Omega_m = 1$ SCDM cosmology. These early models were dramatically discrepant in their predictions of the redshift distributions for $K < 19$ galaxies. In particular, while the former model predicted the existence of an important high-redshift tail in the distribution, the latter essentially did not predict any $K < 19$ galaxies above redshift $z \sim 1$. Kauffmann & Charlot found that the observed redshift distribution of $K < 19$ galaxies was in much closer agreement with the adopted hierarchical model than the PLE model, and thus determined that the former was conclusively favoured.

The rejection of SCDM cosmological models in the following years in favour of ΛCDM models with lower Ω_m values made it necessary to revise the Kauffmann & Charlot test. Also, the PLE evolution models have been revised using more recent versions of the local LF for different morphological types [66]. The test was repeated by Cimatti et al. (2002) [67] with the K20 survey redshift distribution (see also [68]). This new comparison showed that: 1) the discrepancies between the predicted redshift distributions of both the revised PLE and hierarchical models were less extreme than before; 2) the observed redshift distribution of $K_s < 20$ galaxies was intermediate between the two models (but closer to the PLE prediction).

Still today, the most updated versions of both PLE and hierarchical models are not able to reproduce the observed redshift distribution of K_s-selected galaxies. Figure 2.6 shows the results of the most recent version of the Kauffmann & Charlot test, as performed by Somerville et al. (2004) [69] using the observed redshift distribution of the GOODS/CDFS $K_s < 20$ sample[3] [70]. The dashed and dotted-dashed curves in Figure 2.6 show the cumulative fraction of $K < 20$ galaxies at different redshifts, as

[3]Rigurously, the GOODS sample has been selected with $K_s < 22$(AB), equivalent to $K_s \lesssim 20.16$ (Vega)

predicted by updated versions of the hierarchical ΛCDM [64] [71] and PLE [69] models. The thick solid line is the observed GOODS $K_s < 20$ redshift distribution, while the thin solid line is the $K_s < 20$ distribution from the K20 survey. From Figure 2.6, we can see that the new prescriptions for the hierarchical and PLE models are in quite good agreement below redshift $z \sim 1$, while they are still very different at higher redshifts. The observed high-redshift tail of the redshift distribution lies between both model predictions, indicating that neither of them can correctly reproduce the observational results.

The hierarchical models particularly fail in reproducing the number counts of ERGs [72] [67] [69], the number counts of submillimetre galaxies and the fluctuations of the far-IR background [73]. However, ΛCDM models explain galaxy formation and evolution *ab initio* and are able to correctly predict global quantities, such as the number density of dark matter haloes massive enough to host different galaxy populations [74] (cf. Chapters 3 and 4). Thus, it seems that the problem does not lie in the ΛCDM models themselves, but in the treatment or the omission of some physical mechanisms which can influence star formation at very high redshifts. Several possible solutions for this problem have been proposed, such as the adoption of a top-heavy initial mass function (IMF) [74] [75], the inclusion of feedback from a central active nucleus [76], or galaxy-galaxy non-merging collisions [77], but so far they have only been partially successful in explaining all the observational results. A definitive prescription able to reproduce the distribution of all the galaxy populations within the ΛCDM models is still a challenge.

2.6 The relation between ERGs and other galaxy populations

2.6.1 Other red near-IR selected galaxies

The 4000 Å break characterising the presence of evolved stellar populations shifts into near-IR bands for galaxies with redshifts $z > 2$. Thus, sufficiently red $(J - K_s)$ sources are potential candidates for being evolved galaxies at very high redshift.

The existence of a galaxy with $(J-K_s) > 4$ in the Hubble Deep Field North (HDFN) was first reported by Dickinson et al. (2000) [78]. Its faint near-IR magnitudes ($K_s \approx 22$) and the observed optical/near-IR colours suggested diferent possibilities: either a

dusty galaxy at redshift $z > 2$, or a galaxy with an evolved stellar population with some additional reddening at $z > 3$, or even a Lyman-break galaxy at $z > 10$. Totani et al. (2001) [79] studied several objects with similar characteristics in the Subaru Deep Field (SDF) and proposed the name 'hyper extremely red objects' (HEROs) to identify this population. These authors determined that the density of these objects increased importantly at faint $K > 20$ magnitudes and, also, that the colours displayed by these galaxies could not be explained without the presence of dust. They concluded that these objects were likely to be progenitors of the local elliptical galaxies in their initial dusty-starburst phase. The $(J - K) > 4$ colours make the HEROs a sub-population of the ERGs (although Totani et al. considered they were different populations, based on the traditional idea that ERGs were objects at redshifts $z \sim 1 - 2$). As we shall see in Chapter 3, sufficiently deep ERG samples include these plausible high-redshift progenitors of local elliptical galaxies.

A more flexible $(J-K_s) > 2.3$ pure near-IR colour cut has been proposed by Franx et al. (2003) [142] as a suitable method to select galaxies with evolved stellar populations at very high redshift. These authors studied a sample of 14 such galaxies in $\sim 5\,\mathrm{arcmin}^2$ of the Hubble Deep Field South (HDFS) and concluded that the optical and near-IR colours of most of them could only be explained by the presence of an evolved stellar population, discarding the possibility for them to be young very dusty objects. Such colours could also be produced by the presence of emission lines, although it was quite unlikely that emission-line galaxies could account for a surface density of $\sim 3\,\mathrm{arcmin}^{-2}$. Franx et al. also pointed out that the $(J-K_s) > 2.3$ galaxies spanned different $(I-K_s)$ colours and, thus, this population contained objects which would not be selected in typical ERG samples. In Chapter 4, we further discuss the efficiency of the $(I - K_s)$ ERG colour cutoff to select all of the evolved and/or massive systems present at very high redshifts.

2.6.2 Radio galaxies

Powerful radio galaxies are known to be mainly hosted by giant elliptical galaxies (e.g. McLure et al. 1999 [81]) with evolved stellar populations. Thus, several works tried to explore the existence of ERG counterparts for radio galaxies and also the

existence of ERGs in radio galaxy environments. Actually, several of the first studies of ERGs were linked to radio galaxies [32] [16] [82] [83]. However, the connection between the two populations is still not clearly understood.

Different studies determined that the percentage of powerful radio counterparts for ERGs is very low. Willott, Rawlings & Blundell (2000) [84] estimated that only $\sim 3\%$ of the ERGs with $K < 19$ could be radio-loud AGN. Roche et al. (2002) [43], Smail et al.(2002) [42] and Cimatti et al.(2003) [58] found only 1/31, 3/50 and 1/46 ERGs, respectively, with $K_s < 19.5 - 20.5$, $(R - K_s) > 5.0 - 5.3$ and radio flux S(1.4GHz) $> 50\mu$Jy. However, $\sim 30\%$ of the ERGs with $K_s < 20.5$ have been found to have at least some modest radio emission ($S \gtrsim 15\mu$Jy) [42], probably related to active star formation rather than AGNs.

Other studies have revealed the existence of ERG overdensities in the environments of powerful radio sources at redshifts $1 \lesssim z \lesssim 2$ with respect to the blank field, e.g. [85] [86]. Although in most cases the real association between the radio sources and the ERGs could not be proved, the ERG colours were consistent with the possibility that these objects were at similar redshifts and, thus, populating the rich environments around AGNs.

2.6.3 Mid-to-Far-IR and submillimetre galaxies

The possibility that ERGs display extremely red optical/near-IR colours due to the presence of dust, makes them natural candidates for being detected at IR wavelengths. Different studies have explored the connection between ERGs and (ultra)luminous IR galaxies - (U)LIRGs . For instance, Smail et al. [42] estimated the far-IR luminosities of 11 radio-detected ERGs with $K_s < 20.5$, whose optical/near-IR colours were best-fitted by a dusty starburst SED template. Assuming that the local radio-far-IR correlation [87] [88] was valid at higher redshifts, they determined that 5/11 of these ERGs had far-IR luminosities $L_{FIR} > 10^{12} L_\odot$, and thus could be classified as ULIRGs. More recently, Yan et al. (2004) [89] studied the IR properties of a sample of ERGs with $K_s < 20.3$ and $(R - K_s) > 5.3$ over an area of $\sim 64\,\mathrm{arcmin}^2$. $\sim 50\%$ of these ERGs were significantly detected at $24\mu m$ (with flux $S > 40\mu$Jy) and their estimated mean IR luminosities were $L_{IR} > 3 \times 10^{11} L_\odot$ and $L_{IR} > 10^{12} L_\odot$, at redshifts $z = 1.0$ and $z = 1.5$, respectively.

Numerous studies have found ERGs counterparts to submillimetre sources, e.g. [90] [91] [92]. Wehner, Barger & Kneib (2002) [93] studied the submillimetre properties of 38 ERGs with $K \lesssim 21$ and $(I - K) > 4$, and determined that these objects could account for about one half of the $850\,\mu m$ background light. This result has recently been questioned by Webb et al. (2004) [94], who found that the contribution of ERGs to the $850\,\mu m$ background light was only $\sim 7\% - 11\%$. Webb et al. attributed the significant discrepancies between the results to: i) field-to-field variations (cosmic variance), given that they analysed an area ten times larger than the one covered by Wehner et al.; ii) source confusion within the large beam of the submillimetre telescope ($15''$ FWHM). However, these more recent figures are still not conclusive, because fainter near-IR sources have also been discovered to contribute to the submillimetre background. Based on a sample of 15 submillimetre galaxies, Frayer et al. (2004) [95] found that $\sim 80\%$ of these sources could be identified with $K < 23$ counterparts. Submillimetre galaxies appeared to mainly correspond to two different kinds of near-IR selected galaxies, either bright $K < 19$ sources with $(J - K) \approx 2$, or faint $K \sim 21 - 23$ sources with $(J - K) > 3$. These authors determined that, within their survey, the submillimetre galaxies with $(J - K) > 3$ colours could account for $> 40\%$ of the integrated $850\,\mu m$ background light above 5 mJy. From this wide variety of results, it is quite clear that the studies made so far are not sufficient to make up a definitive picture of the importance of $(I - K)$ or $(J - K)$ extremely red near-IR-selected galaxies among the submillimetre galaxy population.

2.6.4 X-ray sources

Different X-ray surveys have identified ERG counterparts to X-ray sources, e.g. [96] [97] [98]. Alexander et al. (2002) [99] determined that most of the X-ray sources with very red optical/near-IR colours were luminous obscured AGNs, characterised by X-ray luminosities $L_{0.5-10\,\mathrm{keV}} > 10^{42}\mathrm{erg\,s^{-1}}$ (see also [100] [101]). A minority of X-ray sources identified with ERGs were only detected in the soft X-ray bands ($0.5\,\mathrm{keV} - 2.0\,\mathrm{keV}$), indicating the existence of less energetic processes, either starbursts, normal galaxy emission or lower-luminosity AGNs.

ERGs with different $(J - K)$ colours have been found to be associated with X-ray sources. Stevens et al. (2003) [103] and Roche et al. (2003) [47] used the Pozzetti &

Mannucci (2000) [57] colour-colour plot to classify ERGs detected in the X-rays. An interesting result is that ERGs associated with luminous AGNs appear on either side of the Pozzetti & Mannucci plot. Possibly this is indicating different degrees of reddening in the host galaxies of these AGN, or also the simultaneous presence of an AGN and active star formation. Roche et al.(2003) also found some non-negligible spatial cross-correlation between ERGs and X-ray sources, suggesting that both populations could be tracing the same large-scale structure.

However, only a minor fraction of the total ERG population is significantly detected in the X-ray bands. Alexander et al.(2002) and Brusa et al. (2002) [102] used stacking analysis to determine the average X-ray properties of the non-individually detected ERGs. They found that the X-ray emission produced by the majority of the ERGs did not correspond to AGN activity. In particular, using optical spectra from the K20 survey, Brusa et al. determined that the only significant stacked X-ray signal was produced by galaxies with [OII]λ3727 emission, indicating that most of the contribution of the ERGs to the X-ray bands was the consequence of active star formation.

2.7 Summary and discussion

In this chapter we have reviewed the main properties of ERGs, as determined by the numerous studies which followed their discovery. The ERG colour cut was probed to be a useful technique for the selection of evolved stellar systems at high redshifts. For many years, most of the efforts have been concentrated in separating the sub-populations of young dusty starbursts and evolved stellar systems within the ERGs. However, it has been progressively suggested that the nature of the extremely red $(I-K_s)$ colours could be more complex than initially thought. The different attempts to cross-correlate the ERGs with other galaxy populations have confirmed this complexity, as a clear unified picture of the relations between different galaxy populations has not been achieved.

Many works have suggested, and now it is commonly believed, that the ERG population should contain the progenitors of the oldest and most massive galaxies observed in the local Universe, in particular cluster elliptical galaxies. However, there are many open questions around such a hypothesis. Firstly, it is not clear whether ERGs could account for *all* the most massive systems present in the local Universe, or at least for

the most massive local early-type galaxies. Actually, the precise determination of the fraction of massive systems which have assembled the bulk of their stellar mass at early epochs is still one of the big challenges of extragalactic astronomy. We intend to help to clarify these issues with the present work.

In Chapter 3, we present our study of the deepest significant sample of ERGs selected to date. We use the broad-band optical/near-IR magnitudes of these objects for modelling their properties and estimate their redshifts. Our main aim is to investigate the evolutionary line traced by the ERG population. In Chapter 4, this work is enhanced by the study of the complete parent sample of near-IR selected galaxies, which allows us to achieve a further understanding of the role of ERGs in the history of galaxy evolution. Finally, in Chapter 5, we explore the bridge between massive ERGs and local massive galaxies to try to understand the later stages of the ERG population.

Chapter 3

A deeper view of Extremely Red Galaxies

3.1 Introduction

In Chapter 2, we reviewed the basic properties of ERGs and explained in detail the importance of the study of these objects to explore the epoch of massive galaxy formation and assess different galaxy formation theories. In this chapter, we present our study of the redshift distribution and derived cosmological properties for a sample of 198 ERGs with $K_s \leq 22$, selected from $50.4\,\mathrm{arcmin}^2$ of the Chandra Deep Field South (CDFS). The layout of this chapter is as follows: in §3.2, we overview the Great Observatories Origins Deep Survey (GOODS) [104] project, on whose data the present work is based. In §3.3, we give details of the ERG sample selection, as performed by Roche et al.(2003) [47], and our multiwavelength photometry. In §3.4, we explain the performance of photometric redshift algorithms and our strategy to obtain redshift estimates for the ERG sample. In §3.5, we present our results: the ERG redshift distribution; the Hubble diagram; the red envelope of galaxy evolution; the evolution of the ERG luminosity function (LF) and the number densities of ERG progenitors of local $L > L^*$ galaxies. We also explore the existence of ERGs beyond redshifts $z = 4$ within our sample and review an ERG cluster candidate at redshift $z \sim 1.5$. Finally, in §3.6, we summarise and discuss our results. Except where explicitly cited in the text, all the contents of the present chapter from §3.3.2 until the end are my own work, made with the collaboration of James Dunlop, Ross McLure and Nathan Roche.

3.2 The GOODS project

3.2.1 General description

The GOODS project [104] aims to explore the distant Universe with the deepest multiwavelength images taken to date using the major available space and ground-based facilities. GOODS is surveying 320 arcmin^2 of the sky, equally divided into two fields: the Chandra Deep Field South (CDFS) and the Hubble Deep Field North (HDFN). The GOODS/HST Treasury Program consists of optical and near-IR data taken with the Advanced Camera for Surveys (ACS) on board the Hubble Space Telescope (HST), with four broad non-overlapping filters: F435W (B), F606W (V), F775W (I_{775}), and F850LP (z). The exposure times were 3, 2.5, 2.5 and 5 HST orbits, respectively. Other available or in-progress imaging data in the GOODS fields include X-ray maps from Chandra and XMM-Newton, and near-to-mid-IR images from the Spitzer Space Telescope, at 3.6μm, 4.5μm, 5.8μm and 8.0μm with the *Infrared Array Camera (IRAC)* and at 24μm with the *Multiband Imaging Photometer (MIPS)*. In particular, the CDFS has also been mapped with the Infrared Spectrometer and Array Camera (ISAAC) on the 'Antu' Very Large Telescope (Antu-VLT), with the H, J and K_s-band filters, as part of the GOODS European Southern Observatory (ESO) Imaging Survey (GOODS/EIS). The GOODS/CDFS imaging is being complemented with spectroscopy programs, conducted with the VLT FOcal Reducer/low dispersion Spectrograph (VLT/FORS) and the VIsible MultiObject Spectrograph (VLT/VIMOS).

In addition, ultra deep HST/ACS observations (412 HST orbits) have been performed with the four GOODS/ACS filters, in a small area of $\sim$ 27.5 arcmin^2 within the CDFS called the *Hubble Ultradeep Field (HUDF)*. These observations were complemented by ultra-deep near-IR images taken with the HST-Near Infrared Camera and Multi Object Spectrometer (HST/NICMOS) with the F110W (J) and F160W (H) filters (http://www.stsci.edu/hst/udf).

The GOODS data are kindly relased to the astronomical community in a fully reduced mode[1]. The unprecedented quality of the GOODS images covering from X-rays to radio wavelengths in a significant area of the sky offers a unique opportunity to investigate galaxy formation and evolution since very high redshifts.

[1]The GOODS data are available at http://www.stsci.edu/ftp/science/goods/ and links therein.

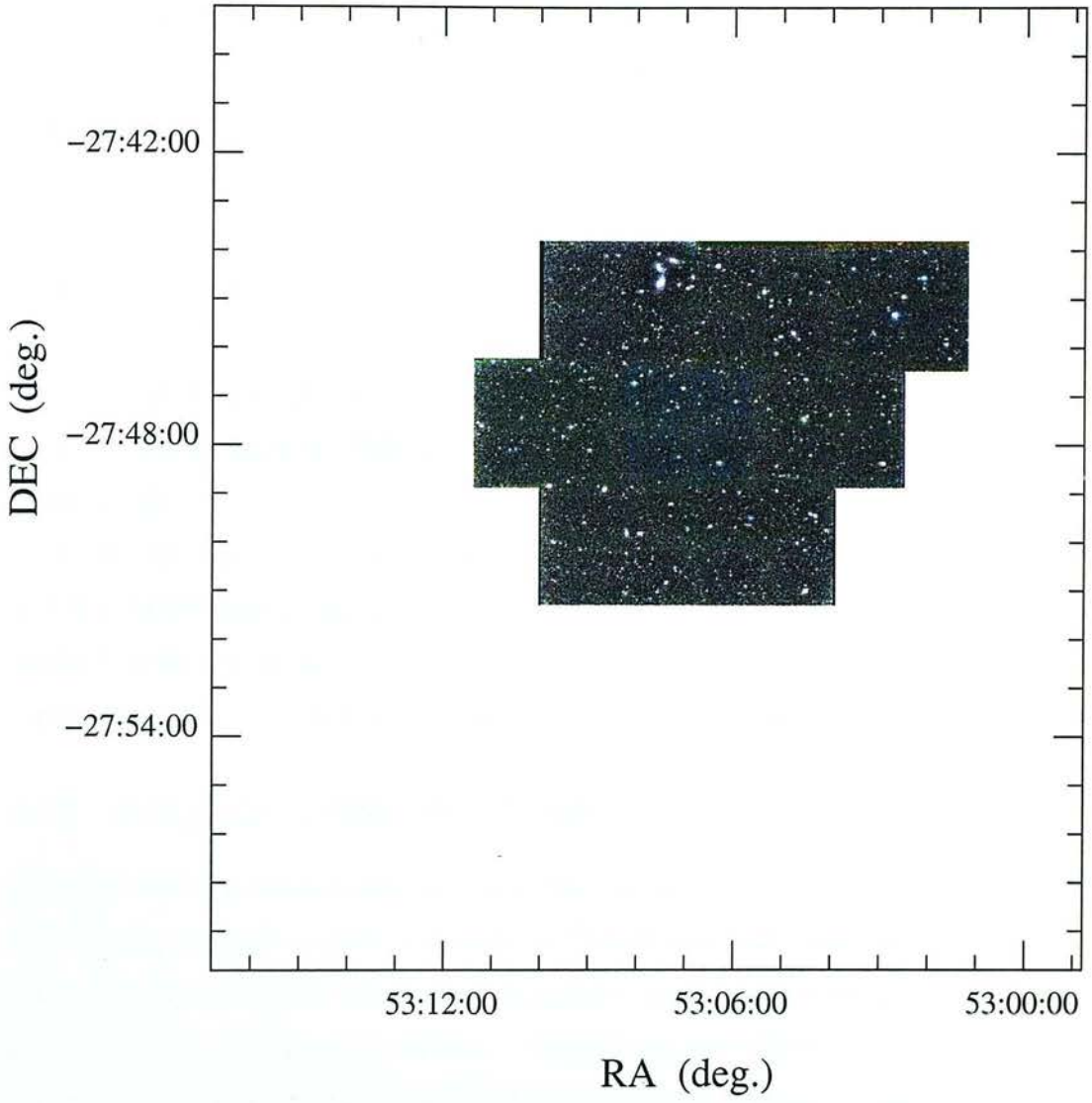

Figure 3.1: Schematic diagram of the sub-region covered by the deep v0.5 GOODS/EIS VLT/ISAAC near-infrared imaging within the larger GOODS/CDFS field with full HST-ACS coverage. This sub-region is referred as the 'GOODS/CDFS deep ISAAC field' throughout this work. Composite J,H,K_s-band mosaic taken from http://www.eso.org/science/goods/releases/20020408/.

3.2.2 The GOODS/CDFS deep ISAAC field

The galaxy samples we analyse in the present work have been selected from 50.4 arcmin^2 of the GOODS/CDFS field, only one third of the CDFS area with full HST/ACS coverage. Deep near-IR images in the J, H and K_s bands were made public for this

50.4 arcmin^2 sub-region in April 2002, as part of the GOODS/EIS v0.5 data release. In the following, we refer to this area as the *GOODS/CDFS deep ISAAC field*, and its location within the full GOODS/CDFS field is shown in Figure 3.1. The GOODS/EIS v0.5 release consisted of 24 maps, covering 8 ISAAC pointings in each of the three near-IR filters. The total exposure times were 2.20-4.20 h, 3.87-4.80 h and 5.78-7.94 h in J, H and K_s, respectively. Each map was astrometrically and photometrically calibrated, and the individual zero-points and corresponding weighting maps were provided as part of the public release. The ISAAC images have a pixel scale of 0.1484 arcsec/pixel and the point-spread function (PSF) full-width half maximum (FWHM) in the K_s-band is ~ 0.40 arcsec.

At the moment of writing, the public release of deep ISAAC images for the whole GOODS/CDFS field is still in progress. Most of the J and K_s-band images were made available in May 2004, as part of the GOODS/EIS v1.0 release. The release of the deep H-band data and a few additional J and K_s-band images is still due for completion.

3.2.3 HST/ACS optical/near-IR imaging

The other GOODS datasets mainly used in this work are the GOODS/CDFS HST/ACS images in four broad bands B, V, I_{775} and z. The B-band data was taken and publicly released in a single epoch, while the V, I_{775} and z-band images were taken in 5 epochs and made public in progressive releases. The total exposure times were 3, 2.5, 2.5 and 5 HST orbits, respectively. The final, fully-reduced, stacked 5-epoch images for each filter, in conjunction with the corresponding weighting maps, were made available in August 2003 (v1.0 GOODS HST/ACS data release). These stacked images corresponded to 18 tiles which covered the whole GOODS/CDFS field and were drizzled to a scale of 0.03 arcsec/pixel to optimise the PSF sampling. The PSF FWHM of the ACS z-band images is ~ 0.10 arcsec.

3.3 The ERG sample

3.3.1 Sample selection

Roche et al.(2003) [47] (hereafter R03) used the ISAAC v0.5 K_s-band and the HST/ACS I_{775}-band images to select a sample of 198 ERGs with $K_s \leq 22$ and $(I_{775} - K_s) > 3.92$ in

the GOODS/CDFS deep ISAAC field[2]. They perfomed the source extraction on the K_s-band images using the public code SEXTRACTOR [105], applying a detection criterion of $1.4\sigma_{sky}$ in at least six contiguous pixels, and using the corresponding weighting maps. A 3.0-pixel FWHM Gaussian kernel was employed to improve the source detection (cf. SEXTRACTOR user's guide [106]). They measured total Kron-type K_s magnitudes (SEXTRACTOR 'MAG_AUTO') for each source and used these magnitudes to cut the sample at $K_s \leq 22$. They also measured aperture magnitudes in 2-arcsec diameter circular apertures, which were used to compute colours. SEXTRACTOR was run in 'two-image' mode to perform photometry in the J and H bands, using the K_s-band maps as reference. 2-arcsec-diameter aperture magnitudes were also measured on the J and H-band maps.

Roche et al. perfomed a separate detection of sources on the I_{775}-band images, applying a threshold of $1.75\sigma_{sky}$ in at least eight contiguous pixels. The K_s-band catalogs were cross-correlated with the I_{775}-band catalogs, matching sources within 1.0-arcsec angular distance. The aperture magnitudes in both bands were used to separate the sources with colours $(I_{775} - K_s) > 3.92$. 155 and 43 K_s-selected sources with and without I_{775}-band counterparts, respectively, satisfied this colour cut, producing a final ERG sample of 198 objects. All the selected ERGs are at least 3σ detections on the K_s-band images.

It is worthwhile to mention that other previous studies of ERGs exist in the CDFS, although they only reach shallower magnitudes, $K_s \lesssim 20$. For example, the K20 survey has yielded spectroscopic redshifts for EROs in 32.2 arcmin^2 of this field [36]. More recently, Moustakas et al. (the GOODS team) 2004 [55] selected a sample of EROs from the whole GOODS/CDFS field. The area covered by this brighter ERO sample is three times greater than the area covered by the R03 sample studied here. However, the Moustakas et al. sample only reaches a depth of $K_s \sim 20.2$ (equivalent to $K_s = 22$, AB), and so the present study probes a different (and complementary) region of parameter space to that already explored by the GOODS team.

[2]The cut $(I_{775} - K_s) > 3.92$ is equivalent to $(I - K_s) > 3.75$ referenced to the standard I filter, which has a slightly longer effective wavelength ($\lambda_{\rm eff.}(I) = 0.806\,\mu$m against $\lambda_{\rm eff.}(I_{775}) = 0.771\,\mu$m).

3.3.2 Multiwavelength photometry

We looked for counterparts of the Roche et al. K_s-selected ERGs on the HST/ACS images. We performed photometric measurements for the four ACS bands on the GOODS 5-epoch stacked images (V1.0 HST/ACS data release), using the corresponding weighting maps. We looked for counterparts of the K_s-selected ERGs on the I_{775} and z-band images within an angular radius of $1''$. For B and V bands we restricted the search of counterparts to $0.5''$ to minimise the presence of interlopers. We also performed the magnitude measurements using the public code SEXTRACTOR. Many ERGs appeared as non-detected in the B and V bands, and some of them as non-detected in the I_{775} or z bands. The algorithms for computing photometric redshifts depend critically on the adopted values of limiting magnitudes in the case of non detections, and a careful treatment of potential 'dropouts' is necessary to prevent the photometric redshift algorithms from finding fake high redshift sources. Therefore, in each case of a SEXTRACTOR non-detection, we used the IRAF task 'phot' to measure aperture magnitudes centred at the ERG K_s-band position. We measured $2''$-diameter aperture magnitudes on each ACS filter for those ERGs with $z_{2''} < 26\,(\mathrm{AB})$. Beyond $z_{2''} = 26\,(\mathrm{AB})$, we found that little flux was missed using $1''$ instead of $2''$-diameter aperture magnitudes. Thus, for objects with $z_{2''} > 26\,(\mathrm{AB})$, we used $1''$-diameter aperture magnitudes to reduce the random errors, and corrected the values systematically using the average offset between the $2''$ and $1''$-diameter aperture magnitudes measured in each $\Delta = 1$ magnitude bin. After this procedure, only a few objects remained as formally non-detected in the V or redder ACS bands.

As a final comment on the photometry, we note that, while we were finishing the work presented in this chapter, the GOODS/CDFS HUDF images were made public (March 2004). We used the ACS/NICMOS ultra deep optical and near-IR images of the HUDF to revise the photometry of three ERGs which were included in an initial list of potential very high redshift sources (cf.§3.5.6). The procedure we followed to perform photometric measurements on these images is similar to the one used for the 5-epoch stacked GOODS HST/ACS images.

3.4 Redshift estimates

3.4.1 Photometric redshift algorithms

Introduction

The most reliable method of determining a galaxy redshift is measuring the shift of the continuum and characteristic lines in its spectrum. However, as was discussed in §2.4.3, obtaining spectra for high-redshift sources is usually restricted to a relatively small numbers of objects, due to the technical limitations of the currently available spectrographs. In the last years, particularly with the advent of 10m-class telescopes, wide and deep surveys have allowed for the construction of large galaxy catalogs. Most of these galaxies are inaccesible to spectroscopy and, thus, alternative methods are necessary to obtain redshift estimates for these objects.

The idea of using photometry to obtain redshift estimates has been firstly proposed by Baum (1962) [107], but these techniques have not been widely used until the nineties, when it became necessary to obtain redshifts for large samples of galaxies. Photometric redshift algorithms are mainly divided into two classes: those based on an empirical 'training-set' method and those based on a SED-fitting procedure. The 'training-set' approach [108] consists in deriving empirical relations between magnitudes and redshifts using galaxies with known spectroscopic redshifts. Although these methods have the advantage of not making any assumption on galaxy SED evolution, their applicability to faint objects is quite limited, because the magnitude-redshift relations for these objects can be very different to those for the bright objects used to calibrate the training-sets. SED-fitting techniques, on the other hand, are based on the comparison of the observed galaxy SED with reference templates, which can be empirical or synthetic. The efficiency of these methods relies on the presence of strong spectral features, as the 4000 Å or the Lyman breaks, in the case of broad-band photometry, or strong emission lines when narrower filters are used. In the next sections, we explain in some detail the algorithms we used to obtain redshift estimates, both based on SED fitting but which follow very different approaches.

HYPERZ

The public code HYPERZ [109] applies a SED-fitting technique to estimate redshifts. The best template matching the observed galaxy SED is determined through a *maximum likelihood* estimation. Each SED model is basically characterised by four free parameters: the star formation history of the galaxy, the age, the redshift and the extinction A_V. If we assume that the observed galaxy flux in each band is normally distributed around the 'true' SED model, a good maximum-likelihod estimator can be defined with a χ^2 distribution:

$$\chi^2(z) = \sum_{i=1}^{N_{filters}} \left[\frac{f_{obs.,i} - b\, f_{temp.,i}(z)}{\sigma_i} \right]^2 , \tag{3.1}$$

where $f_{obs.,i}$ and $f_{temp.,i}$ are the observed and template fluxes in the filter i; σ_i is the corresponding error of the observed i-filter flux and b is a normalisation constant. The best-fit parameters for a galaxy are those corresponding to the SED model which minimises eq.(3.1).

The HYPERZ template library contains synthetic and empirical SEDs. The 408 available synthetic spectra were constructed using the GISSEL98 evolutionary code by Bruzual & Charlot [110]. These templates correspond to galaxies with 51 different ages and 8 different star-formation histories: single burst, exponentially-decaying star-formation with characteristic times 1 Gyr, 2 Gyr, 3 Gyr, 5 Gyr, 15 Gyr, 30 Gyr, and constant star formation. These star-formation histories roughly reproduce the SEDs of local galaxy types: burst, E, S0, Sa, Sb, Sc, Sd and Irr, respectively. All the models assume a solar metallicity, but a parallel set of templates with evolving metallicities is also provided. The library also contains a set of empirical SEDs by Coleman, Wu & Weedman (1980) [111]. The templates to be applied in the SED fitting can be selected by the user.

The effects of dust extinction are taken into account by the convolution of the SED templates with a pre-selected reddening law. Five different reddening laws can be used in HYPERZ: two different laws for the Milky Way [112] [21] [25], a LMC law [25], a SMC law [26] [113] and a Calzetti reddening law [27]. The extinction A_V value is a free-parameter of the modelling, but the range of possible A_V values is set by the user, as is the range of possible values for the redshift z_{phot}.

HYPERZ generates several files in the output. The .z_phot output file contains the parameter values associated to the best-fit solution for each source, namely the most likely values for the redshift z_{phot} (the HYPERZ *primary solution*), its χ^2 associated probability, the SED type, the age, the extinction A_V and the k-corrected absolute magnitude in a given filter. Also, the second most-likely solution in redshift space is provided (the HYPERZ *secondary solution*). The output file .log_phot gives the best-fit parameters and associated χ^2 probability in each fixed redshift step for each source, allowing for the reconstruction of the whole probability distribution in redshift space. The redshift distribution allows to assess the significance of the HYPERZ primary solution and to study the possible existence of degeneracies.

BPZ

The public Bayesian photometric redshift (BPZ) code [114] is also based on a SED fitting procedure, but uses a Bayesian rather than a frequentist statistical approach. A detailed comparison of these statistical methods is beyond the scope of this work (see e.g. [115]), so we only briefly mention here the basic differences in the philosophies of the two approaches. In the frequentist approach, probability is a measurement of randomess. The variable x on which the probability wants to be measured is assumed to be a random variable which can take different possible values. After a number of trials, it can be determined the frequency with which x takes each of those possible values. The probability assigned to each value of x is the corresponding frequency in the case in which the number of trials tends to infinity. In the Bayesian approach, on the other hand, the probability is a measurement of the plausibility of a fixed hypothesis, e.g. that x takes a specific fixed value, conditioned to some known piece of information.

In particular, for the problem of redshift estimations, the purpose of the Bayesian approach is to determine the probability that a source belongs to a spectral type T and is at redshift z, knowing e.g. its magnitudes m_i in different filters $p(T, z|m_i)$. One of the main differences with the maximum likelihood approach is that the Bayesian technique allows for the use of priors, which include additional information relevant to the considered hypothesis, not contained in the data. The use of priors makes the Bayesian approach to be actually a mixture of a SED-fitting and a 'training-set' techniques. In the case of BPZ, the prior used is the probability redshift distribution

expected for a galaxy with magnitude m_o in a given filter, as it was calibrated using the HDFN galaxy catalogs. The final estimated redshift and spectral type in the Bayesian approach are derived from the averages over all the possible likelihoods weighted with the prior probabilities.

In the present work we used the code HYPERZ to obtain estimated redshift for our galaxy samples. The choice of this algorithm was mainly based on the complete information on the best-fit galaxy model which is provided in the HYPERZ output. Also, HYPERZ allows for the computation of probability density distributions in redshift space. On the other hand, we used the code BPZ to obtain a second, independent redshift estimate for our objects. Our strategy for the use of both algorithms will be expained in Section 3.4.3 and in the relevant sections of Chapter 4.

3.4.2 Caveats

Although photometric redshift algorithms allow for the possibility of having redshift estimates for large samples of galaxies, the potential limitations and problems should be kept in mind. Firstly, to obtain reliable estimates, it is important to have accurate photometry in at least a minimum of four or five bands. This problem is usually overcome with current multiwavelength surveys. The other most important problem associated with photometric redshift techniques is the existence of degeneracies in parameter space. This is in principle independent of the quality of the photometry, although the availability of magnitudes in multiple bands can contribute to lift these degeneracies. Degeneracies in redshift space may arise by the confusion of spectral features, the most common being the confusion between the 4000Å and the Lyman breaks. For red sources as the ERGs, the so-called age-dust degeneracy is also important, i.e. the red colours can either be explained by an old-galaxy model or by the model of a young galaxy heavily extincted by dust. In extreme cases, the existence of degeneracies in parameter space might lead to 'catastrophically' wrong estimated redshifts and other derived parameters.

In this work, as in most of the literature, we considered the HYPERZ primary solution as the 'true' model for each galaxy, except in the cases otherwise stated. We attempted to mitigate the impact of degeneracies taking into account, for instance, the probabilty density distribution of each galaxy in redshift space, whenever possible.

Table 3.1: The effective wavelengths of the filters used in HYPERZ.

Passband	B	V	I_{775}	z	J	H	K_s
$\lambda_{eff.}$ (Å)	4331.7	5961.2	7712.7	9043.5	12535.5	16514.6	21612.5

However, a more rigurous and complete treatment of degeneracies should take into account the probabilty distributions in the whole parameter space for each source. We discuss the photometric redshift uncertainties and degeneracies for our galaxy samples throughout this work.

3.4.3 Strategy for redshift estimations

We computed photometric redshifts for the ERGs in the R03 sample with the public code HYPERZ, using the seven passbands described in Sections §3.3.1 and §3.3.2 (B, V, I_{775}, z, J, H and K_s) and the GISSEL98 library of Bruzual & Charlot [110]. The effective wavelengths of the used filters are given in Table 3.1. We restricted HYPERZ to use exclusively models with solar metallicity, to avoid having a large number of free parameters. Metallicity is a secondary-importance parameter for the determination of the redshifts [109]. To account for dust obscuration, we applied a Calzetti et al. (2000) reddening law [27], allowing the extinction in the V-band (A_V) to vary between 0 and 1. For the most extincted objects, we ran HYPERZ again allowing A_V to vary between 0 and 3. In general, this did not produce any substantial changes in the redshift estimations, but did have some impact on the estimated absolute magnitudes and ages.

We also used the public code BPZ to obtain a second, independent set of redshift estimates for the ERGs in our sample. The agreement between the redshifts estimated by the HYPERZ and the BPZ codes is quite good in most cases. Accordingly, with a few exceptions discussed individually in later sections, we have adopted the HYPERZ results for the ERG sample simply because it provides not only the redshift probability distribution, but also several other useful quantities in the output, as we described in Section §3.4.1 .

Figure 3.2 shows examples of the best-fit SEDs (left-hand panels) and redshift

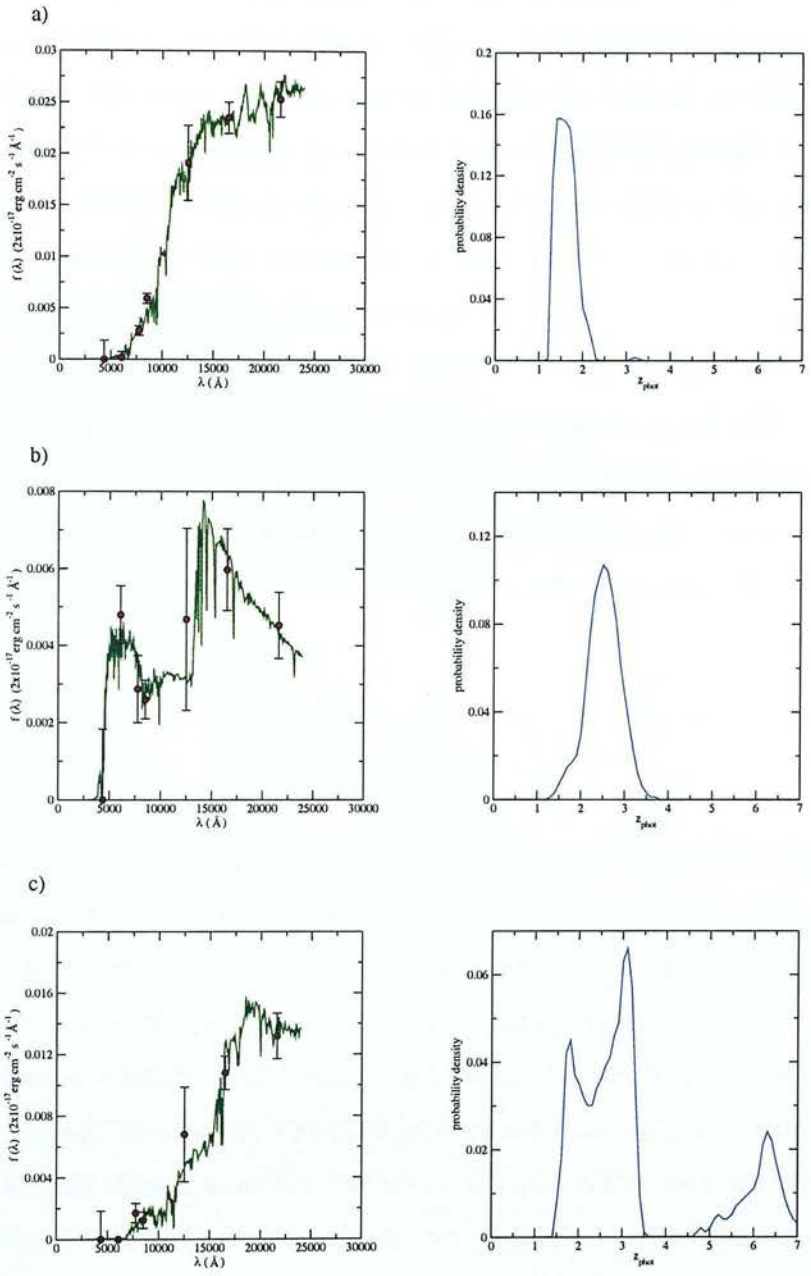

Figure 3.2: Examples of spectral energy distributions (left-hand plots) and redshift probability density distributions (right-hand plots) for three ERGs in the deep ISAAC field. a) an ERG with HYPERZ primary solution $z_{\rm phot} = 1.40$, b) an ERG with primary solution $z_{\rm phot} = 2.52$, c) an ERG with primary solution $z_{\rm phot} = 3.10$. The circles in the SED plots correspond to the measured aperture magnitudes in each filter. The green solid-line curves indicate the best-fit template in each case.

probability density distributions (right-hand panels) for three of the ERGs in the R03 sample. In the SED plots, the circles correspond to the measured aperture magnitudes in each filter. The green solid-line curves indicate the best-fit templates. The SED shown in fig. 3.2-a) corresponds to an object with HYPERZ primary solution $z_{phot} = 1.40$. The accuracy in the fitting and the small error bars in the photometry are reflected in a relatively small uncertainty in the redshift estimation. The SED shown in fig. 3.2-b) corresponds to an object with primary solution $z_{phot} = 2.52$. In this case, the larger error bars in the photometry produce a wider redshift probability density distribution. Finally, the SED in fig. 3.2-c) corresponds to an ERG with primary solution $z_{phot} = 3.10$. This is an example of an object with significant degeneracy in redshift space: the corresponding redshift distribution also shows non-negligible probabilities for this object to be either at $z_{phot} \sim 1.8$ or at $z_{phot} > 5$.

3.5 Results

3.5.1 The redshift distribution

Figure 3.3 shows our derived redshift distribution for the ERGs in the GOODS/CDFS deep ISAAC field. A few objects have been excluded either because their light is contaminated by bright neighbours or because they are quite likely to be stars given their very blue $(J - K_s)$ colours. These objects are characterised by very low probabilities of being at any redshift as deduced by HYPERZ. We constructed the histogram in fig. 3.3-a) taking into account HYPERZ primary solutions only, for ease of comparison with the Hubble diagrams shown in §3.5.2. For the ERGs with identification numbers e1504 and e1605 in the R03 sample, we adopted the redshifts estimated by the BPZ code instead of the HYPERZ primary solution, for reasons which are explained in §3.5.6. This histogram, as well as all the results presented hereafter, include the revised redshifts of the potential high-z candidate ERGs e778, e1113 and e1272, as they were determined after measuring the photometry of these objects on the NICMOS and ACS ultra deep images of the HUDF. We also show in fig. 3.3-a) the redshift distribution for the shallower sample of ERGs in the field of the GOODS/CDFS with full HST/ACS coverage, as obtained by Moustakas et al. (2004) [55](shaded histogram). The Moustakas et al. histogram has been divided by a factor of 3.08 in order to normalise their

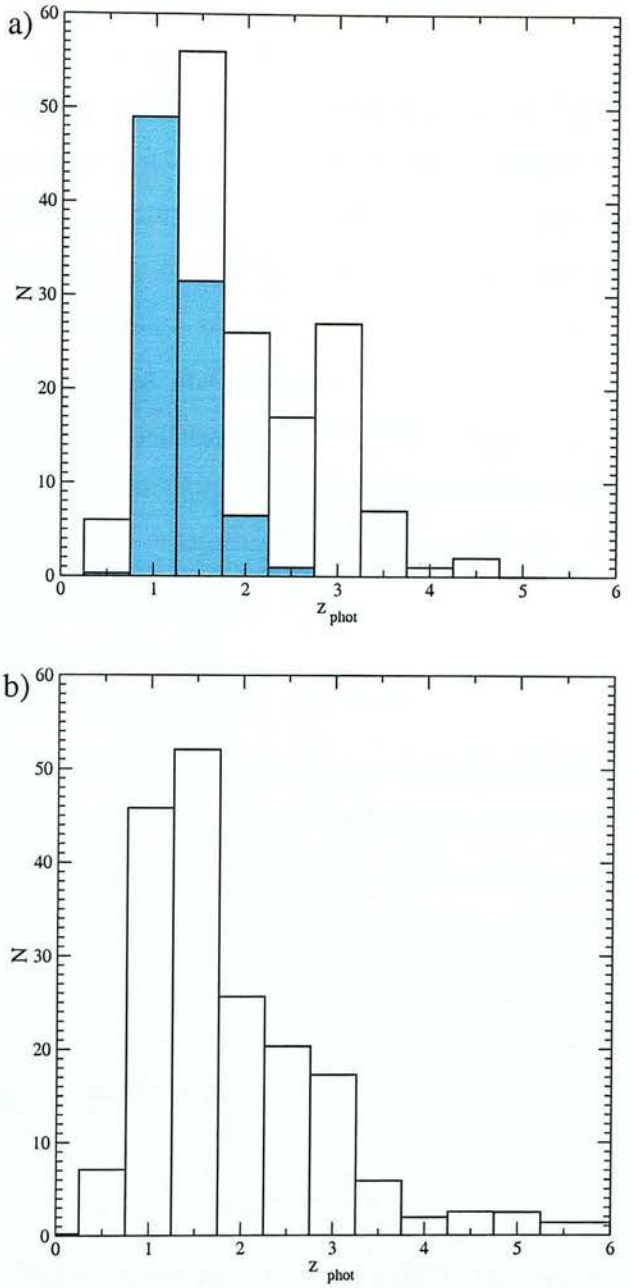

Figure 3.3: The redshift distribution of the ERGs in the deep ISAAC field sample: a) taking into account only HYPERZ primary solutions, b) taking into account the probability density distribution of each ERG in redshift space and small corrections due to the incompleteness of the sample. In the upper plot a), the redshift distribution of the shallower sample of ERGs selected by Moustakas et al. (2004) [55] in a wider area of the GOODS/CDFS has been added for comparison (cyan shaded histogram), after division by a factor of 3.08 in order to normalise their distribution to produce the same number of objects in the redshift bin centred at $z_{phot} = 1$ as found in the present study.

redshift distribution, to produce the same number of objects in the redshift bin centred at $z_{phot} = 1$ as found in the present study.

The redshift distribution for the ERG sample in the GOODS/CDFS deep ISAAC field spans the range $z_{phot} \sim 0.5-4.75$. Moustakas et al. sample, which is approximately two magnitudes shallower, only includes objects up to redshift $z_{phot} = 2.5$. The maximum of our redshift distribution of $K_s < 22$ ERGs is located at redshift $z_{phot} \sim 1.5$. We find a secondary maximum at redshift $z_{phot} \sim 3$. However, this secondary peak is not statistically significant and disappears when probability densities are used to construct the redshift distribution as shown in fig. 3.3-b). This latter histogram also includes very small corrections for the incompleteness of the sample[3] and, thus, should be taken as a more realistic representation of the redshift distribution of the ERGs in the GOODS/CDFS deep ISAAC field.

3.5.2 The Hubble diagram: K_s vs. z_{phot}

Figure 3.4 shows the Hubble diagram (K_s vs. z_{phot}) for the ERGs in the GOODS/CDFS deep ISAAC field, corresponding to the redshift distribution presented in fig. 3.3. The plots labelled as a) and b) show the raw and dust-corrected K_s magnitudes as a function of redshift, respectively. Total (SEXTRACTOR 'MAG_AUTO') K_s magnitudes are considered in this case. We computed the dust-corrected K_s magnitudes using the V-band extinction value A_V applied to the best-fit SED in HYPERZ. The rest-frame wavelength sampled by the K_s-band is

$$\lambda_{rf} = \frac{\lambda_{K_s}}{1 + z_{phot}}, \tag{3.2}$$

where λ_{K_s} is the effective wavelength of the K_s filter, i.e. $\lambda_{K_s} = 2.16\,\mu$m. In a dust-screen model, the extinction at a wavelength λ_{rf} is related to the extinction in the V-band (A_V) by

$$A_{\lambda_{rf}} = \frac{k(\lambda_{rf})\, A_V}{R_V}. \tag{3.3}$$

[3]Roche et al. ERG sample is considered to be $\sim$ 100% and $\sim$ 80% complete to $K_s \approx 21.5$ and at $21.5 < K_s < 22.0$, respectively.

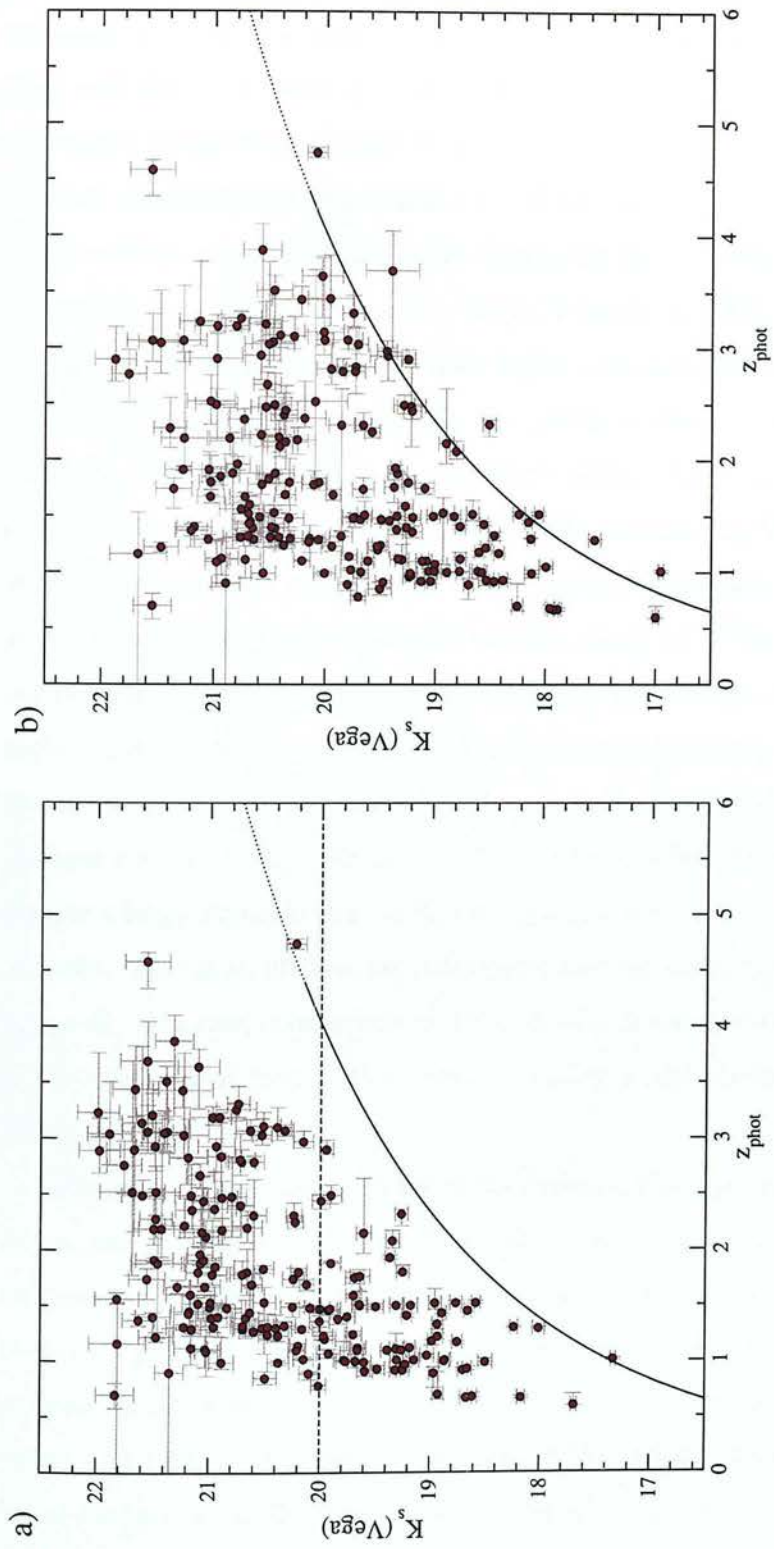

Figure 3.4: The Hubble diagram (total K_s magnitude versus photometric redshifts) for the ERGs in the deep ISAAC field. a) Original K_s magnitudes; b) dust-corrected K_s magnitudes. The circles correspond to HYPERZ primary solutions. The error bars indicate 1σ confidence levels. The dashed line on a) delimits the region of the Hubble diagram to which $K_s = 20$ surveys have access. The filled curve corresponds to the empirical K-z relation for massive radio galaxies obtained by Willott et al. (2003) [116], which approximately indicates the passive evolution of a $3L^*$ starburst formed at redshift $z_f = 10$. The dotted line is a nominal extrapolation of the same law.

For the Calzetti et al. reddening law [27], $R_V = 4.05 \pm 0.80$ and $k(\lambda_{\rm rf})$ is a power law in λ_{rf} (cf. eq.(2.5)). The dust-corrected K_s magnitude for each source is given by the difference (K_s-$A_{\lambda_{rf}}$). It is important to note that we assume the validity of the dust-screen model and the Calzetti et al. reddening law for modelling the extinction observed in ERGs. We explored the use of other reddening laws in HYPERZ and found that both the Milky Way and Large Magellanic Cloud-type laws produce very similar raw and dust-corrected Hubble diagrams for the ERGs in the R03 sample. The study of other geometries for the distribution of dust is beyond the scope of this work, but one should be aware that they could change the relation given by eq. (3.3) between the extinction $A_{\lambda_{rf}}$ and the extinction in the V-band A_V. This might have some impact on the derived properties of the most highly extincted ERGs.

In both plots 3.4-a) and 3.4-b), the circles indicate HYPERZ primary solutions. The error bars correspond to 1σ confidence levels. The overlaid solid curve shows the empirical K-z relation fitted for massive radio galaxies by Willott et al. (2003) [116], which approximately corresponds to the locus of passively evolving present-day 3L* galaxies formed instantaneously at redshift $z_f = 10$. The dotted line is a nominal extrapolation of the same law. In fig. 3.4-a), we have used a dashed line to indicate the region of the Hubble diagram to which the surveys limited at $K_s = 20$ have access. Up to such a magnitude, only sources with $z_{phot} < 3$ are detected within our survey. For a limiting magnitude $K_s = 22$, the ERGs span the redshift interval $z_{phot} \sim 0.5 - 4.75$ and display a large dispersion in the K_s vs. z_{phot} relation. In the raw K_s-magnitude Hubble diagram, there is an obvious lack of objects near the radio-galaxy locus beyond redshift $z_{phot} \sim 3$. However, comparison with fig. 3.4-b) shows that this effect is a consequence of the presence of dust, rather than indicating a real absence of intrinsically bright, high-redshift ERGs.

The position of a galaxy in the dust-corrected K_s-z_{phot} diagram depends, of course, on its age as well as its mass. The radio-galaxy K-z relation can be interpreted as indicating the behaviour of the highest mass galaxies formed at very high redshift. However, galaxies may appear to be as bright or brighter than high-redshift radio galaxies without being as massive provided their stellar populations are sufficiently young and bright. However, as we show in Section 4.5, most of the galaxies around the radio-galaxy line do in fact appear to at least be massive enough to be the already

assembled progenitors of the local $L > L^*$ population. The comparison of fig. 3.4-a) and 3.4-b) also shows that the dispersion in the $K_s - z_{phot}$ relation for ERGs is not an effect produced by the presence of different amounts of dust. We see an even larger dispersion for the ERGs in the dust-corrected Hubble diagram. This fact indicates that the ERG population comprises objects spanning a wide range in mass.

To obtain an estimate of the minimum mass of each ERG, we used the k- and evolutionary (k + e)-corrected K_s-band absolute magnitude of each source and computed a lower limit for the luminosity the galaxy would have at redshift $z = 0$, assuming passive evolution. The K_s-band absolute magnitude $M_{K_s}(t_0)$ the galaxy would have today is given by:

$$\begin{aligned} M_{K_s}(t_0) &= m_{K_s} - 5\,logd - 25 - \\ &\quad - \left[2.5\,log(1+z) + 2.5\,log\left(\frac{\int_0^\infty E(\lambda, t_0)\, S_{K_s}(\lambda)\, d\lambda}{\int_0^\infty E(\frac{\lambda}{1+z}, t_0)\, S_{K_s}(\lambda)\, d\lambda}\right)\right] - \\ &\quad -2.5\,log\left(\frac{\int_0^\infty E(\frac{\lambda}{1+z}, t_0)\, S_{K_s}(\lambda)\, d\lambda}{\int_0^\infty E(\frac{\lambda}{1+z}, t_1)\, S_{K_s}(\lambda)\, d\lambda}\right), \end{aligned} \tag{3.4}$$

where m_{K_s} is the observed K_s-band apparent magnitude, d is the luminosity distance in Mpc, t_1 is the galaxy age at the time its light was emitted and t_0 is the age the galaxy would have today at redshift $z = 0$. $E(\lambda, t)$ is given by the galaxy SED and $S_{K_s}(\lambda)$ is the K_s-band filter transmission function. The term between square brackets in the second line of eq.(3.4) constitutes the k-correction, while the term in the third line is the e-correction [117]. We explain the details of the calculation of the (k + e)-corrected K_s-band absolute magnitudes in §3.5.5. The luminosity L and the absolute magnitude M in a given band are related by $L/L^* = 10^{-0.4(M-M^*)}$, where we considered $M^*_{K_s} = -24.2$ for h=0.7, from the 2dF local luminosity function (Cole et al. 2001 [118]). Although the exact mass-to-light ratio depends on the assumed initial mass function (IMF) and the age of each galaxy, we estimate the mass of each ERG as $(L/L^*) \times 10^{11} M_\odot$, where L is the luminosity the galaxy would have today at redshift $z = 0$. In this way, we only attempt to obtain an estimate of the ERG masses, and leave a more rigurous calculation of these values for Chapter 4. Computing the estimates as explained above, we find that the ERGs in the deep ISAAC field span two decades in mass, from $\sim 3 \times 10^9 M_\odot$ to $\sim 3 \times 10^{11} M_\odot$.

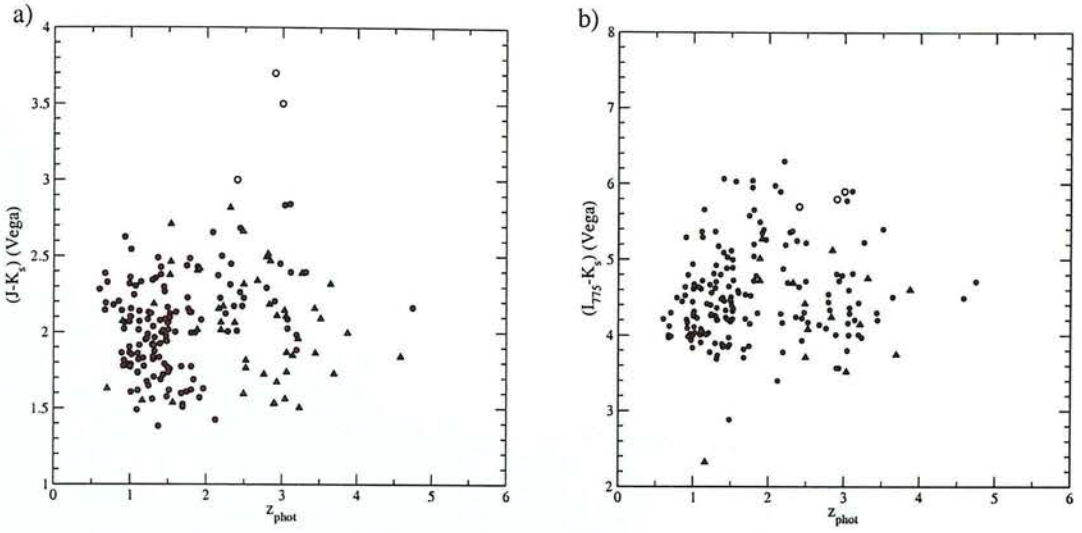

Figure 3.5: $(J - K_s)$ (a) and $(I_{775} - K_s)$ colours (b) vs. photometric redshifts. The filled circles correspond to exact values and the filled up-triangles, to lower limits for the sources with error $\varepsilon > 0.5$ in the J or I_{775} aperture magnitudes. The empty circles indicate the colours of the three high redshift massive galaxies in the HDFS reported by Saracco et al. (2004) [119].

3.5.3 The red envelope of galaxy evolution

Figures 3.5-a) and 3.5-b) show the $(J - K_s)$ and $(I_{775} - K_s)$ colours, respectively, as a function of photometric redshift for the ERGs in the deep ISAAC field. Only HYPERZ primary solutions have been considered in this case. In fig. 3.5-a), the red filled circles correspond to those objects with J-band 2″-diameter aperture magnitude above the 2σ-confidence limit, in this case $J \leq J_{lim.} = 23.5$. The green up-triangles indicate lower limits to the colours of those objects with $J > 23.5$, computed as $(23.5 - K_s)$. In fig. 3.5-b), the mixture of techniques we applied to measure aperture magnitudes on ACS images, i.e. SEXTRACTOR plus IRAF 'phot', does not allow us to set the 2σ confidence limit at a given I_{775}-band magnitude. Thus, we considered as precise colours (red circles) those with I_{775}-band magnitude error $\varepsilon < 0.5$. For objects with I_{775}-band magnitude error $\varepsilon > 0.5$ we computed lower limits for the colours as $(I_{775} - \varepsilon - K_s)$ (green up-triangles). For comparison, we have added in both plots, 3.5-a) and 3.5-b), the colours of the three massive galaxies in the HDFS at redshift $z_{phot} \geq 2.4$ reported by Saracco et al. (2004) [119] (empty circles).

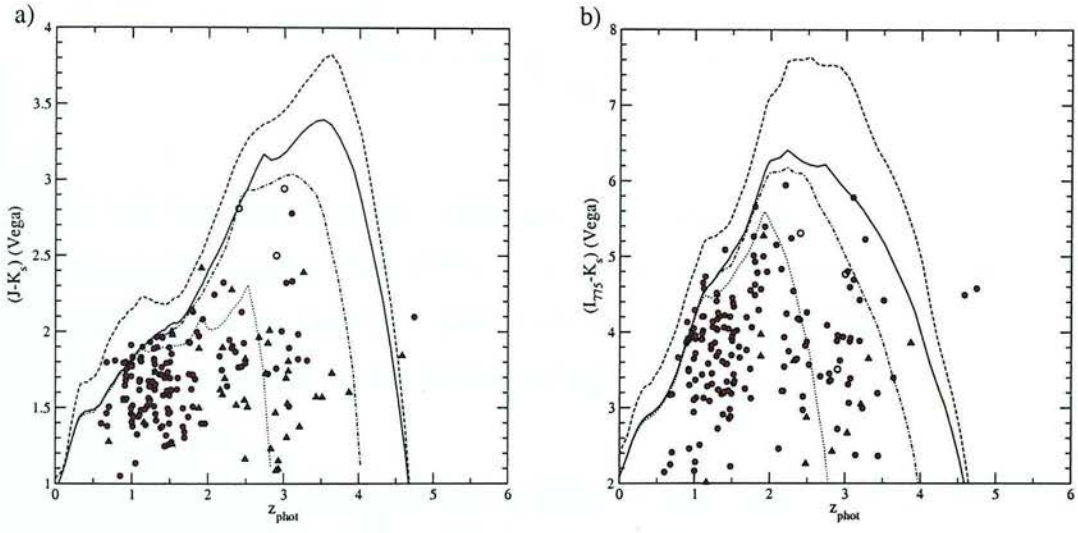

Figure 3.6: Dust-corrected $(J - K_s)$ (a) and $(I_{775} - K_s)$ colours (b) vs. photometric redshifts. The labels for the filled circles, filled up-triangles and open circles are the same as in fig. 3.5. The different lines show the expected colours for starbursts at different redshifts with passive evolution thereafter and metallicity $Z = Z_\odot$: $z_f = 5$ (solid), $z_f = 4$ (dashed-dotted) and $z_f = 3$ (dotted). The dashed line corresponds to a similar starburst at redshift $z_f = 5$, but with a higher metallicity $Z = 2.5\,Z_\odot$.

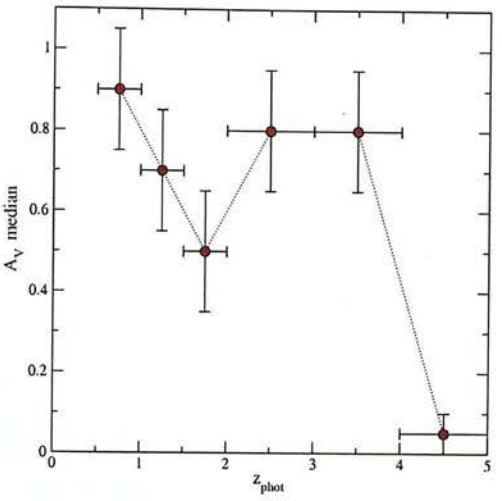

Figure 3.7: The median of the V-band extinction values applied to the best-fit SEDs vs. photometric redshifts. Only HYPERZ primary solutions are taken into account. The horizontal and vertical error bars indicate the binning in redshift space and the largest binning used in HYPERZ for the iteration through the A_V values, respectively.

The extremely red colours observed in ERGs are due to two coupled factors: age and dust. As our aim is to study which evolutionary model produces the reddest colours observed in the ERGs, we need to correct for the dust effects in order to separate the contribution to the red colours of the evolved stellar populations. Figures 3.6-a) and 3.6-b) show the dust-corrected $(J - K_s)$ and $(I_{775} - K_s)$ colours, respectively, as a function of redshift. We computed the dust-corrections for the colours subtracting from each magnitude the corresponding extinction value given by eq. (3.3). The symbol labels in both plots of fig. 3.6 are equivalent to those in fig. 3.5. We used the public code GALAXEV by Bruzual & Charlot (2003) [120] to compute the expected $(J - K_s)$ and $(I_{775} - K_s)$ colours of different kinds of dust-free passively evolving galaxies, in order to obtain a suitable model for the red envelope delimited by the ERG largest colours. We found that an instantaneous starburst at redshift $z_f = 5$ with passive evolution thereafter and solar metallicity (solid lines in fig. 3.6) models quite well the dust-corrected red envelope. A similar starburst formed at redshift $z_f = 5$, but with a higher metallicity $Z = 2.5\,Z_\odot$ (dashed line), has been added for comparison. The plots in fig. 3.6 show that solar metallicity $Z = Z_\odot$ is sufficient to explain the reddest

colours observed. Even the few apparent outliers at redshift $z_{phot} \sim 0.5 - 2.0$ can be explained by such a model once the error bars are taken into account, which are ~ 0.2 mag for these objects. On the other hand, the modelling of the expected colours for starbursts at different redshifts allows us to investigate the epoch since when the ERGs lying at redshifts $z_{phot} \gtrsim 2$ have been following passive evolution. The dotted and dashed-dotted lines in fig. 3.6 correspond to the modelled colours for starbursts at redshifts $z_f = 3$ and $z_f = 4$, respectively (both with passive evolution thereafter and solar metallicity $Z = Z_{\odot}$). We see that the reddest ERGs lying at redshifts $z_{phot} \sim 2\,(3)$ have been passively evolving since redshift $z_{phot} \sim 3\,(4)$. This does not necessarily mean that these objects have been formed in these epochs, but corresponds to the formation redshifts of the youngest stellar population present in them.

The comparison of fig. 3.5 and fig. 3.6 provides a simple and useful way to understand the extent to which the presence of dust is responsible for the original extremely red colours of ERGs. This fact is summarised in fig. 3.7, where we show the median of the V-band extinction values A_V necessary to deredden the ERG best-fit SEDs at different redshifts. We see that considerable median extinction values ($A_V \geq 0.5$) are necessary to explain the red colours observed in ERGs up to redshift $z_{phot} \sim 4$. For objects below redshift $z_{phot} = 1$, the modelled A_V values are very large, illustrating that only extremely dusty starbursts can classify as ERGs at relatively low redshifts. The median of the extinction A_V is lower at redshifts $z_{phot} \sim 1 - 2$, where perhaps the essentially non-dusty evolved stellar populations are expected to make the most of their contribution. At redshifts $z_{phot} \sim 2 - 4$, where according to fig. 3.6 most of the objects seem to have experienced recent starbursts, the median of the extinction A_V increases again. For objects beyond redshift $z_{phot} = 4$, nearly no extinction is required indicating that, at this stage, the extremely red colours are mainly due to the shift of the Lyman break to optical wavelengths rather than dust.

3.5.4 The evolving luminosity function of ERGs

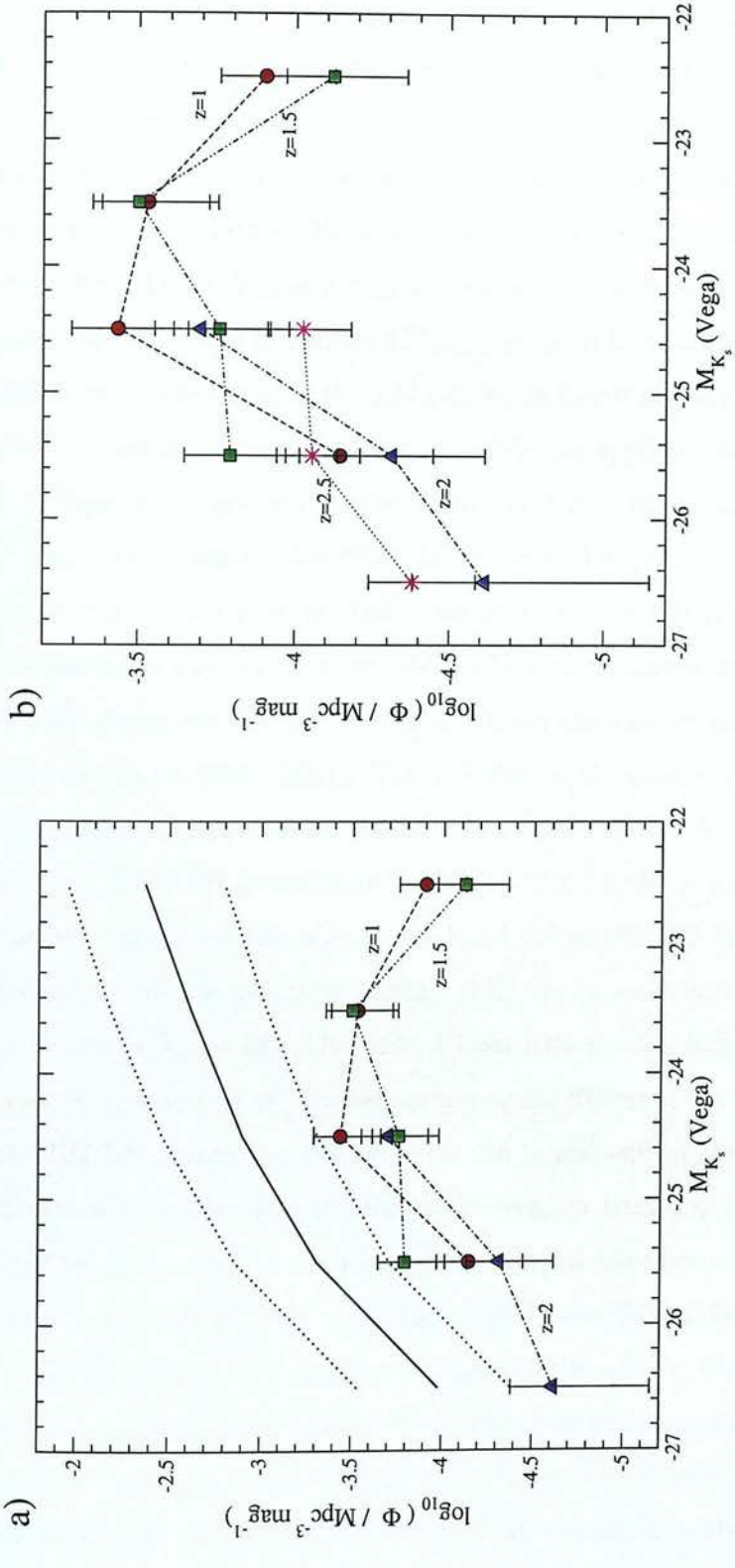

Figure 3.8: The luminosity function of ERGs at different redshifts: $\langle z_{phot} \rangle = 1.0$ (circles), $\langle z_{phot} \rangle = 1.5$ (squares) and $\langle z_{phot} \rangle = 2.0$ (up-triangles). In panel a), the average global K_s-band LF in the HDFN and HDFS fitted by Bolzonella et al. (2002) [122] has been overlaid for comparison (solid line). The error bars for the K_s-band LF have been estimated using the maximum uncertainty in the normalisation parameter ϕ^*, obtained for the HDFS (dotted lines). In panel b), the star-like symbols show the ERG LF at $\langle z_{phot} \rangle = 2.5$.

Figures 3.8-a) and 3.8-b) show the luminosity function (LF) of the ERGs in the deep ISAAC field in different redshift intervals. We assigned to each object the K_s-band k-corrected absolute magnitude (M_{K_s}) obtained as part of the HYPERZ output. We considered HYPERZ primary solutions for binning the data in redshift space. We computed the comoving densities per absolute magnitude bin by dividing the number of sources in each bin by the corresponding comoving volume. To take into account the limits of the survey ($K_s = 22$), we corrected the contribution of each source by a weighting factor V_{maxbin}/V_{maxobs}, where V_{maxbin} is the volume determined by the maximum redshift of the bin and V_{maxobs} is the volume corresponding to the maximum redshift at which the source would still be included in the survey (provided it is lower than the maximum redshift of the bin). We also applied a correction factor to account for a slight incompleteness of the sample at $21.5 < K_s < 22.0$.

Fig. 3.8-a) shows the ERG LF at redshifts $\langle z_{phot} \rangle = 1.0$, $\langle z_{phot} \rangle = 1.5$ and $\langle z_{phot} \rangle = 2.0$, indicated by circles, squares and up-triangles, respectively. The error bars correspond to the maximum of the Poissonian errors and the errors due to cosmic variance, which we take on average as 40% in the number counts at these redshifts (cf. Somerville et al. 2003 [121]). The inclusion of the cosmic variance is fundamental for highly-clustered populations, as ERGs at redshifts $z \sim 1 - 2$ are known to be. The global K_s-band LF at redshifts $1 < z_{phot} < 2$ has been added for comparison. The solid line represents the average K_s-band LF of the HDFS and HDFN, as fitted by Bolzonella, Pelló & Maccagni (2002) [122] for datasets in these fields up to a limiting magnitude of $K_s \sim 23$. The dotted lines indicate the largest error bars in the normalisation parameter ϕ^*, corresponding to the fitting of the HDFS data. As expected, our ERG LF reproduces the shape of the bright end of the global K_s-band LF. The differences at fainter magnitudes are at least in part due to the nature of the ERG colour selection. In Chapter 4, we shall present a complete comparison of the ERG and the total K_s-band LF in the GOODS/CDFS deep ISAAC field.

We find only 3 very luminous galaxies with $-27 < M_{K_s} < -26$ with estimated redshifts $z_{phot} \epsilon$ [0.75;2.25], 2 of which have redshifts in the interval [1.75;2.25]. These 2 sources have $(I_{775} - K_s) \geq 5.9$ and $(J - K_s) > 2.3$. For the absolute magnitude range $-26 < M_{K_s} < -24$, we do not observe any evolution in the ERG LF from redshifts $\langle z_{phot} \rangle = 1.0$ to $\langle z_{phot} \rangle = 2.0$. Any fluctuation in the mean values of the LF in this

absolute magnitude bin can be accounted for within the cosmic variance error bars. For absolute magnitudes $-24 < M_{K_s}$ we do not observe any evolution in the LF from redshifts $\langle z_{phot} \rangle = 1.0$ to $\langle z_{phot} \rangle = 1.5$. The limits of the survey do not allow us to explore the LF at redshift $\langle z_{phot} \rangle = 2.0$ for such faint objects.

In figure 3.8-b), we show again the ERG LF at redshifts $\langle z_{phot} \rangle = 1.0, 1.5, 2.0$ and we add the ERG LF at $\langle z_{phot} \rangle = 2.5$, for comparison. We computed the latter taking into account all the objects in the redshift interval [2.0,3.0]. At these redshifts, we have adopted a slightly lower value for the typical cosmic variance, only 30% in the number of counts on average [121]. This plot shows that the bright end of the ERG LF does not decrease significantly from redshifts $\langle z_{phot} \rangle = 2.0$ to $\langle z_{phot} \rangle = 2.5$. This result confirms the existence of a population of extremely red bright galaxies at high redshifts. We find 7 objects with estimated redshifts in the interval [2.0,3.0] and absolute magnitudes $-27 < M_{K_s} < -26$, 6 of which have $(I_{775} - K_s) \geq 4.8$, placing them among the very reddest objects at these redshifts. Moreover, all of these objects have $(J - K_s) \geq 2.2$. In the next section we investigate the change of the absolute magnitudes of ERGs after evolution to redshift $z = 0$ and explore the comoving densities of potential progenitors of the local $L > L^*$ population.

3.5.5 Comoving densities of $L > L^*$ progenitors

In this section we study the comoving densities of ERGs that will still contribute to the bright end of the K_s-band LF once they evolve down to redshift $z = 0$. If we assume passive evolution for ERGs from the epoch of observation, the maximum dimming of the absolute magnitude M_{K_s} can be estimated and, thus, a lower limit to the luminosity each object would have at redshift $z = 0$ obtained. To do this, we need to estimate an evolutionary correction (e-correction) factor at redshift $z = 0$ which, when added to the HYPERZ k-corrected absolute magnitude, yields the absolute magnitude the galaxy would have today. The expressions for the k- and e-corrections are given by the last two terms of eq.(3.4). However, it should be noted that, in eq.(3.4), the e-corrections from ages t_1 to t_0 are applied first at redshift z and, then, the magnitudes are k-corrected at time t_0. In our case, on the contrary, we have the HYPERZ k-corrected magnitude at time t_1 and then we apply the e-correction from times t_1 to t_0 at redshift $z = 0$.

The e-correction for each galaxy depends on its spectral type and age. We used the

public code GALAXEV [120] to compute the absolute magnitudes at redshift $z = 0$ of the spectral types corresponding to our ERGs at different ages. The correction applied to each object is the difference in the absolute magnitude the object would have today at age t_0 and at the age it had when its light was emitted t_1. The objects that are considered to be progenitors of the local $L > L^*$ population are those with $(k + e)$-corrected absolute magnitude $M_{K_s} < M^*_{K_s}$, given the relationship $L/L^* = 10^{-0.4(M-M^*)}$. In a passive evolution scenario, these ERGs must have contained a minimum stellar mass of $\sim 10^{11}\,M_\odot$ when their light was emitted.

Figure 3.9 shows the comoving densities at different redshifts of the 27 ERGs in the GOODS/CDFS deep ISAAC field which are expected to have $L > L^*$ at redshift $z = 0$ under passive evolution (red filled circles). We used $M^*_{K_s} = -24.2$ for h=0.7 (Cole et al. 2001 [118]). Once more, we computed the comoving densities dividing the number of sources in each redshift bin by the corresponding comoving volume. We divided the sample in bins of width $\Delta z_{phot} = 0.5$ up to redshift $z_{phot} = 2$, and $\Delta z_{phot} = 1$ for redshifts $2 < z_{phot} < 4$. To compute these comoving densities, we did not use HYPERZ primary solutions but a redshift probability density distribution that we constructed normalising for each source the percentage probabilities given in the HYPERZ output file _log.phot. In this way, each source may contribute in a fraction to different redshift bins. Only sources with HYPERZ primary solutions $z_{phot} < 4$ have been taken into account. We applied a weighting factor of the kind V_{maxbin}/V_{maxobs}, as it was explained in §3.5.4, to the normalised probability density distribution of each source. However, in each case, the weighting factor has been estimated using only the k-corrected absolute magnitude M_{K_s} given by HYPERZ in the output. A more rigurous procedure should take into account a probability density distribution for the absolute magnitudes in correspondence with the probability density distribution for redshifts. We also corrected for the incompleteness of the sample. The error bars for the comoving densities correspond to Poissonian errors in the number of sources, which are dominant in this case. We added for comparison the comoving density of the local $L > L^*$ population (star-like symbol), which we computed as the average of the values obtained integrating the local K_s-band LFs fitted by Cole et al. (2001) [118] and Kochanek et al. (2001) [66].

Our results show that there is no significant change in the comoving densities of ERG

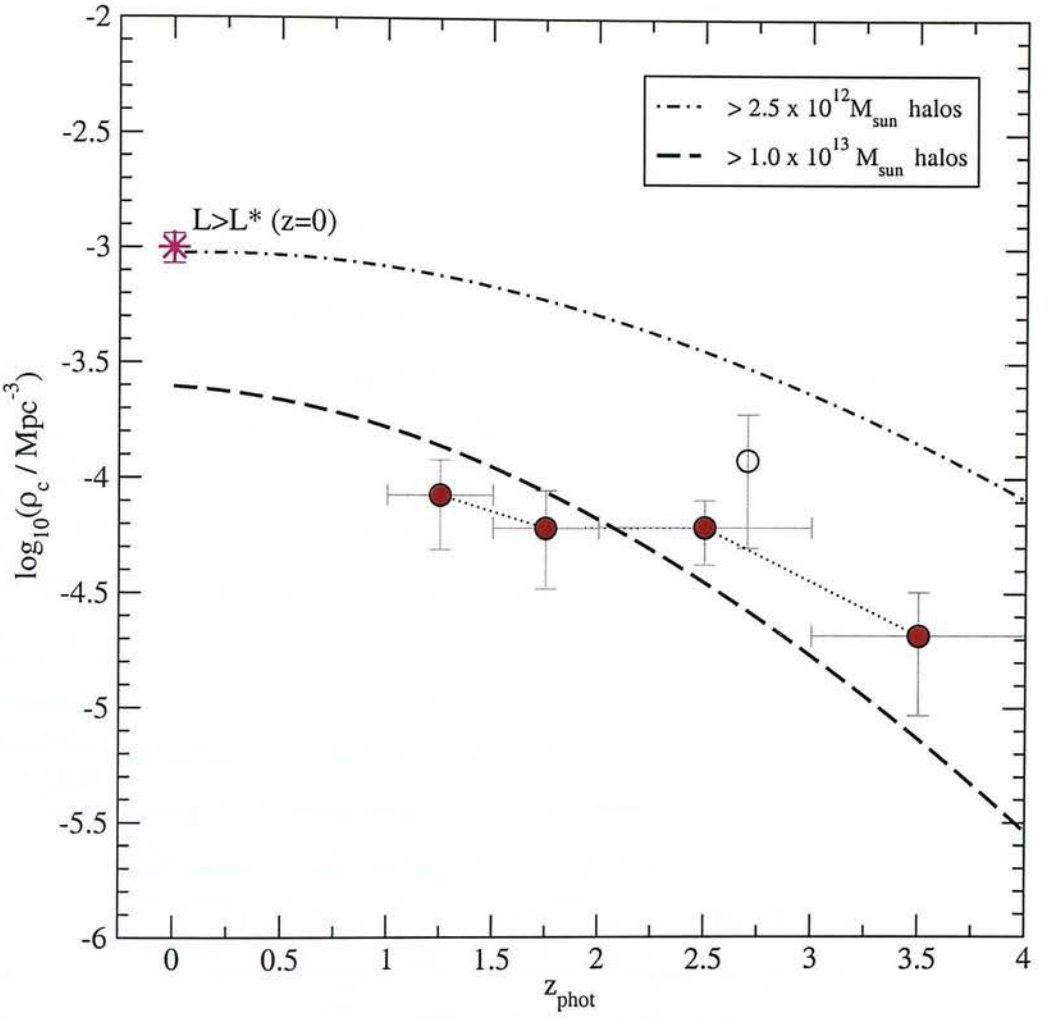

Figure 3.9: Lower limits on the comoving densities of ERGs progenitors of local $L > L^*$ galaxies as a function of redshift (red filled circles). The horizontal error bars indicate the binning in redshift space. The vertical error bars correspond to Poissonian errors in the number of objects. The lower limit on the comoving density of progenitors of $L > L^*$ galaxies at redshift $\langle z_{phot} \rangle = 2.7$ obtained by Saracco et al.(2004) [119] (empty circle) and the comoving density of local $L > L^*$ galaxies (star-like symbol) [118] [66] have been added for comparison. The dashed-dotted and dashed lines show the comoving densities of dark matter haloes with masses $M > 2.5 \times 10^{12} M_\odot$ and $M > 1.0 \times 10^{13} M_\odot$, respectively, as obtained from ΛCDM models of structure formation.

progenitors of $L > L^*$ galaxies between redshifts $1.5 < z_{phot} < 2.0$ and $2 < z_{phot} < 3$, which is consistent with the results presented in §3.5.4 for the bright end of the ERG LF. Actually, all the galaxies with $-27 < M_{K_s} < -26$ in §3.5.4 are included in the progenitors of $L > L^*(z = 0)$ subsample. The values we obtain for the comoving densities are: $\rho_c = (8.5 \pm 3.5) \times 10^{-5}\,\mathrm{Mpc}^{-3}$ for $\langle z_{phot} \rangle = 1.25$, $\rho_c = (6.1 \pm 2.8) \times 10^{-5}\,\mathrm{Mpc}^{-3}$ for $\langle z_{phot} \rangle = 1.75$, $\rho_c = (6.1 \pm 1.9) \times 10^{-5}\,\mathrm{Mpc}^{-3}$ for $\langle z_{phot} \rangle = 2.5$ and $\rho_c = (2.1 \pm 1.1) \times 10^{-5}\,\mathrm{Mpc}^{-3}$ for $\langle z_{phot} \rangle = 3.5$. It is important to note that the relatively small comoving densities at $\langle z_{phot} \rangle = 1.25$ and $\langle z_{phot} \rangle = 1.75$ (more than 10 times smaller than the corresponding value we adopted for local $L > L^*$ galaxies) could in part be due to the ERG colour cutoff. If this is the case, we should conclude that the ERGs at redshifts $z \sim 1-2$ cannot account for the whole population of progenitors of the local $L > L^*$ galaxies. Although the ERGs reproduce quite well the shape of the bright end of the global K_s-band LF shown in fig.3.8, the values are lower, indicating that larger comoving densities of bright objects are expected to be obtained in a K_s-selected sample without a colour selection. The relationship between the ERG and the total K_s-band galaxy populations will be much clarified in Chapter 4, where we present a comparative study of both populations in the same field.

The conclusion of a constant comoving density of $L > L^*$ progenitors from redshifts $1.5 < z_{phot} < 2.0$ to $2 < z_{phot} < 3$ is in principle only applicable to ERGs, and may of course not hold for a total K_s-selected sample. The mean value we obtain for the lower limit to the comoving density of $L > L^*$ progenitors at $\langle z_{phot} \rangle = 2.5$ is only one half of the mean value obtained by Saracco et al. (2004) at a similar redshift (empty circle in fig. 3.9), but there is no significant discrepancy between the results given the large error bars. We conclude that Saracco et al. large mean comoving density might be due to a simple cosmic variance effect and much larger samples of ERGs are necessary to establish a robust conclusion on the fraction of ERGs progenitors of local luminous galaxies at these redshifts[4].

In fig. 3.9 we show the comoving densities of dark matter haloes with masses

[4]Saracco et al. claim to reproduce about 40% of the comoving density of the local luminous elliptical galaxies, after comparison with the local comoving density of $L > L^*$ early-type galaxies obtained from the LF fitted by Marzke et al. (1998) using B-band data. Instead, we prefer to compare the comoving densities with the local values obtained integrating more recent LFs directly fitted on K-band data (Cole et al. 2001 [118], Kochanek et al. 2001 [66]).

$M > 1.0 \times 10^{13}\,M_{\odot}$ (dashed lines) at different redshifts, as they are predicted by ΛCDM models of structure formation [41] [64]. We also show the comoving densities of dark matter haloes with masses $M > 2.5 \times 10^{12}\,M_{\odot}$ (dashed-dotted lines), a mass threshold deliberately selected to coincide with the comoving densities of $L > L^*$ galaxies at $z = 0$. At any redshift, our comoving densities of progenitors of local $L > L^*$ galaxies are lower than the corresponding comoving densities of dark matter haloes massive enough to host these galaxies. For instance, the comoving densities of $M > 2.5 \times 10^{12}\,M_{\odot}$ haloes decreases less than a factor ~ 2 from redshifts $z = 0$ to $z = 1.5$, while the comoving densities of ERGs which are $L > L^*$ progenitors are more than 5 times below this value. This leads to two extreme interpretations: i) even taking into account the possible production of mergers (i.e. the increasing comoving densities of dark matter haloes more massive than a given mass threshold with time), ERGs do not seem to be sufficient to account for all the progenitors of local $L > L^*$ galaxies. This would reinforce the idea that the ERG colour cutoff must be at least partially responsible for this deficiency, which appears to be more important at lower ($z_{phot} \sim 1-2$) than higher ($z_{phot} \sim 3-4$) redshifts. ii) ERGs do account for the progenitors of local $L > L^*$ galaxies but the passive evolution scenario is not completely valid. Galaxies which are not sufficiently massive at a given redshift might build up more stellar mass at later epochs and, thus, should also be considered as progenitors of the local $L > L^*$ galaxy population. The massive ERGs at $z > 2$ could instead be progenitors of much more massive ($\sim 4L^*$) local galaxies, in which case our results show that all of them are already in place at redshift $z \sim 3.5$. It is important to clarify here that a fixed luminosity cut does not rigurously correspond to a fixed mass cut, because the mass-to-light (M/L) ratios depend on the spectral type and the age of each galaxy. However, all the galaxies which are $L > L^*$ progenitors under passive evolution must have assembled a minimum stellar mass $\sim 10^{11} M_{\odot}$ and, thus, can be considered as massive. We further investigate and discuss the two hypothesis proposed here in Chapter 4, in the light of the comparison of the ERG and the total K_s-band galaxy populations selected in the same field.

Interestingly, the progenitors of $L > L^*$ galaxies are among the reddest ERGs. At different redshifts, these massive galaxies have $\langle (I_{775} - K_s) \rangle \approx 4.8-5.1$ within the present sample. The mean $(J - K_s)$ colours increase with redshift, as it is expected when the

4000Å break enters the region between the J and K_s filters. In all cases, $(J - K_s) > 2$. Some of these massive galaxies are among the reddest objects in $(J - K_s)$ at redshifts $z_{phot} > 2$, due to the combined effects of the break and considerable amounts of dust (we find V-band extinction values of up to $A_V = 1.8$ for these massive objects). The characteristics of these sources are consistent with the HERO population discovered by Totani et al.(2001) [79]. However, not all the $(J - K_s)$ reddest objects evolve to $L > L^*$ sources in a passive evolution scenario. In some cases, the extremely red $(J - K_s)$ colours are almost exclusively due to very large dust extinctions. Recently, some extremely red $(J - K_s)$ sources have been found to be counterparts of sub-millimetre sources, which are known to be mainly located at redshifts $2 < z < 4$ [123] [124] [125]. However it is not yet clear whether the ERGs associated with sub-millimetre sources are primarily high or low mass objects [95].

3.5.6 Sources beyond redshift z = 4 - the ERG - Lyman-break connection

In this section, we focus on the properties of the Lyman break galaxies in the deep ISAAC field included in the R03 ERG sample. These objects could be candidates for massive galaxies at very high redshift. Here we summarise the detailed properties of the individual objects and discuss the probability that they are genuinely located at such high redshifts.

Several studies have already been published on the selection of very high redshift candidate sources in the GOODS fields [126] [127] [128] [129]. In most of these studies a colour cutoff selection technique has been applied (usually $(I_{775} - z) > 1.3 - 1.5, AB$) to select candidates at redshifts $z > 5$. We find 9 of these candidate sources in the deep ISAAC field ERG sample. However, we cannot confirm any of these sources as being at very high redshift. We argue that the fraction of low-mass star and lower-redshift ERG contaminants is usually under-estimated when a single-colour selection criterion is applied. Multicolour photometry appears to be a much more powerful way to obtain reliable candidate lists of very high redshift objects, and allows the investigation of degerate solutions in redshift space.

Using 5-epoch GOODS HST/ACS (V1.0) and VLT/ISAAC data, we obtained an initial HYPERZ output list containing 12 sources with a primary solution at $z_{phot} > 4$,

which adopted as candidates for detailed inspection. We present the properties of the complete list of 12 candidate sources in Table 3.2. We used the public code BPZ to obtain estimated redshifts for these objects in an independent way. We also made an individual study of each of our 12 candidate sources, inspecting their ACS images and analysing their magnitudes and colours in different bands. After a first analysis, we rejected the following 7/12 $z > 4$ candidates for the reasons explained below:

- **e114-e566-e967-e2386**: these sources appear to be at redshifts $z_{phot} > 5.3$ from HYPERZ and all of them have $(I_{775} - z) \sim 1.3 - 1.5, AB$. Only e566 is not confirmed by the BPZ code as a very high redshift source (it is estimated to be at redshift $z_{phot} = 1.28$). However, the probabilities associated with the HYPERZ primary solutions, obtained from the χ^2 minimisation, are very low (P < 19%) in all cases. e967 corresponds to source number 4 in Stanway et al. [126] list and source number 8 in the list of Bremer et al. [128]. e114 and e2386 are sources number 13 and 9 in the Bremer et al. [128] list, respectively. These sources are unresolved on the ACS images and have quite blue near-IR colours, $(J - K_s) < 1.7$ (Vega) in all cases. e967 and e2386 are significant detections in the V-band ($V = 27.9 \pm 0.4$ and $V = 27.4 \pm 0.3$, AB, respectively) and e566, in the B-band ($B = 23.7 \pm 0.1$, AB). Thus, it is more likely that they are cool stars than high redshift galaxies. Indeed, e967 has been spectroscopically confirmed as such (cf. [129]). These cool stars are known to be among the main contaminants of very high redshift candidates.

- **e1504**: this source has HYPERZ primary solution $z_{phot} = 4.63$, but actually has a probability $P \equiv 0$ at any redshift between 0 and 10. The BPZ code gives an estimated redshift of $z_{phot} = 1.44$ for this source. Besides, although it is not detected in the V-band, even when its flux is manually measured with the IRAF task 'phot', it is a significant detection in the B-band ($B = 27.2 \pm 0.3$, AB). This source corresponds to object number 9 in the Stanway et al. [126] list.

- **e1605**: this source has HYPERZ primary solution $z_{phot} = 6.71$ (with an associated probability $P \approx 90\%$), but the BPZ code gives $z_{phot} = 2.84$. This source is not detected on the z-band images, but it could have some flux in the I_{775}-band ($I_{775} = 27.9 \pm 1.3, AB$). Its very red near-IR colour, i.e. $(J - K_s) > 2.5$ (Vega),

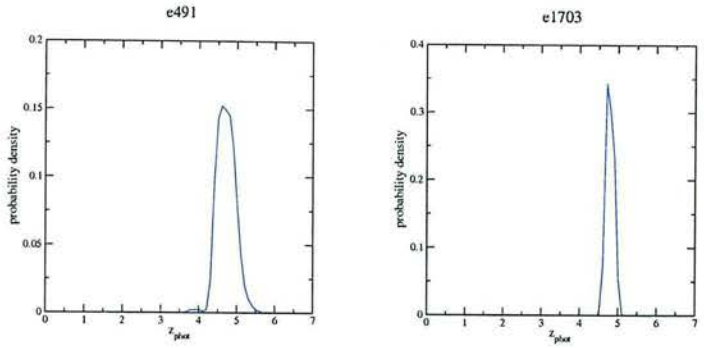

Figure 3.10: The redshift probability density distributions of the accepted z > 4 candidate sources in deep ISAAC ERG sample.

suggests that the estimated redshift from the BPZ code is more reliable in this case.

- **e2006**: this source has two HYPERZ solutions with similar probabilities. The primary solution is $z_{phot} = 6.21$ (P $\approx$ 73%) and the secondary one is $z_{phot} = 1.15$ (P $\approx$ 60%). The BPZ estimation is $z_{phot} = 6.37$. We measured $(I_{775} - z) = 2.1 \pm 0.8$ for this object and we do not find it is significantly detected in either the B or V bands. However, the higher redshift solution would imply it is an extremely bright galaxy with a k-corrected absolute magnitude $M_{K_s} = -28.5$ and estimated mass $\sim 6.7 \times 10^{11} M_{\odot}$, so we consider that in this case the HYPERZ secondary solution is more likely to be the right answer.

3/12 high-z candidate ERGs lie in the HUDF, whose images have been made publicly available in March 2004. After revision of the photometry on the HST-ACS and HST-NICMOS ultra-deep optical and near-IR images, we reject also these 3/12 high-z candidates:

- **e778**: using 5-epoch GOODS HST/ACS (V1.0) and VLT/ISAAC data, the HYPERZ primary solution for this source is $z_{phot} = 4.74$ (with an associated probability P $\approx$ 98%). The BPZ redshift estimation is $z_{phot} = 5.42$. However, after revision of the photometry on the HUDF images, this source appears to be a significant detection in the B-band. The revised HYPERZ primary solution is $z_{phot} = 1.56$.

- **e1113**: this source initially had a HYPERZ primary solution $z_{phot} = 5.07$ (P $\approx$ 56%) and secondary solution $z_{phot} = 1.10$ (P $\approx$ 26%). The BPZ code favoured a low redshift solution $z_{phot} = 1.05$. We did not detect this source in either the B or V bands on the GOODS V1.0 images. However, it is a clear detection in both the B and V bands on the HUDF images. The revised HYPERZ primary solution is $z_{phot} = 1.43$. This source corresponds to object number 2 in Stanway et al. [126] list.

- **e1272**: this source initially had a HYPERZ primary solution $z_{phot} = 5.03$ (P $\approx$ 82%) and no significant secondary solution. The BPZ estimation was $z_{phot} = 5.48$. It was not a significant detection in either the B or V bands on the GOODS V1.0 images, but it is on the HUDF maps. The revised HYPERZ primary solution is $z_{phot} = 1.91$.

Table 3.2: List of ERGs in the GOODS/CDFS deep ISAAC field with HYPERZ primary solutions $z_{phot} > 4$. The first column is the identification number. The second and third columns indicate the coordinates of the source obtained from the K_s-band images. The fourth and fifth columns show the redshifts estimated by HYPERZ and the BPZ code, respectively. Column six lists comments on the individual objects.

ERG id	RA(J2000)	DEC(J2000)	HYPERZ	BPZ	accepted?	COMMENTS
114	3:32:22.46	-27:50:47.16	$5.60^{+0.03}_{-0.14}$	5.75	N	Unresolved. $(J-K_s)_{Vega} = 0.8 \pm 0.3$
566	3:32:24.78	-27:49:12.91	$6.69^{+0.11}_{-0.12}$	1.28	N	Unresolved. $(J-K_s)_{Vega} = 1.1 \pm 0.3$. $B_{AB} = 23.7 \pm 0.1$
967	3:32:18.17	-27:47:46.48	$5.39^{+0.03}_{-0.08}$	5.70	N	Spectroscopically confirmed star. $V_{AB} = 27.9 \pm 0.4$
1504	3:32:18.17	-27:46:16.33	$4.63^{+0.10}_{-0.06}$	1.44	N	$B_{AB} = 27.2 \pm 0.3$
1605	3:32:19.67	-27:46:02.04	$6.71^{+0.75}_{-0.32}$	2.84	N	$(J-K_s)_{Vega} > 2.5$. Not detected in z band.
2386	3:32:19.23	-27:45:45.39	$5.33^{+0.05}_{-0.04}$	5.56	N	Unresolved. $(J-K_s)_{Vega} = 1.2 \pm 0.2$
2006	3:32:28.81	-27:44:30.54	$6.21^{+0.17}_{-0.33}$	6.37	N	Significant secondary solution $z_{phot} = 1.15$
778	3:32:41.76	-27:48:24.92	$4.74^{+0.20}_{-0.25}$	5.42	N	Revised UDF photometry implies $z_{phot} = 1.56$
1113	3:32:34.65	-27:47:20.89	$5.07^{+0.16}_{-0.08}$	1.05	N	Revised UDF photometry implies $z_{phot} = 1.43$
1272	3:32:41.69	-27:46:55.40	$5.03^{+0.21}_{-0.13}$	5.48	N	Revised UDF photometry implies $z_{phot} = 1.91$
491	3:32:25.95	-27:49:30.38	$4.58^{+0.24}_{-0.09}$	5.22	Y	No significant HYPERZ secondary solutions.
1703	3:32:37:74	-27:45:05.41	$4.74^{+0.04}_{-0.05}$	5.38	Y	No significant HYPERZ secondary solutions.

Table 3.3: A complementary list of the $z > 4$ candidate objects selected by other authors which are present in the R03 ERG sample, and for which we obtain lower redshift estimates.

ERG id	Author	Author's id	HYPERZ
e82	Bremer et al.	7	$1.40^{+0.30}_{-0.04}$
e309	Bremer et al.	6	$2.32^{+0.11}_{-0.05}$
e225	Dickinson et al.	SiD013	$1.74^{+0.08}_{-0.10}$
e1423	Bremer et al.	2	$1.60^{+0.28}_{-0.08}$

We accept the remaining 2/12 as z > 4 candidates, whose redshift probability density distributions we show in fig. 3.10:

- **e491**: the HYPERZ primary solution is $z_{phot} = 4.58$ (with an associated probability P $\approx$ 98%). The BPZ code estimates a redshift $z_{phot} = 5.22$. There are no significant secondary solutions for the redshift of this source in HYPERZ. The K_s-band k-corrected absolute magnitude for this galaxy is $M_{K_s} = -25.6$ and we estimate a mass of $5.8 \times 10^{10} M_\odot$. This object has $(I_{775} - z) = 0.6 \pm 0.3$ and it is not detected in either the B or V bands.

- **e1703**: this source has a HYPERZ primary solution $z_{phot} = 4.74$ (P $\approx$ 90%) and no significant secondary solution. The BPZ redshift is $z_{phot} = 5.38$. The estimated K_s-band k-corrected absolute magnitude for this source is $M_{K_s} = -27.3$ and the estimated mass is $2.7 \times 10^{11} M_\odot$. It has $(I_{775} - z) = 0.97 \pm 0.14$ and it is not detected in either the B or V bands.

Finally, in Table 3.3, we list other ERGs in the R03 sample which are among the very-high redshift candidates selected by other authors, and for which we obtain lower redshift estimates. From the sources listed in this table, only e309 has a very-high-redshift secondary solution, although with negligible significance, at $z_{phot} = 6.74$.

To summarise, we conclude that, within the limits of the survey analysed here, only a few ERGs are likely to be at very high redshifts. Deeper near-IR selected samples of galaxies are necessary to confirm or refute the rarity of these objects assembled at very early epochs.

Table 3.4: Redshift estimates for the Chandra source XID:58 in the CDFS and 7 other ERGs presumably associated with it.

ERG id	z_{phot} (primary)	z_{phot} (secondary)
e1333	$3.10^{+0.11}_{-0.18}$	1.78
e1341	$1.52^{+0.06}_{-0.13}$	1.01
e1390	$1.29^{+0.01}_{-0.01}$	1.67
e1404	$1.52^{+0.02}_{-0.03}$	1.78
e1423	$1.60^{+0.28}_{-0.09}$	1.34
e1435 (XID:58)	$1.85^{+0.08}_{-0.08}$	1.30
e1464	$3.19^{+0.07}_{-0.10}$	1.48
e1481	$1.30^{+0.12}_{-0.12}$	1.01

3.5.7 Review of the ERG cluster candidate at redshift $z \sim 1.5$

Roche et al. (2003) [47] found 10 ERGs within a 20″ radius of the Chandra source XID:58 (RA=3:32:11.85, DEC=-27:46:29.14, J2000), which is itself a counterpart of the ERG identified as e1435 in the R03 list. This overdensity suggested the presence of an ERG cluster at redshift $z \sim 1.5$, based on the photometric redshift of the Chandra source XID:58, estimated as $z_{phot} = 1.44$ by Mainieri (2003) [130]. Based on the source colours, Roche et al. argued that 7/9 of the ERGs around XID:58 (e1435) could be part of that cluster. In table 3.4, we present our redshift estimates (both primary and secondary) for e1435 and the 7 surrounding sources that could be associated with it. Our estimated redshifts seem to confirm the presence of a cluster at redshift $z_{phot} \sim 1.5$. However, it is not clear whether all the sources listed above belong to it. e1333 and e1464 seem to be higher redshift sources, although the HYPERZ secondary solution might locate e1464 at redshift $z_{phot} = 1.48$. For e1435 (counterpart of XID:58) we estimate a redshift $z_{phot} = 1.85$, a value somewhat higher than Mainieri's estimation. Our secondary solution, on the contrary, is closer to their value. The sources which seem to be part of a cluster at redshift $z_{phot} \sim 1.5$ are e1341, e1404, e1423 and e1481.

Roche et al. also suggested that the 2/9 remaining ERGs around XID:58 could be associated with another X-ray source (Chandra XID:149), which is spectroscopically

confirmed to be at redshift $z = 1.033$ (Szokoly et al. 2004 [131]). Our estimated redshifts for these 2 remaining ERGs are listed in Table 3.5. The HYPERZ primary solutions seem to confirm that these 2 ERGs are actually associated with the X-ray source XID:149.

Table 3.5: Redshift estimates for 2 ERGs presumably associated to the Chandra source XID:149 at $z = 1.033$ in the CDFS.

ERG id	z_{phot} (primary)	z_{phot} (secondary)
e1311	$1.05^{+0.02}_{-0.02}$	0.61
e1467	$1.07^{+0.04}_{-0.04}$	5.24

3.6 Summary and discussion

In this chapter we have presented estimated redshifts for the Extremely Red Galaxies selected by Roche et al. (2003) [47] in the 50.4 arcmin^2 of the GOODS/CDFS deep ISAAC field to a limiting magnitude $K_s = 22$. This is the deepest significant sample of ERGs selected to date and constitutes a complement to other shallower but wider surveys of ERGs in the same field [55].

We used multicolour photometry in seven passbands (B,V, I_{775}, z, J, H and K_s) to compute photometric redshifts using the public code HYPERZ [109]. The B,V, I_{775} and z magnitudes have been measured on the stacked 5-epoch GOODS ACS images (V1.0 data release). We obtained the redshift distribution and the corresponding Hubble diagram ($K_s - z_{phot}$), which show the existence of ERGs up to redshifts $z_{phot} \sim 4.75$ at this depth. The ERG population is characterised by a large dispersion in the K_s-z_{phot} relation. We find that this dispersion is even more important in the dust-corrected Hubble diagram, indicating that the ERG populaton is composed of objects spanning a wide range in mass. We estimate that the $K_s < 22$ ERGs in the CDFS deep ISAAC field sample span two decades in mass, from $\sim 3 \times 10^9 M_\odot$ to $\sim 3 \times 10^{11} M_\odot$.

We also studied the red envelope of galaxy evolution, determining the galaxy template which best described the ERG dust-corrected reddest colours observed in the R03 sample as a function of redshift. We found that a starburst formed at redshift $z_f = 5$

with passive evolution thereafter and solar metallicity provided a very good description of the red envelope of ERG evolution for objects selected with $K_s < 22$. After applying the dust-corrections, the colours of some of the originally dusty ERGs were still sufficiently red and could only be explained by the presence of an old stellar population. Thus, our work indicates that the simplified traditional picture for ERGs as being either old elliptical galaxies or young dusty starbursts can no longer be sustained. The colours of many of the reddest ERGs can only be explained by the combined effects of evolved stellar populations and dust.

We have also explored the evolution of the ERG luminosity function from redshifts $\langle z_{phot} \rangle = 1$ to $\langle z_{phot} \rangle = 2.5$. The ERG LF at redshifts $1 < z_{phot} < 2$ reproduces the shape of the bright end of the global K_s-band LF, as perhaps expected. We find no evolution in the bright end of the LF of ERGs from redshifts $\langle z_{phot} \rangle = 1.0$ to $\langle z_{phot} \rangle = 2.5$ ($-26 < M_{K_s} < -25$) and from redshift $\langle z_{phot} \rangle = 2.0$ to $\langle z_{phot} \rangle = 2.5$ ($-27 < M_{K_s} < -26$). This effect cannot be deduced from inspection of the Hubble diagram for ERGs, constructed using the raw K_s magnitudes. Only after the application of dust corrections are some ERGs revealed as bright and massive galaxies at high redshift.

One of our main goals in the study of an ERG sample was to trace the progenitors of very luminous local galaxies ($L > L^*$). Only a small fraction ($\sim 15\%$) of the ERGs in the R03 sample can evolve into such luminous galaxies under passive evolution. At redshifts $z_{phot} \sim 1-2$, we find that the comoving density of ERGs progenitors of $L > L^*$ galaxies is less than $\sim 1/10$ of the local value. Between redshifts $z = 0$ and $z = 1.5$, ΛCDM models only predict a decrease in the comoving densities of dark matter haloes massive enough as to host these galaxies by a factor $\sim 1.5-2$. This suggests that either ERGs cannot account for the whole population of local luminous galaxies or the passive evolution scenario is not completely valid. We further investigate these two hypothesis in Chapter 4. This deficiency appears as being more dramatic at lower ($z_{phot} \sim 1-2$) than higher ($z_{phot} \sim 3-4$) redshifts, suggesting that ERGs could be rather better tracing the progenitors of local $L > L^*$ galaxies present at early epochs.

Finally, we have investigated the existence of Lyman break galaxies massive enough to be included in an ERG sample. Out of an initial candidate list of 12 sources, we only confirmed 2 ERGs as having high probabilities of being located at redshifts $z_{phot} > 4$.

Deep observations in wider areas are crucial in order to constrain lower limits on the fraction of massive galaxies with the bulk of their stellar mass already assembled at very high redshifts.

The work we presented in this chapter allowed to trace the evolution of the ERG population up to very high redshifts. However, a complete understanding of this evolution can only be achieved through a parallel study of the ERGs and the total K_s-selected sample from which these ERGs have been extracted. Consequently, in Chapter 4 we present the comparative study of both populations with two objectives: to investigate the evolution of all the K_s-selected galaxies and to clarify the role of ERGs within this population and, in general, in the history of structure formation.

Chapter 4

The evolution of K_s-selected galaxies

4.1 Introduction

In Chapter 3, we studied the evolution of ERGs up to redshift $z \sim 4$. We constructed the ERG LF and determined that its bright end does not evolve from redshifts $\langle z_{phot} \rangle = 2.0$ to $\langle z_{phot} \rangle = 2.5$, connecting this fact with the presence of progenitors of local $L > L^*$ galaxies at redshifts $z_{phot} > 2$. Also, we showed that the comoving densities of ERG progenitors of local $L > L^*$ galaxies at different redshifts are below the total expected values, indicating either that ERGs cannot account for all the progenitors of massive galaxies at redshift $z = 0$, or that the underlying assumption of passive evolution is not completely valid. Our aim is to further test these two hypothesis by a comparative study of the deep ISAAC field ERG sample and the total population of $K_s \leq 22$ galaxies selected in the same area. The selection of the ERG and the total K_s-band samples from the same field is essential to accurately compare the properties of both populations, by minimising the potential existence of systematic errors due to cosmic variance. Thus, this chapter has two main purposes: to investigate the evolution of the total K_s-band galaxy population and to understand the role of $(I_{775} - K_s) > 3.92$-selected ERGs in this evolution.

The layout of the present chapter is as follows. First, in §4.2, we give details of the $K_s \leq 22$ galaxy sample selection and the multiwavelength photometry. In §4.3, we explain our strategy for redshift estimations and discuss the calibration of the redshift

estimates with spectroscopic data and with the previous estimates for ERGs determined in Chapter 3. In §4.4, we present our results: we discuss raw and dust-corrected Hubble diagrams, the evolution of the LF, and the evolution of massive systems up to redshift $z_{phot} = 4$. In §4.5, we predict IR magnitudes and colours for our K_s-selected galaxies in three Spitzer/IRAC channels: $3.6\mu m$, $4.5\mu m$ and $5.8\mu m$. Finally, in §4.6 we summarise and discuss our results. Except where explicitly cited in the text, all the contents of the present chapter are my own work, made with the collaboration of James Dunlop, Ross McLure and Nathan Roche.

4.2 The $K_s \leq 22$ galaxy sample

4.2.1 Sample selection and multiwavelength photometry

We used the public reduced near-IR images of the GOODS/CDFS deep ISAAC field (GOODS/EIS v0.5 release) to select a sample of $K_s \leq 22$ galaxies in the same area as the ERG sample studied in Chapter 3. As we explained in §3.2.2, the GOODS/EIS v0.5 release consists of 24 maps covering 8 ISAAC pointings in three filters J, H and K_s. The zero-point for each map as well as the corresponding weighting map were part of the public v0.5 release. We constructed our K_s-band catalog using the 8 reduced K_s-band images and extracting sources with the public code SEXTRACTOR [105] on each map separately. As one of our aims was to compare our results with those obtained for the ERGs in Chapter 3, we needed to select the K_s-band sample in the same way as done for the deep ISAAC field ERGs. Consequently, we used the same SEXTRACTOR parameters used by R03 for the extraction of sources, i.e. a detection threshold of $1.4\sigma_{sky}$ in at least six contiguous pixels. We employed a Gaussian kernel with a 3-pixel FWHM and the corresponding weighting maps. The low signal-to-noise edges of each map have been excluded from the detection procedure, leaving a total effective area for detections of 50.4 arcmin^2. There is some overlap between the eight K_s-band maps constituting the deep ISAAC field (even after the trimming of the edges). Thus, as we ran SEXTRACTOR on each of the maps separately, we discarded repeated sources appearing on different map catalogs. We used total Kron-type (SEXTRACTOR 'MAG_AUTO') magnitudes for limiting the sample to objects with magnitude $K_s \leq 22$ (and above a 3σ detection limit, although only a few objects

with $K_s \leq 22$ were below this threshold). The number of sources in this first $K_s = 22$ catalog was 1756. For measuring colours and applying photometric redshift algorithms, we used circular 2-arcsec diameter aperture magnitudes. This aperture size is the same as used for the ERGs in Chapter 3. We ran SEXTRACTOR in 'double-image mode' to perform aperture photometry on the J and H band images, using the corresponding K_s-band images for the detection of sources. For a minority of objects ($< 10\%$), a 2-arcsec diameter aperture produced a difference > 0.5 mag between the aperture and the total K_s magnitudes. For these objects we used a larger aperture of $2\sqrt{2} \approx 2.83$-arcsec diameter. The aperture sizes we adopted for the near-IR photometry have been deliberately selected to coincide with aperture sizes used to construct the ACS catalogs, as we explain below.

We looked for counterparts of our 1756 K_s-band sources in the public r.1.0z GOODS/CDFS ACS catalogs, within a matching radius of 1 arcsec. The GOODS/ACS catalogs (http://www.stsci.edu/ftp/science/goods/catalogs/) have been constructed by the GOODS teams running SEXTRACTOR on the version v1.0 of the reduced stacked GOODS/CDFS ACS images. The extraction of sources has been made on the z-band images and SEXTRACTOR has been run in 'double-image mode' to perform photometry on the B, V and I_{775} bands. The GOODS/ACS catalogs provide photometry in 11 different circular apertures for each source. For each of our K_s-band counterparts, we used the magnitudes corresponding to the same aperture size we had selected in the near-IR bands. We found that 25/1756 of our $K_s \leq 22$ sources did not have a counterpart in the GOODS/CDFS ACS catalog. We made an individual inspection of each of these 25 sources on the K_s-band images and found that 13/25 were spurious K_s-band detections, most of them close to the (already trimmed) edges of the corresponding K_s-band map and, in some cases, with no flux in the J or H bands. Another one of the 25 sources appears in a region where the ACS images are damaged by satellite tracks, so all the optical information is missed for this object. After exclusion of these 14 sources, the remaining sample had 1742 objects. In each case of non-detected flux (SEXTRACTOR magnitude 99.0) in any optical or near-IR band, we measured the flux manually in the corresponding aperture using the IRAF task 'phot' on the stacked GOODS HST/ACS V1.0 and the VLT/ISAAC v0.5 images. For faint objects in every ACS band (all of them ERGs), we repeated the same procedure explained in §3.3.2,

leaving only a few sources as formally non-detected in the V or redder bands in the multiwavelength catalogs we used as input for the photometric redshift algorithms.

As a final comment on the photometry of K_s-selected galaxies, we note that we used the photometric measurements made on the public GOODS HUDF images in the B, V, I_{775} and z bands for three ERGs. These objects were initially recognised as possible $z > 4$ candidates, but the better quality of the HUDF data allowed to reveal them as being at lower redshifts (cf.§3.5.6).

4.2.2 Completeness

We used the IRAF tasks 'gallist' and 'mkobjects' to create a $K_s \leq 22$ mock catalog of 200 objects with a power-law luminosity distribution and insert them into each of the 8 ISAAC K_s-band maps. We ran SEXTRACTOR again on these images, using the same original extraction parameters, and checked the fraction of artificial sources recovered in each case. From this, we estimated that our sample was 100%, 89%, 86%, and 80% complete at $K_s \leq 20.0$, $20.0 < K_s \leq 21.0$, $21.0 < K_s \leq 21.5$ and $21.5 < K_s \leq 22.0$, respectively.

4.2.3 The ERG sample

In this chapter we compare the redshift distribution and derived properties for the $K_s \leq 22$-selected galaxies with the corresponding results obtained in Chapter 3 for the R03 ERGs selected in the same field. However, in order to assess the validity of the comparison of the present K_s-selected sample with a subsample of ERGs obtained in an independent way, we checked the number of objects with $(I_{775} - K_s) > 3.92$ among the new $K_s \leq 22$ sources, obtaining a number of 205. 186/205 of these objects are in common with the sources selected by R03 as ERGs with the same colour cutoff (which are 198 objects in total), producing an overlap of both ERG samples > 90%. Thus, the comparison of results for the present K_s-selected sample and the R03 ERGs is entirely valid.

4.2.4 Star/galaxy separation

We cleaned our catalogs for stars/QSOs using the SEXTRACTOR stellarity parameter 'CLASS_STAR', as measured on the ACS z-band images and appears on the

GOODS/CDFS ACS catalogs. We found that 107/1742 $K_s \leq 22$ sources had z-band counterparts with CLASS_STAR$\geq$ 0.8. 64 out of these 107 objects are confirmed by the SIMBAD astronomical database (http://simbad.u-strasbg.fr/Simbad) as stars or QSOs, so we removed them from our catalogs, leaving 1678 sources for the photometric redshift algorithm input files. The inspection of the redshift output catalogs showed that 15 out of the remaining 43 objects with CLASS_STAR$\geq$ 0.8 could not be satisfactorily modelled by any galaxy SED template (cf. §4.3) and had zero probability of being at any redshift. Thus, we considered that these 15 objects were also very likely to be stars/QSOs and excluded them from our sample, leaving 1663 sources in the final $K_s \leq 22$ galaxy catalog.

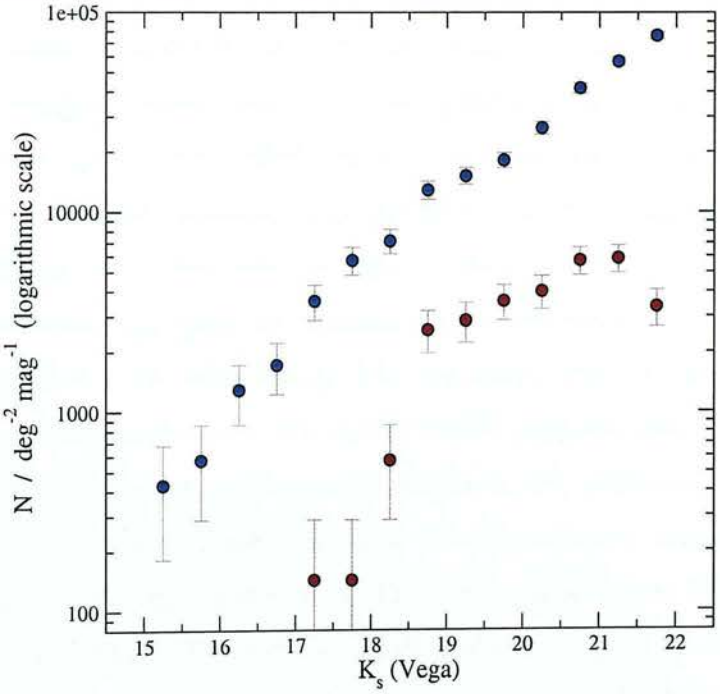

Figure 4.1: Differential number counts for the K_s-selected galaxies in the GOODS/CDFS deep ISAAC field (blue circles), in comparison with the number counts for the ERGs selected in the same region by R03 (red circles).

4.2.5 Number counts

Figure 4.1 shows the differential number counts for our sample of K_s-selected galaxies (blue circles) in comparison with the number counts for ERGs obtained by R03 (red circles). Both sets of counts have been corrected for incompleteness. The ERG number-count curve is characterised by a flattening of the count slope beyond $K_s \approx 19.5$. In §4.4.3, we show that this fact is related to the existence of a turnover in the ERG LF at redshift $z_{phot} \approx 1$.

4.3 Redshift estimates

4.3.1 Strategy for redshift estimations

We used the public code HYPERZ [109] to compute photometric redshifts for our sample of K_s-selected sources, using the seven passbands described in §4.2.1 (B, V, I_{775}, z, J, H and K_s) and the GISSEL98 SED template library (Bruzual & Charlot 1993 [110]). A detailed explanation of the HYPERZ performance has been given in §3.4.1. We only recall here that we refer to the HYPERZ 'primary solution' as the redshift estimate z_{phot} (and corresponding set of parameters) which produce the maximum likelihood in the SED fitting. The 'secondary solution' is the second most likely solution in parameter space. We ran HYPERZ using the same parameter values as in §3.4.3. In particular, we applied a Calzetti et al. [27] reddening law with the V-band extinction A_V varying between 0 and 1. For those objects taking the maximum possible reddening, we made a second HYPERZ run allowing the V-band extinction A_V to vary from 0 to 3. We used the public code BPZ [114] to obtain a second, independent redshift estimate for a subset of the sources that HYPERZ found to be at high redshift, namely:

- very bright K_s-band sources with primary solution $z_{phot} > 2$
- sources with significant flux in the B-band ($B_{AB} \leq 27.5$) and primary solution $z_{phot} > 3$
- all sources with primary solution $z_{phot} > 4$.

For those objects which BPZ also placed at high redshift, we accepted the HYPERZ primary solution as the definitive solution for the object. On the other hand, when

BPZ determined a lower redshift estimate, we adopted the HYPERZ secondary solution, which was in agreement with BPZ in most of these alternative cases. For seven sources, we found that neither the HYPERZ primary nor secondary solutions provided as low a redshift estimate as the BPZ determination. In these cases, we adopted the BPZ estimates as the definitive redshifts. One extra source had a very high redshift HYPERZ primary solution and a low redshift secondary solution in agreement with BPZ. However, the real redshift for this source is $z_{phot} = 1.669$, based on spectroscopic determinations (cf.§4.3.2), which both photometric redshift algorithms fail to correctly estimate. In this case only, we adopt the spectroscopic value as the definitive redshift. For the eight sources with either BPZ or spectroscopic redshift replacements, we do not have the complementary information provided by HYPERZ in the output, i.e. SED best-fit template, k-corrected K_s-band absolute magnitude, age, etc.

As we explained in §4.2.4, after running HYPERZ on our catalog of 1678 $K_s \leq 22$ sources, we determined that 15 of these objects were likely to be stars/QSOs, based on their stellarity parameter and the fact that they did not have a satisfactory fitting by any of the templates in the HYPERZ SED library. After rejecting these objects, our final $K_s \leq 22$ catalog consisted of 1663 galaxies, including $\sim 95\%$ of the ERGs in the R03 sample. (The few ERGs mentioned in §3.5.6 as likely stellar contaminants are now automatically rejected from the present $K_s \leq 22$ galaxy sample).

4.3.2 Photometric redshift calibration

We used the public master list of spectroscopic redshifts available for the GOODS/CDFS to calibrate our photometric redshift estimates. Spectroscopic data in the GOODS/CDFS have been obtained by different authors, e.g. [132] [133] [131]. The spectroscopic redshifts available for the sources in the r.1.0z GOODS/CDFS ACS catalog have been compiled in a master list at http://www.eso.org/science/goods/spectroscopy/CDFS_Mastercat.

Figure 4.2(a) compares our redshift estimates with the spectroscopic redshifts for the $K_s \leq 22$ sources included in different CDFS spectroscopy samples. We restricted the comparison to sources with good quality flags for the spectroscopic redshift determinations. The error bars in the photometric redshifts correspond to 1σ-confidence levels. We observe quite good agreement between the redshift estimates and the real

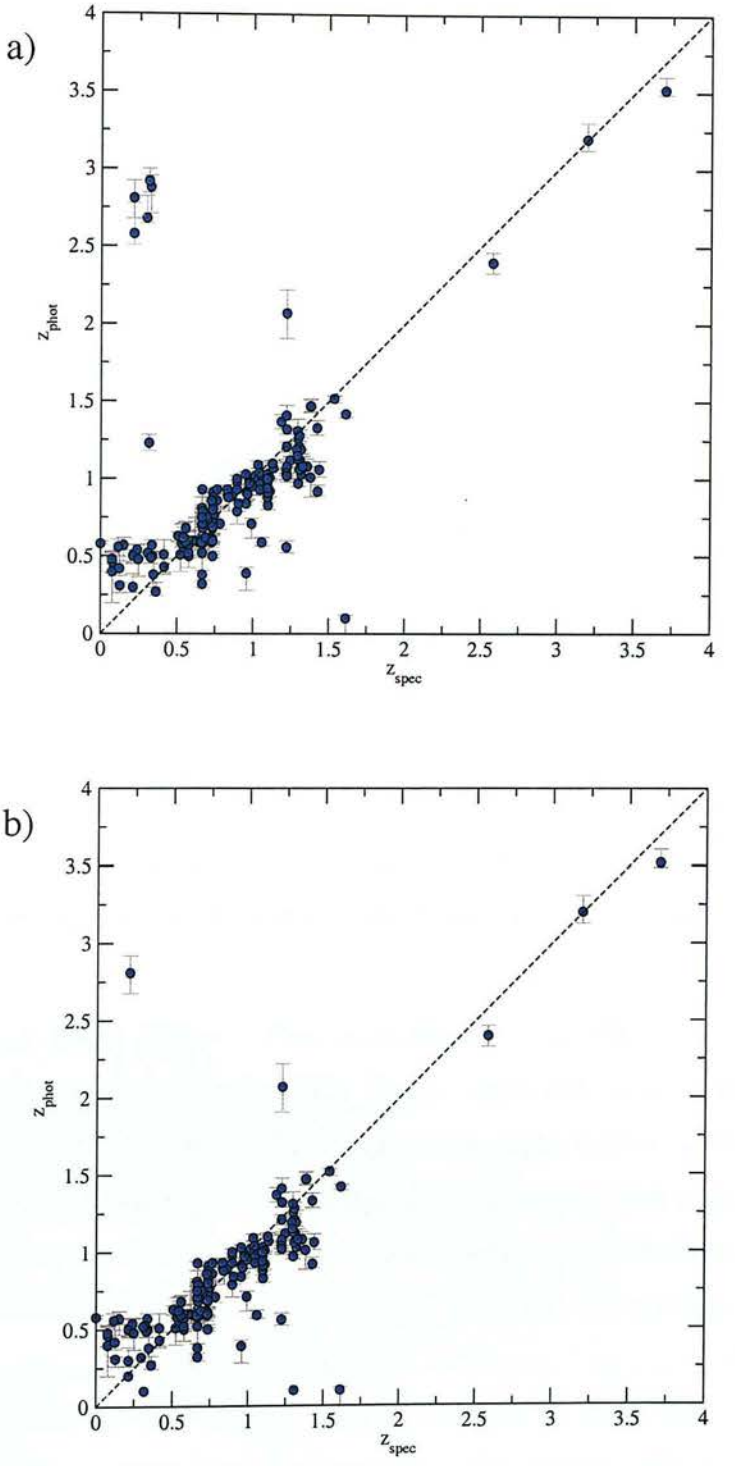

Figure 4.2: Photometric redshifts vs. spectroscopic redshifts for $K_s \leq 22$-selected galaxies in the GOODS/CDFS deep ISAAC field: a) before the calibration; b) after the calibration.

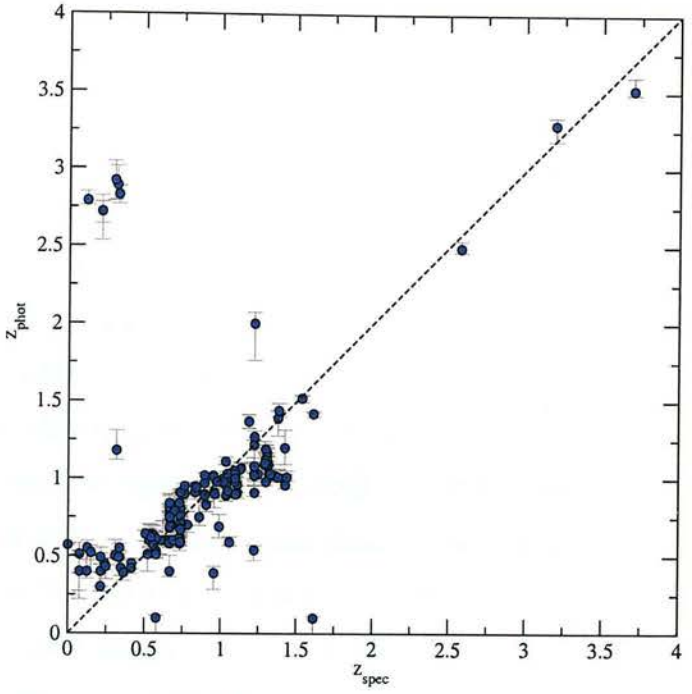

Figure 4.3: Photometric redshifts obtained using the J and K_s-band data from the GOODS/EIS v1.0 release vs. spectroscopic redshifts. This plot does not include the calibration procedure explained in §4.3.2 and, thus, should be compared with fig.4.2(a).

redshifts in most cases. However, there is an excess of low redshift sources which we identified as being at redshifts $z_{phot} > 2.5$. These sources with mismatching results are indicating that the photometric redshift algorithms might have a tendency to favour high redshift values when degenerate solutions in parameter space exist. To compensate for this effect, we calibrated our photometric redshifts with the following criteria: for sources with significant B-band flux ($B_{AB} \leq 27.5$) and a large difference between the HYPERZ primary and secondary solutions, i.e. $(z_{prim} - z_{sec}) \geq 1$, we adopted the HYPERZ secondary lower-redshift solution in the cases in which this redshift had at least 40% of the probability of the primary one. For sources with $B_{AB} > 27.5$ and $(z_{prim} - z_{sec}) \geq 1$, which are more likely to be at high redshift, we adopted a threshold of 70% between the relative probabilities of the secondary and the primary solutions to adopt the former as the preferred answer. These criteria have been applied in addition to those explained in §4.3.1, without affecting the cases in which the HYPERZ

secondary solution was already selected for providing a better agreement with the corresponding BPZ estimation. In summary, we adopted the HYPERZ secondary solution for 136/1663 sources, while 1519/1663 remained with the primary one (and 8/1663 had either BPZ or spectroscopic value replacements). The comparison of our photometric estimates with the spectroscopic redshifts after the calibration procedure is shown in Figure 4.2(b). The resulting relative errors between our estimates and the real redshifts are $|z_{phot} - z_{spec}|/(1 + z_{spec}) < 0.1$ for the majority ($> 77\%$) of the compared sources. In particular, we obtain a median of $|z_{phot} - z_{spec}|/(1 + z_{spec}) \approx 0.04$ for either the compared sources with $z_{spec} > 1.5$ or $z_{phot} > 1.5$. These values are among the typical uncertainties obtained in photometric redshift estimates available in the literature.

While we were performing the present study, a new release of the GOODS/CDFS ISAAC data in the K_s and J bands has been made public (GOODS/EIS v1.0 release, May 2004). The new release includes the determination of a uniform photometric calibration across the entire GOODS/CDFS field. We revised the K_s and J-band photometry of our K_s-selected sample in the new ISAAC maps. After running HYPERZ and BPZ under the same conditions as explained in §4.3.1, we determined the existence of a basically negligible impact of any possible difference between the ISAAC v0.5 and v1.0 calibrations on our estimated redshifts. The resulting z_{phot} vs. z_{spec} plot obtained using the v1.0 J and K_s-band data is shown in figure 4.3. This plot does not include the calibration procedure explained above and, thus, should be compared with fig. 4.2(a).

4.3.3 The ERG photometric redshifts

The calibration procedure explained in Section 3.2 was not implemented in Chapter 3 because CDFS spectroscopic redshifts were not yet completely available and because the overlap with the R03 ERG sample was small. Thus, we needed to verify that our new selection of a K_s-band sample and the calibration of the photometric estimates based on spectroscopic redshifts still produced results in agreement with those obtained in Chapter 3 for the ERG subsample.

Figure 4.4 shows the new redshift estimates we determined for the ERGs versus the redshift estimates obtained in Chapter 3. The error bars correspond to 1σ-confidence levels. Both sets of redshifts appear to be in very good agreement, except for a few outliers which correspond to cases of very strong degeneracies in parameter space.

This correlation confirms that, in spite of the differences in the redshift calibration implemented in the present work, the redshift estimates obtained for the ERGs are consistent and the comparison of derived properties for our total K_s-selected sample with the results obtained in Chapter 3 for the ERGs is valid.

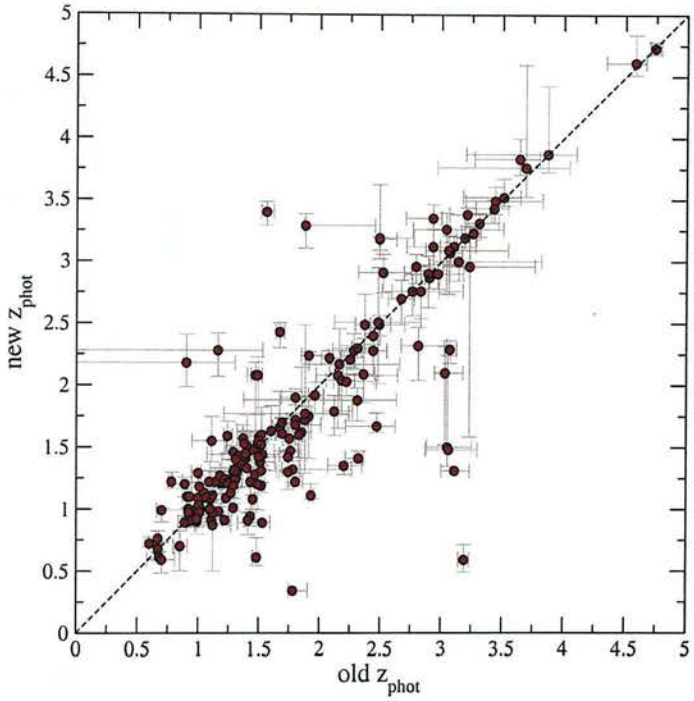

Figure 4.4: New redshift estimates for the ERGs in the deep ISAAC field versus the redshift estimates obtained in Chapter 3.

4.4 Results

4.4.1 The redshift distribution

Figure 4.5(a) shows the redshift distribution of the total sample of K_s-selected galaxies (solid lines) compared with the redshift distribution for the ERGs obtained in Chapter 3 (dashed lines). The corresponding histograms have been constructed taking into account the probability density distribution in redshift space for each object, as given by HYPERZ in the output. The consideration of probability densities yields more realistic representations of the redshift distributions, because they take into account all

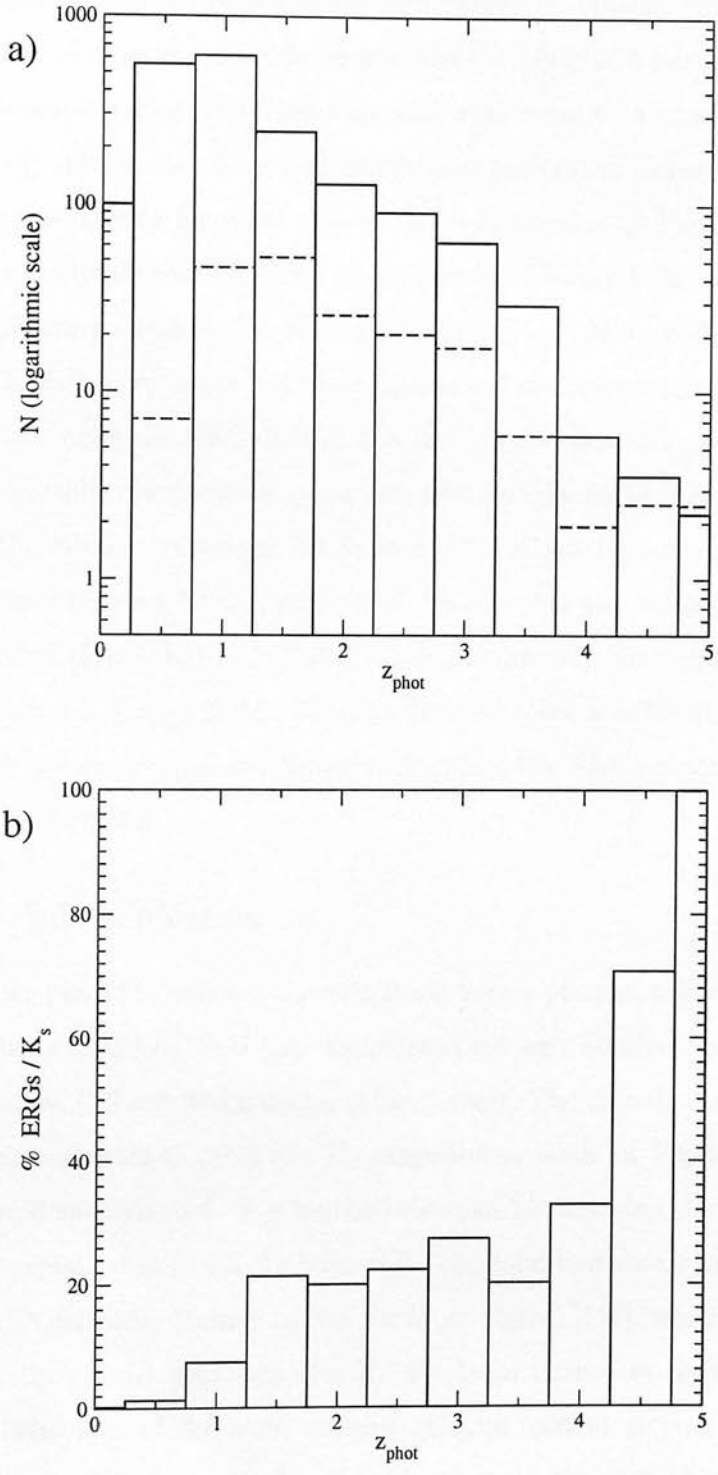

Figure 4.5: a) The redshift distribution of the total $K_s \leq 22$ sample of galaxies (solid lines) compared with the redshift distribution of the ERGs, as obtained in Chapter 3 (dashed lines). b) The percentage of ERGs found among K_s-selected galaxies as a function of redshift.

the uncertainties and degeneracies inherent to photometric redshift techniques. For the minority (< 9%) of objects for which we adopted the HYPERZ secondary solution or a BPZ/spectroscopic replacement, we only took into account a single redshift determination, as any information on a well-determined probability density distribution in redshift space was missing for these objects. Both histograms in Figure 4.5(a) include corrections for incompleteness, i.e. we multiplied by a factor 1.12, 1.16 and 1.25 the contribution of sources with $20.0 < K_s \leq 21.0$, $21.0 < K_s \leq 21.5$ and $21.5 < K_s \leq 22.0$, respectively. The distribution of the total K_s-selected galaxy sample peaks at redshift $z_{phot} \sim 0.5 - 1.0$, while the ERG distribution has a maximum at $z_{phot} \sim 1.5$. The difference in the redshift distributions is a consequence of the ERG colour cutoff. Figure 4.5(b) shows the relative fraction of ERGs among K_s-selected galaxies, allowing for an easier comparison between both populations. We see that the fraction of K_s-selected galaxies which are $(I_{775} - K_s) > 3.92$ ERGs is approximately constant ($\sim 20\% - 30\%$) between redshifts $1.5 \lesssim z_{phot} \lesssim 4.0$. We only find two sources with estimated redshifts $z_{phot} > 4$ in our present sample and these are the same two ERGs reported as confident $z > 4$ candidates in §3.5.6.

4.4.2 The Hubble diagram

In Figure 4.6 we plot the observed K_s magnitude versus photometric redshift z_{phot} for the ERGs in the deep ISAAC field (red circles), as they were obtained in Chapter 3, and for all the other $K_s \leq 22$-selected galaxies (blue circles). The Hubble diagram in Figure 4.6(a) has been constructed using raw K_s magnitudes, while in Figure 4.6(b) the K_s magnitudes are dust-corrected. The method we used to deredden the K_s magnitudes is the same as explained in §3.5.2. In both plots, the solid line shows the empirical K-z relation for radio galaxies obtained by Willott et al. (2003) [116], which approximately corresponds to the passive evolution of a $3L^*$ starburst formed at redshift $z = 10$ and indicates the behaviour of the most massive galaxies formed at very high redshifts. The redshift associated with each K_s-selected galaxy in the present sample is either a HYPERZ solution or a BPZ/spectroscopic replacement, in accord with the criteria explained in §4.3.1 and §4.3.2.

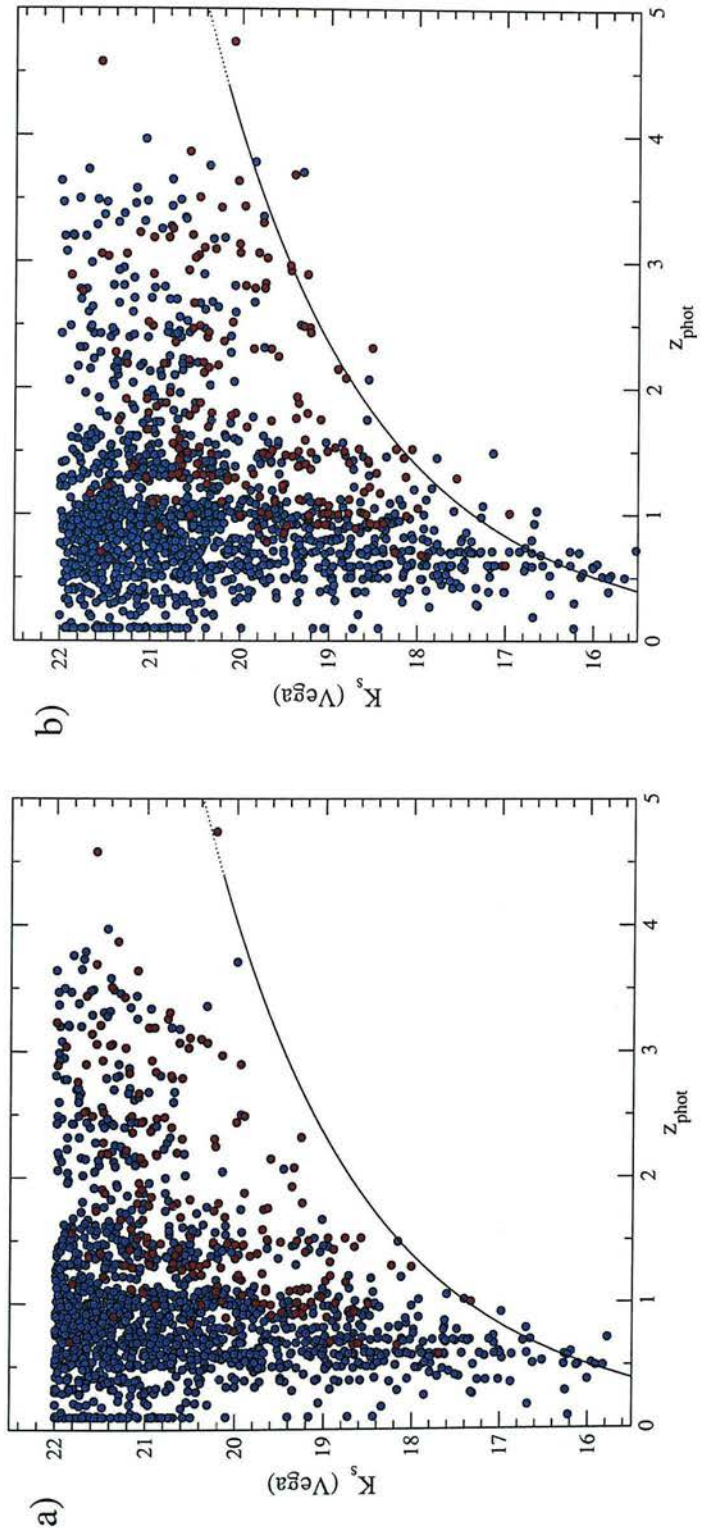

Figure 4.6: Total raw K_s magnitude (a) and dust-corrected K_s magnitude (b), plotted against photometric redshift z_{phot}. The blue circles correspond to the $K_s \leq 22$-selected galaxies in the deep ISAAC field which are not in the R03 ERG sample. The red circles correspond to the ERGs, with the redshifts estimated in Chapter 3. The solid line shows the empirical K-z relation for radio galaxies as obtained by Willott et al. (2003) [116], which approximately coincides with the passive evolution of a $3L^*$ starburst instantaneously formed at redshift $z = 10$. The dotted line is a nominal extrapolation of the same law.

The comparison of the K_s-z_{phot} relation for extremely red and bluer K_s-selected galaxies yields two main conclusions. First, ERGs show the same large dispersion in the Hubble diagram as all the other K_s-selected galaxies (although the ERG colour cutoff produces the absence of these objects at the lower redshifts). Second, as was discussed in §3.5.2, the raw Hubble diagram is characterised by a lack of objects near the radio galaxy line at redshifts $z_{phot} \gtrsim 3$. We see that this effect is still present when all the other K_s-selected galaxies are included. Comparison of Figures 4.6(a) and 4.6(b) shows that most of the observer-frame K_s-band intrinsically brightest objects at very high redshifts are ERGs enshrouded by large amounts of dust. However, we note the presence of three bright objects at $z_{phot} > 3$ which are not $(I_{775} - K_s) > 3.92$ ERGs. All of the intrinsically brightest objects at $z_{phot} > 3$ have $(J - K_s) > 2.2$ (Vega), but some of them are missed when a typical ERG $(I_{775} - K_s)$ colour cut is applied (in the present case, in particular, the three extra sources have $(I_{775} - K_s) < 3.7$). Most of these objects correspond to galaxies in the final stages of a continuous but decaying process of star formation, sufficiently old ($\sim 1 - 2$ Gyr) to have developed a 4000Å-break which produces red observer-frame $(J - K_s)$ colours. Yet, in some of them, the still rather active star formation produces considerable amounts of ultraviolet (UV) flux which, in conjunction with only modest dust extinction, prevents these sources from displaying extremely red $(I_{775} - K_s)$ colours. In §4.4.4, we present some further discussion on the influence of the selection effects on the inclusion of the most massive galaxies when constructing K_s-band galaxy samples.

4.4.3 The evolution of the K_s-band/ERG luminosity functions

In this section, we study the rest-frame K_s-band LF for the ERGs and the total sample of K_s-selected galaxies at different redshifts, in order to investigate any possible difference in their evolution. We computed the K_s-band LF binning the $K_s \leq 22$-sample of 1663 galaxies in both redshift and absolute magnitude space, in the same way as was done for the ERG sample in Chapter 3. A single redshift estimate has been considered for each source (either the HYPERZ primary, the secondary, or a BPZ/spectroscopic solution, as detailed in §4.3.1 and §4.3.2). In the cases in which we adopted the HYPERZ primary solution, the corresponding k-corrected absolute magnitude M_{K_s} was directly obtained from the HYPERZ output. In all the other cases, where the esti-

mated redshifts are relatively low, we computed the absolute magnitude M_{K_s} assuming that the k-corrections have negligible dependence on the SED shape (an assumption particularly valid for the K_s band at relatively low redshifts). To take into account the limits of the survey ($K_s = 22$), we weighted each source by a factor V_{maxbin}/V_{maxobs}, where V_{maxbin} is the volume determined by the maximum redshift of the corresponding bin and V_{maxobs} is the volume determined by the maximum redshift at which the source would still be detected in the survey (provided it is lower than the maximum redshift of the bin). We also applied weighting factors of 1.12, 1.16 and 1.25 for sources with $20.0 < K_s \leq 21.0$, $21.0 < K_s \leq 21.5$ and $21.5 < K_s \leq 22.0$, respectively, to correct for incompleteness of the sample (cf.§4.2.2).

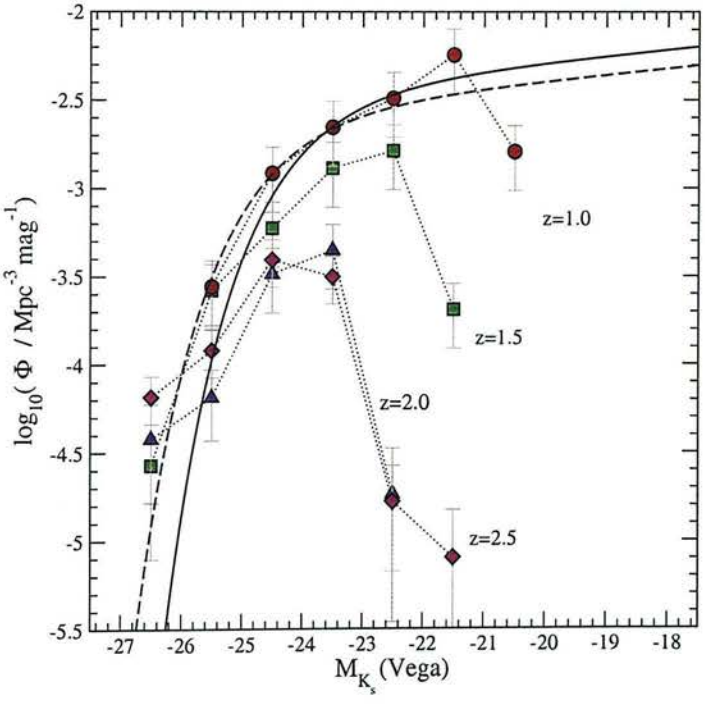

Figure 4.7: The rest-frame K_s-band luminosity function at redshifts $\langle z_{phot} \rangle = 1.0, 1.5, 2.0$ and 2.5 (circles, squares, up triangles and diamonds, respectively). The solid line corresponds to the Schechter function fitted to the local K-band LF measured on 2MASS data by Kochanek et al. (2001) [66]. The dashed line shows the evolution of the LF at redshift $z = 1$, as estimated by Drory et al. (2003) [134].

Figure 4.7 shows the total K_s-band LF at redshifts $\langle z_{phot} \rangle = 1.0, 1.5, 2.0$ and 2.5

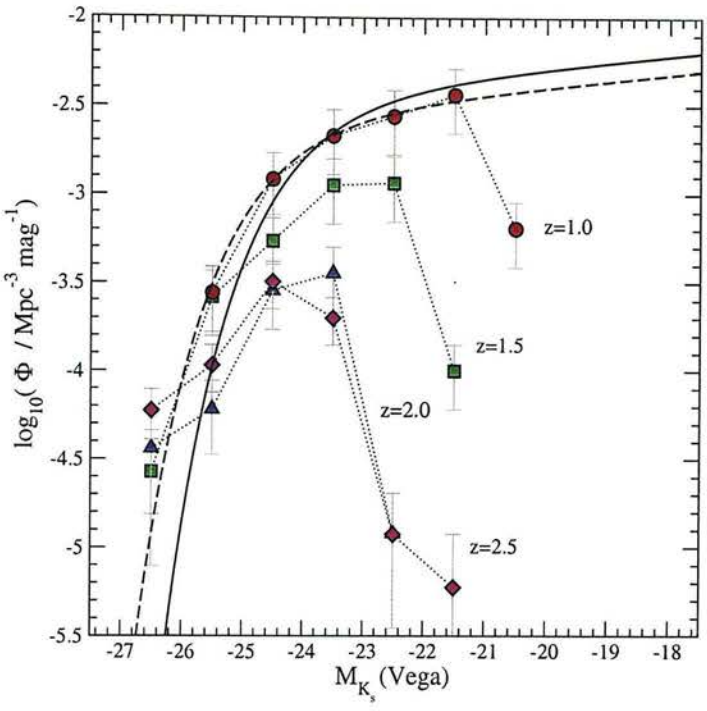

Figure 4.8: The raw rest-frame K_s-band luminosity function at redshifts $\langle z_{phot} \rangle = 1.0, 1.5, 2.0$ and 2.5 (no V_{max} corrections, no corrections for incompleteness). The symbols are the same as in Figure 4.7.

(circles, squares, up triangles and diamonds, respectively). The error bars correspond to the maximum of Poissonian errors and the errors due to cosmic variance, which we considered on average as 40% and 30% of the number counts at redshifts $z < 2$ and $2 < z < 3$, respectively [121]. Although not all the K_s-selected galaxies are expected to display the strong clustering observed in ERGs [47], we adopted the same cosmic variance error bars as in Chapter 3 for conservative reasons. We do not present the LF at redshift $\langle z_{phot} \rangle = 0.5$ because our surveyed volume is small at those redshifts and the LF is quite affected by the presence of large scale structure at $z = 0.67 - 0.73$ [132] [133]. We show, for comparison, the local K-band LF obtained by Kochanek et al. (2001) [66] using Two Micron All Sky Survey (2MASS) data, and its evolution to redshift $z = 1$ as estimated by Drory et al. (2003) [134](solid and dashed lines, respectively). Drory et al. [134] found that the density of bright objects increases from redshift $z = 0$ to $z = 1$. Our results confirm this, and show no evidence for the bright

end to decrease again up to at least redshifts $\langle z_{phot} \rangle = 2.5$. A similar effect was observed for the ERG LF in §3.5.4. Figure 4.7 confirms that the behaviour of a constant (or even possibly increasing) evolution for the bright end of the LF is a property of the total K_s-selected galaxy population. At intermediate magnitudes, on the contrary, our results suggest a non-negligible decrease in the density of objects, although wider and deeper surveys are necessary to better quantify this evolution. To demonstrate that none of our conclusions depend on the V_{max} corrections or the corrections for incompleteness, we show in Figure 4.8 the 'raw' K_s-band LF, i.e. the LF constructed without applying any of these corrections. We note that the analysis of the raw LF allows us to extract exactly the same conclusions as in the case of the corrected version presented in Figure 4.7.

The four panels in Figure 4.9 compare the evolution of the total (blue symbols) and the ERG (red symbols) K_s-band LFs with redshift. The latter is the same as presented in §3.5.4. For each LF individually, we adopted the maximum of the Poisson errors and the errors due to cosmic variance. Any possible error produced by uncertainties in our redshift estimations is expected to be contained within the Poisson/cosmic variance error bars. Figure 4.10 shows the relative error $dz_{phot}/(1 + z_{phot})$ in the redshift estimation of each one of the sources making the K_s-band LF at different redshifts. The absolute error dz_{phot} corresponds to 1σ-confidence levels, as obtained from HYPERZ. The sources with $dz_{phot} = 0$ correspond to cases in which the HYPERZ secondary solution has been adopted for the redshift estimate. In every redshift bin, the median of the relative errors for the redshift estimates is $dz_{phot}/(1+z_{phot}) < 0.07$ and the number of sources with $dz_{phot}/(1+z_{phot}) > 0.2$ is very small ($< 1.5\%$ in all cases). The vertical lines in Figure 4.9 indicate the estimated completeness limits of the LF at different redshifts (dotted and dashed lines for the total and the ERG LFs, respectively). We computed the completeness limits taking into account the median of the k-corrections for each galaxy population and the maximum redshift of each corresponding redshift bin.

A clear feature in the evolution of the LF is the increasing role of ERGs in reproducing the bright end of the total K_s-band LF with increasing redshift, reaching a maximum at $\langle z_{phot} \rangle = 2.0$, where a considerable fraction of the brightest K_s-selected galaxies are ERGs. Also, from the comparison of the total and the ERG K_s-band LFs

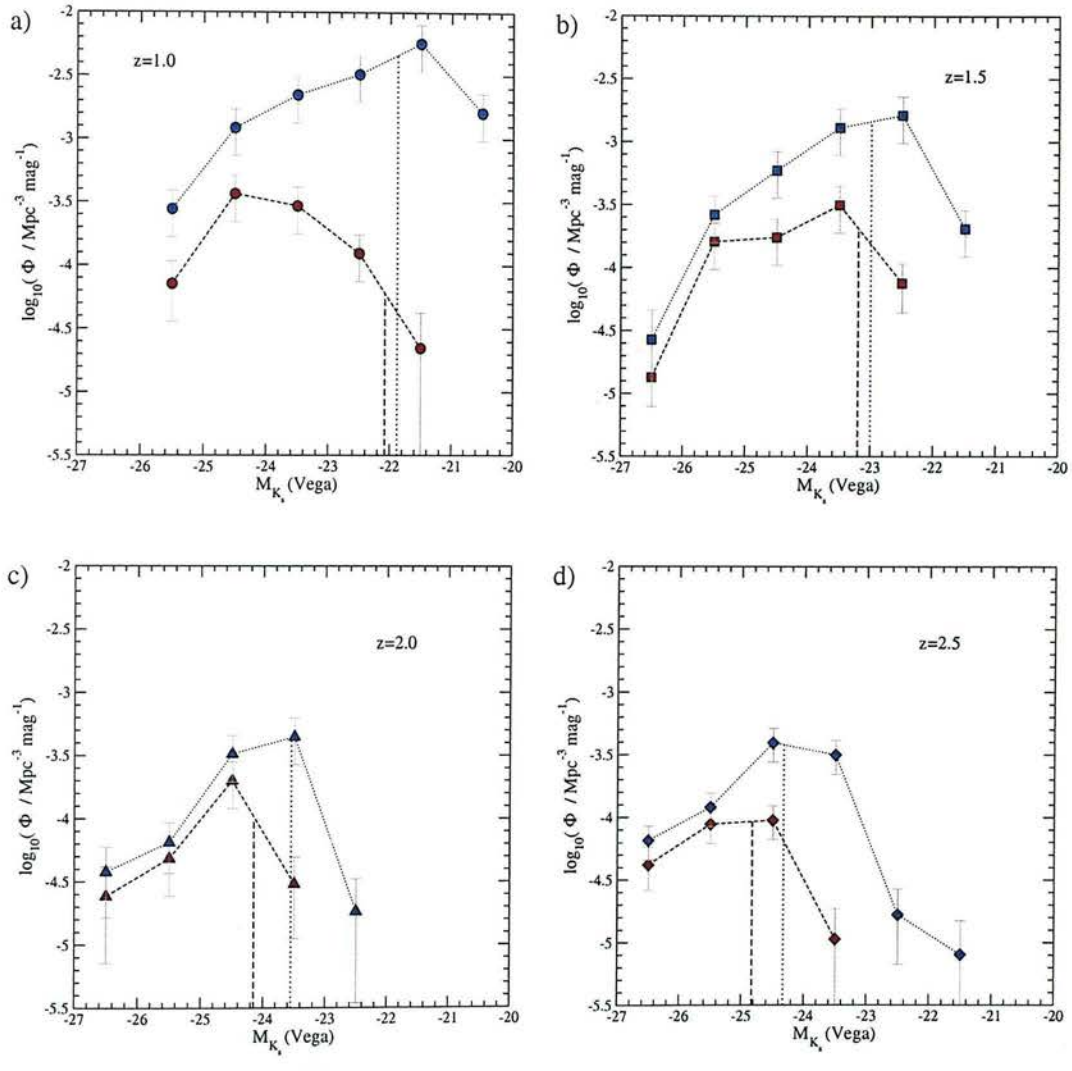

Figure 4.9: Compared evolution of the total K_s-band (blue symbols) and the ERG (red symbols) LFs with redshift. The error bars for each point are the maximum of Poissonian errors and the errors due to cosmic variance. The dotted and dashed vertical lines indicate the completeness limits at each redshift for all the K_s-selected galaxies and the ERGs, respectively.

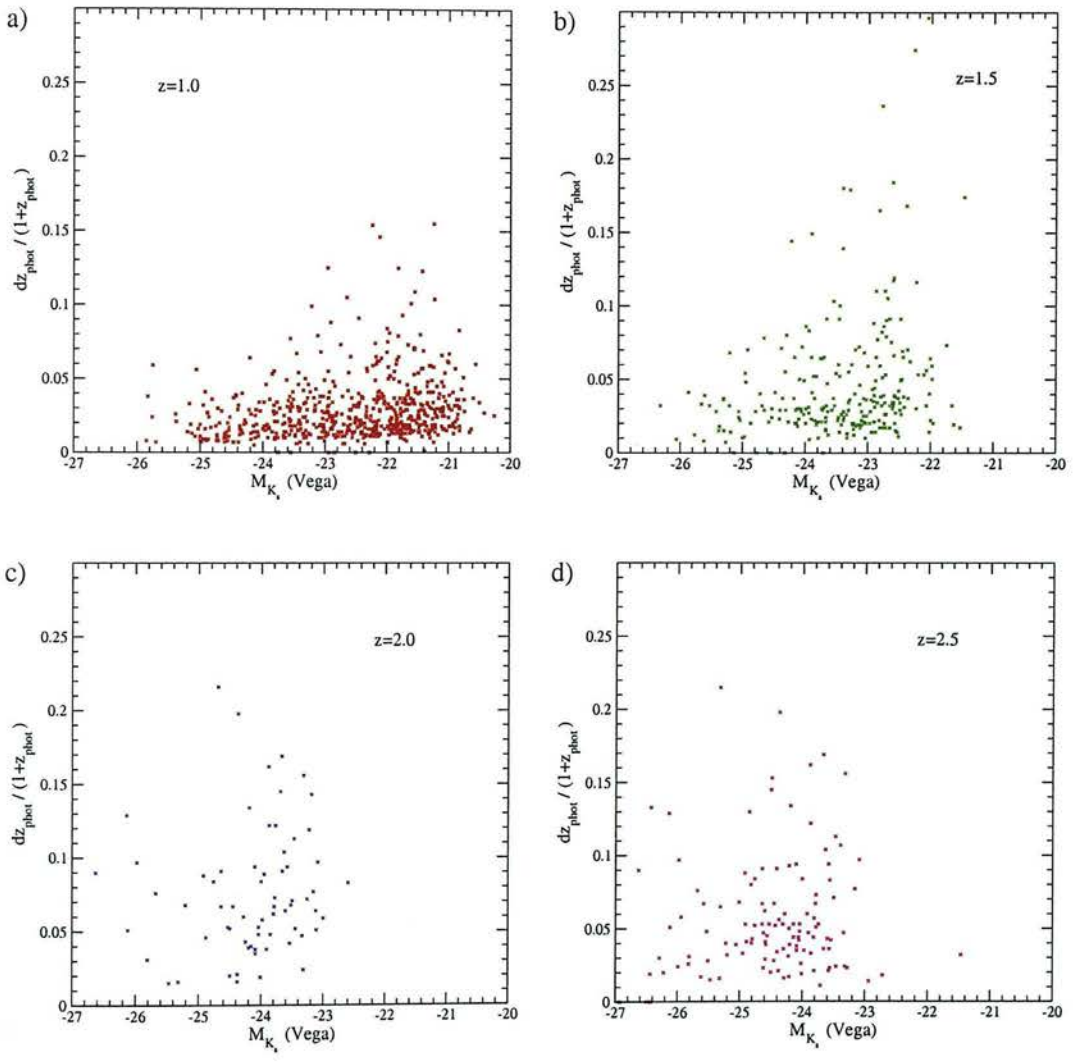

Figure 4.10: The relative errors of the redshift estimates for the sources considered in the computation of the K_s-band LF at different redshifts. The redshift bins considered in a), b) and c) have width $\Delta z_{phot} = 0.5$, while the redshift bin considered in d) has width $\Delta z_{phot} = 1$.

at redshift $\langle z_{phot} \rangle = 1.0$, we conclude that the latter has a bell-like shape rather than the shape of a Schechter function. This result is in agreement with the different shapes for the LFs of red and blue z-band selected galaxies at redshift $z \sim 1$, determined by Kodama et al.(2004) [135]. At redshift $\langle z_{phot} \rangle = 1.5$, the total K_s-band and the ERG LFs are more similar, but a significant density of blue galaxies is still necessary to account for the total K_s-band galaxy population at intermediate magnitudes. At $2 \lesssim z_{phot} \lesssim 3$, our completeness limits only allow us to explore the bright end of the K_s-band LF, which appears mainly dominated by the ERGs.

4.4.4 The evolution of massive galaxies

In §3.5.5, it was shown that the comoving densities of ERG progenitors of the local $L > L^*$ galaxy population, under passive evolution, were below the values expected by the evolution of dark matter haloes in a Λ-Cold Dark Matter (ΛCDM) formalism [41] [64]. This fact has been interpreted as either a deficiency of the ERG population to account for all the progenitors of the local $L > L^*$ galaxies, or as due to the incomplete picture described by a passive evolution scenario. Our aim here is to further test these two possibilities using a similar approach: studying the evolution of the comoving number density of massive systems and, in general, the evolution of the stellar mass content of the Universe with redshift. The evolution of the stellar mass density has recently been studied in different fields up to redshift $z \sim 2$ [136] [137] [138], and in small-area surveys up to redshift $z \sim 3$ [139] [140] [141]. Here we extend the analysis of the comoving mass density evolution up to redshift $z \sim 4$, as obtained from the study of our deep sample of K_s-selected galaxies in the GOODS/CDFS field.

We computed the rest-frame K_s-band luminosity of each of our galaxies using the k-corrected absolute magnitude M_{K_s}, associated with the HYPERZ primary or secondary solution, on a case-by-case basis. In the cases in which we adopted the HYPERZ secondary solution, the absolute magnitude M_{K_s} has been extrapolated as we explained in §4.4.3. To estimate the mass of our galaxies, we used, in each case, the galaxy luminosity and a mass-to-light (M/L_{K_s}) ratio depending on the corresponding HYPERZ best-fit SED type and age. For the eight objects with BPZ/spectroscopic redshifts, any information on the galaxy SED type or age is missing, so these sources are not taken into account in all the analysis made in this section. We used the public code GALAXEV

[120] to construct a grid of mass-to-light (M/L_{K_s}) ratios depending on galaxy age. In the K_s-band, these ratios have little dependence on either the dust corrections or the galaxy star formation history. Thus, to model the M/L_{K_s} ratios as a function of age, we used only two galaxy templates, sufficiently representative of the different HYPERZ library SEDs. Both GALAXEV templates had a solar metallicity and no dust corrections, but corresponded to two different exponentially-declining star formation histories: fast ($\tau \sim 0.1\,\mathrm{Gyr}$) and slow ($\tau \sim 5\,\mathrm{Gyr}$). The final M/L_{K_s} value adopted for each galaxy was the one corresponding to the GALAXEV template most similar to the HYPERZ best-fit SED, and to the HYPERZ best-fit age (obtained interpolating between the M/L_{K_s} values in our age grid). We used a Salpeter initial mass function (IMF) , for ease of comparison with most of the values quoted in the literature. To compute comoving densities, we used the complete probability distribution in redshift space to determine the potential contribution of each object at different redshifts (note, however, that a more rigourous procedure should take into account a probability density in the whole parameter space). For the sources for which we adopted the HYPERZ secondary solution, a single redshift has been considered, as in these cases we cannot recover a well-determined probability density function.

Figure 4.11 shows the comoving number densities of galaxies which have assembled a stellar mass $M > 5 \times 10^{10} M_\odot$ (a) and $M > 1 \times 10^{11} M_\odot$ (b), as a function of redshift. The blue circles correspond to all the K_s-band selected galaxies in the deep ISAAC field, while the red circles indicate the contribution of the ERGs selected in the same area. The horizontal error bars indicate the binning in redshift space. The vertical error bars correspond to cosmic variance (40%, 30% and 15% of the number counts at redshifts $z_{phot} < 2$, $2 < z_{phot} < 3$ and $3 < z_{phot} < 4$, respectively), which is the dominant source of error in this case. V_{maxbin}/V_{maxobs} and incompleteness correction factors have been applied throughout. In both panels (a) and (b), the star-like symbol (diamond) indicates the local number densities of all (early-type) galaxies with stellar masses above the corresponding mass cuts. The local number densities have been obtained by integrating the K-band-derived mass functions computed by Bell et al. (2003), converted to a Salpeter IMF.

From inspection of Figure 4.11, we see that a considerable fraction ($\sim$ 20%-25%) of the galaxies with mass $M > 5 \times 10^{10} M_\odot$ and $M > 1 \times 10^{11} M_\odot$ is in place before redshift

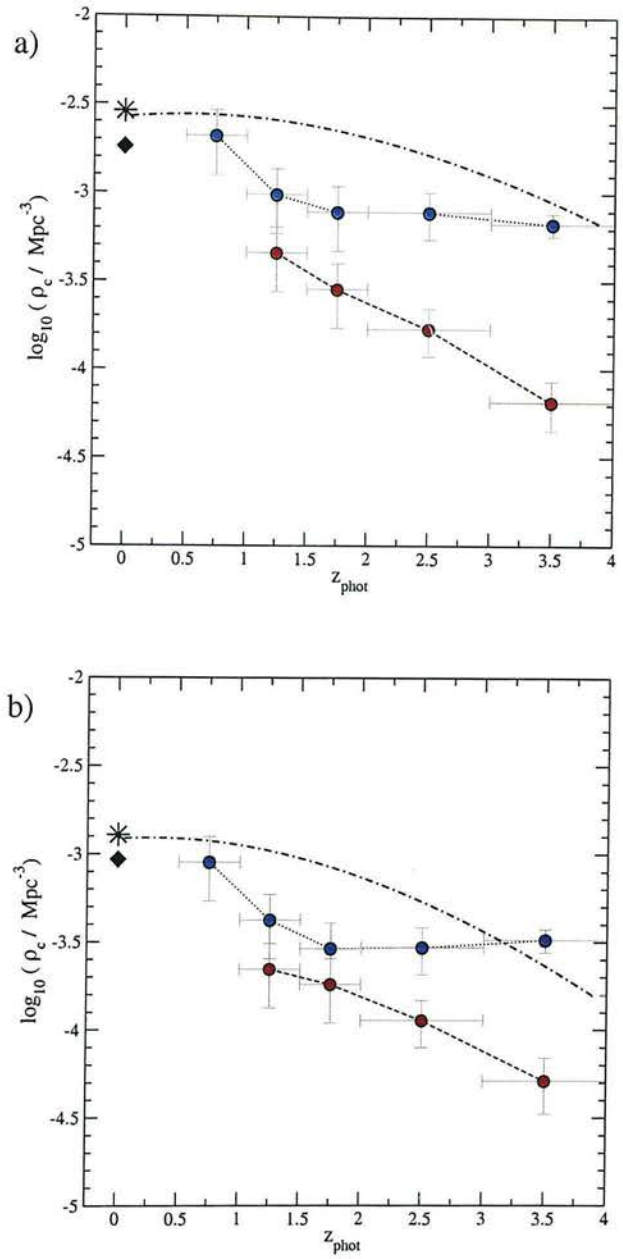

Figure 4.11: The comoving number density of galaxies with stellar mass $M > 5 \times 10^{10} M_\odot$ (a) and $M > 1 \times 10^{11} M_\odot$ (b). The blue circles indicate the densities of all the K_s-band selected galaxies, while the red circles show the contribution of the ERGs selected in the same field. In both plots (a) and (b), the star-like symbol and diamond indicate the corresponding local values for all and early-type galaxies, respectively [143]. The dotted-dashed lines indicate the evolution of the number density of haloes with total mass $M > 8 \times 10^{11} M_\odot$ (a) and $M > 2 \times 10^{12} M_\odot$ (b), as obtained from ΛCDM models of structure formation.

$z_{phot} \sim 4$. The number density is virtually constant down to redshift $z_{phot} \approx 2$ and the assembly of the remaining massive systems appears to have been produced at redshifts $z_{phot} \lesssim 1.5$. This evolution suggests the existence of a two-fold mechanism for the construction of massive galaxies: while most of the systems are assembled at relatively low redshifts, as expected in hierarchical models of galaxy formation, a substantial fraction is assembled very efficiently at very early times.

As in §3.5.5, we compare the comoving number densities of massive galaxies with the corresponding densities of dark matter haloes massive enough to host these systems, as they are predicted by ΛCDM models of structure formation. In Figure 4.11, the dotted-dashed lines represent the expected evolution of the number densities of haloes with total masses $M > 8 \times 10^{11} M_{\odot}$ (a) and $M > 2 \times 10^{12} M_{\odot}$ (b). The halo mass thresholds have been deliberately selected to coincide with the local number densities of galaxies with stellar mass $M > 5 \times 10^{10} M_{\odot}$ and $M > 1 \times 10^{11} M_{\odot}$, respectively. In the case of a single halo occupation number, we would expect the evolution of the number densities of galaxies to follow the evolution of the corresponding number density of haloes. This is what we observe up to redshift $z_{phot} \sim 1$. However, between redshifts $z_{phot} \sim 1$ and $z_{phot} \sim 3$, the predicted number densities of host haloes are significantly larger than the observed densities of already assembled massive galaxies. The latter are approximately constant up to redshift $z_{phot} \sim 4$, while the number of haloes decrease with redshift, in such a way that the number of galaxies and haloes coincide again at $z_{phot} \gtrsim 3$. This comparison suggests that, at very high redshift, the timescale in which halo merging and galaxy collapse occur are quite similar and, thus, the number density of galaxies traces the number density of haloes. At $z_{phot} \lesssim 3$, on the contrary, halo merging could be faster than galaxy collapse, explaining why the observed density of massive galaxies is only a fraction of the density of the corresponding haloes. By $z_{phot} \lesssim 1$, the assembly of massive galaxies is mostly complete, and the number of galaxies and haloes coincides again. We note that, even while we have an excess of galaxies with mass $M > 1 \times 10^{11} M_{\odot}$ with respect to the corresponding number of haloes at $z_{phot} \gtrsim 3$, this excess is not significant and could be contained within the error bars if the error of 15% in the number counts were somewhat underestimating the cosmic variance at those redshifts. Future deeper surveys will be able to test whether the predicted number densities of haloes is still compatible with the observational data

beyond redshift $z_{phot} \sim 4$, and set tighter constraints on the high formation redshifts of the oldest massive systems.

As we stated at the beginning of this section, one of our main aims is to assess the role of ERGs to account for the progenitors of the most massive systems and the validity of the passive evolution assumption. We make clear that, of course, only a subset of ERGs can potentially be the progenitors of the most massive local galaxies. The whole of the ERG population spans a wide variety of redshifts and masses (cf. §3.5.2), and many ERGs are completely irrelevant for the present discussion. The comparison of the number densities for the massive ERGs and all the massive K_s-selected galaxies in Figure 4.11(a) and 4.11(b) illustrates the fact that ERGs trace the high mass end of the K_s-selected galaxies. However, we observe that ERGs cannot account for all the systems with mass $M > 1 \times 10^{11} M_{\odot}$. At redshifts $z_{phot} \sim 1 - 2$, ERGs constitute $\sim 50\% - 70\%$ of all the K_s-selected galaxies which have assembled a stellar mass $M > 1 \times 10^{11} M_{\odot}$. Figure 4.11(b) also suggests the existence of an evolutionary sequence between massive K_s-selected galaxies at very high redshift and massive ERGs. We note that the comoving number densities of K_s-selected galaxies at $\langle z_{phot} \rangle$=3.5 is only slightly larger than the number density of ERGs with similar mass at redshift $z_{phot} \sim 1$, indicating that most of the massive systems at very high redshift might have evolved into ERGs by redshift $z_{phot} \sim 1$. The extremely red colours could be the consequence of the ageing of the stellar populations and this would be evidence for passive evolution since very high redshift. However, as stated in §3.5.5, the colours of some of the reddest ERGs can only be explained by the superposition of an evolved stellar population and dust. This would indicate that, in some of these galaxies, the passive ageing of the stellar populations could be interrupted by the production of new star formation. But, except for these possible temporary periods of additional star formation, ERGs seem to account for the fraction of massive galaxies at high redshift which have plausibly been evolving under passive evolution. In any case, we see that the massive galaxies which could have evolved passively since very high redshifts are only a fraction of the local value and, thus, a passive evolution scenario alone is not able to explain the construction of all the massive systems.

At $z_{phot} > 2$, on the contrary, we find a significant fraction of K_s-selected galaxies with mass $M > 1 \times 10^{11} M_{\odot}$ which are not $(I_{775} - K_s)$-selected ERGs. Regarding the

effects of completeness, we estimate that our K_s-selected sample is complete for galaxies with mass $M > 1 \times 10^{11} M_\odot$ up to redshift $z_{phot} \sim 4$, based on the median of the k-corrections and the maximum possible M/L_{K_s} ratio at that redshift. The median of the k-corrections is somewhat larger when only the ERGs are considered, and we estimate that the ERG sample is complete to a mass $M = 1 \times 10^{11} M_\odot$ up to redshift $z_{phot} \sim 3$. Thus, incompleteness only affects the comparison of the ERG and all the K_s-selected galaxy densities in the highest redshift bin. Most of our massive galaxies at $z_{phot} > 2$ have $(J - K_s) > 2$, indicating that a red $(J - K_s)$ colour cut provides a more efficient method to select massive systems at very high redshift than an $(I_{775} - K_s)$ cut (Franx et al. 2003 [142]). In §4.5, we predict the IR colours of our K_s-selected sources in different Spitzer/IRAC channels and present some further discussion on the efficiency of different pure IR colours to select high redshift galaxies.

Another point of interest is the analysis of how the total stellar mass budget is distributed at different redshifts. Figure 4.12 shows the evolution of the total stellar mass density (circles) with redshift, as derived from our sample of K_s-selected galaxies. The large and small squares indicate the contribution of galaxies with masses $M > 1 \times 10^{11} M_\odot$ and $7 \times 10^{10} M_\odot < M < 1 \times 10^{11} M_\odot$, respectively. (Our K_s =22-limited sample is estimated to be complete for galaxies with masses $M > 1 \times 10^{11} M_\odot$ and $M > 7 \times 10^{10} M_\odot$ up to redshifts $z_{phot} \approx 4$ and $z_{phot} \approx 3$, respectively). The symbols with a star at $z = 0$ show the corresponding local values obtained from the integration of the local galaxy stellar mass function [118] [143]. The solid line is the evolution of the stellar mass density as expected from the integration of the star-formation rates derived from Sloan Digital Sky Survey (SDSS) data [144]. From Figure 4.12, we see that most of the stellar mass is assembled at redshifts $0.5 \lesssim z_{phot} \lesssim 1.5$, in agreement with the tendency previously observed by other authors. At $\langle z_{phot} \rangle = 1.75$, we find that the total stellar mass density is already $\sim 25\% - 30\%$ of the local value, a percentage somewhat higher than the value of $\sim 13\%$ obtained by Rudnick et al.(2003) [141] at $z \sim 2$, using a small-area survey in the Hubble Deep Field South (HDFS), and more similar to the value of $\sim 20\%$ to $\sim 35\%$ determined by Fontana et al. (2004) [138] from the K20 survey. Our observed value of the total stellar mass density at $\langle z_{phot} \rangle = 1.75$ is $(1.37 \pm 0.55) \times 10^8 M_\odot \mathrm{Mpc}^{-3}$ (taking into account cosmic variance), which is in excellent agreement with the value $(1.45^{+0.41}_{-0.62}) \times 10^8 M_\odot \mathrm{Mpc}^{-3}$, as predicted by Fontana et al. [138]

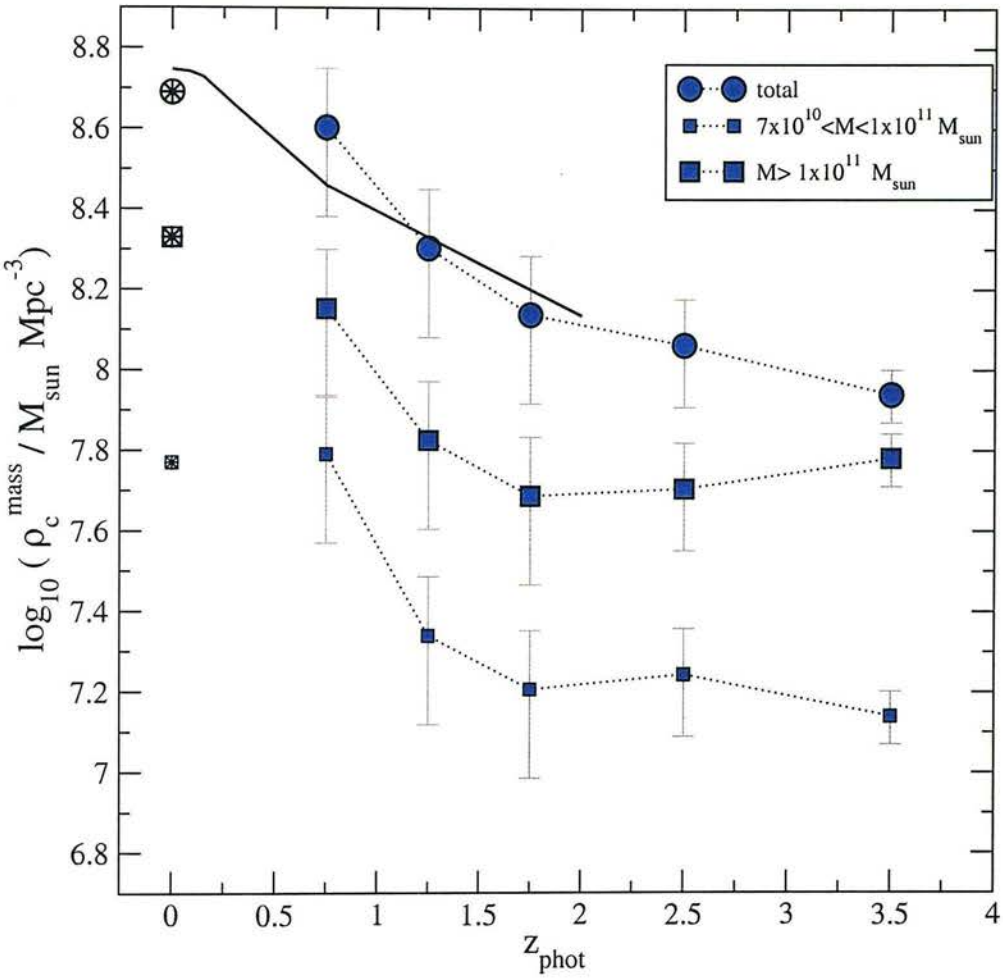

Figure 4.12: The distribution of the stellar mass density as a function of redshift, as derived from our deep sample of K_s-selected galaxies. The circles indicate the total stellar mass density. The large (small) squares are the contributions of galaxies with masses $M > 1 \times 10^{11} M_\odot$ ($7 \times 10^{10} M_\odot < M < 1 \times 10^{11} M_\odot$), for which our $K_s = 22$ -limited sample is estimated to be complete up to redshift $z_{phot} \approx 4$ ($z_{phot} \approx 3$). The symbols with a star at $z_{phot} = 0$ show the corresponding local values obtained from the integration of the local galaxy stellar mass function [118] [143]. The solid line is the evolution of the stellar mass density as obtained from the integration of the star-formation rates derived from Sloan Digital Sky Survey (SDSS) data [144].

by the extrapolation of the Schechter fits to the mass function of the K20 survey at these redshifts. It is worthwhile to note, however, that the observed mass density at $\langle z_{phot} \rangle = 1.75$ in a survey limited at $K_s = 20$ is only $\sim 50\%$ of the total value [138], while a survey extended up to $K_s = 22$ is able to recover most of the mass at that redshift, as we see from the comparison with the assembled stellar mass obtained from the integration of the star-formation rates derived from SDSS data. Beyond $z_{phot} \sim 2$, we observe only a slow decrease of the total stellar mass density, in spite of the increasing incompleteness for the intermediate and lower mass galaxies. We obtain lower limits of $\sim 24\%$ and $\sim 18\%$ of the local values for the total stellar mass assembled at redshifts $\langle z_{phot} \rangle = 2.5$ and $\langle z_{phot} \rangle = 3.5$, respectively. A detailed comparison of our total stellar mass densities at different redshifts with other values found in the literature is presented in Figure 4.13. The blue circles with error bars represent our values, as calculated from our sample of K_s-selected galaxies in the deep ISAAC field. Dickinson et al.2003 [139] values (green down-triangles) correspond to the average of the values obtained with the 1-component and 2-component models with solar metallicity (see Table 3 in [139]). Rudnick et al. 2003 [141] values (violet diamonds) are computed only on galaxies with rest-frame V-band luminosity $L_V > 1.4 \times 10^{10} L_\odot$ and, thus, miss a significant fraction of the mass. Glazebrook et al. 2004 [136] values (cyan up-triangles) only correspond to galaxies with estimated mass $\log(M) > 10.46$ and are at least partially incomplete above redshift $z \sim 1.2$. The orange squares and double squares are, respectively, the values computed and extrapolated by Fontana et al. 2004 [138] using the K20 survey data. It should be emphasized that all the determinations of stellar mass densities at redshifts $z > 2$ previous to this study have been made on pencil-beam surveys, with coverage areas $\lesssim 5\,\mathrm{arcmin}^2$.

The analysis of the distribution of the stellar mass budget in Figure 4.12 also allows us to extract an interesting conclusion: a minimum of $\sim 45\%$ and a maximum of $\sim 70\%$ of the stellar mass at redshifts $z_{phot} \gtrsim 3$ is contained in galaxies with assembled mass $M > 1 \times 10^{11} M_\odot$. This result is related to the significant number density of massive systems we find to be present before redshift $z_{phot} \sim 4$, and indicates that galaxy/star formation at very high redshift is an extremely efficient process. These massive galaxies present at very high redshift have presumably been formed from the early collapse of the high peaks of the density fluctuation field, e.g. [145]. Such regions of high density are

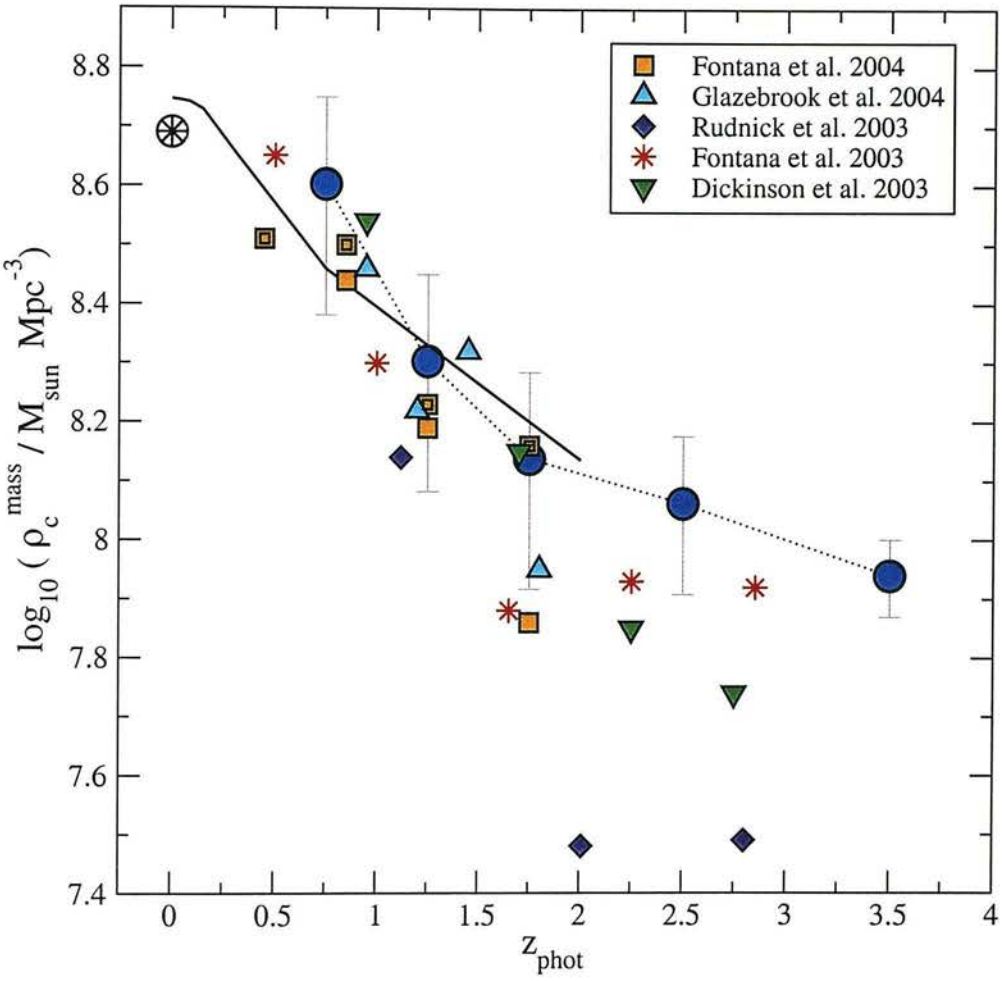

Figure 4.13: The comparison of the total stellar mass densities obtained from the present study (blue circles, with error bars) with values previously obtained by other authors: [139] (down-triangles); [140] (asterisks); [141] (diamonds); [136] (up-triangles); [138] (squares and double squares for the observed and extrapolated values in the K20 survey, respectively). The circle with a star at $z_{phot} = 0$ show the local value of the total stellar mass density obtained from the integration of the local galaxy stellar mass function [118] [143]. The solid line is the evolution of the stellar mass density as obtained from the integration of the star-formation rates derived from Sloan Digital Sky Survey (SDSS) data [144]. All the values in this figure assume a Salpeter IMF and a cosmology with $H_o = 70\,km\,s^{-1}Mpc^{-1}$, $\Omega_M = 0.3$ and $\Omega_\Lambda = 0.7$.

predicted to be strongly clustered, a fact which is perfectly consistent with the strong clustering observed in red K_s-selected galaxies at $2 < z_{phot} < 4$ [48] and in the ERGs up to the faintest magnitudes [47]. Evidence for a similar 'anti-hierarchical' behaviour in favour of biased galaxy formation has also been found by other authors from the study of galaxies at redshift $z \sim 1$ [135]. Our results are consistent with a scenario, already suggested by previous studies, in which a significant fraction of the massive galaxies we see today have been assembled at very high redshifts ($z \gtrsim 4$), evolved to $(I - K_s)$ ERGs by redshift $z \sim 1$ and possibly became members of massive galaxy clusters in the local Universe. This first detailed study of a significant deep sample of K_s-selected galaxies allows us to show and summarise in one plot (Figure 4.11b) the evolutionary line traced by the massive K_s-selected galaxies and the massive ERGs since very high redshifts.

4.5 Predictions of Spitzer/IRAC magnitudes

HYPERZ provides the possibility of extrapolating the galaxy magnitudes beyond the observed bands using the best-fit SED template for each object. We used the observer-frame best-fit templates of each of our K_s-selected galaxies to predict their expected magnitudes in three of the Spitzer/IRAC channels, i.e. $3.6\mu m$, $4.5\mu m$ and $5.8\mu m$, as well as the derived IR colour distribution as a function of photometric redshifts. We present in this section the predicted colour distributions for all our K_s-selected galaxies. The complete catalog of K_s-selected galaxies with the individual Spitzer/IRAC predicted magnitudes is presented in the Appendix A. To convert from fluxes to magnitudes, we used the IRAC zero-flux points: 277.5Jy, 179.5Jy and 116.6Jy at $3.6\mu m$, $4.5\mu m$ and $5.8\mu m$, respectively [146].

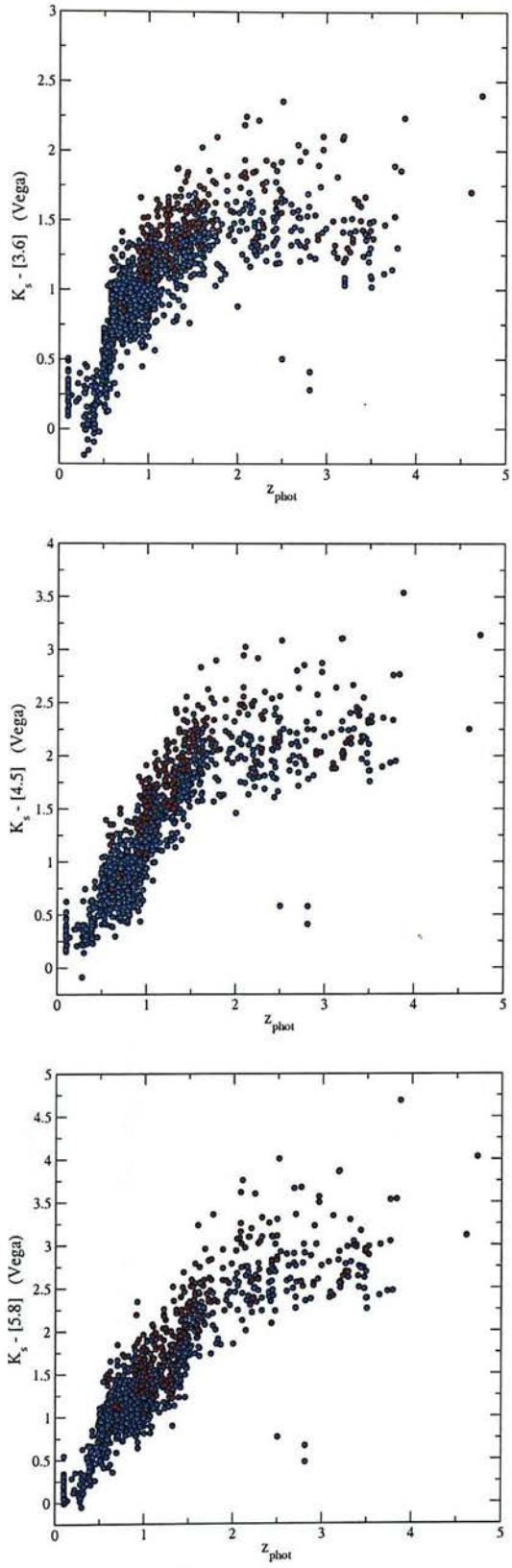

Figure 4.14: Predicted IR colours of $K_s \leq 22$-selected sources versus estimated redshift.

Table 4.1: $K_s \leq 22$-selected sources in the present sample which are among Yan et al. (2004) [148] IRAC extremely red objects. The columns list the following: 1) our identification number; 2) Yan et al. identification; 3)-4) RA and DEC on the K_s-band images; 5) our estimated redshift; 6) Yan et al. estimated redshift; 7) our measured K_s-band magnitude; 8) Yan et al. measured K_s-band magnitude; 9)-10)-11) our predicted magnitudes in the IRAC channels $3.6\mu m$, $4.5\mu m$ and $5.8\mu m$, respectively ; 12)-13)-14) magnitudes measured by Yan et al. in the IRAC channels $3.6\mu m$, $4.5\mu m$ and $5.8\mu m$, respectively. All magnitudes are in the Vega system. To convert Yan et al. magnitudes quoted in the AB system to Vega magnitudes, we used: $K_{s_{Vega}} = K_{s_{AB}} - 1.84$, $[3.6]_{Vega} = [3.6]_{AB} - 2.79$, $[4.5]_{Vega} = [4.5]_{AB} - 3.26$ and $[5.8]_{Vega} = [5.8]_{AB} - 3.73$.

id	id ^{Y}	RA(J2000)	DEC(J2000)	z_{phot}	$z_p{}^{Y}$	K_s	$K_s{}^{Y}$	[3.6]	[4.5]	[5.8]	$[3.6]^{Y}$	$[4.5]^{Y}$	$[5.8]^{Y}$
1418	4	3:32:41.76	-27:48:24.98	3.40	2.7	21.87	21.79	20.5	19.8	19.3	19.61	19.00	18.57
1539	7	3:32:32.17	-27:46:51.48	2.96	2.7	21.80	21.89	19.9	19.1	18.4	19.36	18.67	17.90
1429	8	3:32:35.09	-27:46:47.46	2.70	2.9	21.07	20.98	19.3	18.6	17.8	18.65	18.11	17.28
146	9	3:32:39.17	-27:48:32.33	2.71	2.8	21.18	21.03	19.8	19.2	18.6	19.14	18.69	18.01
14115	13	3:32:39.12	-27:47:51.45	1.92	1.9	21.10	20.80	19.5	18.9	18.5	19.19	18.77	18.14
14181	16	3:32:35.72	-27:46:38.73	1.42	2.4	21.32	21.50	19.9	19.3	19.2	19.35	18.84	18.27
14106	17	3:32:33.67	-27:47:51.07	1.70	1.6	20.54	20.55	19.2	18.5	18.3	18.92	18.50	18.22

Figure 4.14 shows the predicted $K_s - [3.6\mu m]$ (a), $K_s - [4.5\mu m]$ (b) and $K_s - [5.8\mu m]$ (c) colours of K_s-selected sources versus estimated redshift. The red circles correspond to the ERGs and the blue circles to all the other K_s-selected galaxies. We observe that $(I_{775} - K_s)$ selected ERGs do not have discriminating near-IR colours, and a pure IR colour cut does not seem to select the same population as an $(I_{775} - K_s)$ cut, as was pointed out by Wilson et al. (2004) [147] (these authors compared a pure IR colour cut with an $(R - K_s)$ cut). From the analysis of Spitzer/IRAC data, these authors also conclude that a $K_s - [3.6\mu m]$ red colour could be more effective to select high redshift ($z > 1.3$) galaxies. The predicted IR colours for our deep sample of K_s-selected galaxies leads us to a similar conclusion. However, a $K_s - [3.6\mu m]$ colour cut sufficiently red to avoid $z < 1$ contaminants might miss some of the higher redshift objects. On the contrary, the $K_s - [5.8\mu m]$ colour appears as a rather better redshift indicator, and a red $K_s - [5.8\mu m]$ cut could more effectively separate the higher redshift galaxies. The relatively tight relation existing between the $K_s - [5.8\mu m]$ colour and redshift suggests that the three very blue sources with $z_{phot} \sim 2.5 - 3.0$ might have erroneous estimated redshifts.

It is interesting to compare the predicted magnitudes for a subset of our sources with recent results obtained by direct photometric measurements on IRAC images. Yan et al. (2004) [148] recently selected a sample of 17 IRAC objects with $f_\nu(3.6\mu m)/f_\nu(z_{850}) > 20$ in the HUDF. We find that 8/17 of these objects are members of our $K_s \leq 22$-selected sample. The remaining objects are not in our sample either because they are fainter K_s-band galaxies or because they lie outside of our field of view[1]. 1/8 of the common objects (identification number 1 in [148]) has a very uncertain estimated redshift in Yan et al. and is excluded from their refined sample. The remaining 7/8 common objects are listed in Table 4.1. Our estimated redshifts for the seven common sources are in good agreement with the Yan et al. estimations (median of $\delta z/(1+z) \approx 0.07$). We note that, however, our predictions underestimate the observed magnitudes in the IRAC bands by a median of ≈ 0.5 mag. The comparison of the measured K_s magnitudes in both cases shows that this systematic offset cannot be attributed to, for example, aperture effects. However, given that the sources listed in Table 4.1 have been deliberately selected by Yan et al. on the basis of their flux excess on the IRAC bands, it is unsurprising

[1]The deep ISAAC field studied in this work only partially overlaps the HUDF.

(and reassuring) that, for this highly biased subset of sources, our predicted IRAC fluxes are systematically low. We anticipate a much better agreement of our predicted values with the observed IRAC magnitudes for the majority of our sample, when the GOODS/CDFS IRAC data become available.

4.6 Summary and discussion

In this work we have presented the redshift distribution and resulting cosmological implications for a sample of 1663 K_s-selected galaxies with $K_s \leq 22$ (Vega), and made an extensive comparison of the results with those obtained in Chapter 3 for the R03 ERG sample in the same field. This is the deepest significant study to date of K_s-selected galaxies and the role of ERGs within this population.

We have studied the evolution of the rest-frame K_s-band LF and concluded that there is no evidence for a decrease of its bright end up to at least redshift $\langle z_{phot} \rangle = 2.5$. A similar conclusion has been reached for the ERGs in Chapter 3, because these objects account for most of the bright end of the K_s-band LF at high redshifts. Also, from the comparison of both the total K_s-band and the ERG LFs, we find that the latter appears to have a bell-like shape instead of the shape of a Schechter function at redshift $z_{phot} \sim 1$. The total K_s-band and the ERG LFs become progressively more similar with redshift, reaching a maximum at $\langle z_{phot} \rangle = 2.0$. The limiting magnitude of our sample does not allow us to properly explore the faint end of the LF above this redshift.

We also study the evolution of the massive systems present in our sample of K_s-selected galaxies. We determined that a significant fraction ($\sim$ 20%-25%) of the galaxies with mass $M > 1 \times 10^{11} M_\odot$ is in place before redshift $z_{phot} \sim 4$. However, the assembly of most of the remaining massive systems appears to have occurred at later epochs, at redshift $z_{phot} \lesssim 1.5$. ERGs at redshifts $z_{phot} \sim 1 - 2$ account for most of the massive galaxies which have plausibly evolved under passive evolution since very high redshifts, but $30\% - 50\%$ of the galaxies with assembled stellar mass $M > 1 \times 10^{11} M_\odot$ at redshift $z_{phot} \sim 1 - 2$ are not ERGs. On the other hand, ERGs account for only a fraction of the massive systems present in the local Universe, indicating that, in any case, passive evolution could not entirely explain the construction of all the massive galaxies.

We found that the comoving number densities of galaxies with stellar mass $M > 1 \times$

$10^{11}M_{\odot}$ at redshifts $z_{phot} \sim 1-3$ is significantly smaller than the corresponding densities of dark matter haloes massive enough to host these systems. We suggest that this could be evidence for differential timescales in halo merging and galaxy collapse. At redshifts $z_{phot} \gtrsim 3$, however, the number of massive galaxies coincides with the corresponding number of haloes, probably indicating that galaxy collapse was a much faster and efficient process at very high redshift, virtually simultaneous with the virialisation of the haloes.

From the analysis of the distribution of the stellar mass budget at different redshifts, we conclude that between 45% and 70% of the stellar mass assembled at redshifts $3 < z_{phot} < 4$ is contained in galaxies with mass $M > 1 \times 10^{11}M_{\odot}$. These massive galaxies present at very high redshift have presumably been formed from the early collapse of the high peaks of the density fluctuation field. Our study of the evolution of massive systems up to redshifts $z_{phot} \sim 4$ seems to confirm the existence of an evolutionary sequence in which most of the massive galaxies formed at very high redshift become $(I - K_s)$ selected ERGs by redshift $z_{phot} \sim 1$, and are the progenitors of the massive early-type galaxies observed in local clusters.

The follow up in the Spitzer/IRAC channels will be necessary to directly observe the rest-frame K_s-band light of the high-redshift ($z > 1$) galaxies in our sample. This will allow an independent test of our extrapolated stellar luminosities and masses at high redshift.

Chapter 5

The morphology of massive galaxies at high z

5.1 Introduction

The study of morphology is a complementary tool to explore galaxy evolution. Structural parameters are known to be related to the galaxy physical properties. For example, regular-shape morphologies are found in galaxies with quiescent or virtually no star formation, while the presence of high-frequency spatial structure is an indicator of intense star formation activity [149] [50].

From the point of view of morphology, local galaxies have traditionally been classified using the original [150] or the revised [151] [152] Hubble sequence. Those galaxies which do not correspond to any of the Hubble-sequence types are often referred as *peculiar*. At higher redshift, the determination of regular, Hubble-sequence type galaxies constitutes an alternative method to study the presence of already-assembled stellar systems. As we explained in §2.4.2, the surface brightness distribution $I(r)$ of an axisymmetric galaxy can be modelled by:

$$I(r) = I_0 \, exp\left[\left(-\frac{r}{r_0}\right)^{1/n}\right], \tag{5.1}$$

Although many elliptical galaxies have been found to be fitted by an $n = 4$ radial profile (de Vaucouleurs' law [52]), it was later recognised that the Sérsic index n is actually correlated to the galaxy absolute magnitude in the B band [153]. Pure discs,

on the other hand, are characterised by an exponential law ($n = 1$). However, different factors can contribute to distorting the profile of a galaxy with respect to the shape described by eq.(5.1). Surface brightness asymmetries have been found to be linked to on-going star-formation activity and also to galaxy mergers [154] [50].

Many morphological studies have been performed in order to place constraints on galaxy evolution. Among the most recent works, Ravindranath et al. [155] analysed GOODS/CDFS ACS images to determine that the population of rest-frame $M_B < -19.5$ disks is basically the same at redshift $z \sim 1$ as at lower ($z \sim 0.2$) redshifts. At redshift $z \sim 2.5$, however, the ratio of regular (elliptical and disk) galaxies appears to be lower than in the local Universe [156]. On the other hand, the correlation of galaxy sizes with luminosities and masses has been recently investigated by Trujillo et al. (2004) [157], who found that rest-frame V-band luminous objects were ~ 4 times smaller at redshift $z \sim 2.5$ than today. However, the relation between sizes and stellar mass seems to remain approximately constant, a fact that can be explained by the different mass-to-light ratios of galaxies at different redshifts.

In this chapter, we investigate the morphology of our deep ISAAC field $K_s \leq 22$-selected galaxies present at redshifts $z_{phot} < 2$ which have an estimated stellar mass $M > 10^{11} M_{\odot}$. Our aim is to determine the existence of any possible link between the structural parameters and other physical properties such as the redshift, the age or the mass. We also explore whether massive ERGs have different morphological properties to other massive K_s-selected galaxies. The structure of this chapter is as follows. In §5.2, we define our sample for morphological studies and present K_s and z-band postage stamps of some of the most massive galaxies found in the GOODS/CDFS deep ISAAC field. In §5.3, we explain the method we used to study galaxy morphology and give some details of the treatment of the analysed images and the corresponding point-spread functions (PSFs). Finally, in §5.4 and §5.5, we present and discuss our results. The work presented in this chapter is collaborative: the K_s-band morphology parameters of the present sample of massive galaxies were obtained by Ross McLure, as part of a multi-object run of his profile-fitting algorithm for a large sample of flux-limited K_s-selected galaxies. The morphology results were analysed by myself, in conjunction with the physical properties for the galaxies in the sample, as determined in Chapters 3 and 4. The z-band modelling was undertaken by myself, using Ross McLure's code.

5.2 The sample

Our aim in this chapter is to investigate the morphology of the most massive galaxies present in the GOODS/CDFS deep ISAAC field. In Chapter 4, we computed estimated masses for our $K_s \leq 22$-selected galaxies using the HYPERZ best-fit SED model for each object and assuming a Salpeter IMF. We found that 146/1663 of our galaxies had estimated stellar mass $M > 10^{11} M_{\odot}$, and 78 out of these 146 were determined to be at redshifts $z_{phot} < 2$. We restricted our morphological study to this lower redshift subsample, to guarantee the availability of good signal-to-noise images in all cases. One of the 78 galaxies with $M > 10^{11} M_{\odot}$ at redshift $z_{phot} < 2$ has a stellarity parameter CLASS_STAR ≥ 0.8, as determined by SEXTRACTOR on the ACS z-band images. However, this object was not excluded from our $K_s \leq 22$ galaxy sample analysed in Chapter 4 because it was not confirmed as a star or a QSO by the SIMBAD astronomical database, and because HYPERZ provided a non-negligible probability for this source to be at redshift $z_{phot} = 0.58$. On the contrary, the inspection of the ACS images and the results of modelling its surface brightness profile with the algorithm explained below, revealed that this is actually a point-like source. Thus, we excluded this object from our analysis, leaving 77 sources for the final morphology sample. In figures 5.1 and 5.2 we present, as an example, postage stamps of some of these massive galaxies, as they appear on the ISAAC K_s and the ACS z-band images, respectively.

We analysed the morphology of each of our galaxies on both ISAAC K_s and ACS z-band images. This allowed us to partially mitigate the plausible differences introduced by the morphological k-corrections, i.e. the differences in the morphology due to the mapping of different rest-frame wavelengths at different redshifts. As we shall explain in §5.3.2, both GOODS K_s and z-band images have sufficient resolution to enable a quantitative modelling of the surface brightness profile of each galaxy.

5.3 Morphology modelling

5.3.1 The surface-brightness-profile fitting algorithm

We modelled the morphology of each galaxy in our sample using a 2-dimensional (2D) surface-brightness-profile fitting algorithm. The modelling code was developed by Ross McLure and constitutes an improved version of that described in [158] and references

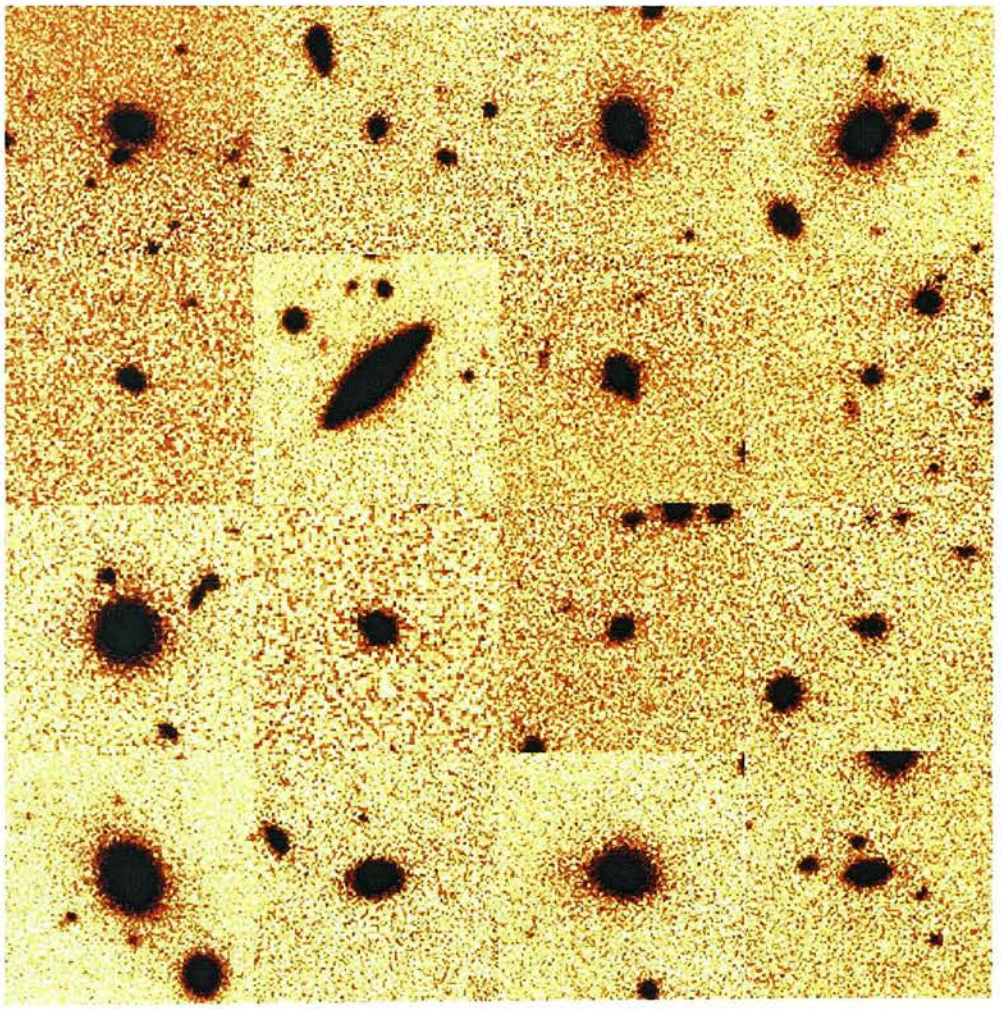

Figure 5.1: K_s-band postage stamps of massive galaxies at $z_{phot} < 2$ in the GOODS/CDFS deep ISAAC field. The scale of each stamp is $\sim 19'' \times 19''$.

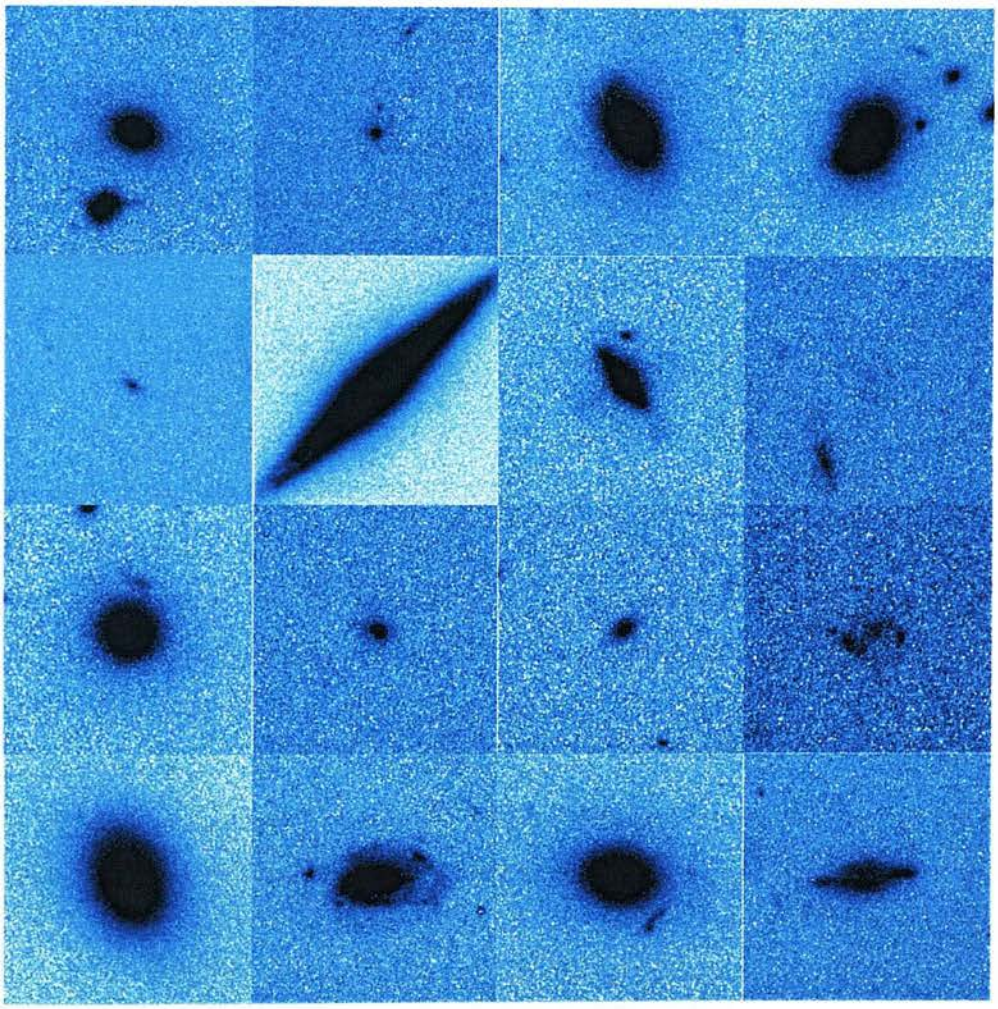

Figure 5.2: ACS z-band counterparts of the massive galaxies at $z_{phot} < 2$ in the GOODS/CDFS deep ISAAC field shown in figure 5.1. The scale of each stamp is $\sim 7.7'' \times 7.7''$.

therein. We summarise here the main characteristics of this code, which has two basic running modes: a single-component modelling or a bulge+disc decomposition. For the single-component modelling, the surface brightness profile of the galaxy is assumed to be described by eq.(5.1). The code then convolves the image of each model galaxy using the corresponding point-spread function (PSF). The model galaxy is constructed iterating over seven free parameters: the coordinates (x, y) of the model centroid, the position angle of the galaxy PA, the axial ratio a/b, the central surface brightness I_0, the characteristic scalelength r_0 and the Sérsic index n[1]. For the bulge+disc decomposition, the surface brightness profile of the galaxy is assumed to be the sum of two components:

$$I(r) = I_B\, exp\left[\left(-\frac{r}{r_B}\right)^{1/n_B}\right] + I_D\, exp\left(-\frac{r}{r_D}\right), \tag{5.2}$$

where I_B and I_D are the central surface brightnesses of the bulge and disc, respectively, and r_B and r_D are the respective scalelengths. The Sérsic index of the bulge n_B is also a free parameter of the model, while the disc is assumed to have a pure exponential radial profile. The centroid (x, y) is assumed to be the same for both the disc and the bulge. The other free parameters are the position angles and the axial ratios of both the bulge and the disc, and the *bulge fraction* B/T, i.e. the fraction of the integrated galaxy luminosity contained in the bulge.

In both the single and the two-component running modes, the best-fit model is determined using a maximum-likelihood estimator:

$$\chi^2_{red.} = \frac{1}{\nu}\sum_{i=1}^{N}\left[\frac{y_i - y_i^0(a_1, \ldots, a_s)}{\sigma_i}\right]^2, \tag{5.3}$$

where N is the number of pixels in the image, y_i is the measured intensity of the pixel i and $y_i^0(a_1, \ldots, a_s)$ is the corresponding modelled intensity value, which depends on the s free parameters $a_1, \ldots, a_s$; σ_i is the error associated to y_i, which for normal galaxies is basically given by photon shot noise; ν is the number of degrees of freedom, in this case $N - s$. The global minimum of eq.(5.3) is determined by the modelling code using a *downhill simplex method* [159]. In the output, the code generates the best-fit model

[1] As the original code has been developed for the modelling of quasar host galaxies, it also incorporates the luminosity of a central point-like source as an additional free parameter. We set this parameter to zero in all the present study.

for the galaxy, a residual image with the differences between the real image and the fitted axisymmetric model, and a χ^2 map showing the contribution of each term in eq.(5.3). Also, a set of measurements of total and aperture photometry are provided for both the bulge and the disc components.

A rigurous computation of the error bars on the different modelled best-fit parameters requires the production of simulations which have not yet been made at the moment of writing this thesis. The recalculation of the best-fit parameters using simulated datasets allows confidence-limit regions in parameter space to be determined. The projections of these confidence-limit regions on each free parameter provide robust values for the error bars [159]. For blue galaxies, the uncertainties associated to the modelling in the K_s band are expected to be greater than those for the z band, given the lower resolution of the K_s-band images. For red galaxies, the lower signal-to-noise in the z band partially compensates the better resolution of these images and, thus, the errors for the modelling should be approximately of similar order.

5.3.2 The input images and point-spread functions (PSFs)

The GOODS/CDFS ISAAC images have a pixel scale of $0.1484''$ and the PSF FWHM in the K_s-band is $\sim 0.40''$. This makes the ISAAC K_s-band images of sufficient quality to perform 2D modelling of galaxy morphology. We cut out 128×128-pixel ($\sim 19'' \times 19''$) stamps for each of the galaxies in our morphology sample, centred at the galaxy K_s-band centroid as given by SEXTRACTOR. The K_s-band images used for this morphological study correspond to the GOODS/EIS v1.0 release. The length of the input images must be 2^n (n integer) pixels because the modelling code implements a fast Fourier transform (FFT) to convolve the input image with the corresponding PSF. We also cut out identical-size stamps of the weighting maps centred at the corresponding galaxy positions, which were used by the code to compute the weighting factors in eq.(5.3).

We used non-saturated stars in the field as input PSFs. Although usually it is preferable if the star used as the PSF is close on the image to the modelled galaxy, our tests demonstrated that no significant differences in the modelling results were obtained using different stars on the GOODS/CDFS ISAAC images, at least for our

galaxy sample.

The v1.0 GOODS/CDFS ACS images have a pixel scale of 0.03″ and the PSF FWHM in the z band is $\sim$ 0.10″. With such a resolution, we needed to cut stamps of at least 256×256 pixels ($\sim$ 7.7″ × 7.7″) to obtain reasonable-size input images for each of our galaxies. These larger size images demanded longer computing times for the modelling code. For the sake of efficiency, we decided to resample the input stamps to a pixel size of 0.06″ × 0.06″, which still allowed us to take advantage of the excellent ACS resolution. Thus, we also used 128×128-pixel stamps for the z-band modelling.

For the HST ACS, synthetic PSFs can be constructed using the public code TINYTIM (http://www.stsci.edu/software/tinytim/). TINYTIM can produce a model PSF depending on the ACS filter and detector position. However, our tests of the modelling of our galaxies using both a TINYTIM and an empirical PSF (i.e. stars in the field) showed that, for the particular case of the GOODS/CDFS z-band images, the latter produced lower $\chi^2_{red.}$ fits and cleaner residual images. Thus, we also utilised stars as PSF for the z-band morphology modelling.

5.4 Results

5.4.1 The morphology of massive galaxies

The modelling code allows for the study of different aspects of galaxy morphology. In this chapter, we concentrate on the study of the structural parameters of our massive galaxies, to try to understand any possible link between these parameters and other galaxy properties such as the redshift, colour or stellar mass. Also, we analyse the differences between the results produced by the morphology modelling in two different wavebands, K_s and z. In all the cases in which the modelling code produced satisfactory fittings (i.e. $\chi^2_{red.} \sim 1$), we assumed that the morphology of our galaxies was described by the axisymmetric models given by eqs.(5.1) or (5.2). The existence of non-negligible residuals might reveal the presence of asymmetries in the galaxies, possibly linked to active star formation or the production of mergers.

In figure 5.3, we show the single-component best-fit β index, i.e. the reciprocal of the Sérsic index n, as obtained for the 77 galaxies with M > $10^{11}M_\odot$ and $z_{phot} < 2$ in the deep ISAAC field, from the model fitting in the K_s band (upper panel) and the

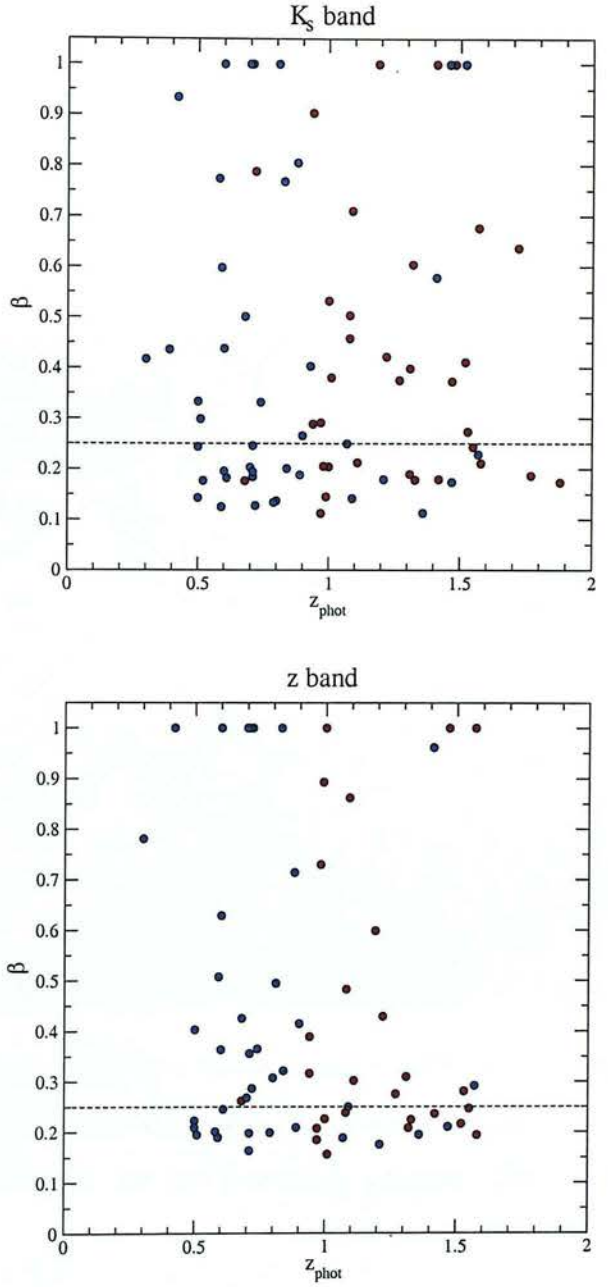

Figure 5.3: The best-fit single-component $\beta = 1/n$ index for massive galaxies at redshifts $z_{phot} < 2$, as obtained from the morphology modelling in the K_s band (upper panel) and the z band (lower panel), versus photometric redshifts. The red circles correspond to ERGs, the blue circles indicate the other K_s-selected galaxies.

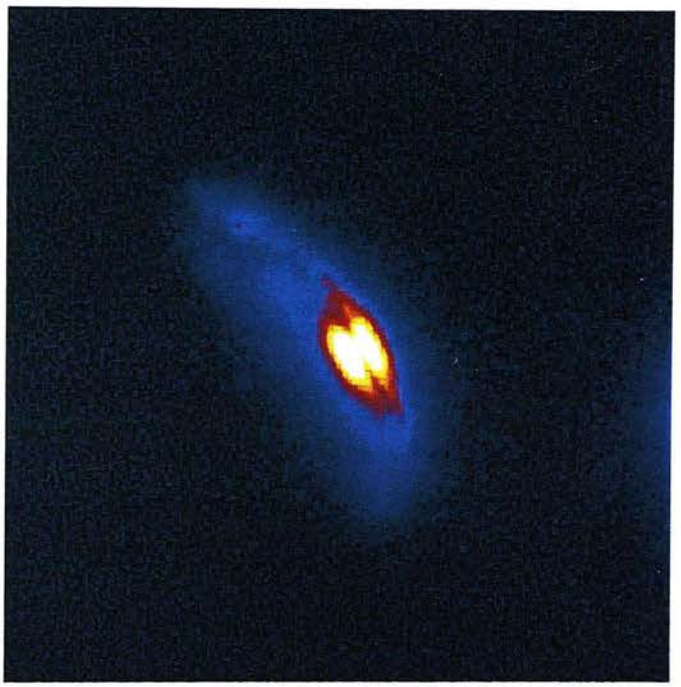

Figure 5.4: ACS z-band image of a merger in the GOODS/CDFS deep ISAAC field, estimated to be at redshift $z_{phot} = 0.39$. The false-colour scale has been chosen to highlight the distorted morphology of the two interacting galaxies. The image shows a field of $\sim 7.7'' \times 7.7''$.

z band (lower panel). The red circles correspond to the R03 ERGs (34 sources) and the blue circles to the other K_s-selected galaxies (43 sources). The spanned ranges of β values are similar for both the ERGs and the bluer K_s-selected sources. The dashed line shows the β index corresponding to a pure de Vaucouleurs law. We observe that $\sim 50\% - 60\%$ of the objects in our morphology sample have β indices concentrated around $\beta \approx 0.25$. The concentration is similar for the ERGs and other K_s-selected galaxies. A secondary peak for the concentration is found at $\beta \approx 1$. In the K_s band, the dispersion is somewhat larger as a consequence of the poorer-quality resolution in comparison with the z-band images. A few objects have been excluded from the z-band plot, all of them corresponding to cases of very irregular morphology or faint sources in the z-band, for which the modelling code yields relatively high reduced χ^2 values. At redshifts $z_{phot} > 1$, most of these objects are ERGs, for which the z-band light might be significantly affected by dust extinction. Among the lower redshift galaxies deliberately excluded in the z-band plots, it is worthwhile to mention the source with identification number 2158 at $z_{phot} = 0.39$ (cf. the $K_s \leq 22$ galaxy catalog in the Appendix A), whose z-band image we show in figure 5.4. Although the K_s-band image resolution does not allow to separate the components of this source, the z-band ACS image clearly reveals that it is actually composed by two galaxies with very distorted morphologies, indicating the presence of a merger.

Figure 5.5 shows the bulge fraction B/T versus the estimated redshifts for the galaxies in our morphology sample. The upper panel shows the results of the K_s-band modelling, while the lower panel shows the results in the z-band. The symbol labels are the same as in fig. 5.3. We see that both the massive ERGs and other massive K_s-selected galaxies display a wide variety of bulge fractions. In both populations and at different redshifts, some objects appear as being pure discs ($B/T = 0$). From the inspection of the K_s and z-band images and the results of the modelling code, we found that different kinds of objects can be best-fitted by pure disc radial profiles. For example, visually identified spiral galaxies are modelled as discs, and the spiral arms - which are well resolved on the ACS images- appear on the corresponding residual image. Some irregular objects are also best modelled by pure discs, although with different goodness in the fitting, depending on the case. However, most of the massive galaxies appear to have a non-negligible bulge fraction. A proper division of the bulge-dominated

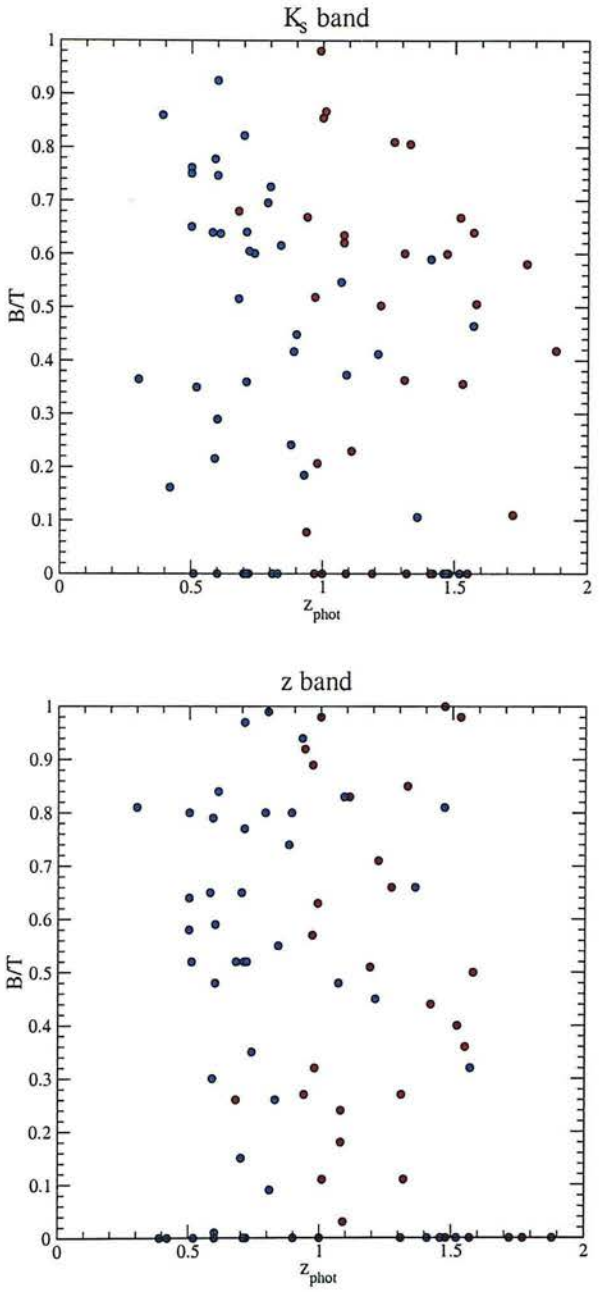

Figure 5.5: The bulge fraction versus estimated redshifts for galaxies with mass M > $10^{11}M_{\odot}$ at $z_{phot} < 2$, as obtained from the morphology modelling in the K_s band (upper panel) and the z band (lower panel). The symbol labels are the same as in fig. 5.3.

objects, though, needs to be made taking into account both the bulge fraction B/T and the Sérsic index of the bulge n_B. The cases with $n_B \approx 1$ actually correspond to pure discs, independently of the B/T value. We separate and further analyse the bulge-dominated subsample in §5.4.2.

Another structural parameter of interest is the half-light radius r_h, i.e. the distance from the center of the galaxy within which half of the integrated light in the corresponding band is concentrated. Figure 5.6 shows the half-light radii of our galaxies as a function of photometric redshifts, as obtained from a single-component morphology modelling in the K_s band. The advantage of analysing the half-light radius in the K_s band is that this parameter can be conceived as an index of the concentration of the mass as well as the light. We see that most of the massive galaxies in the deep ISAAC field have half-light radii $r_h \sim 0.2 - 6\,\mathrm{kpc}$. While the bluer galaxies span more or less uniformely this radius range, most of the ERGs appear to be more compact, with half of their light concentrated within $r_h \lesssim 3\,\mathrm{kpc}$. The dashed line in figure 5.6 shows the envelope delimited by the r_h versus z_{phot} distribution: the maximum observed value of r_h decreases with increasing redshift. We note that a few objects have best-fit half-light radii $r_h \lesssim 1\,\mathrm{kpc}$. These correspond to marginally resolved sources, for which the morphology models could have somewhat significant uncertainties.

On the other hand, a few galaxies have half-light radii $r_h \gtrsim 6\,\mathrm{kpc}$ within our sample, all of them located at redshifts $0.5 < z_{phot} < 1.0$. One of them (object identification number 16115 of the $K_s \leq 22$ catalog in the Appendix A) appears to be blended with another source on the K_s-band images and, thus, the resulting radius obtained by the modelling code is an overestimation of the real value. Actually, the K_s-band modelling for this object does not yield a good-quality fit and the associated minimum reduced chi-square is $\chi^2_{red.} > 2$. In the z-band, on the contrary, the companion source is well resolved, and the modelling of the object 16115 indicates a half-light radius of $r_h \sim 4\,\mathrm{kpc}$. The inspection of the images and the modelling results for the other three objects with $r_h \gtrsim 6\,\mathrm{kpc}$ indicate that they are disc-dominated and/or spiral galaxies.

Among the 34 massive ERGs, only 5 have a half-light radius $r_h > 4\,\mathrm{kpc}$. 4/5 of these ERGs are bulge-dominated objects and the remaining one is a disc. The photometry of 3 of these large, bulge-dominated ERGs is best-fitted by HYPERZ by templates of evolved galaxies, indicating formation redshifts $z_f > 3$. Thus, the photometric and

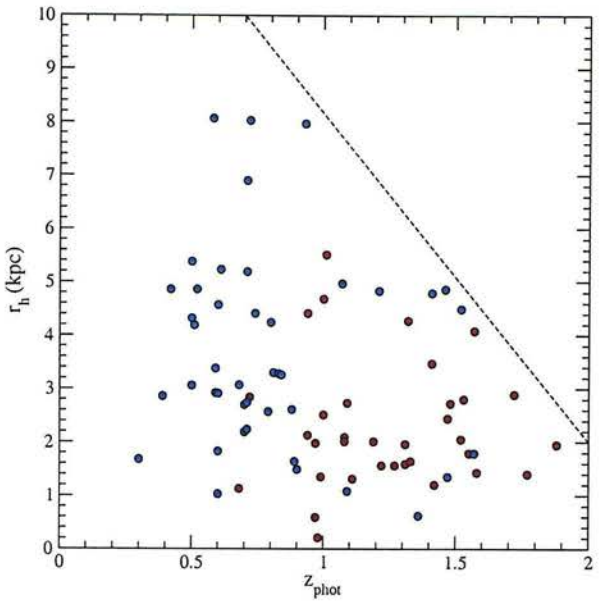

Figure 5.6: Half-light radii versus estimated redshifts for galaxies with mass $M > 10^{11} M_{\odot}$ at $z_{phot} < 2$ in the deep ISAAC field, as obtained from a single-component modelling in the K_s band. The symbol labels are the same as in fig. 5.3.

morphological characteristics of these objects indicate that they are firm candidates for progenitors of the most massive early-type galaxies found in local clusters.

The connection between the largest ERGs and the other largest K_s-selected galaxies present at lower redshifts is not clear. However, two possible different scenarios are suggested:

i) large ERGs are not linked with the large discs observed at redshifts $0.5 < z_{phot} < 1.0$. Large massive ERGs evolve passively to the present day, with no additional accretion of mass and basically preserving their size and shape. The large massive discs at lower redshifts, on the other hand, have been formed from smaller, less massive galaxies (possibly also ERGs at $z_{phot} > 1$), which live in haloes where sufficient gas is still available to allow for the condensation of new stars and galaxy growth. This intuitively seems to be the most consistent picture with the idea of passive evolution of the ERG progenitors of local cluster elliptical galaxies.

ii) large massive discs at redshifts $0.5 < z_{phot} < 1.0$ are formed after the accretion of material on some of the higher-redshift large massive ERGs. There is some observa-

tional evidence that massive discs could become cluster early-type S0 galaxies by the present day. Several works on the evolution of cluster galaxy morphology from redshifts $z \sim 0.5$ to $z \sim 0$ indicate that the ratio of spiral galaxies in regular clusters increases with redshift at the expense of a decrease in the ratio of S0 galaxies [160] [161].
It is possible that, actually, both i) and ii) are valid, the first explaining the evolution of present-day cluster ellipticals and, the second one, the evolution of the cluster early-type S0. We continue the discussion of these hypotheses in §5.4.2.

5.4.2 Bulge-dominated objects

As we mentioned in §5.4.1, the determination of the bulge-dominated objects among our morphology sample of massive galaxies needs to be done on the basis of the bulge fraction B/T and also on the Sérsic index of the bulge n_B, as obtained from the two-component modelling. We found 29 objects of our morphology sample (15 ERGs and 14 other K_s-selected galaxies) which had best-fit parameters $B/T > 0.5$ and $n_B > 2$ in the K_s band. We considered this group of objects as our *bulge-dominated* subsample of massive galaxies at redshifts $z_{phot} < 2$. [2]

Figures 5.7 and 5.8 show the bulge fractions B/T versus estimated redshifts z_{phot} for the bulge-dominated subsample, as modelled in the K_s and z bands, respectively. The comparison of both figures indicates that not all the objects that are bulge-dominated in the K_s band necessarily appear as bulge-dominated in the z band. However, most of the discrepant cases correspond to ERGs, where the z-band modelling is more prone to uncertainties due to the lower signal-to-noise produced by dust extinction. As probably expected, virtually all the massive K_s-band bulge-dominated objects at redshifts $z_{phot} > 1$ are ERGs. The HYPERZ best-fit models for most of the bulge-dominated ERGs correspond to evolved galaxies, indicating formation redshifts $z_{phot} > 3$. Among the other bulge-dominated K_s-selected galaxies, however, only 2/15 objects appear to be best-fitted by very-old-galaxy templates, with similar high formation redshifts as the ERGs. This could be indicating that the remaining 13 bulge-dominated objects were more recently assembled, probably after the production of mergers. The merging sub-

[2]The source with identification number 16115 is also a bulge-dominated object, following our definition. However, given its bad-quality fitting in the K_s band due to the contamination of a close companion, we decided to exclude it from the present analysis.

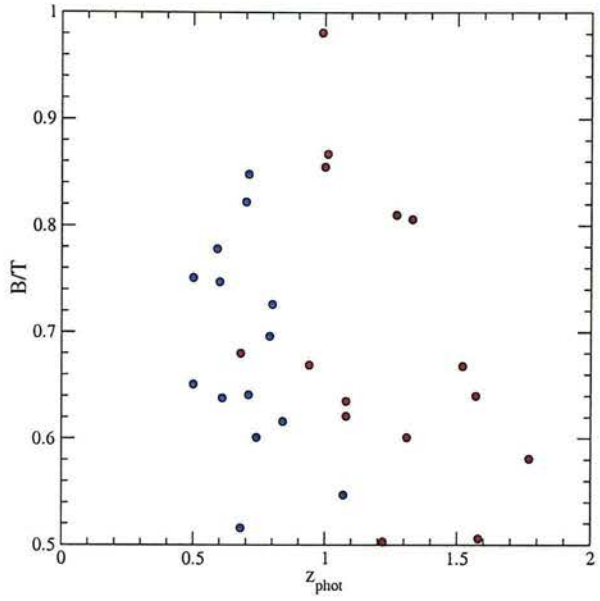

Figure 5.7: K_s-band bulge fraction versus photometric redshifts for bulge-dominated galaxies with mass $M > 10^{11} M_{\odot}$ in the deep ISAAC field. The symbol labels are the same as in fig. 5.3.

structures could in principle be much older but, after the production of the merger, the colours of the resulting galaxy might mimic those of a young structure recently formed in a sudden burst. The deficit of massive bulge-dominated systems at $0.5 < z_{phot} < 1.0$ with high assembly redshifts might be due to cosmic variance effects, given the strong clustering expected for the population of old massive spheroids. However, alternative explanations cannot be excluded. For instance, many massive bulge-dominated ERGs at $z_{phot} \sim 1 - 2$ could actually have a non-negligible disc component which becomes increasingly important at lower redshifts (this can be the consequence of a real evolution but also in part of the surface-brightness dimming with redshift). In this case, these massive ERGs could be the progenitors of massive disc galaxies rather than bulge galaxies at intermediate redshifts. The massive discs could then evolve into cluster early-type S0 by the present day. As we pointed out in §5.4.1, this idea is consistent with the observed evolution of galaxy types within clusters from redshifts $z \sim 0.5$ to $z \sim 0$. The *Butcher-Oemler effect* [162] indicates that the fraction of blue galaxies increases from local to intermediate-redshift clusters. More recently, Dressler et al.

(1997) [160] determined that that the fraction of S0 galaxies is 2-3 times smaller in clusters at $z \sim 0.5$ than in local ones, with a simultaneous increase of the fraction of spirals. Our results suggest that many of the massive ERGs found at $z_{phot} > 1$ could be progenitors of local cluster S0 galaxies, after having an intermediate state of spirals.

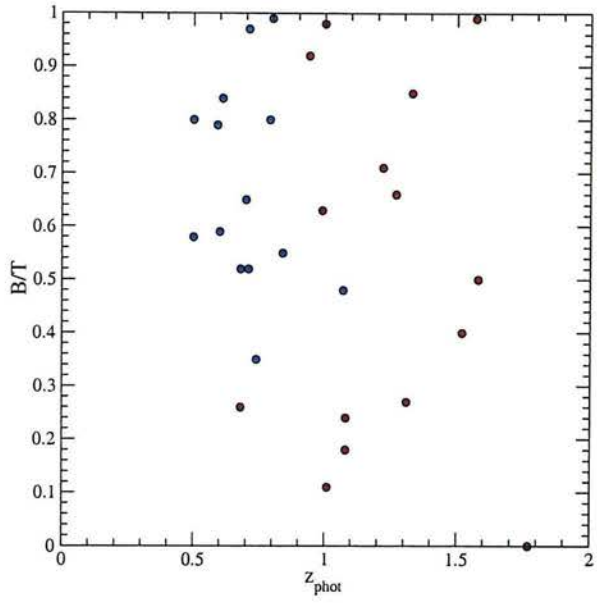

Figure 5.8: z-band bulge fraction versus photometric redshifts for bulge-dominated galaxies with mass $M > 10^{11} M_{\odot}$ in the deep ISAAC field. The symbol labels are the same as in fig. 5.3.

5.5 Summary and discussion

In this chapter we presented the results of a quantitative 2D modelling of the K_s and z-band morphologies of 77 $K_s \leq 22$-selected galaxies with estimated mass $M > 10^{11} M_{\odot}$ and estimated redshifts $z_{phot} < 2$ in the GOODS/CDFS deep ISAAC field. Our results show that both massive ERGs and other massive K_s-selected galaxies present a wide variety of morphologies in the whole analysed redshift range. This diversity indicates that other factors rather than the mass or the star-formation history (responsible for the observed galaxy colours) might have an important influence on the determination of galaxy morphology. The effects of environment are expected to play a major role on

this diversity and possibly a complete understanding of galaxy morphology will never be achieved from the inspection of individual galaxies, without a detail inspection of their surroundings. A coordinated study with, for example, galaxy clustering could greatly improve our knowledge on galaxy morphology.

The largest objects present in our sample are spiral galaxies at redshifts $z_{phot} \sim 0.5-1.0$. Our results suggest that these large discs could have been formed from the accretion of material onto the largest, mainly bulge-dominated ERGs present at redshifts $z_{phot} > 1$. This would imply that the plausible passive evolution characterising massive ERGs since very high redshifts (cf. §4.4.4) could correspond to the evolution of their main component, i.e. the bulge. The disc component would become more important with time and, by redshifts $z_{phot} \sim 0.5-1.0$, the massive bulge-dominated ERGs convert into giant disc-dominated galaxies. By redshift $z = 0$, these galaxies would have consumed most of the gas available in their haloes and lost angular momentum, converting into rather inactive S0 galaxies. Within our sample, the key point which allows us to reach this conclusion is the fact that the colours of most of the massive bulge-dominated objects at redshifts $0.5 < z_{phot} < 1.0$ are not consistent with those expected for evolved passive galaxies, but correspond to relatively young galaxies formed in a single, intense burst, probably indicating recent star-formation or merger assembly history. Only a minor fraction of the bulge-dominated objects at intermediate redshifts in our sample appear to have been formed at very high redshifts. These few objects are possibly the most genuine candidates for progenitors of pure passively-evolving local cluster ellipticals.

These results should be much further tested with the study of large samples of galaxies which significantly span the redshift range $0 \lesssim z \lesssim 1.5$. The study of clusters up to redshifts $z \sim 0.5$ performed in recent years support our conclusions. The continuing sampling and detailed study of galaxies at $z \lesssim 1.5$ - a period which actually covers more than the last two thirds of the age of the Universe - is fundamental to enhance our understanding on the later evolution of ERGs, once the k-corrections take these objects out of the selection limits of this population.

Chapter 6

Conclusions

6.1 The role of ERGs in the history of structure formation

In this thesis, we aimed to investigate the evolution of ERGs and their role in the history of galaxy formation. With this purpose, we studied the redshift distribution and derived cosmological properties of the deepest significant sample of ERGs selected to date, covering $50.4\,\mathrm{arcmin}^2$ of the GOODS/CDFS up to $K_s = 22$. This work has been enhanced by the study of the total parent sample of $K_s \lesssim 22$-selected galaxies, which allowed us to better understand the evolution of massive galaxies since very high redshifts, $z \sim 4$.

For many years, it has been thought that the ERG population should contain the progenitors of the most massive local eary-type galaxies found in local clusters. The little scatter observed in the colours of cluster spheroidal galaxies up to redshifts $z \approx 0.5$ indicated that these systems had probably been evolving passively since very early times. Stellar synthesis models predicted that galaxies formed in relatively short timescales at very high redshifts would display extremely red optical/near-IR colours by redshift $z \sim 1$. Therefore, the study of ERGs has traditionally been recognised as an efficient method to select the progenitors of the oldest, most massive systems present in the local Universe. However, the numerous studies performed over the years determined that the ERG population was actually quite complex, and most of the efforts have been devoted to disentagle the presence of evolved massive spheroids among the ERGs.

Although individual ERGs have been previously found to exist up to redshifts

$z \sim 3-4$, this work showed and quantified for the first time the compared evolutionary lines traced by the ERGs and other K_s-selected galaxies since very high redshifts. We determined that $\sim 20\% - 25\%$ of the local galaxies with assembled stellar mass $M > 10^{11} M_{\odot}$ were in place before redshift $z \sim 4$, and most of these massive galaxies have become ERGs by $z \sim 1.5$. These systems could be the counterparts of the presumably very massive submillimetre galaxies and the hosts of the oldest massive quasars. We found that the remaining local massive systems were assembled later, at redshifts $z \lesssim 1.5$, in agreement with previous studies, which determined that most of stellar mass has been formed at $0.5 \lesssim z \lesssim 1.5$. Although significant, the number densities of massive systems present at high redshifts does not seem to pose a problem for the predictions of hierarchical models of galaxy formation. We found that the number density of massive galaxies at redshift $z \sim 4$ coincides very well with the expected number densities of dark matter haloes sufficiently massive to host these systems, possibly indicating that the accretion of the stellar mass proceeded very efficiently at very high redshifts. Thus, the population of massive ERGs at $z \gtrsim 1$ appears to contain the imprints of the most efficient times of galaxy formation.

Our work has also allowed us to test the hypothesis of passive evolution. Our results show that only a minor fraction of the massive systems present in the local Universe could have evolved passively since very high redshifts. The upper limit to this fraction is given by the densities of ERGs at redshifts $z \gtrsim 1$. However, the results of our study of the morphology of massive galaxies suggest that some of the most massive ERGs could be suffering the quiescent accretion of new stellar mass, and develop into giant spiral galaxies at intermediate redshifts. This hypothesis is consistent with the idea of the ERGs as progenitors of local cluster S0 galaxies. Studies of the evolution of morphology in galaxy clusters indicate that local S0 galaxies were probably formed from later type galaxies at $z \sim 0.5$. If this is the case, only a minority of the massive ERGs at $z \gtrsim 1$ would really be passive systems and continue with a plausible pure passive evolution until the present day.

6.2 Prospects for the future

The work presented in this thesis suggests many possibilities for future work. Firstly, obtaining spectra for significant samples of ERGs is still a challenge. Unfortunately, at the present, the lack of good-resolution IR multiobject spectrometers with significant fields of view makes this objective unfeasible. In the inmediate future, ERG study will mostly continue relying on photometric measurements. As has been shown by many studies including this thesis, photometric techniques can be an efficient way to model the general properties of large samples of galaxies, provided multiwavelength data of sufficient quality is available. In the following years, surveys conducted with state-of-the-art wide-field near-IR and optical cameras should be able to produce very large catalogs of ERGs, with sufficient depth to allow for an unprecendented sampling of the ERG population up to at least the redshifts studied in this work, $z \sim 4$. The coverage of very large areas of the sky will be fundamental to overcome the cosmic variance effects and validate (or not) the results obtained from the study of smaller fields.

Another important goal is to push our investigation of galaxy evolution to even higher redshifts. From our work we concluded that a significant fraction of massive galaxies seems to be present before redshift $z \sim 4$. Thus, to discover the first epoch of formation of these massive systems is one of the most exciting challenges for future observational astronomy. This will also constitute a decisive test for current galaxy formation theories. We have seen that pure near-IR colour cuts can be more efficient than $(I - K_s)$ cuts for selecting evolved sources at high redshift, with smaller fractions of low-redshift contaminants. Thus, the selection of pure near-IR selected galaxies in very deep fields appears to be one of the best methods to discover the presence of the first assembled massive systems.

The follow up of K_s-selected galaxies in the mid-IR will be a necessary tool to directly map the rest-frame K_s-band emission of the highest-redshift objects. This will allows one to confirm or reject the estimated luminosities and masses for the ERGs and other K_s-selected galaxies, as obtained using only optical/near-IR photometry. At longer wavelengths, mid-IR data will be of importance to clarify to which extent the presence of dust is responsible for the extremely red colours displayed by the ERGs. The different cameras on the Spitzer Space Telescope, which cover from near to far-IR wavelengths, will offer a unique opportunity to study the dust emission in ERGs.

Finally, our understanding of the ERG population can be very much enhanced from further investigation of the relations with other galaxy populations. Some recent works suggest that submillimetre galaxies not detected in optical wavelengths could have counterparts among the ERGs. The modelling of properties of ERGs counterpart of far-IR/submillimetre galaxies will shed light on the nature of the most obscured star-forming galaxies at different redshifts. On the other hand, a topic of major interest is the investigation of AGN activity among the high-mass, high-redshift ERGs and also in their environments. This could provide additional clues on ERG evolution and the relation between AGNs and their respective host galaxies. These few examples simply illustrate some of the remaining open questions for the ERGs and point towards a more general fact: only through clarifying the links between different galaxy populations we shall be able to achieve a definitive reconstruction of the history of structure formation.

Appendix A

Catalog of $K_S \leq 22$-selected galaxies

We present in Table A.1 the full catalog of 1663 $K_s \leq 22$-selected galaxies. The first column gives the source identification number; the second and third columns give the corresponding coordinates on the K_s-band images; the fourth column lists the total Kron-type K_s magnitude, as measured by SEXTRACTOR. The fifth column shows the redshifts estimated by HYPERZ, according to the criteria explained in §4.3 (an asterisk indicates a BPZ/spectroscopic determination). The last three columns contain our predicted Spitzer/IRAC magnitudes in three channels: $3.6\mu m$, $4.5\mu m$ and $5.8\mu m$. We predicted the IRAC magnitudes using the observer-frame HYPERZ best-fit SED for each source. In the cases in which we adopted the HYPERZ secondary solution or a BPZ/spectroscopic determination, we did not have the full observer-frame SED provided by HYPERZ in the output and, thus, we could not recover the source fluxes in the IRAC channels. These cases are indicated with a 0.0 value in the IRAC magnitude columns. All magnitudes are in the Vega system.

Table A.1: Full catalog of K_s-selected galaxies. The K_s magnitudes in the fourth column are measured total magnitudes. The redshifts in the fifth column correspond to HYPERZ estimates, except for the values indicated with an asterisk, which correspond to BPZ or spectroscopic determinations (see §4.3 for details). The sixth, seventh and eighth columns correspond to our predicted Spitzer/IRAC magnitudes in three channels: $3.6\mu m$, $4.5\mu m$ and $5.8\mu m$, respectively. A 0.0 value indicates that no predicted magnitude is available for the corresponding source. All magnitudes are in the Vega system.

id	RA(J2000)	DEC(J2000)	K_s	z_{phot}	[3.6]	[4.5]	[5.8]
11163	3:32:05.20	-27:45:49.78	21.81 ± 0.15	1.60	20.6	20.1	19.9
11175	3:32:05.24	-27:45:52.71	19.63 ± 0.02	1.38	18.4	17.9	18.0
1174	3:32:05.27	-27:44:40.20	21.72 ± 0.12	0.65	21.2	21.1	21.1
11183	3:32:05.39	-27:44:01.37	20.43 ± 0.04	0.60	19.7	19.7	19.6
1151	3:32:05.39	-27:44:29.18	20.61 ± 0.04	0.99	19.5	19.3	19.2
11166	3:32:05.43	-27:45:54.32	21.15 ± 0.06	1.11	20.3	20.1	20.1
11142	3:32:05.48	-27:45:25.30	19.27 ± 0.01	0.90	18.2	18.1	17.9
11171	3:32:05.50	-27:45:51.68	21.57 ± 0.08	2.05	20.2	19.7	19.1
11114	3:32:05.51	-27:45:11.78	21.74 ± 0.09	0.54	21.2	21.0	21.0
11112	3:32:05.52	-27:45:09.12	21.55 ± 0.09	0.10	21.4	21.4	21.5
119	3:32:05.53	-27:46:04.50	21.65 ± 0.09	0.65	0.0	0.0	0.0
1119	3:32:05.56	-27:46:00.18	21.49 ± 0.09	0.90	20.8	20.7	20.6
11151	3:32:05.60	-27:45:40.83	21.58 ± 0.09	0.54	21.2	21.0	21.1
1177	3:32:05.75	-27:44:47.11	21.10 ± 0.06	1.66	19.7	19.0	18.8
1124	3:32:05.94	-27:46:01.80	17.94 ± 0.00	0.49	17.8	17.5	17.4
11123	3:32:05.95	-27:45:20.45	20.56 ± 0.03	0.96	19.8	19.7	19.6
11106	3:32:05.98	-27:45:07.20	18.60 ± 0.01	0.83	17.7	17.8	17.5
1136	3:32:06.17	-27:44:17.31	21.87 ± 0.12	1.31	21.0	20.7	20.9
1180	3:32:06.24	-27:44:48.57	21.86 ± 0.07	0.89	20.7	20.7	20.6
11144	3:32:06.26	-27:45:36.72	18.07 ± 0.00	0.61	17.3	17.3	17.2
11107	3:32:06.29	-27:45:08.21	20.96 ± 0.07	0.10	0.0	0.0	0.0
1199	3:32:06.30	-27:45:02.72	20.45 ± 0.03	1.59	19.2	18.6	18.4
11169	3:32:06.39	-27:45:54.96	19.33 ± 0.01	1.11	17.9	17.6	17.6
11188	3:32:06.48	-27:44:03.52	18.84 ± 0.01	0.91	17.8	17.9	17.6
1144	3:32:06.53	-27:44:24.79	19.49 ± 0.03	0.39	0.0	0.0	0.0
11118	3:32:06.57	-27:45:14.05	20.22 ± 0.02	2.30	18.7	18.0	17.3
11135	3:32:06.57	-27:45:30.75	21.05 ± 0.05	1.55	19.8	19.2	19.0
111	3:32:06.59	-27:46:13.38	21.86 ± 0.16	3.21	20.9	20.1	19.6
1176	3:32:06.66	-27:44:45.85	21.28 ± 0.08	0.90	20.6	20.5	20.3
11125	3:32:06.68	-27:45:23.97	20.52 ± 0.03	0.90	19.9	19.8	19.6
1187	3:32:06.71	-27:44:55.21	20.92 ± 0.04	2.28	19.3	18.7	18.0
11136	3:32:06.71	-27:45:32.99	20.57 ± 0.03	0.58	19.8	19.8	19.7
11161	3:32:06.71	-27:45:47.50	21.47 ± 0.09	0.10	0.0	0.0	0.0
11126	3:32:06.81	-27:45:24.35	19.45 ± 0.01	0.99	18.3	18.1	18.1
11162	3:32:06.85	-27:45:50.19	19.21 ± 0.01	0.80	18.6	18.6	18.4
1121	3:32:06.97	-27:46:00.24	20.27 ± 0.03	1.38	19.0	18.5	18.6
11185	3:32:07.03	-27:44:01.79	21.24 ± 0.06	2.18	19.5	18.9	18.3
11184	3:32:07.04	-27:44:05.99	19.18 ± 0.01	0.59	18.5	18.4	18.3
11178	3:32:07.17	-27:43:56.06	18.90 ± 0.01	0.97	17.9	17.7	17.8
1137	3:32:07.42	-27:44:17.51	20.02 ± 0.02	1.61	18.7	18.2	18.0
114	3:32:07.47	-27:46:10.97	21.42 ± 0.14	1.11	20.6	20.4	20.5
1190	3:32:07.48	-27:44:57.50	21.36 ± 0.11	0.67	21.0	20.9	20.8
11152	3:32:07.48	-27:45:38.48	21.95 ± 0.09	0.10	21.7	21.6	21.7
11197	3:32:07.49	-27:44:08.57	21.32 ± 0.06	0.99	20.5	20.3	20.2
11157	3:32:07.49	-27:45:40.76	21.92 ± 0.13	0.14	22.0	21.9	22.2
11180	3:32:07.55	-27:43:56.60	19.45 ± 0.01	0.92	18.4	18.3	18.2
11190	3:32:07.64	-27:44:02.78	20.92 ± 0.04	0.10	0.0	0.0	0.0
1160	3:32:07.89	-27:44:34.33	21.00 ± 0.05	0.59	0.0	0.0	0.0
1116	3:32:07.90	-27:46:00.56	19.39 ± 0.02	0.52	0.0	0.0	0.0
1128	3:32:07.99	-27:45:54.68	21.84 ± 0.08	0.70	21.0	21.0	20.9
11164	3:32:08.21	-27:45:50.17	20.49 ± 0.04	1.60	19.5	19.0	18.8
1114	3:32:08.24	-27:46:02.71	21.59 ± 0.07	1.10	20.4	20.2	20.2
11182	3:32:08.28	-27:44:00.42	21.46 ± 0.07	0.10	21.2	21.1	21.4
11153	3:32:08.35	-27:45:42.98	21.99 ± 0.08	1.27	21.1	20.8	20.9
11160	3:32:08.42	-27:45:46.84	21.64 ± 0.08	1.67	20.4	19.8	19.6
11176	3:32:08.57	-27:43:50.25	21.97 ± 0.14	0.65	0.0	0.0	0.0
11156	3:32:08.58	-27:45:44.08	21.33 ± 0.07	0.96	20.4	20.4	20.1
1197	3:32:08.65	-27:45:01.81	18.16 ± 0.00	0.82	17.2	17.2	17.0
11110	3:32:08.69	-27:45:08.05	18.87 ± 0.01	0.94	17.6	17.4	17.3

id	RA(J2000)	DEC(J2000)	K_s	z_{phot}	[3.6]	[4.5]	[5.8]
1147	3:32:08.91	-27:44:24.80	21.57 ± 0.06	2.76	20.4	19.7	19.1
11130	3:32:08.93	-27:45:26.30	21.34 ± 0.07	0.54	0.0	0.0	0.0
1173	3:32:08.98	-27:44:43.82	20.80 ± 0.06	2.23	19.9	19.4	18.9
1123	3:32:09.17	-27:45:57.13	21.03 ± 0.05	1.40	19.9	19.4	19.5
11104	3:32:09.25	-27:45:05.09	20.69 ± 0.03	1.40	19.3	18.9	18.9
1125	3:32:09.44	-27:45:58.50	21.46 ± 0.07	2.40	20.2	19.6	19.0
11177	3:32:09.55	-27:43:55.95	18.79 ± 0.01	0.59	18.2	18.0	18.0
1130	3:32:09.63	-27:44:09.43	21.94 ± 0.10	0.72	21.1	21.1	20.9
11194	3:32:09.77	-27:44:08.88	21.77 ± 0.07	0.71	20.7	20.9	20.6
1166	3:32:09.77	-27:44:42.52	16.22 ± 0.00	0.10	16.3	16.3	16.4
11133	3:32:09.77	-27:45:29.38	19.97 ± 0.02	0.59	19.3	19.4	19.2
11131	3:32:09.79	-27:45:26.53	21.71 ± 0.07	0.70	20.9	20.8	20.7
1139	3:32:09.86	-27:44:19.19	21.76 ± 0.07	0.67	20.6	20.6	20.4
1152	3:32:09.88	-27:44:29.64	21.34 ± 0.06	2.09	19.9	19.3	18.7
11167	3:32:10.05	-27:45:51.96	21.86 ± 0.12	0.70	21.3	21.3	21.2
11132	3:32:10.06	-27:45:26.93	20.46 ± 0.03	0.48	20.1	19.9	19.7
1117	3:32:10.08	-27:46:10.66	20.22 ± 0.06	1.19	19.5	19.2	19.2
11195	3:32:10.12	-27:44:09.85	21.80 ± 0.10	0.53	21.4	21.2	21.0
1134	3:32:10.18	-27:44:16.46	20.49 ± 0.04	0.56	0.0	0.0	0.0
1194	3:32:10.26	-27:44:58.40	21.93 ± 0.14	0.84	21.6	21.7	21.4
1164	3:32:10.28	-27:44:37.10	21.61 ± 0.07	0.82	20.9	20.9	20.7
11116	3:32:10.31	-27:45:12.82	21.24 ± 0.07	0.10	0.0	0.0	0.0
16172	3:32:10.34	-27:47:54.26	18.14 ± 0.02	0.60	17.6	17.5	17.3
1110	3:32:10.40	-27:46:05.02	20.50 ± 0.03	0.92	19.6	19.4	19.2
16123	3:32:10.40	-27:47:22.71	20.61 ± 0.12	1.16	19.4	19.1	19.2
16262	3:32:10.42	-27:46:35.91	21.23 ± 0.14	0.68	20.1	20.1	19.9
1641	3:32:10.42	-27:48:21.87	21.63 ± 0.22	0.93	20.8	20.7	20.6
16127	3:32:10.44	-27:47:20.82	20.72 ± 0.10	0.74	20.2	20.4	20.1
11159	3:32:10.45	-27:45:39.14	21.33 ± 0.07	1.57	19.9	19.2	18.9
1167	3:32:10.46	-27:44:39.21	21.82 ± 0.12	0.82	20.8	20.8	20.5
16139	3:32:10.47	-27:47:32.53	20.70 ± 0.10	1.33	19.5	19.1	19.2
16253	3:32:10.50	-27:46:28.91	19.33 ± 0.03	1.47	17.9	17.4	17.3
1642	3:32:10.50	-27:48:17.71	21.70 ± 0.18	0.91	20.7	20.7	20.4
1162	3:32:10.51	-27:44:37.00	20.90 ± 0.04	0.89	20.0	20.0	19.8
1673	3:32:10.57	-27:47:01.81	18.16 ± 0.01	0.60	17.8	17.8	17.6
1687	3:32:10.57	-27:47:06.24	19.12 ± 0.03	0.97	18.2	17.9	17.9
16230	3:32:10.61	-27:46:20.40	21.09 ± 0.18	2.44	19.3	18.8	18.1
16112	3:32:10.65	-27:47:13.66	19.82 ± 0.07	0.50	19.7	19.5	19.4
16117	3:32:10.67	-27:47:17.45	20.79 ± 0.10	1.88	19.2	18.5	18.1
11174	3:32:10.70	-27:43:46.99	20.69 ± 0.05	0.10	20.5	20.5	20.7
16203	3:32:10.71	-27:48:07.14	17.89 ± 0.01	0.60	0.0	0.0	0.0
16218	3:32:10.71	-27:48:19.47	19.52 ± 0.03	1.36	18.0	17.4	17.4
16239	3:32:10.76	-27:46:27.73	17.94 ± 0.02	1.01	17.0	16.7	16.6
16146	3:32:10.76	-27:47:38.09	21.12 ± 0.17	2.17	19.9	19.4	18.9
1656	3:32:10.78	-27:46:47.44	20.59 ± 0.11	1.01	20.1	19.9	20.0
16136	3:32:10.80	-27:47:32.46	21.36 ± 0.15	0.86	20.7	20.8	20.4
1168	3:32:10.85	-27:44:41.28	20.22 ± 0.02	0.60	19.4	19.4	19.3
1165	3:32:10.86	-27:44:38.81	20.13 ± 0.03	0.72	19.8	19.8	19.6
11138	3:32:10.88	-27:45:33.48	21.56 ± 0.08	0.10	0.0	0.0	0.0
1112	3:32:10.89	-27:46:05.47	20.77 ± 0.04	2.28	19.3	18.7	18.1
16121	3:32:10.91	-27:47:22.44	16.98 ± 0.01	0.56	16.8	16.7	16.6
16157	3:32:10.93	-27:47:45.74	20.76 ± 0.11	1.37	19.9	19.5	19.6
11154	3:32:10.95	-27:45:44.50	20.40 ± 0.03	0.94	19.6	19.5	19.4
16234	3:32:10.97	-27:46:23.33	20.66 ± 0.09	3.19	19.5	18.7	18.2
1188	3:32:11.00	-27:44:59.36	20.24 ± 0.03	1.48	19.0	18.6	18.5
1183	3:32:11.02	-27:44:56.03	18.85 ± 0.01	0.89	18.0	18.0	17.8
11147	3:32:11.05	-27:45:37.51	21.85 ± 0.10	0.59	0.0	0.0	0.0
1649	3:32:11.07	-27:46:41.11	21.96 ± 0.18	1.45	20.6	20.0	19.9
16161	3:32:11.12	-27:47:47.98	20.57 ± 0.07	1.03	19.5	19.1	18.9
16132	3:32:11.15	-27:47:28.08	19.71 ± 0.03	0.64	18.8	18.8	18.5
16236	3:32:11.17	-27:46:19.78	20.40 ± 0.07	1.31	19.0	18.7	18.8
11134	3:32:11.21	-27:45:33.28	18.72 ± 0.01	1.22	17.7	17.5	17.6
1688	3:32:11.22	-27:47:05.65	21.66 ± 0.15	0.58	20.6	20.7	20.5
1138	3:32:11.24	-27:44:19.29	21.07 ± 0.04	1.90	19.7	19.1	18.9
16251	3:32:11.26	-27:46:30.33	21.04 ± 0.12	1.63	19.5	18.8	18.6

id	RA(J2000)	DEC(J2000)	K_s	z_{phot}	[3.6]	[4.5]	[5.8]
112	3:32:11.27	-27:46:14.58	20.87 ± 0.09	0.54	0.0	0.0	0.0
1689	3:32:11.28	-27:47:06.67	21.51 ± 0.15	1.08	20.7	20.5	20.5
1120	3:32:11.31	-27:45:59.63	21.65 ± 0.07	0.61	20.8	20.7	20.6
1635	3:32:11.32	-27:48:24.51	19.10 ± 0.02	0.69	18.4	18.5	18.2
1657	3:32:11.40	-27:46:49.89	18.18 ± 0.01	0.62	17.5	17.6	17.3
16223	3:32:11.42	-27:46:18.56	21.87 ± 0.29	2.04	20.4	19.7	19.2
1141	3:32:11.48	-27:44:22.12	20.10 ± 0.03	0.10	0.0	0.0	0.0
1613	3:32:11.48	-27:48:15.67	16.19 ± 0.00	0.61	15.8	15.8	15.6
1191	3:32:11.51	-27:44:57.23	20.83 ± 0.04	0.60	20.1	20.1	20.0
16105	3:32:11.51	-27:47:13.27	17.37 ± 0.01	0.70	0.0	0.0	0.0
115	3:32:11.55	-27:46:13.51	19.90 ± 0.05	1.01	18.9	18.7	18.8
16242	3:32:11.56	-27:46:22.95	19.40 ± 0.03	1.02	18.6	18.4	18.4
16165	3:32:11.56	-27:47:49.22	21.93 ± 0.25	0.60	21.3	21.2	21.2
1667	3:32:11.58	-27:46:59.16	18.81 ± 0.02	0.74	18.1	18.3	17.8
1127	3:32:11.60	-27:45:54.18	18.45 ± 0.01	1.09	17.3	17.1	17.2
16126	3:32:11.66	-27:47:23.78	21.23 ± 0.13	0.94	20.3	20.2	20.0
11103	3:32:11.68	-27:45:04.58	21.93 ± 0.12	0.52	21.5	21.4	21.2
1610	3:32:11.69	-27:48:33.65	21.80 ± 0.18	0.74	21.1	21.2	20.9
11109	3:32:11.71	-27:45:07.61	20.46 ± 0.04	0.72	20.1	20.1	20.0
1175	3:32:11.72	-27:44:44.20	20.96 ± 0.05	0.10	21.0	21.0	21.2
16249	3:32:11.76	-27:46:28.13	20.93 ± 0.08	1.62	19.2	18.5	18.2
16240	3:32:11.78	-27:46:24.48	20.89 ± 0.08	0.98	19.6	19.4	19.4
11179	3:32:11.82	-27:43:55.29	21.55 ± 0.07	1.15	20.6	20.4	20.5
1131	3:32:11.85	-27:44:13.48	19.41 ± 0.01	0.10	0.0	0.0	0.0
163	3:32:11.85	-27:48:37.94	21.33 ± 0.16	0.84	20.6	20.6	20.4
1126	3:32:11.89	-27:45:56.57	21.62 ± 0.07	2.40	20.3	19.8	19.2
113	3:32:11.92	-27:46:15.51	21.48 ± 0.14	2.43	19.9	19.2	18.5
1693	3:32:11.92	-27:47:06.80	20.30 ± 0.05	0.62	19.5	19.5	19.3
1652	3:32:11.93	-27:46:44.69	19.02 ± 0.02	1.13	17.8	17.5	17.3
11121	3:32:11.96	-27:45:18.05	20.62 ± 0.03	0.72	19.8	19.9	19.6
16238	3:32:11.98	-27:46:20.97	19.39 ± 0.03	1.00	18.1	17.8	17.8
1148	3:32:12.06	-27:44:24.78	21.41 ± 0.06	0.87	20.6	20.6	20.4
11129	3:32:12.19	-27:45:30.05	17.63 ± 0.01	0.59	17.3	17.2	17.2
11168	3:32:12.20	-27:45:54.42	19.45 ± 0.01	0.99	18.6	18.4	18.3
16235	3:32:12.21	-27:46:20.72	18.26 ± 0.01	0.81	17.6	17.7	17.4
16170	3:32:12.22	-27:47:50.49	21.28 ± 0.10	1.00	20.4	20.1	20.0
1140	3:32:12.24	-27:44:20.12	21.99 ± 0.11	0.10	0.0	0.0	0.0
16210	3:32:12.24	-27:48:17.07	21.09 ± 0.10	1.24	19.8	19.3	19.3
16200	3:32:12.27	-27:48:07.91	21.17 ± 0.10	0.91	20.1	20.2	20.0
11117	3:32:12.29	-27:45:13.09	18.79 ± 0.01	0.59	18.1	18.1	18.0
16111	3:32:12.29	-27:47:13.96	21.36 ± 0.13	0.59	20.7	20.6	20.6
11128	3:32:12.30	-27:45:27.44	18.40 ± 0.01	0.61	18.2	18.2	18.1
11122	3:32:12.35	-27:45:18.63	20.79 ± 0.03	1.03	19.6	19.4	19.4
16106	3:32:12.35	-27:47:11.43	22.00 ± 0.16	1.22	20.6	20.3	20.5
1616	3:32:12.35	-27:48:35.85	18.65 ± 0.02	0.60	18.4	18.4	18.2
11173	3:32:12.36	-27:43:53.61	17.93 ± 0.01	0.49	17.9	17.5	17.5
16211	3:32:12.38	-27:48:16.54	21.73 ± 0.16	2.67	20.4	19.8	19.2
16204	3:32:12.42	-27:48:10.02	21.26 ± 0.12	0.40	0.0	0.0	0.0
11191	3:32:12.44	-27:44:02.75	21.19 ± 0.06	2.14	19.8	19.2	18.7
11165	3:32:12.45	-27:45:51.44	20.69 ± 0.03	0.58	19.7	19.8	19.6
16228	3:32:12.46	-27:46:21.43	19.82 ± 0.05	1.09	18.5	18.1	18.1
16131	3:32:12.46	-27:47:29.11	18.51 ± 0.01	1.01	17.6	17.3	17.4
1161	3:32:12.47	-27:44:37.89	20.66 ± 0.05	0.72	20.0	20.2	19.8
1184	3:32:12.51	-27:44:54.90	20.90 ± 0.04	0.88	20.0	20.1	19.8
16254	3:32:12.52	-27:46:29.22	18.72 ± 0.01	1.19	17.4	17.1	17.1
16174	3:32:12.52	-27:47:53.63	19.88 ± 0.04	0.54	0.0	0.0	0.0
1111	3:32:12.59	-27:46:05.51	21.13 ± 0.07	1.47	20.0	19.5	19.5
16220	3:32:12.64	-27:46:12.03	21.63 ± 0.22	0.45	21.8	21.4	21.5
11192	3:32:12.76	-27:44:07.84	20.86 ± 0.04	0.59	19.7	19.6	19.5
1634	3:32:12.78	-27:48:23.20	19.98 ± 0.06	1.10	19.2	19.0	19.0
16247	3:32:12.82	-27:46:27.64	21.31 ± 0.14	0.98	20.4	20.1	20.2
1185	3:32:12.83	-27:44:55.72	20.61 ± 0.04	1.30	19.7	19.3	19.4
1648	3:32:12.89	-27:46:41.27	20.09 ± 0.07	3.12	19.1	18.4	17.9
1621	3:32:12.89	-27:48:33.10	20.79 ± 0.15	2.00	20.4	19.8	19.4
167	3:32:12.89	-27:48:40.41	19.92 ± 0.09	0.69	19.4	19.6	19.2

id	RA(J2000)	DEC(J2000)	K_s	z_{phot}	[3.6]	[4.5]	[5.8]
1196	3:32:12.91	-27:44:59.87	20.64 ± 0.04	1.37	19.3	18.9	19.0
11120	3:32:12.92	-27:45:16.96	21.79 ± 0.08	0.60	20.9	21.0	20.8
1181	3:32:12.93	-27:44:51.33	21.19 ± 0.07	2.70	20.1	19.5	19.0
11148	3:32:12.93	-27:45:38.72	20.50 ± 0.04	0.99	19.7	19.6	19.5
11102	3:32:12.94	-27:45:02.72	21.99 ± 0.10	0.77	21.0	21.2	20.8
1612	3:32:12.94	-27:48:36.69	20.73 ± 0.11	0.53	20.8	20.6	20.4
16195	3:32:12.99	-27:48:05.65	21.46 ± 0.18	1.08	20.8	20.5	20.5
1643	3:32:13.01	-27:46:37.87	18.92 ± 0.02	1.31	17.7	17.4	17.4
116	3:32:13.02	-27:46:05.08	21.60 ± 0.08	0.80	20.8	20.8	20.6
16140	3:32:13.06	-27:47:34.89	20.92 ± 0.11	2.49	19.4	18.8	18.1
11141	3:32:13.12	-27:45:35.14	20.52 ± 0.04	1.01	19.8	19.6	19.6
16178	3:32:13.13	-27:47:54.87	19.92 ± 0.04	0.61	19.1	19.0	18.8
11115	3:32:13.14	-27:45:01.12	21.56 ± 0.06	1.62	20.4	19.8	19.6
16144	3:32:13.18	-27:47:38.20	20.48 ± 0.08	0.62	20.1	20.2	20.0
11149	3:32:13.33	-27:45:39.41	21.94 ± 0.08	0.60	21.1	21.2	21.0
11170	3:32:13.35	-27:45:54.64	21.92 ± 0.12	0.50	0.0	0.0	0.0
11155	3:32:13.45	-27:45:43.53	21.71 ± 0.08	0.96	20.8	20.7	20.6
16103	3:32:13.46	-27:47:10.60	20.70 ± 0.08	2.60	19.4	18.9	18.2
16101	3:32:13.55	-27:47:07.73	20.97 ± 0.09	0.20	0.0	0.0	0.0
11105	3:32:13.60	-27:45:05.39	19.81 ± 0.02	0.62	19.0	19.0	18.8
16167	3:32:13.60	-27:47:49.52	21.64 ± 0.15	0.96	21.3	21.3	21.0
16187	3:32:13.61	-27:47:59.42	20.74 ± 0.08	1.62	19.6	19.0	18.8
1662	3:32:13.62	-27:46:49.67	21.90 ± 0.18	1.56	20.4	19.8	19.6
16173	3:32:13.63	-27:47:53.75	19.58 ± 0.04	1.57	18.2	17.5	17.2
1146	3:32:13.66	-27:44:24.02	21.25 ± 0.05	0.72	20.5	20.5	20.3
16222	3:32:13.75	-27:46:16.73	20.82 ± 0.10	0.73	20.1	20.1	19.9
16188	3:32:13.75	-27:47:59.49	20.65 ± 0.12	1.02	20.4	20.2	20.3
11127	3:32:13.81	-27:45:25.58	18.61 ± 0.01	1.08	17.4	17.2	17.2
11124	3:32:13.82	-27:45:21.32	21.45 ± 0.08	0.43	21.4	21.1	21.1
16257	3:32:13.82	-27:46:33.16	21.33 ± 0.12	2.17	19.5	18.9	18.2
16158	3:32:13.85	-27:47:45.44	21.97 ± 0.19	1.07	21.6	21.4	21.4
11146	3:32:13.93	-27:45:37.34	20.00 ± 0.02	0.58	19.2	19.2	19.1
16145	3:32:13.95	-27:47:38.03	21.51 ± 0.15	1.38	20.4	20.0	20.1
1186	3:32:13.97	-27:44:54.58	20.49 ± 0.04	0.94	19.7	19.5	19.4
118	3:32:14.01	-27:46:05.42	21.64 ± 0.08	0.76	20.8	21.0	20.6
11113	3:32:14.03	-27:45:09.01	21.97 ± 0.11	3.47	20.8	20.1	19.5
16258	3:32:14.03	-27:46:34.38	19.12 ± 0.03	0.92	18.3	18.1	17.9
16171	3:32:14.10	-27:47:50.95	20.55 ± 0.07	0.93	19.7	19.7	19.5
1671	3:32:14.13	-27:46:59.79	21.93 ± 0.16	0.90	20.9	20.8	20.7
16206	3:32:14.13	-27:48:11.74	20.93 ± 0.10	0.93	20.2	20.1	20.0
1113	3:32:14.18	-27:46:06.21	20.49 ± 0.04	0.78	19.8	19.9	19.6
16209	3:32:14.21	-27:48:16.42	21.25 ± 0.14	1.31	20.8	20.3	20.4
1658	3:32:14.24	-27:46:47.76	20.58 ± 0.07	0.88	19.9	19.9	19.7
16120	3:32:14.26	-27:47:21.19	18.16 ± 0.01	1.49	16.9	16.3	16.2
11196	3:32:14.27	-27:44:09.81	21.51 ± 0.07	0.92	20.6	20.5	20.4
1690	3:32:14.29	-27:47:04.39	21.37 ± 0.12	0.39	0.0	0.0	0.0
1692	3:32:14.30	-27:47:05.93	20.26 ± 0.06	0.49	20.2	19.7	19.7
16107	3:32:14.31	-27:47:13.13	17.91 ± 0.01	0.63	17.2	17.2	16.9
1189	3:32:14.35	-27:44:55.87	19.77 ± 0.02	0.59	19.0	19.0	18.9
117	3:32:14.36	-27:46:07.24	21.64 ± 0.12	0.72	20.8	20.8	20.6
1122	3:32:14.39	-27:45:57.88	21.81 ± 0.09	0.59	20.7	20.7	20.5
16192	3:32:14.39	-27:47:55.91	21.51 ± 0.13	1.46	20.5	20.0	20.1
1135	3:32:14.41	-27:44:16.01	21.58 ± 0.07	0.72	20.7	20.7	20.5
11150	3:32:14.42	-27:45:40.81	17.47 ± 0.00	0.42	17.5	17.1	17.1
1195	3:32:14.43	-27:44:56.66	20.13 ± 0.02	0.72	19.2	19.2	19.0
16243	3:32:14.44	-27:46:24.73	18.47 ± 0.01	0.71	17.7	17.8	17.5
1129	3:32:14.46	-27:43:50.97	21.24 ± 0.11	1.42	20.4	19.9	19.9
11189	3:32:14.46	-27:44:05.45	21.37 ± 0.06	0.32	21.5	21.2	21.3
1169	3:32:14.59	-27:44:40.27	21.36 ± 0.06	2.28	20.0	19.4	18.8
1192	3:32:14.60	-27:44:54.74	21.46 ± 0.12	1.77	20.4	19.8	19.6
16153	3:32:14.63	-27:47:44.22	21.30 ± 0.12	1.00	20.2	19.9	19.9
16216	3:32:14.65	-27:48:15.42	21.00 ± 0.10	0.62	20.5	20.4	20.3
1678	3:32:14.66	-27:47:02.74	20.35 ± 0.05	0.66	19.2	19.1	19.0
1155	3:32:14.77	-27:44:33.24	19.36 ± 0.01	0.61	18.5	18.6	18.4
11187	3:32:14.79	-27:44:02.46	21.15 ± 0.05	1.62	19.7	19.1	18.9

id	RA(J2000)	DEC(J2000)	K_s	z_{phot}	[3.6]	[4.5]	[5.8]
16143	3:32:14.83	-27:47:38.16	18.56 ± 0.01	0.73	17.8	17.9	17.5
1686	3:32:14.87	-27:47:05.29	21.53 ± 0.18	1.17	20.3	20.1	20.2
11186	3:32:14.89	-27:43:58.30	20.81 ± 0.06	1.01	20.0	19.7	19.6
16190	3:32:14.90	-27:48:02.94	21.16 ± 0.12	0.13*	0.0	0.0	0.0
16189	3:32:14.91	-27:48:00.12	19.96 ± 0.04	0.90	18.8	18.6	18.4
16208	3:32:14.91	-27:48:15.67	20.17 ± 0.07	0.81	19.6	19.7	19.3
1668	3:32:14.94	-27:46:59.65	20.76 ± 0.10	0.57	20.4	20.1	20.0
166	3:32:14.95	-27:48:40.78	21.33 ± 0.18	1.22	19.8	19.3	19.2
11172	3:32:14.97	-27:45:54.29	20.42 ± 0.04	1.41	19.5	19.1	19.2
1115	3:32:14.97	-27:46:03.93	21.59 ± 0.11	0.89	20.7	20.7	20.6
1614	3:32:14.97	-27:48:33.46	20.43 ± 0.12	0.79	19.7	19.9	19.4
16259	3:32:14.98	-27:46:33.45	21.58 ± 0.13	1.06	20.6	20.4	20.4
11193	3:32:14.99	-27:44:08.16	21.70 ± 0.10	0.10	21.4	21.3	21.4
1653	3:32:15.10	-27:46:44.53	20.97 ± 0.10	0.98	20.3	20.1	20.0
1193	3:32:15.13	-27:44:59.15	20.72 ± 0.05	1.28	19.9	19.6	19.6
16116	3:32:15.22	-27:47:16.24	21.71 ± 0.19	0.82*	0.0	0.0	0.0
1163	3:32:15.23	-27:44:38.15	19.97 ± 0.03	0.99	19.0	18.7	18.7
1697	3:32:15.23	-27:47:08.15	20.84 ± 0.10	0.91	20.2	20.2	20.1
1636	3:32:15.23	-27:48:21.34	20.95 ± 0.10	1.37	19.8	19.4	19.5
1623	3:32:15.28	-27:48:29.61	20.95 ± 0.15	3.34	19.7	19.0	18.4
1154	3:32:15.35	-27:44:31.94	21.39 ± 0.06	1.83	20.2	19.7	19.4
11108	3:32:15.35	-27:45:06.97	19.80 ± 0.02	0.89	18.9	18.9	18.7
11101	3:32:15.37	-27:45:01.64	21.51 ± 0.07	1.42	20.3	19.8	19.8
16260	3:32:15.46	-27:46:31.42	18.71 ± 0.03	0.60	0.0	0.0	0.0
1681	3:32:15.47	-27:47:04.30	20.51 ± 0.09	0.51	20.6	20.4	20.2
1632	3:32:15.47	-27:48:26.33	19.98 ± 0.06	0.56	19.8	19.7	19.7
1157	3:32:15.51	-27:44:32.87	21.61 ± 0.09	1.22	20.8	20.5	20.6
11143	3:32:15.52	-27:45:36.38	18.56 ± 0.01	0.90	17.6	17.6	17.4
1178	3:32:15.58	-27:44:44.78	21.90 ± 0.11	0.87	21.0	21.0	20.8
11158	3:32:15.63	-27:45:46.14	21.07 ± 0.08	1.64	19.8	19.1	18.9
1158	3:32:15.65	-27:44:34.28	21.18 ± 0.08	0.10	0.0	0.0	0.0
11119	3:32:15.70	-27:45:15.46	20.74 ± 0.04	2.32	19.1	18.4	17.7
1118	3:32:15.76	-27:46:04.87	20.11 ± 0.03	1.55	19.0	18.5	18.3
16256	3:32:15.78	-27:46:30.49	19.23 ± 0.03	0.44	0.0	0.0	0.0
1150	3:32:15.80	-27:44:27.00	21.03 ± 0.06	2.43	19.5	19.0	18.3
1156	3:32:15.80	-27:44:34.60	21.62 ± 0.08	1.01	20.6	20.4	20.4
16108	3:32:15.81	-27:47:13.60	17.12 ± 0.01	0.71	16.6	16.7	16.3
16232	3:32:15.82	-27:46:22.43	21.71 ± 0.16	1.23	20.8	20.5	20.6
11140	3:32:15.87	-27:45:33.79	22.00 ± 0.15	0.10	21.7	21.6	21.7
16125	3:32:15.87	-27:47:23.12	19.14 ± 0.03	0.79	18.5	18.7	18.2
16163	3:32:15.89	-27:47:49.87	18.54 ± 0.01	0.64	18.0	18.0	17.7
11111	3:32:15.96	-27:45:07.90	20.73 ± 0.05	0.72	20.0	19.9	19.8
1142	3:32:15.98	-27:44:23.05	18.79 ± 0.01	0.50	18.5	18.3	18.2
16142	3:32:16.00	-27:47:36.66	21.23 ± 0.12	2.19	19.8	19.2	18.7
16176	3:32:16.01	-27:47:49.85	18.73 ± 0.02	0.97	17.7	17.4	17.4
1170	3:32:16.06	-27:44:41.34	21.97 ± 0.17	2.60	20.5	20.0	19.4
16250	3:32:16.12	-27:46:27.84	19.90 ± 0.04	0.97	18.9	18.6	18.6
16196	3:32:16.12	-27:48:05.77	21.32 ± 0.17	1.07	20.9	20.6	20.5
21102	3:32:16.14	-27:49:41.75	16.87 ± 0.00	0.59	16.4	16.4	16.3
16147	3:32:16.16	-27:47:36.61	21.73 ± 0.19	0.40	22.0	21.6	21.6
16199	3:32:16.16	-27:48:06.96	21.85 ± 0.30	1.00	21.7	21.5	21.6
1143	3:32:16.19	-27:44:23.22	19.74 ± 0.03	0.48	19.5	19.3	19.2
21125	3:32:16.21	-27:49:54.13	20.59 ± 0.06	1.61	19.0	18.4	18.1
1679	3:32:16.22	-27:47:03.22	20.52 ± 0.08	1.21	19.8	19.5	19.6
1665	3:32:16.24	-27:46:55.92	21.75 ± 0.22	2.49	20.4	19.8	19.2
1179	3:32:16.26	-27:44:47.73	21.09 ± 0.07	1.42	19.8	19.3	19.3
21126	3:32:16.26	-27:49:55.48	19.27 ± 0.02	1.57	17.9	17.2	17.0
1611	3:32:16.29	-27:48:37.40	20.77 ± 0.11	0.31	0.0	0.0	0.0
1171	3:32:16.31	-27:44:42.01	20.50 ± 0.05	0.10	20.3	20.2	20.4
21156	3:32:16.32	-27:50:13.26	19.99 ± 0.04	0.93	19.0	18.9	18.7
21145	3:32:16.33	-27:50:05.52	21.86 ± 0.18	1.00	21.2	21.1	21.0
11139	3:32:16.36	-27:45:33.62	21.99 ± 0.19	1.28	20.4	20.0	20.3
16215	3:32:16.36	-27:46:08.72	21.29 ± 0.18	0.93	21.0	21.0	20.6
1639	3:32:16.38	-27:48:24.21	19.82 ± 0.06	1.08	18.9	18.6	18.6
1159	3:32:16.43	-27:44:32.88	21.05 ± 0.09	0.87	20.2	20.2	20.0

id	RA(J2000)	DEC(J2000)	K_s	z_{phot}	[3.6]	[4.5]	[5.8]
1677	3:32:16.45	-27:47:02.37	20.57 ± 0.06	1.05	19.5	19.2	19.3
21110	3:32:16.47	-27:49:45.25	20.34 ± 0.05	0.49	20.1	19.8	19.7
21164	3:32:16.47	-27:50:19.87	20.71 ± 0.05	0.10	20.5	20.4	20.5
16156	3:32:16.50	-27:47:45.18	20.90 ± 0.09	0.79	20.3	20.4	20.1
16129	3:32:16.52	-27:47:27.11	17.87 ± 0.01	0.69	17.2	17.3	17.0
2192	3:32:16.52	-27:49:34.42	19.58 ± 0.03	0.71	18.9	18.9	18.7
21196	3:32:16.55	-27:50:38.70	21.18 ± 0.09	0.80	20.3	20.4	20.1
161	3:32:16.63	-27:48:43.49	21.55 ± 0.25	1.77	20.6	20.0	19.7
1096	3:32:16.68	-27:44:39.95	19.57 ± 0.03	0.88	18.7	18.6	18.5
2131	3:32:16.71	-27:50:51.33	21.99 ± 0.15	2.43	20.7	20.3	19.8
21146	3:32:16.76	-27:50:07.76	18.82 ± 0.02	0.59	18.2	18.2	18.1
1017	3:32:16.78	-27:46:05.41	20.55 ± 0.06	1.35	19.0	18.6	18.6
16168	3:32:16.79	-27:47:50.80	18.12 ± 0.01	0.60	17.6	17.6	17.4
10214	3:32:16.80	-27:45:51.25	20.75 ± 0.08	1.82	19.5	18.9	18.6
21248	3:32:16.83	-27:49:07.89	20.96 ± 0.07	3.29	19.7	18.9	18.4
21203	3:32:16.83	-27:50:44.05	21.44 ± 0.10	3.28	20.0	19.1	18.5
1068	3:32:16.84	-27:44:23.24	21.80 ± 0.18	0.88	21.3	21.3	21.0
2160	3:32:16.84	-27:49:16.51	21.13 ± 0.09	0.69	20.3	20.5	20.2
16159	3:32:16.88	-27:47:45.92	21.41 ± 0.14	1.66	20.0	19.4	19.2
16150	3:32:16.90	-27:47:27.06	20.69 ± 0.13	2.68	19.6	19.0	18.3
10172	3:32:16.93	-27:45:19.42	19.83 ± 0.03	1.21	18.5	18.1	18.2
21141	3:32:16.93	-27:50:04.07	20.50 ± 0.04	1.42	19.1	18.6	18.7
21103	3:32:16.94	-27:49:40.16	21.48 ± 0.13	0.77	20.7	20.7	20.4
21129	3:32:16.95	-27:49:55.85	21.50 ± 0.11	1.09	20.4	20.1	20.0
2178	3:32:16.95	-27:49:30.15	18.51 ± 0.01	0.50	18.3	18.1	18.0
2118	3:32:16.95	-27:51:02.67	20.20 ± 0.04	0.71	19.3	19.4	19.1
10152	3:32:16.99	-27:45:11.71	21.75 ± 0.11	1.05	20.9	20.7	20.7
16182	3:32:16.99	-27:47:57.52	20.68 ± 0.06	0.61	19.9	19.9	19.7
219	3:32:17.00	-27:51:13.56	20.10 ± 0.08	0.60	19.7	19.7	19.6
1676	3:32:17.01	-27:47:02.88	20.09 ± 0.06	0.59	19.6	19.6	19.4
1696	3:32:17.02	-27:47:09.22	19.05 ± 0.02	0.71	18.4	18.5	18.2
21130	3:32:17.04	-27:49:57.00	21.12 ± 0.07	3.83	19.2	18.3	17.6
2159	3:32:17.04	-27:49:21.80	16.13 ± 0.00	0.50	15.8	15.6	15.5
10224	3:32:17.06	-27:45:57.55	21.50 ± 0.11	0.97	20.3	20.1	20.0
1630	3:32:17.09	-27:48:23.08	21.44 ± 0.14	1.36	20.5	20.1	20.1
1036	3:32:17.10	-27:44:07.67	19.48 ± 0.02	0.70	18.5	18.6	18.3
10168	3:32:17.10	-27:45:17.69	20.97 ± 0.09	1.34	20.1	19.8	19.9
104	3:32:17.12	-27:46:11.69	19.83 ± 0.04	2.49	18.5	17.9	17.2
16227	3:32:17.12	-27:46:19.36	21.74 ± 0.24	2.64	20.0	19.5	18.9
1023	3:32:17.14	-27:46:04.03	21.45 ± 0.17	1.29	20.4	20.0	20.2
16217	3:32:17.15	-27:46:11.39	19.94 ± 0.07	1.75	18.4	17.6	17.3
21113	3:32:17.15	-27:49:48.11	19.74 ± 0.03	0.49	19.5	19.2	19.1
21240	3:32:17.17	-27:48:53.31	21.43 ± 0.09	1.57	20.3	19.9	19.7
1660	3:32:17.18	-27:46:49.19	18.67 ± 0.02	0.70	17.9	18.0	17.7
21191	3:32:17.20	-27:50:37.09	19.83 ± 0.03	1.72	18.3	17.5	17.2
2151	3:32:17.23	-27:49:14.43	20.95 ± 0.07	1.40	19.8	19.3	19.4
10131	3:32:17.24	-27:45:00.10	21.38 ± 0.12	2.43	20.0	19.5	18.8
1647	3:32:17.25	-27:46:40.56	20.11 ± 0.05	1.06	19.1	18.9	18.8
2115	3:32:17.25	-27:51:13.42	19.02 ± 0.02	1.12	17.5	17.2	17.2
1695	3:32:17.27	-27:47:08.35	20.31 ± 0.07	1.00	19.4	19.1	19.0
21249	3:32:17.27	-27:49:08.05	20.99 ± 0.06	2.24	18.8	18.1	17.4
16197	3:32:17.28	-27:48:07.29	18.70 ± 0.01	0.71	18.0	18.1	17.8
1631	3:32:17.29	-27:48:23.21	21.50 ± 0.16	1.00	20.6	20.4	20.3
21208	3:32:17.30	-27:48:43.93	21.76 ± 0.17	0.72	20.8	20.9	20.6
2126	3:32:17.30	-27:50:59.33	20.97 ± 0.07	1.00	20.1	19.9	20.0
21176	3:32:17.31	-27:50:25.01	20.74 ± 0.05	0.10	20.8	20.7	20.9
21192	3:32:17.31	-27:50:39.55	21.16 ± 0.09	0.50	21.0	20.8	20.7
10165	3:32:17.35	-27:45:17.68	21.80 ± 0.14	2.43	20.6	20.1	19.4
10180	3:32:17.37	-27:45:29.12	20.52 ± 0.06	1.55	19.5	18.9	18.7
2158	3:32:17.38	-27:49:20.72	16.01 ± 0.00	0.39	16.2	15.8	15.8
21100	3:32:17.40	-27:49:39.41	21.30 ± 0.09	0.40	0.0	0.0	0.0
16193	3:32:17.43	-27:48:05.22	18.10 ± 0.01	0.70	17.6	17.6	17.3
10166	3:32:17.45	-27:45:18.19	21.50 ± 0.13	0.77	20.6	20.6	20.3
10203	3:32:17.45	-27:45:44.47	21.96 ± 0.13	0.78	20.9	21.1	20.7
169	3:32:17.45	-27:48:38.27	20.42 ± 0.12	0.84	20.0	20.1	19.8

id	RA(J2000)	DEC(J2000)	K_s	z_{phot}	[3.6]	[4.5]	[5.8]
21118	3:32:17.45	-27:49:50.25	21.91 ± 0.12	1.46	20.5	19.9	20.0
21138	3:32:17.45	-27:50:03.20	19.16 ± 0.02	1.41	17.7	17.1	17.0
1053	3:32:17.48	-27:44:15.26	19.49 ± 0.03	0.53	19.4	19.2	19.0
1085	3:32:17.49	-27:44:36.85	18.30 ± 0.01	0.72	17.7	17.9	17.4
10179	3:32:17.49	-27:45:28.28	19.36 ± 0.02	0.81	18.4	18.6	18.2
105	3:32:17.50	-27:46:14.05	19.93 ± 0.04	0.82	18.7	18.7	18.3
10111	3:32:17.51	-27:44:46.47	21.10 ± 0.06	1.20	19.8	19.6	19.7
16134	3:32:17.52	-27:47:27.94	20.23 ± 0.07	0.81	19.6	19.8	19.4
1033	3:32:17.55	-27:44:05.36	21.96 ± 0.14	0.88	21.1	21.1	20.8
21105	3:32:17.56	-27:49:41.05	20.31 ± 0.03	0.20	0.0	0.0	0.0
1056	3:32:17.58	-27:44:18.33	21.89 ± 0.12	1.52	20.5	19.8	19.7
10233	3:32:17.58	-27:46:03.36	21.72 ± 0.13	2.16	20.1	19.6	19.0
1698	3:32:17.58	-27:47:09.01	20.35 ± 0.07	0.72	19.6	19.6	19.2
10252	3:32:17.59	-27:44:00.08	21.60 ± 0.14	2.49	20.0	19.4	18.6
10215	3:32:17.59	-27:45:51.75	19.61 ± 0.02	2.08	17.7	16.9	16.2
21131	3:32:17.59	-27:49:56.47	20.59 ± 0.04	1.47	19.3	18.8	18.7
16205	3:32:17.61	-27:48:11.52	18.61 ± 0.02	0.76	17.6	17.6	17.2
21178	3:32:17.61	-27:50:26.65	21.10 ± 0.07	1.03	20.3	20.1	20.1
1624	3:32:17.65	-27:48:30.46	20.86 ± 0.13	1.14	20.0	19.7	19.7
1691	3:32:17.70	-27:47:02.85	21.37 ± 0.11	0.10	21.1	21.1	21.3
10208	3:32:17.73	-27:45:47.75	19.41 ± 0.02	0.68	18.9	19.0	18.7
10239	3:32:17.74	-27:43:46.22	20.84 ± 0.11	0.84	20.2	20.2	19.9
10232	3:32:17.74	-27:46:03.29	20.17 ± 0.03	0.89	19.0	19.0	18.8
1645	3:32:17.74	-27:46:40.23	20.55 ± 0.06	1.42	19.2	18.7	18.7
16109	3:32:17.75	-27:47:14.86	17.65 ± 0.01	0.72	17.3	17.3	17.0
1640	3:32:17.77	-27:48:23.85	20.41 ± 0.08	0.56	20.4	20.3	20.3
10121	3:32:17.79	-27:44:50.97	21.61 ± 0.12	1.46	20.5	19.9	20.0
2176	3:32:17.79	-27:49:26.32	18.60 ± 0.01	0.53	18.6	18.4	18.2
2138	3:32:17.80	-27:50:52.93	19.75 ± 0.02	1.33	17.9	17.4	17.5
2157	3:32:17.82	-27:49:16.02	20.94 ± 0.06	0.96	20.1	20.1	19.9
2123	3:32:17.85	-27:50:59.40	15.08 ± 0.00	0.42	15.4	15.0	14.9
2142	3:32:17.86	-27:50:50.22	20.17 ± 0.03	0.40	0.0	0.0	0.0
10194	3:32:17.88	-27:45:36.24	20.79 ± 0.06	0.51	20.6	20.4	20.3
16233	3:32:17.88	-27:46:21.19	21.03 ± 0.15	0.75	20.1	20.2	19.9
16177	3:32:17.92	-27:47:54.98	21.94 ± 0.21	1.19	20.7	20.3	20.3
16110	3:32:17.93	-27:47:21.51	16.65 ± 0.00	0.71	16.0	16.1	15.7
1644	3:32:17.94	-27:46:39.56	21.15 ± 0.12	1.77	19.3	18.5	18.0
2181	3:32:17.94	-27:49:30.14	21.98 ± 0.11	0.32	0.0	0.0	0.0
10154	3:32:17.95	-27:45:12.86	21.44 ± 0.12	3.97	20.1	19.3	18.6
21193	3:32:17.97	-27:50:32.44	21.17 ± 0.09	0.52	20.9	20.7	20.6
1077	3:32:17.98	-27:44:31.40	19.79 ± 0.03	1.14	18.6	18.2	18.2
2130	3:32:17.98	-27:50:52.74	21.23 ± 0.07	3.19	19.1	18.1	17.4
16115	3:32:18.00	-27:47:18.47	15.78 ± 0.00	0.72	15.2	15.1	14.9
21218	3:32:18.01	-27:48:50.19	21.35 ± 0.08	0.32	0.0	0.0	0.0
21117	3:32:18.03	-27:49:53.12	16.74 ± 0.00	0.70	15.8	15.9	15.5
10171	3:32:18.06	-27:45:18.86	21.72 ± 0.12	3.65	20.5	19.6	19.0
10109	3:32:18.07	-27:44:33.50	20.34 ± 0.03	0.61	19.3	19.2	19.1
10126	3:32:18.10	-27:44:55.21	21.33 ± 0.10	1.56	20.1	19.5	19.2
21109	3:32:18.11	-27:49:41.91	21.76 ± 0.10	0.69	21.0	21.0	20.8
1620	3:32:18.13	-27:48:33.40	21.27 ± 0.19	2.24	20.2	19.6	19.0
21235	3:32:18.13	-27:49:00.64	21.57 ± 0.10	1.00	20.5	20.3	20.4
1043	3:32:18.18	-27:44:09.89	21.82 ± 0.12	0.86	21.1	21.1	20.9
16221	3:32:18.19	-27:46:16.40	20.53 ± 0.09	1.41	19.2	18.7	18.7
1680	3:32:18.19	-27:47:02.59	21.74 ± 0.14	0.81	20.9	21.0	20.6
10110	3:32:18.20	-27:44:31.19	20.31 ± 0.04	0.70	19.5	19.6	19.3
1066	3:32:18.20	-27:44:22.06	21.50 ± 0.08	0.70	20.5	20.6	20.2
16237	3:32:18.20	-27:46:21.78	20.15 ± 0.06	1.42	18.8	18.3	18.2
1699	3:32:18.21	-27:47:08.98	19.71 ± 0.04	1.18	18.4	18.1	18.1
16152	3:32:18.22	-27:47:43.87	20.49 ± 0.07	0.59	19.9	19.9	19.7
16194	3:32:18.30	-27:48:04.81	19.71 ± 0.03	0.79	18.7	18.8	18.3
2140	3:32:18.31	-27:50:55.28	18.58 ± 0.01	1.52	17.3	16.6	16.5
16162	3:32:18.33	-27:47:47.81	21.16 ± 0.11	0.52	20.9	20.7	20.6
1016	3:32:18.36	-27:46:06.83	21.74 ± 0.13	0.78	20.7	20.9	20.5
21121	3:32:18.36	-27:49:52.05	21.73 ± 0.10	0.99	20.7	20.5	20.5
2195	3:32:18.36	-27:49:37.36	19.51 ± 0.02	0.59	18.8	18.8	18.6

id	RA(J2000)	DEC(J2000)	K_s	z_{phot}	[3.6]	[4.5]	[5.8]
21224	3:32:18.37	-27:49:03.04	19.17 ± 0.02	0.10	0.0	0.0	0.0
10138	3:32:18.40	-27:45:04.30	20.63 ± 0.08	3.18	19.4	18.6	18.0
16180	3:32:18.42	-27:47:56.96	20.25 ± 0.06	0.98	19.4	19.2	19.2
10177	3:32:18.43	-27:45:36.59	17.00 ± 0.00	0.60	16.4	16.5	16.2
1012	3:32:18.44	-27:45:56.05	17.43 ± 0.00	0.60	16.9	16.8	16.7
108	3:32:18.47	-27:46:09.69	20.73 ± 0.06	0.91	19.9	19.9	19.6
1650	3:32:18.52	-27:46:42.04	20.15 ± 0.04	0.56	19.6	19.6	19.4
21128	3:32:18.52	-27:49:57.87	17.53 ± 0.01	0.71	16.8	16.9	16.6
2152	3:32:18.52	-27:49:13.84	20.41 ± 0.05	1.10	19.4	19.1	19.2
1617	3:32:18.53	-27:48:34.07	19.65 ± 0.06	1.10	18.8	18.6	18.6
21177	3:32:18.53	-27:50:28.27	21.22 ± 0.08	1.72	19.9	19.2	19.0
1619	3:32:18.54	-27:48:30.99	20.20 ± 0.09	1.45	19.3	18.8	18.8
16225	3:32:18.56	-27:46:19.08	20.68 ± 0.10	1.06	19.6	19.3	19.4
1659	3:32:18.58	-27:46:48.99	19.27 ± 0.03	0.76	18.4	18.5	18.1
1685	3:32:18.60	-27:47:05.11	20.22 ± 0.06	1.01	19.2	18.9	18.9
16148	3:32:18.67	-27:47:41.46	20.22 ± 0.07	0.60	20.0	20.0	19.8
2153	3:32:18.68	-27:49:15.70	21.26 ± 0.07	0.69	20.5	20.6	20.3
2162	3:32:18.69	-27:49:19.98	18.64 ± 0.01	1.00	17.6	17.3	17.3
21172	3:32:18.69	-27:50:23.92	21.43 ± 0.10	0.58	21.3	21.3	21.2
1047	3:32:18.70	-27:44:12.77	18.73 ± 0.01	0.81	18.0	18.1	17.7
2186	3:32:18.71	-27:49:31.78	21.45 ± 0.09	0.90	20.6	20.6	20.4
10249	3:32:18.72	-27:43:51.65	20.59 ± 0.06	1.40	19.2	18.7	18.8
10129	3:32:18.73	-27:44:58.78	20.90 ± 0.07	0.52	0.0	0.0	0.0
10160	3:32:18.73	-27:45:14.35	20.77 ± 0.05	0.52	0.0	0.0	0.0
1622	3:32:18.73	-27:48:34.03	19.78 ± 0.06	0.53	0.0	0.0	0.0
1046	3:32:18.74	-27:44:15.84	17.80 ± 0.01	0.60	17.3	17.3	17.1
16246	3:32:18.74	-27:46:27.27	19.01 ± 0.03	1.46	17.9	17.3	17.4
16226	3:32:18.75	-27:46:19.20	21.35 ± 0.17	0.95	19.9	19.7	19.5
1618	3:32:18.76	-27:48:28.92	21.88 ± 0.19	0.86	21.0	21.2	20.7
1637	3:32:18.77	-27:48:20.76	21.11 ± 0.12	0.98	20.4	20.2	20.2
10106	3:32:18.78	-27:44:44.21	20.93 ± 0.07	2.40	19.7	19.1	18.5
16149	3:32:18.78	-27:47:44.42	18.68 ± 0.01	0.73	17.9	18.0	17.6
21119	3:32:18.78	-27:49:51.19	21.45 ± 0.10	1.31	20.3	20.0	20.0
21245	3:32:18.80	-27:49:09.89	20.00 ± 0.04	0.60	19.6	19.7	19.5
10175	3:32:18.84	-27:45:29.19	15.83 ± 0.00	0.50	15.6	15.4	15.3
16137	3:32:18.84	-27:47:34.27	18.60 ± 0.01	0.69	17.6	17.8	17.4
21107	3:32:18.89	-27:49:41.74	21.28 ± 0.08	1.67	20.0	19.4	19.1
2180	3:32:18.92	-27:49:29.40	20.58 ± 0.04	0.48	0.0	0.0	0.0
16185	3:32:18.93	-27:47:58.48	20.50 ± 0.06	0.93	19.7	19.7	19.5
21209	3:32:18.93	-27:48:44.33	21.79 ± 0.18	0.61	21.0	21.1	20.9
16175	3:32:18.97	-27:47:55.18	19.98 ± 0.05	0.79	19.5	19.7	19.2
16119	3:32:18.99	-27:47:18.26	21.40 ± 0.11	0.60	20.5	20.5	20.4
1045	3:32:19.00	-27:44:11.92	19.38 ± 0.03	0.92	18.5	18.4	18.2
21251	3:32:19.00	-27:49:11.24	21.78 ± 0.10	0.64	20.8	20.8	20.7
10148	3:32:19.02	-27:45:10.37	20.21 ± 0.03	0.70	19.5	19.6	19.3
10216	3:32:19.03	-27:45:53.07	19.84 ± 0.02	0.57	18.9	18.7	18.5
10243	3:32:19.04	-27:43:52.95	19.15 ± 0.02	0.58	18.6	18.6	18.5
1075	3:32:19.05	-27:44:29.81	20.92 ± 0.06	0.89	0.0	0.0	0.0
1099	3:32:19.08	-27:44:39.02	21.30 ± 0.08	2.81	20.2	19.6	19.1
1654	3:32:19.08	-27:46:45.05	21.56 ± 0.15	0.89	20.6	20.6	20.3
21184	3:32:19.09	-27:50:32.55	20.06 ± 0.03	0.99	18.9	18.7	18.7
16186	3:32:19.12	-27:47:59.71	19.02 ± 0.03	1.67*	0.0	0.0	0.0
10107	3:32:19.19	-27:44:46.31	18.34 ± 0.01	0.18*	0.0	0.0	0.0
10144	3:32:19.20	-27:45:07.43	20.88 ± 0.07	0.65	20.3	20.3	20.1
10118	3:32:19.21	-27:44:50.68	19.23 ± 0.02	0.90	18.3	18.1	17.9
16245	3:32:19.22	-27:46:32.24	17.51 ± 0.01	0.70	16.9	17.0	16.7
2191	3:32:19.23	-27:49:34.25	21.62 ± 0.08	1.00	20.5	20.3	20.4
21190	3:32:19.23	-27:50:33.97	21.60 ± 0.09	1.00	20.6	20.4	20.4
1627	3:32:19.25	-27:48:30.18	18.66 ± 0.02	0.49	0.0	0.0	0.0
1090	3:32:19.26	-27:44:38.89	19.82 ± 0.03	0.52	0.0	0.0	0.0
21232	3:32:19.26	-27:48:56.10	18.82 ± 0.01	0.58	17.9	17.9	17.7
10155	3:32:19.31	-27:45:13.96	19.24 ± 0.02	0.62	18.7	18.7	18.5
1672	3:32:19.33	-27:47:01.04	19.00 ± 0.02	1.10	17.9	17.6	17.6
16164	3:32:19.34	-27:47:48.84	21.69 ± 0.17	0.48	0.0	0.0	0.0
1040	3:32:19.35	-27:44:09.07	20.43 ± 0.05	0.95	19.8	19.6	19.6

id	RA(J2000)	DEC(J2000)	K_s	z_{phot}	[3.6]	[4.5]	[5.8]
1067	3:32:19.35	-27:44:22.68	21.88 ± 0.14	2.23	20.4	19.9	19.4
16114	3:32:19.35	-27:47:16.06	19.76 ± 0.04	1.00	18.7	18.4	18.4
16133	3:32:19.39	-27:47:28.25	21.59 ± 0.13	3.49	20.4	19.6	19.1
16102	3:32:19.41	-27:47:09.59	21.90 ± 0.29	1.32	20.8	20.4	20.4
21188	3:32:19.41	-27:50:33.76	21.53 ± 0.08	0.59	20.8	20.8	20.7
2171	3:32:19.43	-27:49:25.86	20.33 ± 0.04	0.59	19.7	19.8	19.6
2172	3:32:19.43	-27:49:28.25	20.54 ± 0.04	0.97	19.4	19.1	19.1
21242	3:32:19.48	-27:49:06.96	21.00 ± 0.05	0.97	19.9	19.7	19.7
21223	3:32:19.50	-27:48:56.08	20.36 ± 0.05	1.63	19.3	18.7	18.5
21181	3:32:19.53	-27:50:30.95	20.58 ± 0.04	0.10	20.3	20.3	20.4
16219	3:32:19.55	-27:46:16.28	19.67 ± 0.05	0.86	19.0	19.1	18.8
1684	3:32:19.56	-27:47:05.07	20.19 ± 0.06	0.73	19.6	19.7	19.3
1054	3:32:19.58	-27:44:17.21	21.48 ± 0.10	0.39	21.4	21.0	21.0
1674	3:32:19.58	-27:46:53.12	20.27 ± 0.05	0.80	19.3	19.5	19.0
1628	3:32:19.60	-27:48:30.70	19.18 ± 0.03	0.71	18.9	19.1	18.8
1083	3:32:19.61	-27:44:34.59	21.08 ± 0.10	0.82	20.5	20.5	20.3
21124	3:32:19.65	-27:49:55.63	21.60 ± 0.09	0.10	21.6	21.5	21.6
10230	3:32:19.67	-27:46:02.08	20.81 ± 0.06	0.64*	0.0	0.0	0.0
16213	3:32:19.68	-27:48:09.69	21.97 ± 0.19	0.97	20.8	20.6	20.7
21167	3:32:19.68	-27:50:23.43	17.70 ± 0.00	0.59	17.1	17.1	16.9
212	3:32:19.70	-27:51:10.35	21.79 ± 0.16	0.21	21.5	21.5	21.7
16141	3:32:19.71	-27:47:31.46	21.09 ± 0.14	1.41	20.0	19.6	19.6
21160	3:32:19.71	-27:50:16.04	21.70 ± 0.12	1.21	20.4	19.9	19.9
10136	3:32:19.75	-27:45:02.83	21.88 ± 0.14	0.76	21.0	21.0	20.8
214	3:32:19.75	-27:51:13.02	21.79 ± 0.27	0.32	21.9	21.7	21.8
16214	3:32:19.77	-27:46:10.00	19.72 ± 0.06	1.21	18.4	18.1	18.2
10167	3:32:19.80	-27:45:18.74	21.41 ± 0.09	2.91	19.6	19.0	18.3
1014	3:32:19.80	-27:46:10.40	19.46 ± 0.04	2.07	18.1	17.4	16.8
162	3:32:19.80	-27:48:39.22	20.57 ± 0.10	1.08	19.4	19.1	19.2
10162	3:32:19.82	-27:45:14.85	21.62 ± 0.10	0.10	21.3	21.3	21.5
16122	3:32:19.85	-27:47:21.13	18.12 ± 0.01	0.71	17.1	17.3	16.8
21123	3:32:19.85	-27:49:54.10	20.74 ± 0.06	1.55	19.7	19.1	18.9
10169	3:32:19.89	-27:45:17.88	20.92 ± 0.07	1.32	19.8	19.5	19.5
1633	3:32:19.89	-27:48:22.09	21.38 ± 0.15	0.98	21.0	20.8	20.7
1626	3:32:19.93	-27:48:31.14	18.29 ± 0.01	0.60	17.5	17.5	17.3
10113	3:32:19.96	-27:44:49.77	19.69 ± 0.03	0.71	19.1	19.3	18.9
2141	3:32:19.97	-27:50:52.67	20.19 ± 0.04	1.10	19.3	19.1	19.2
10209	3:32:19.98	-27:45:47.64	21.40 ± 0.09	1.06	20.6	20.3	20.4
21142	3:32:19.98	-27:50:05.16	19.54 ± 0.02	0.69	18.7	18.8	18.5
2185	3:32:19.99	-27:49:30.83	21.65 ± 0.10	0.99	20.7	20.5	20.5
21198	3:32:20.00	-27:50:39.89	21.09 ± 0.07	0.69	20.4	20.6	20.3
16255	3:32:20.04	-27:46:31.83	21.14 ± 0.10	0.50	20.7	20.5	20.4
10112	3:32:20.05	-27:44:47.21	19.95 ± 0.03	2.08	18.2	17.5	16.9
164	3:32:20.07	-27:48:39.41	20.54 ± 0.12	0.68	19.9	20.0	19.8
2197	3:32:20.09	-27:49:37.46	21.37 ± 0.09	0.75	20.4	20.4	20.1
1063	3:32:20.11	-27:44:22.51	18.72 ± 0.01	1.12	17.5	17.2	17.0
21150	3:32:20.13	-27:50:08.87	19.58 ± 0.02	0.50	19.5	19.3	19.3
21210	3:32:20.14	-27:48:44.65	21.75 ± 0.16	2.60	20.3	19.7	19.1
10125	3:32:20.16	-27:44:53.63	21.38 ± 0.10	0.63	0.0	0.0	0.0
16207	3:32:20.16	-27:48:14.76	21.78 ± 0.22	1.36	20.8	20.3	20.4
10248	3:32:20.18	-27:43:56.30	21.97 ± 0.14	1.29	20.7	20.4	20.6
1091	3:32:20.22	-27:44:39.24	20.57 ± 0.07	2.02	19.3	18.7	18.2
21214	3:32:20.22	-27:48:50.54	17.06 ± 0.00	0.60	16.5	16.5	16.3
21157	3:32:20.23	-27:50:13.90	21.38 ± 0.11	2.21	20.5	20.0	19.5
16212	3:32:20.24	-27:48:18.48	17.34 ± 0.01	0.71	16.5	16.7	16.2
16229	3:32:20.26	-27:46:20.56	20.60 ± 0.09	1.31	0.0	0.0	0.0
2137	3:32:20.26	-27:50:50.02	21.10 ± 0.10	3.26	20.1	19.3	18.7
16118	3:32:20.27	-27:47:18.11	20.91 ± 0.08	0.80	20.0	20.2	19.8
1011	3:32:20.30	-27:45:54.46	17.79 ± 0.01	0.52	17.8	17.7	17.6
16166	3:32:20.42	-27:47:48.95	21.66 ± 0.16	2.44	20.2	19.7	19.1
16224	3:32:20.43	-27:46:16.68	21.98 ± 0.22	1.28	21.8	21.4	21.5
2154	3:32:20.43	-27:49:14.32	20.50 ± 0.04	0.59	19.9	19.9	19.8
1669	3:32:20.44	-27:46:59.68	21.58 ± 0.17	0.84	21.1	21.2	20.9
2199	3:32:20.44	-27:49:35.95	21.57 ± 0.09	0.79	20.6	20.7	20.3
10159	3:32:20.45	-27:45:14.32	21.69 ± 0.13	0.59	21.1	20.9	20.9

id	RA(J2000)	DEC(J2000)	K_s	z_{phot}	[3.6]	[4.5]	[5.8]
10240	3:32:20.46	-27:43:55.03	19.02 ± 0.02	0.59	18.4	18.3	18.2
16135	3:32:20.46	-27:47:32.27	17.87 ± 0.01	0.60	17.5	17.5	17.4
16184	3:32:20.47	-27:47:58.17	21.81 ± 0.19	3.76	20.1	19.2	18.5
16191	3:32:20.47	-27:48:00.34	20.43 ± 0.08	0.69	19.7	19.8	19.4
1625	3:32:20.47	-27:48:29.19	18.68 ± 0.02	0.95	17.9	17.6	17.5
16160	3:32:20.49	-27:47:46.12	21.65 ± 0.18	0.80	20.9	20.8	20.6
2177	3:32:20.50	-27:49:27.04	21.77 ± 0.12	0.91	20.8	20.9	20.7
1028	3:32:20.51	-27:44:04.56	21.00 ± 0.09	0.31	20.7	20.4	20.5
10210	3:32:20.51	-27:45:47.88	21.56 ± 0.11	1.13	20.4	20.2	20.2
21173	3:32:20.53	-27:50:23.62	21.24 ± 0.09	0.41	0.0	0.0	0.0
106	3:32:20.59	-27:46:10.79	21.70 ± 0.21	0.83	21.1	21.2	20.9
21132	3:32:20.60	-27:49:57.19	21.73 ± 0.11	0.86	21.2	21.2	21.0
10140	3:32:20.62	-27:45:07.12	17.85 ± 0.01	0.53	0.0	0.0	0.0
16113	3:32:20.63	-27:47:16.84	18.12 ± 0.01	0.72	17.5	17.6	17.3
16100	3:32:20.65	-27:47:08.63	21.16 ± 0.12	2.44	19.7	19.2	18.5
1682	3:32:20.66	-27:47:01.49	21.15 ± 0.10	0.58	20.6	20.5	20.5
21216	3:32:20.66	-27:48:48.90	21.29 ± 0.11	0.10	21.2	21.2	21.4
10103	3:32:20.67	-27:44:46.34	18.00 ± 0.01	0.59	17.4	17.4	17.2
16124	3:32:20.68	-27:47:21.44	21.93 ± 0.19	0.62	22.0	21.9	21.8
21168	3:32:20.70	-27:50:22.08	20.98 ± 0.06	0.93	20.3	20.3	20.0
16248	3:32:20.72	-27:46:24.31	21.64 ± 0.17	0.99	20.4	20.2	20.2
2196	3:32:20.72	-27:49:32.61	20.31 ± 0.03	0.90	19.1	19.0	18.8
10123	3:32:20.73	-27:44:53.79	17.77 ± 0.01	0.71	17.0	17.1	16.8
165	3:32:20.77	-27:48:36.88	21.39 ± 0.20	3.43	19.9	19.0	18.4
1629	3:32:20.82	-27:48:22.48	21.56 ± 0.15	0.10	21.3	21.3	21.4
21170	3:32:20.83	-27:50:25.72	20.61 ± 0.05	0.62	19.9	20.0	19.8
21197	3:32:20.84	-27:50:38.82	21.41 ± 0.09	3.32	20.0	19.2	18.7
21112	3:32:20.85	-27:49:40.95	21.88 ± 0.19	0.98	20.9	20.6	20.5
1069	3:32:20.88	-27:44:23.05	21.89 ± 0.16	0.81	0.0	0.0	0.0
1683	3:32:20.91	-27:47:05.58	16.70 ± 0.01	0.60	16.1	16.0	15.8
10235	3:32:20.94	-27:43:46.29	21.91 ± 0.20	3.50	20.8	20.1	19.6
1675	3:32:20.94	-27:47:01.28	21.13 ± 0.10	0.78	20.1	20.2	19.8
21171	3:32:20.94	-27:50:27.51	21.22 ± 0.06	0.87	20.2	20.2	19.9
1058	3:32:20.96	-27:44:03.18	21.36 ± 0.09	2.13	19.8	19.2	18.7
16241	3:32:20.96	-27:46:25.34	21.56 ± 0.17	1.55	19.9	19.2	19.1
16252	3:32:20.99	-27:46:27.98	20.02 ± 0.06	0.99	19.1	18.8	18.8
21169	3:32:20.99	-27:50:23.56	20.72 ± 0.10	3.19	19.9	19.1	18.5
2182	3:32:21.04	-27:49:28.83	20.75 ± 0.05	0.64	20.0	20.1	19.9
16155	3:32:21.10	-27:47:44.33	20.24 ± 0.07	0.76	19.8	19.8	19.6
21115	3:32:21.10	-27:49:50.92	19.20 ± 0.02	0.76	18.6	18.7	18.4
2121	3:32:21.13	-27:51:02.21	19.20 ± 0.02	0.69	18.7	18.8	18.5
10149	3:32:21.14	-27:45:10.72	20.18 ± 0.04	0.62	19.7	19.7	19.5
16130	3:32:21.14	-27:47:25.85	21.33 ± 0.13	1.95	20.0	19.4	19.0
2173	3:32:21.14	-27:49:25.67	21.73 ± 0.11	0.67	20.9	20.9	20.8
16244	3:32:21.21	-27:46:25.89	20.80 ± 0.10	1.04	19.9	19.6	19.7
10101	3:32:21.23	-27:44:42.96	21.83 ± 0.14	0.10	0.0	0.0	0.0
16183	3:32:21.24	-27:47:57.44	21.79 ± 0.19	0.69	21.1	21.2	20.9
10201	3:32:21.25	-27:45:35.92	20.89 ± 0.05	1.67	19.3	18.7	18.4
1024	3:32:21.25	-27:46:02.60	21.88 ± 0.14	0.98	21.2	20.9	20.9
1076	3:32:21.26	-27:44:35.56	16.11 ± 0.00	0.51	16.1	15.7	15.7
2183	3:32:21.26	-27:49:29.54	20.90 ± 0.06	0.73	20.2	20.4	20.0
10218	3:32:21.27	-27:45:54.69	20.46 ± 0.06	1.36	19.7	19.3	19.4
2112	3:32:21.27	-27:51:06.60	19.99 ± 0.03	0.69	19.2	19.3	19.0
2122	3:32:21.29	-27:51:01.52	19.93 ± 0.03	1.57	18.5	17.9	17.6
1638	3:32:21.32	-27:48:24.66	21.03 ± 0.18	1.88	19.6	19.0	18.6
1663	3:32:21.34	-27:46:55.03	21.28 ± 0.15	0.98	21.0	20.8	20.8
21163	3:32:21.34	-27:50:19.39	21.61 ± 0.12	0.43	0.0	0.0	0.0
10213	3:32:21.38	-27:45:50.63	21.47 ± 0.10	1.00	20.7	20.4	20.4
10202	3:32:21.40	-27:45:36.16	19.28 ± 0.02	2.22	18.2	17.7	17.2
2179	3:32:21.41	-27:49:29.64	21.87 ± 0.12	0.61	0.0	0.0	0.0
1670	3:32:21.42	-27:46:59.46	21.93 ± 0.26	1.46	21.2	20.6	20.7
21234	3:32:21.42	-27:49:01.85	19.12 ± 0.01	0.80	18.4	18.4	18.2
10134	3:32:21.43	-27:45:02.48	20.17 ± 0.04	0.60	19.7	19.8	19.6
21114	3:32:21.43	-27:49:48.69	21.22 ± 0.10	0.86	20.6	20.6	20.4
10222	3:32:21.49	-27:45:56.96	21.70 ± 0.15	1.32	21.3	21.0	21.2

id	RA(J2000)	DEC(J2000)	K_s	z_{phot}	[3.6]	[4.5]	[5.8]
1049	3:32:21.51	-27:44:15.43	21.91 ± 0.21	2.95	20.4	19.8	19.3
21239	3:32:21.53	-27:49:05.83	19.94 ± 0.03	0.80	19.2	19.2	19.0
21201	3:32:21.53	-27:50:40.57	20.71 ± 0.07	1.42	19.8	19.3	19.3
216	3:32:21.54	-27:51:08.53	21.75 ± 0.20	1.32	20.4	19.9	20.0
10147	3:32:21.55	-27:45:08.86	21.96 ± 0.16	0.82	21.3	21.3	21.1
21106	3:32:21.57	-27:49:41.71	19.75 ± 0.02	0.92	18.6	18.5	18.4
1666	3:32:21.58	-27:46:56.85	21.26 ± 0.14	0.91	20.1	20.2	19.7
16202	3:32:21.61	-27:48:10.40	21.62 ± 0.21	1.17	20.9	20.6	20.6
16201	3:32:21.62	-27:48:08.88	21.11 ± 0.13	0.74	20.3	20.3	20.1
1038	3:32:21.64	-27:44:11.20	19.31 ± 0.03	0.49	0.0	0.0	0.0
2136	3:32:21.64	-27:50:52.23	19.91 ± 0.03	0.91	19.2	19.2	19.0
1661	3:32:21.68	-27:46:50.50	20.52 ± 0.08	0.91	19.6	19.6	19.4
16138	3:32:21.69	-27:47:34.07	21.32 ± 0.17	1.93	20.0	19.4	19.0
21183	3:32:21.71	-27:50:31.57	20.03 ± 0.04	0.63	19.5	19.5	19.3
10182	3:32:21.72	-27:45:29.15	21.04 ± 0.09	2.45	19.6	19.1	18.5
1097	3:32:21.75	-27:44:42.10	18.44 ± 0.01	0.50	18.3	18.1	17.9
16128	3:32:21.75	-27:47:24.48	19.35 ± 0.04	0.91	18.3	18.3	17.9
168	3:32:21.83	-27:48:35.03	21.42 ± 0.28	2.45	20.1	19.6	19.0
1086	3:32:21.85	-27:44:34.53	21.68 ± 0.14	3.79	20.6	20.0	19.4
16104	3:32:21.89	-27:47:08.20	21.57 ± 0.19	0.76	20.7	20.7	20.5
21231	3:32:21.95	-27:48:55.63	20.65 ± 0.05	0.43	0.0	0.0	0.0
1651	3:32:21.96	-27:46:42.75	21.85 ± 0.33	0.81	21.4	21.6	21.2
10199	3:32:21.97	-27:45:42.18	21.19 ± 0.11	2.87	20.3	19.7	19.2
1664	3:32:21.97	-27:46:55.94	17.07 ± 0.01	0.74	16.5	16.7	16.2
213	3:32:21.98	-27:51:11.92	20.96 ± 0.09	1.32	19.1	18.6	18.5
16169	3:32:21.99	-27:47:50.35	21.75 ± 0.26	0.10	0.0	0.0	0.0
21244	3:32:22.03	-27:49:07.67	21.65 ± 0.13	0.48	21.7	21.4	21.4
1042	3:32:22.06	-27:44:10.09	21.89 ± 0.14	0.10	21.9	21.8	21.9
21220	3:32:22.07	-27:48:51.40	21.54 ± 0.20	0.73	20.6	20.6	20.3
21104	3:32:22.08	-27:49:40.02	21.47 ± 0.07	0.85	20.5	20.5	20.2
2145	3:32:22.10	-27:50:52.32	20.44 ± 0.07	1.72	19.4	18.8	18.5
16198	3:32:22.11	-27:48:06.62	21.81 ± 0.23	0.52	0.0	0.0	0.0
2128	3:32:22.12	-27:51:01.78	18.39 ± 0.01	0.72	17.5	17.6	17.2
1098	3:32:22.18	-27:44:40.45	21.62 ± 0.10	0.72	20.8	21.0	20.6
1518	3:32:22.23	-27:48:33.12	20.65 ± 0.09	1.32	19.8	19.4	19.5
21228	3:32:22.24	-27:48:58.29	21.84 ± 0.11	1.45	20.5	20.0	20.0
10219	3:32:22.25	-27:45:50.39	19.64 ± 0.03	0.72	19.0	19.1	18.8
21233	3:32:22.25	-27:49:01.35	20.71 ± 0.05	1.08	19.7	19.4	19.3
21211	3:32:22.28	-27:48:45.18	21.63 ± 0.13	0.82	20.4	20.4	20.1
21247	3:32:22.28	-27:49:09.32	21.53 ± 0.08	1.50	20.0	19.4	19.2
10244	3:32:22.32	-27:43:53.82	21.67 ± 0.18	2.15	20.6	20.1	19.6
1037	3:32:22.32	-27:44:08.69	17.18 ± 0.00	0.58	16.3	16.3	16.2
1020	3:32:22.33	-27:45:59.72	18.88 ± 0.01	0.71	18.2	18.2	17.9
21246	3:32:22.34	-27:49:10.57	21.73 ± 0.17	0.38	0.0	0.0	0.0
1052	3:32:22.35	-27:44:15.91	21.87 ± 0.12	0.71	21.0	21.1	20.8
1572	3:32:22.36	-27:47:25.57	21.37 ± 0.12	1.07	20.5	20.2	20.3
21161	3:32:22.36	-27:50:18.15	19.94 ± 0.03	0.69	19.4	19.4	19.2
15113	3:32:22.37	-27:48:15.56	20.81 ± 0.06	2.96	18.9	18.1	17.4
21230	3:32:22.39	-27:48:58.09	21.54 ± 0.08	1.47	20.3	19.8	19.8
155	3:32:22.42	-27:48:33.71	21.55 ± 0.13	3.35	19.9	19.1	18.5
1543	3:32:22.46	-27:46:55.61	20.39 ± 0.05	0.93	19.9	19.9	19.8
2189	3:32:22.46	-27:49:34.92	17.59 ± 0.01	0.72	17.1	17.2	16.9
1092	3:32:22.47	-27:44:38.50	21.29 ± 0.08	3.46	20.0	19.2	18.7
15106	3:32:22.49	-27:48:04.74	21.25 ± 0.07	2.19	19.9	19.4	18.8
1533	3:32:22.51	-27:48:17.62	20.63 ± 0.05	0.98	20.0	19.8	19.9
10139	3:32:22.52	-27:45:04.71	19.95 ± 0.03	0.60	19.3	19.3	19.1
21116	3:32:22.53	-27:49:49.75	18.10 ± 0.01	0.68	17.5	17.5	17.3
1022	3:32:22.54	-27:46:03.84	20.25 ± 0.03	1.47	19.1	18.5	18.5
15114	3:32:22.54	-27:48:15.15	20.44 ± 0.05	1.44	18.9	18.2	18.1
10195	3:32:22.56	-27:45:38.94	21.05 ± 0.07	1.60	19.1	18.2	17.8
21252	3:32:22.57	-27:49:12.18	20.60 ± 0.04	0.62	19.8	19.9	19.7
1070	3:32:22.58	-27:44:25.93	17.07 ± 0.00	0.68	16.3	16.3	16.0
10207	3:32:22.61	-27:45:46.56	19.46 ± 0.02	0.87	18.5	18.4	18.1
218	3:32:22.62	-27:51:12.44	20.42 ± 0.05	0.99	19.4	19.1	19.1
21158	3:32:22.64	-27:50:15.08	19.02 ± 0.01	0.59	18.2	18.2	18.0

id	RA(J2000)	DEC(J2000)	K_s	z_{phot}	[3.6]	[4.5]	[5.8]
10108	3:32:22.66	-27:44:45.19	21.42 ± 0.07	0.85	20.6	20.5	20.3
1050	3:32:22.66	-27:44:02.99	18.98 ± 0.01	0.48	0.0	0.0	0.0
1061	3:32:22.66	-27:44:21.37	21.95 ± 0.13	1.28*	0.0	0.0	0.0
10226	3:32:22.70	-27:45:54.60	20.87 ± 0.05	0.83	20.0	19.9	19.7
21195	3:32:22.70	-27:50:37.85	21.50 ± 0.11	0.47	21.4	21.0	21.0
10163	3:32:22.71	-27:45:16.61	21.23 ± 0.07	1.41	19.8	19.4	19.4
1581	3:32:22.72	-27:47:37.21	21.65 ± 0.10	0.37	0.0	0.0	0.0
10132	3:32:22.75	-27:44:59.27	21.22 ± 0.07	0.66	20.3	20.3	20.1
1094	3:32:22.78	-27:44:38.90	21.88 ± 0.11	0.40	0.0	0.0	0.0
10185	3:32:22.79	-27:45:28.04	20.68 ± 0.06	2.32	19.0	18.4	17.6
2148	3:32:22.79	-27:50:44.47	21.28 ± 0.08	0.11	21.1	21.1	21.3
10181	3:32:22.80	-27:45:30.00	21.59 ± 0.10	1.48	0.0	0.0	0.0
2190	3:32:22.81	-27:49:34.35	20.40 ± 0.04	0.78	19.7	19.7	19.5
10170	3:32:22.82	-27:45:18.25	20.58 ± 0.05	0.89	19.6	19.6	19.4
2156	3:32:22.82	-27:49:12.79	21.66 ± 0.11	0.69	20.8	20.9	20.6
1093	3:32:22.83	-27:44:37.98	21.85 ± 0.15	0.42	0.0	0.0	0.0
1584	3:32:22.84	-27:47:42.41	21.17 ± 0.08	1.21	19.9	19.5	19.5
1010	3:32:22.86	-27:46:07.20	21.02 ± 0.07	1.80	19.9	19.3	19.0
10143	3:32:22.87	-27:45:07.69	21.08 ± 0.09	0.52	20.7	20.5	20.4
1051	3:32:22.89	-27:44:15.72	21.53 ± 0.10	0.11	0.0	0.0	0.0
1041	3:32:22.91	-27:44:03.36	21.70 ± 0.11	1.21	20.3	19.9	19.9
21227	3:32:22.92	-27:48:57.35	20.22 ± 0.04	1.08	19.1	18.9	19.0
2113	3:32:22.92	-27:51:04.49	19.97 ± 0.03	0.84	19.0	19.0	18.7
15133	3:32:22.94	-27:46:28.41	22.00 ± 0.15	0.79	21.0	21.3	20.7
15121	3:32:22.95	-27:46:17.94	21.46 ± 0.10	1.21	20.0	19.5	19.5
2146	3:32:23.07	-27:50:46.72	21.37 ± 0.10	0.79	20.8	20.9	20.6
10223	3:32:23.08	-27:45:58.00	20.03 ± 0.03	0.53	19.6	19.2	19.1
10145	3:32:23.09	-27:45:09.06	19.62 ± 0.02	0.89	18.5	18.4	18.0
2129	3:32:23.10	-27:50:56.74	21.33 ± 0.11	2.80	19.9	19.2	18.6
21222	3:32:23.11	-27:48:49.39	21.87 ± 0.15	2.32	20.6	20.1	19.5
10100	3:32:23.12	-27:44:42.21	20.06 ± 0.03	2.90	18.9	18.2	17.7
109	3:32:23.14	-27:46:12.40	18.02 ± 0.01	0.71	17.1	17.1	16.8
21165	3:32:23.14	-27:50:21.65	21.11 ± 0.05	0.39	21.0	20.7	20.7
1064	3:32:23.15	-27:44:23.01	18.95 ± 0.01	0.68	18.2	18.2	17.9
10217	3:32:23.15	-27:45:54.58	18.96 ± 0.01	1.08	17.8	17.4	17.3
2110	3:32:23.16	-27:51:06.07	20.83 ± 0.06	2.04	19.1	18.4	17.8
15124	3:32:23.17	-27:46:20.24	21.19 ± 0.07	0.98	20.3	20.1	20.1
2163	3:32:23.17	-27:49:21.44	20.65 ± 0.05	1.01	19.5	19.3	19.3
10141	3:32:23.19	-27:45:06.20	21.99 ± 0.17	0.42	22.0	21.6	21.6
21108	3:32:23.25	-27:49:41.73	21.80 ± 0.12	0.95	20.8	20.7	20.7
2127	3:32:23.25	-27:51:01.68	18.48 ± 0.01	0.90	17.6	17.5	17.3
1587	3:32:23.26	-27:47:42.58	21.28 ± 0.07	1.00	20.2	19.9	19.9
1590	3:32:23.27	-27:47:44.71	21.73 ± 0.09	0.93	20.8	20.8	20.7
2175	3:32:23.28	-27:49:26.14	19.20 ± 0.01	0.97	18.1	17.9	17.9
1080	3:32:23.32	-27:44:32.17	21.25 ± 0.07	1.08	20.1	19.8	19.9
10116	3:32:23.34	-27:44:48.12	21.60 ± 0.12	0.70	20.9	20.9	20.8
21226	3:32:23.34	-27:48:52.57	17.65 ± 0.01	0.48	17.9	17.7	17.6
10246	3:32:23.37	-27:43:56.96	20.91 ± 0.06	0.60	20.3	20.4	20.1
2139	3:32:23.38	-27:50:52.27	20.11 ± 0.03	1.30	19.1	18.7	18.9
21175	3:32:23.42	-27:50:24.82	20.48 ± 0.04	0.52	19.9	19.8	19.6
1556	3:32:23.44	-27:47:09.10	20.55 ± 0.03	1.33	19.5	19.1	19.3
1035	3:32:23.46	-27:44:06.34	21.70 ± 0.14	0.88	21.0	20.9	20.6
107	3:32:23.49	-27:46:12.18	20.51 ± 0.06	0.75	19.8	19.9	19.6
1569	3:32:23.49	-27:47:22.54	21.83 ± 0.10	1.32	21.1	20.7	20.8
1555	3:32:23.52	-27:47:07.67	21.10 ± 0.06	0.84	20.4	20.5	20.3
2116	3:32:23.58	-27:51:01.43	21.62 ± 0.11	3.48	20.2	19.4	18.8
10164	3:32:23.60	-27:45:17.03	21.57 ± 0.10	0.96	20.6	20.6	20.3
10227	3:32:23.60	-27:46:00.98	18.90 ± 0.01	0.99	17.7	17.3	17.3
15140	3:32:23.60	-27:46:37.80	19.79 ± 0.03	0.46	19.9	19.7	19.7
10251	3:32:23.62	-27:43:57.78	21.98 ± 0.15	1.02	21.1	20.9	21.0
2194	3:32:23.64	-27:49:37.80	18.05 ± 0.01	0.60	17.5	17.4	17.2
211	3:32:23.67	-27:51:14.40	21.05 ± 0.13	0.78	19.9	19.9	19.6
1575	3:32:23.69	-27:47:27.66	21.83 ± 0.12	1.07	21.1	20.8	20.9
15137	3:32:23.70	-27:46:32.91	21.18 ± 0.08	1.34	20.1	19.7	19.9
1044	3:32:23.71	-27:44:11.78	19.05 ± 0.02	1.41	17.9	17.4	17.4

id	RA(J2000)	DEC(J2000)	K_s	z_{phot}	[3.6]	[4.5]	[5.8]
15105	3:32:23.71	-27:48:05.51	21.89 ± 0.11	1.21	20.9	20.5	20.6
10198	3:32:23.72	-27:45:35.95	20.85 ± 0.07	0.86	20.2	20.3	20.0
1031	3:32:23.76	-27:44:03.97	21.94 ± 0.12	3.08	20.6	20.0	19.5
21180	3:32:23.76	-27:50:30.64	21.46 ± 0.09	0.10	21.2	21.1	21.3
1060	3:32:23.80	-27:44:21.38	21.25 ± 0.12	0.72	20.6	20.5	20.3
15145	3:32:23.81	-27:46:39.38	20.61 ± 0.03	1.02	19.4	19.1	19.1
217	3:32:23.83	-27:51:10.42	20.93 ± 0.10	0.79	20.3	20.5	20.1
1558	3:32:23.91	-27:47:10.49	19.70 ± 0.02	0.95	19.0	18.8	18.7
1583	3:32:23.92	-27:47:39.41	19.96 ± 0.03	1.39	19.1	18.6	18.6
10238	3:32:23.95	-27:43:49.16	20.10 ± 0.05	1.12	19.0	18.8	18.8
2174	3:32:23.95	-27:49:25.34	21.93 ± 0.10	2.47	20.4	19.9	19.3
1535	3:32:23.96	-27:48:14.69	21.94 ± 0.12	2.13	20.3	19.6	19.1
1512	3:32:23.97	-27:48:30.57	20.97 ± 0.04	1.20	19.6	19.2	19.3
21120	3:32:23.98	-27:49:52.02	21.74 ± 0.11	2.32	20.6	20.2	19.6
21194	3:32:24.00	-27:50:38.84	19.17 ± 0.02	0.91	18.3	18.3	18.1
1039	3:32:24.01	-27:44:08.30	21.52 ± 0.09	2.10	20.1	19.6	19.1
10137	3:32:24.01	-27:45:03.83	20.64 ± 0.06	1.01	19.7	19.5	19.5
21187	3:32:24.02	-27:50:33.49	20.56 ± 0.05	1.39	19.5	19.1	19.1
1032	3:32:24.04	-27:44:05.58	21.16 ± 0.07	1.30	20.2	19.9	20.0
21250	3:32:24.05	-27:49:11.45	18.68 ± 0.01	0.60	17.8	17.8	17.6
10191	3:32:24.08	-27:45:35.00	21.61 ± 0.10	0.52	21.1	21.0	20.8
1018	3:32:24.09	-27:46:03.22	20.30 ± 0.05	1.12	19.4	19.1	19.2
15131	3:32:24.11	-27:46:25.06	21.89 ± 0.12	0.98	21.1	20.9	20.9
21206	3:32:24.13	-27:50:45.92	19.95 ± 0.03	2.50	19.6	19.6	19.4
10228	3:32:24.15	-27:46:00.23	20.64 ± 0.05	0.78	19.9	20.1	19.7
21122	3:32:24.17	-27:49:52.45	20.32 ± 0.05	1.77	19.1	18.5	18.2
10247	3:32:24.19	-27:43:56.31	21.68 ± 0.11	1.53	20.4	19.8	19.6
1079	3:32:24.20	-27:44:26.67	21.16 ± 0.10	1.03	20.4	20.1	20.1
1514	3:32:24.25	-27:48:30.76	20.73 ± 0.05	3.31	19.4	18.3	17.7
10178	3:32:24.29	-27:45:26.74	21.66 ± 0.11	1.31	20.5	20.1	20.2
1570	3:32:24.34	-27:47:24.95	19.31 ± 0.01	0.69	18.9	19.1	18.7
21133	3:32:24.34	-27:49:57.75	21.43 ± 0.10	2.47	20.4	19.9	19.3
10158	3:32:24.35	-27:45:13.80	21.95 ± 0.19	0.60	20.8	20.6	20.6
15128	3:32:24.37	-27:46:24.16	18.62 ± 0.01	0.93	18.1	18.1	17.9
10245	3:32:24.38	-27:43:52.63	21.97 ± 0.17	2.17	20.4	19.8	19.3
21148	3:32:24.38	-27:50:09.16	21.45 ± 0.16	1.28	20.3	19.9	20.0
21207	3:32:24.43	-27:48:44.04	20.74 ± 0.09	1.58	19.6	18.9	18.6
21189	3:32:24.43	-27:50:33.86	21.09 ± 0.08	0.11	21.0	21.0	21.2
21200	3:32:24.43	-27:50:37.64	21.81 ± 0.12	0.63	20.9	20.8	20.7
21143	3:32:24.46	-27:50:04.33	20.77 ± 0.04	2.51	18.4	17.7	16.8
21205	3:32:24.47	-27:50:45.70	19.79 ± 0.03	1.36	18.5	17.9	17.9
21243	3:32:24.52	-27:49:07.99	21.61 ± 0.09	1.59	20.5	19.9	19.7
21154	3:32:24.54	-27:50:10.12	21.22 ± 0.05	1.39	19.9	19.4	19.5
21135	3:32:24.57	-27:49:58.37	21.69 ± 0.12	0.10	0.0	0.0	0.0
10237	3:32:24.59	-27:43:46.92	18.94 ± 0.02	0.52	18.6	18.4	18.3
15123	3:32:24.60	-27:46:20.19	19.18 ± 0.02	1.11	18.0	17.6	17.7
2149	3:32:24.61	-27:48:51.52	17.80 ± 0.01	0.57	17.4	17.2	17.1
1073	3:32:24.62	-27:44:28.44	19.16 ± 0.02	0.62	18.7	18.8	18.6
2114	3:32:24.62	-27:51:01.56	21.87 ± 0.12	1.96	20.6	20.0	19.6
15147	3:32:24.64	-27:46:39.43	20.70 ± 0.04	1.46	19.3	18.6	18.6
10188	3:32:24.65	-27:45:33.40	21.24 ± 0.09	2.40	20.0	19.5	18.9
1087	3:32:24.66	-27:44:36.97	21.56 ± 0.10	1.63	20.0	19.4	19.1
10173	3:32:24.67	-27:45:21.29	20.04 ± 0.04	0.61	19.6	19.5	19.4
10119	3:32:24.72	-27:44:50.23	21.18 ± 0.07	1.67	19.7	19.1	18.9
2187	3:32:24.73	-27:49:31.85	19.94 ± 0.03	0.69	19.3	19.4	19.1
1527	3:32:24.75	-27:48:24.50	20.86 ± 0.04	0.81	20.1	20.3	19.9
15119	3:32:24.79	-27:46:17.82	19.02 ± 0.01	1.20	17.9	17.6	17.7
2169	3:32:24.84	-27:49:24.88	21.94 ± 0.12	1.42	20.8	20.3	20.4
2132	3:32:24.84	-27:50:52.49	20.14 ± 0.03	1.08	18.9	18.6	18.6
2134	3:32:24.84	-27:50:50.05	20.48 ± 0.04	1.58	19.1	18.5	18.2
15142	3:32:24.85	-27:46:36.22	21.28 ± 0.08	1.73	20.3	19.6	19.3
1552	3:32:24.86	-27:47:06.41	17.86 ± 0.00	0.27	18.0	17.8	17.9
1062	3:32:24.90	-27:44:21.39	21.31 ± 0.09	0.99	20.4	20.2	20.3
2166	3:32:24.90	-27:49:23.73	20.58 ± 0.06	2.19	19.6	19.1	18.6
1563	3:32:24.91	-27:47:15.21	20.82 ± 0.04	1.07	19.6	19.3	19.2

id	RA(J2000)	DEC(J2000)	K_s	z_{phot}	[3.6]	[4.5]	[5.8]
10122	3:32:24.92	-27:44:51.56	21.59 ± 0.09	0.41	0.0	0.0	0.0
1529	3:32:24.93	-27:48:14.65	16.69 ± 0.00	0.19	16.8	16.6	16.7
21199	3:32:24.93	-27:50:39.38	21.88 ± 0.10	2.78	20.6	20.0	19.4
21149	3:32:24.95	-27:50:07.95	20.73 ± 0.05	0.90	19.8	19.7	19.6
21166	3:32:24.95	-27:50:20.14	21.16 ± 0.09	1.12	20.0	19.8	19.9
15122	3:32:24.99	-27:46:19.30	21.54 ± 0.08	1.24	20.4	20.0	20.2
10115	3:32:25.02	-27:44:47.64	19.87 ± 0.03	1.48	18.5	17.9	17.8
1566	3:32:25.03	-27:47:18.36	20.63 ± 0.04	1.31	19.5	19.1	19.2
1019	3:32:25.07	-27:46:05.88	19.74 ± 0.03	0.65	19.4	19.5	19.3
1027	3:32:25.08	-27:44:03.31	15.36 ± 0.00	0.50	15.2	15.0	14.8
1071	3:32:25.10	-27:44:25.68	21.82 ± 0.10	1.03	20.7	20.4	20.4
21229	3:32:25.10	-27:48:52.61	18.76 ± 0.01	0.62	17.6	17.6	17.3
21202	3:32:25.10	-27:50:43.12	19.78 ± 0.03	1.04	18.8	18.5	18.6
10151	3:32:25.13	-27:45:11.88	19.95 ± 0.03	0.80	19.0	19.1	18.8
1576	3:32:25.14	-27:47:24.36	20.00 ± 0.03	0.34	0.0	0.0	0.0
21152	3:32:25.19	-27:50:09.30	19.22 ± 0.01	0.91	18.2	18.3	18.1
2124	3:32:25.19	-27:50:59.99	19.79 ± 0.02	0.88	18.9	18.9	18.7
1013	3:32:25.20	-27:46:06.93	20.26 ± 0.04	0.73	19.4	19.5	19.2
1579	3:32:25.20	-27:47:35.31	20.85 ± 0.04	1.00	19.9	19.7	19.8
2198	3:32:25.20	-27:49:38.49	19.42 ± 0.01	0.50	19.0	18.8	18.7
21186	3:32:25.24	-27:50:33.36	19.79 ± 0.03	0.52	19.7	19.6	19.4
10174	3:32:25.25	-27:45:23.88	18.78 ± 0.01	0.70	18.2	18.2	18.0
10183	3:32:25.25	-27:45:28.91	20.91 ± 0.06	1.30	19.7	19.4	19.6
21139	3:32:25.29	-27:50:03.06	21.91 ± 0.13	1.63	20.6	20.0	19.8
10135	3:32:25.34	-27:45:02.74	20.47 ± 0.04	0.91	19.6	19.7	19.5
1055	3:32:25.35	-27:44:18.23	21.07 ± 0.12	0.10	21.0	20.9	21.1
10153	3:32:25.35	-27:45:12.48	21.64 ± 0.14	1.39	20.5	20.0	20.0
10124	3:32:25.36	-27:44:52.42	21.84 ± 0.18	1.01	20.7	20.4	20.3
1095	3:32:25.40	-27:44:37.99	22.00 ± 0.14	0.52	21.5	21.2	21.2
15109	3:32:25.41	-27:46:17.12	18.72 ± 0.01	0.93	17.8	17.8	17.6
1513	3:32:25.42	-27:48:30.28	20.67 ± 0.04	1.39	20.0	19.6	19.6
1517	3:32:25.44	-27:48:28.67	21.23 ± 0.07	1.50	20.4	19.8	19.7
215	3:32:25.54	-27:51:08.22	21.61 ± 0.14	0.93	20.9	20.9	20.7
10184	3:32:25.57	-27:45:28.98	21.93 ± 0.14	0.58	21.1	21.2	21.0
1562	3:32:25.59	-27:47:14.32	20.16 ± 0.02	2.21	18.9	18.3	17.7
21238	3:32:25.65	-27:49:03.13	21.16 ± 0.10	1.75	20.1	19.4	19.1
10221	3:32:25.66	-27:45:55.63	20.58 ± 0.04	0.99	19.7	19.5	19.4
1560	3:32:25.67	-27:47:11.01	21.33 ± 0.07	1.32	20.4	20.0	20.1
1084	3:32:25.68	-27:44:36.38	21.36 ± 0.08	0.69	20.5	20.6	20.3
15115	3:32:25.71	-27:48:17.12	20.39 ± 0.04	2.10	18.3	17.5	16.8
1059	3:32:25.73	-27:44:20.42	21.38 ± 0.11	0.92	20.4	20.3	20.0
15112	3:32:25.73	-27:48:20.56	20.72 ± 0.05	0.34	0.0	0.0	0.0
21101	3:32:25.73	-27:49:36.31	16.63 ± 0.00	0.52	16.4	16.1	16.1
1074	3:32:25.74	-27:44:27.92	21.27 ± 0.09	0.90	20.5	20.4	20.2
10190	3:32:25.74	-27:45:34.98	21.52 ± 0.16	0.10	21.3	21.3	21.5
15127	3:32:25.74	-27:48:14.69	21.11 ± 0.09	3.12	19.8	18.9	18.2
10231	3:32:25.75	-27:43:47.12	18.43 ± 0.02	0.94	17.3	17.1	16.9
1078	3:32:25.75	-27:44:30.95	18.60 ± 0.01	0.61	17.5	17.4	17.2
10114	3:32:25.77	-27:44:47.01	21.72 ± 0.13	1.60	20.5	19.9	19.7
10130	3:32:25.77	-27:44:59.53	19.48 ± 0.02	0.92	18.5	18.5	18.3
10242	3:32:25.78	-27:43:52.23	21.07 ± 0.09	1.26	20.1	19.9	19.9
1088	3:32:25.78	-27:44:34.77	21.62 ± 0.17	0.49	21.6	21.2	21.2
21241	3:32:25.78	-27:49:01.57	19.64 ± 0.02	0.76	18.9	18.9	18.7
10204	3:32:25.81	-27:45:44.75	21.96 ± 0.13	0.92	20.9	20.8	20.6
21162	3:32:25.85	-27:50:19.60	18.72 ± 0.01	0.94	17.7	17.5	17.4
1065	3:32:25.91	-27:44:01.50	19.48 ± 0.02	0.49	0.0	0.0	0.0
10142	3:32:25.92	-27:45:07.04	19.06 ± 0.02	0.21	0.0	0.0	0.0
10161	3:32:25.93	-27:45:14.25	21.24 ± 0.06	0.67	0.0	0.0	0.0
2184	3:32:25.95	-27:49:30.40	21.47 ± 0.08	4.61	19.9	19.4	18.5
2125	3:32:25.95	-27:50:58.73	19.76 ± 0.02	0.60	19.2	19.2	19.0
1593	3:32:25.98	-27:47:51.32	20.47 ± 0.04	1.32	19.5	19.1	19.3
1021	3:32:25.99	-27:46:04.23	20.83 ± 0.05	0.89	19.9	19.8	19.7
21225	3:32:26.04	-27:48:56.04	21.19 ± 0.09	1.03	20.2	20.0	19.9
10186	3:32:26.05	-27:45:29.89	20.47 ± 0.06	0.49	20.2	19.9	19.8
2135	3:32:26.10	-27:50:50.44	21.64 ± 0.11	0.74	20.9	21.0	20.7

id	RA(J2000)	DEC(J2000)	K_s	z_{phot}	[3.6]	[4.5]	[5.8]
1057	3:32:26.12	-27:44:18.88	21.83 ± 0.13	0.61	0.0	0.0	0.0
1521	3:32:26.13	-27:48:26.24	21.97 ± 0.10	0.46	0.0	0.0	0.0
1082	3:32:26.15	-27:44:33.26	21.25 ± 0.07	1.50	20.1	19.6	19.5
152	3:32:26.15	-27:48:42.36	21.46 ± 0.15	0.77	21.0	21.0	20.9
21111	3:32:26.15	-27:49:46.39	19.82 ± 0.02	0.60	19.1	19.1	18.9
1026	3:32:26.17	-27:46:03.73	21.25 ± 0.08	0.99	20.3	20.1	20.2
1081	3:32:26.20	-27:44:26.38	21.18 ± 0.06	0.59	20.5	20.4	20.4
2111	3:32:26.20	-27:51:10.55	17.72 ± 0.01	0.60	16.9	16.8	16.6
10189	3:32:26.21	-27:45:33.50	21.73 ± 0.12	1.12	20.6	20.4	20.5
21147	3:32:26.21	-27:50:08.37	20.56 ± 0.05	1.45	19.3	18.8	18.7
21153	3:32:26.21	-27:50:05.47	19.65 ± 0.03	0.97	18.6	18.3	18.2
10241	3:32:26.22	-27:43:48.29	21.18 ± 0.13	3.35	19.6	18.8	18.2
1588	3:32:26.22	-27:47:42.97	21.99 ± 0.10	0.11	0.0	0.0	0.0
2165	3:32:26.23	-27:49:21.35	21.35 ± 0.10	3.09	20.3	19.7	19.2
10225	3:32:26.26	-27:45:50.75	18.89 ± 0.01	0.91	17.8	17.9	17.6
15143	3:32:26.27	-27:46:33.49	19.29 ± 0.01	0.93	18.6	18.6	18.4
10193	3:32:26.29	-27:45:36.10	18.73 ± 0.01	0.98	17.6	17.4	17.5
2155	3:32:26.29	-27:49:14.94	18.85 ± 0.01	0.50	18.5	18.4	18.2
1564	3:32:26.30	-27:47:17.58	19.71 ± 0.02	0.98	18.9	18.7	18.8
1574	3:32:26.30	-27:47:22.49	20.26 ± 0.03	0.88	19.5	19.5	19.4
1577	3:32:26.33	-27:47:34.48	20.88 ± 0.05	0.79	20.1	20.3	19.9
10156	3:32:26.35	-27:45:14.06	19.86 ± 0.02	1.09	18.8	18.6	18.6
10157	3:32:26.35	-27:45:15.23	19.09 ± 0.02	0.99	18.0	17.7	17.6
10236	3:32:26.39	-27:43:46.49	21.11 ± 0.12	3.44	19.8	19.0	18.4
21237	3:32:26.41	-27:49:01.64	21.54 ± 0.11	0.94	20.6	20.5	20.5
10104	3:32:26.43	-27:44:43.63	19.47 ± 0.02	0.91	17.9	17.8	17.4
2117	3:32:26.43	-27:51:01.63	21.46 ± 0.11	0.53	21.3	21.0	21.0
10211	3:32:26.46	-27:45:47.06	19.69 ± 0.03	0.54	18.9	18.5	18.5
21204	3:32:26.48	-27:50:44.14	21.09 ± 0.07	2.64	0.0	0.0	0.0
21219	3:32:26.49	-27:48:51.39	20.96 ± 0.07	0.93	20.1	20.1	20.0
10128	3:32:26.52	-27:44:56.31	21.77 ± 0.15	2.70	20.7	20.2	19.6
10127	3:32:26.53	-27:44:54.26	21.80 ± 0.14	0.33	0.0	0.0	0.0
2170	3:32:26.54	-27:49:25.15	20.93 ± 0.06	0.10	0.0	0.0	0.0
15144	3:32:26.59	-27:46:48.82	17.33 ± 0.00	0.29	17.6	17.4	17.5
1592	3:32:26.59	-27:47:50.07	21.65 ± 0.08	1.01	20.5	20.2	20.1
15101	3:32:26.60	-27:48:02.02	21.16 ± 0.07	0.27	0.0	0.0	0.0
21137	3:32:26.60	-27:50:01.84	19.00 ± 0.01	0.62	18.2	18.2	18.1
10120	3:32:26.62	-27:44:50.00	21.81 ± 0.12	2.28	20.4	19.9	19.3
156	3:32:26.66	-27:48:34.80	20.56 ± 0.04	1.00	19.7	19.5	19.6
1546	3:32:26.67	-27:46:58.92	19.00 ± 0.01	0.81	18.4	18.5	18.2
1597	3:32:26.67	-27:47:58.66	19.08 ± 0.01	0.81	18.5	18.6	18.2
10197	3:32:26.74	-27:45:39.90	21.45 ± 0.07	1.62	20.0	19.4	19.2
10250	3:32:26.76	-27:43:58.07	20.97 ± 0.07	1.96	19.6	19.0	18.6
2167	3:32:26.82	-27:49:22.74	20.25 ± 0.04	0.58	19.7	19.7	19.6
1072	3:32:26.83	-27:44:24.66	21.21 ± 0.09	1.86	20.1	19.6	19.4
10206	3:32:26.83	-27:45:45.61	21.30 ± 0.10	0.10	0.0	0.0	0.0
1534	3:32:26.83	-27:48:18.87	20.53 ± 0.03	1.00	19.5	19.1	19.1
21217	3:32:26.83	-27:48:50.38	20.93 ± 0.08	0.68	0.0	0.0	0.0
1025	3:32:26.84	-27:46:02.00	21.41 ± 0.09	1.29	20.1	19.7	19.7
10176	3:32:26.85	-27:45:28.17	18.12 ± 0.01	0.70	17.2	17.2	16.8
1537	3:32:26.88	-27:46:17.88	21.33 ± 0.09	0.49	0.0	0.0	0.0
15104	3:32:26.88	-27:48:03.63	21.65 ± 0.09	0.20	0.0	0.0	0.0
10200	3:32:26.89	-27:45:41.89	21.77 ± 0.10	0.57	21.0	21.0	20.8
10146	3:32:26.95	-27:45:08.62	21.86 ± 0.15	3.20	20.9	19.9	19.4
10234	3:32:26.96	-27:43:46.41	21.47 ± 0.21	0.40	21.6	21.5	21.5
10105	3:32:26.96	-27:44:42.17	21.78 ± 0.13	0.10	21.6	21.5	21.6
21236	3:32:26.96	-27:49:01.39	21.55 ± 0.10	0.44	0.0	0.0	0.0
1530	3:32:27.00	-27:48:28.79	19.94 ± 0.03	0.51	20.2	19.9	19.9
21140	3:32:27.01	-27:50:02.59	21.68 ± 0.12	0.93	21.0	21.0	20.8
1030	3:32:27.02	-27:44:07.11	18.61 ± 0.01	1.10	17.4	17.0	16.8
1029	3:32:27.07	-27:44:04.86	19.51 ± 0.02	0.71	18.9	19.1	18.8
21185	3:32:27.07	-27:50:31.34	21.98 ± 0.12	2.49	20.3	19.8	19.1
2164	3:32:27.10	-27:49:21.82	20.64 ± 0.06	0.68	20.1	20.0	19.9
10102	3:32:27.12	-27:44:43.72	21.15 ± 0.09	1.55	19.8	19.1	18.9
15132	3:32:27.16	-27:46:27.36	21.97 ± 0.17	0.91	21.9	21.9	21.7

id	RA(J2000)	DEC(J2000)	K_s	z_{phot}	[3.6]	[4.5]	[5.8]
21134	3:32:27.16	-27:49:57.81	20.57 ± 0.06	1.15	19.6	19.3	19.4
1048	3:32:27.18	-27:44:16.48	16.27 ± 0.00	0.59	15.7	15.7	15.5
2161	3:32:27.24	-27:49:19.12	21.12 ± 0.09	2.10	19.9	19.4	19.0
1089	3:32:27.25	-27:44:39.00	21.73 ± 0.21	0.28	22.2	22.1	22.4
15146	3:32:27.25	-27:46:38.87	21.68 ± 0.09	1.10	20.7	20.4	20.4
1034	3:32:27.26	-27:44:06.96	20.66 ± 0.06	0.66	20.0	20.1	19.8
102	3:32:27.26	-27:46:12.44	21.82 ± 0.14	1.62	20.2	19.6	19.4
158	3:32:27.27	-27:48:34.21	21.67 ± 0.12	0.86	21.2	21.3	21.1
969	3:32:27.29	-27:44:28.71	17.71 ± 0.01	0.42	17.9	17.6	17.6
21213	3:32:27.29	-27:48:45.60	21.36 ± 0.12	2.42	20.0	19.5	19.0
916	3:32:27.30	-27:46:03.58	18.86 ± 0.01	0.81	18.2	18.4	18.0
10229	3:32:27.35	-27:46:03.43	18.65 ± 0.01	0.59	18.0	17.9	17.8
21159	3:32:27.35	-27:50:15.84	18.82 ± 0.02	0.69	18.1	18.2	17.9
10196	3:32:27.36	-27:45:40.11	21.20 ± 0.12	0.76	20.9	21.0	20.7
9194	3:32:27.36	-27:45:49.96	20.33 ± 0.06	0.86	19.8	19.9	19.6
151	3:32:27.37	-27:48:42.23	20.84 ± 0.08	0.69	20.5	20.4	20.4
21127	3:32:27.40	-27:49:54.64	21.61 ± 0.11	1.11	20.7	20.5	20.5
10212	3:32:27.41	-27:45:49.62	20.25 ± 0.04	0.79	19.5	19.7	19.3
21212	3:32:27.44	-27:48:45.74	21.66 ± 0.24	0.53	21.4	21.1	21.0
9112	3:32:27.46	-27:44:57.48	21.11 ± 0.12	1.00	20.4	20.2	20.3
20205	3:32:27.52	-27:49:09.08	20.38 ± 0.05	0.93	19.4	19.4	19.2
97	3:32:27.53	-27:46:09.07	21.87 ± 0.20	0.79	21.1	21.3	20.9
920	3:32:27.55	-27:46:03.57	17.16 ± 0.01	0.39	17.4	17.1	17.0
9161	3:32:27.56	-27:45:21.86	20.90 ± 0.08	0.71	20.2	20.4	20.0
1523	3:32:27.56	-27:48:25.48	21.36 ± 0.07	3.38	20.0	19.1	18.5
21155	3:32:27.56	-27:50:11.37	21.56 ± 0.15	2.28	20.4	19.9	19.3
103	3:32:27.59	-27:46:09.09	21.99 ± 0.16	0.75	21.0	21.2	20.8
2063	3:32:27.59	-27:49:38.74	17.96 ± 0.01	0.49	18.2	18.0	17.9
971	3:32:27.60	-27:44:31.10	17.31 ± 0.01	0.28	17.5	17.3	17.5
1015	3:32:27.60	-27:46:03.46	17.01 ± 0.01	0.62	16.2	16.1	15.8
2119	3:32:27.62	-27:50:59.60	21.36 ± 0.14	3.49	20.2	19.4	18.8
2089	3:32:27.65	-27:49:56.75	20.17 ± 0.05	0.69	19.6	19.7	19.4
9129	3:32:27.66	-27:45:05.75	21.19 ± 0.08	1.01	20.3	20.1	20.2
101	3:32:27.70	-27:46:13.85	21.72 ± 0.29	0.29	21.3	21.2	21.4
20163	3:32:27.71	-27:50:40.88	18.07 ± 0.01	0.88	17.2	17.1	16.9
939	3:32:27.72	-27:45:54.90	21.66 ± 0.10	0.91	20.8	20.8	20.5
9151	3:32:27.74	-27:45:18.74	20.95 ± 0.06	0.84	20.2	20.2	20.0
21174	3:32:27.75	-27:50:23.56	21.75 ± 0.20	1.34	20.9	20.6	20.7
10220	3:32:27.76	-27:45:54.82	21.64 ± 0.11	0.91	20.8	20.8	20.5
9135	3:32:27.77	-27:45:10.69	21.29 ± 0.12	1.32	20.3	19.9	20.1
10150	3:32:27.78	-27:45:10.10	21.98 ± 0.21	0.58	21.2	21.2	21.1
15110	3:32:27.78	-27:48:12.49	21.67 ± 0.13	1.64	20.7	20.1	19.9
10117	3:32:27.85	-27:44:49.88	21.89 ± 0.17	0.99	20.8	20.6	20.6
20149	3:32:27.85	-27:50:29.55	20.50 ± 0.06	1.48	19.2	18.6	18.6
9180	3:32:27.87	-27:45:39.13	20.82 ± 0.06	0.84	20.0	20.1	19.8
9213	3:32:27.91	-27:43:53.38	21.36 ± 0.10	0.60	21.1	21.0	21.0
961	3:32:27.92	-27:44:21.12	21.73 ± 0.17	0.19	0.0	0.0	0.0
1528	3:32:27.96	-27:48:24.27	20.25 ± 0.03	2.29	18.9	18.2	17.6
1589	3:32:27.97	-27:47:43.49	21.94 ± 0.10	1.02	20.5	20.2	20.2
15148	3:32:27.99	-27:46:39.30	16.26 ± 0.00	0.30	16.6	16.4	16.5
20135	3:32:28.04	-27:50:21.75	21.98 ± 0.14	2.06	20.4	19.9	19.4
911	3:32:28.05	-27:46:06.43	19.77 ± 0.03	1.02	18.5	18.1	18.1
20174	3:32:28.13	-27:48:45.05	21.92 ± 0.18	1.51	20.8	20.3	20.2
20154	3:32:28.14	-27:50:34.95	18.96 ± 0.02	0.50	18.9	18.7	18.6
1540	3:32:28.17	-27:46:48.45	21.45 ± 0.07	1.47	20.2	19.7	19.6
9226	3:32:28.27	-27:44:03.38	19.99 ± 0.05	3.71	19.0	18.1	17.5
20200	3:32:28.27	-27:49:07.97	21.00 ± 0.08	1.13	19.8	19.6	19.7
2079	3:32:28.27	-27:49:49.73	18.75 ± 0.01	0.54	18.4	18.4	18.2
9102	3:32:28.29	-27:44:50.67	21.57 ± 0.09	3.49	20.2	19.3	18.7
9154	3:32:28.32	-27:45:18.89	21.48 ± 0.09	1.39	20.3	19.9	19.9
964	3:32:28.33	-27:44:26.24	17.58 ± 0.01	0.46	17.9	17.7	17.7
9105	3:32:28.43	-27:44:53.42	21.00 ± 0.06	0.98	20.0	19.7	19.8
1531	3:32:28.43	-27:48:19.06	21.86 ± 0.09	0.40	0.0	0.0	0.0
1549	3:32:28.44	-27:47:03.22	17.64 ± 0.01	0.79	17.1	17.3	16.9
963	3:32:28.45	-27:44:19.25	20.37 ± 0.06	1.07	19.6	19.4	19.4

id	RA(J2000)	DEC(J2000)	K_s	z_{phot}	[3.6]	[4.5]	[5.8]
1526	3:32:28.48	-27:48:26.50	18.93 ± 0.01	0.32	19.0	18.8	18.9
9125	3:32:28.51	-27:45:00.02	21.75 ± 0.14	0.88	21.2	21.2	21.1
9152	3:32:28.56	-27:45:19.19	21.19 ± 0.08	0.38	0.0	0.0	0.0
936	3:32:28.58	-27:45:56.97	20.65 ± 0.04	0.34	0.0	0.0	0.0
970	3:32:28.60	-27:44:27.45	21.94 ± 0.18	1.05	21.4	21.1	21.1
9184	3:32:28.60	-27:45:42.21	21.18 ± 0.08	0.95	20.3	20.1	19.9
1591	3:32:28.63	-27:47:49.02	21.55 ± 0.08	1.05	20.9	20.7	20.8
9169	3:32:28.72	-27:45:28.69	20.52 ± 0.04	0.38	20.6	20.4	20.4
15120	3:32:28.74	-27:46:20.37	17.93 ± 0.01	0.89	17.4	17.4	17.2
206	3:32:28.78	-27:51:07.21	21.44 ± 0.11	1.32	0.0	0.0	0.0
945	3:32:28.79	-27:43:55.56	15.34 ± 0.00	0.30	15.8	15.6	15.8
9126	3:32:28.79	-27:45:03.63	21.74 ± 0.11	0.91	21.1	21.2	20.9
1595	3:32:28.79	-27:47:55.47	19.32 ± 0.02	1.31	18.4	18.0	17.9
975	3:32:28.81	-27:44:30.56	20.73 ± 0.06	1.20	19.4	19.1	19.1
1519	3:32:28.82	-27:48:29.71	20.15 ± 0.03	1.22	18.7	18.2	18.2
15135	3:32:28.87	-27:46:28.46	21.66 ± 0.09	0.34	0.0	0.0	0.0
207	3:32:28.89	-27:51:06.20	21.91 ± 0.14	0.69	21.1	21.3	20.9
9165	3:32:28.90	-27:45:25.33	20.55 ± 0.04	0.93	20.0	20.0	19.8
930	3:32:28.93	-27:46:00.88	20.12 ± 0.03	1.00	19.0	18.8	18.8
9238	3:32:28.94	-27:44:11.60	21.31 ± 0.12	2.90	0.0	0.0	0.0
15125	3:32:28.98	-27:46:23.60	18.37 ± 0.01	0.97	17.5	17.2	17.3
20179	3:32:28.98	-27:49:08.27	17.41 ± 0.01	1.03	16.5	16.1	16.0
2041	3:32:29.00	-27:49:23.00	19.01 ± 0.01	0.70	18.0	18.1	17.7
979	3:32:29.05	-27:44:32.24	19.90 ± 0.03	1.28	18.8	18.5	18.6
15129	3:32:29.10	-27:46:28.97	19.77 ± 0.03	0.34	0.0	0.0	0.0
9159	3:32:29.11	-27:45:21.15	20.15 ± 0.04	1.43	18.8	18.2	18.3
9145	3:32:29.16	-27:45:14.81	21.50 ± 0.07	0.35	0.0	0.0	0.0
9186	3:32:29.17	-27:45:43.35	21.35 ± 0.07	0.60	20.9	20.8	20.8
1522	3:32:29.17	-27:48:33.09	19.09 ± 0.01	0.62	18.8	18.9	18.6
154	3:32:29.17	-27:48:37.98	21.15 ± 0.09	0.81	20.7	20.9	20.6
2032	3:32:29.17	-27:49:16.93	21.06 ± 0.07	2.09	19.3	18.7	18.1
965	3:32:29.19	-27:44:13.10	21.87 ± 0.19	1.13	20.9	20.6	20.6
15141	3:32:29.20	-27:46:31.89	21.18 ± 0.05	0.93	20.1	20.0	19.8
1553	3:32:29.21	-27:47:07.64	17.49 ± 0.00	0.79	17.0	17.2	16.8
910	3:32:29.23	-27:46:11.59	19.07 ± 0.02	0.40	19.2	18.8	18.8
9137	3:32:29.24	-27:45:09.79	21.38 ± 0.07	3.52	20.0	19.1	18.5
9108	3:32:29.31	-27:44:55.47	21.34 ± 0.10	1.01	20.5	20.3	20.3
1586	3:32:29.35	-27:47:41.53	21.38 ± 0.05	0.97	20.5	20.3	20.4
2019	3:32:29.35	-27:50:48.87	17.31 ± 0.01	0.51	17.3	17.0	16.9
15100	3:32:29.39	-27:48:00.56	21.36 ± 0.08	1.48*	0.0	0.0	0.0
204	3:32:29.40	-27:51:10.01	18.39 ± 0.01	0.77	17.3	17.4	16.9
20207	3:32:29.51	-27:49:15.39	21.72 ± 0.11	1.23	20.6	20.2	20.3
2060	3:32:29.54	-27:49:34.01	20.95 ± 0.07	0.54	20.7	20.6	20.4
922	3:32:29.55	-27:46:00.32	19.99 ± 0.03	0.40	0.0	0.0	0.0
15111	3:32:29.55	-27:48:12.06	19.86 ± 0.02	2.87	18.5	17.8	17.1
9134	3:32:29.64	-27:45:11.25	20.93 ± 0.05	1.09	19.8	19.6	19.7
9164	3:32:29.65	-27:45:24.65	20.59 ± 0.04	1.36	19.4	18.9	18.9
2073	3:32:29.66	-27:49:45.51	20.94 ± 0.06	1.10	19.9	19.7	19.7
1559	3:32:29.68	-27:47:10.36	20.43 ± 0.03	0.30	20.5	20.4	20.6
1550	3:32:29.69	-27:47:00.46	21.95 ± 0.11	0.40	0.0	0.0	0.0
9136	3:32:29.71	-27:45:07.26	19.85 ± 0.02	0.91	19.1	19.1	18.9
2091	3:32:29.72	-27:49:57.22	21.66 ± 0.12	0.98	20.8	20.5	20.5
2035	3:32:29.80	-27:49:19.23	21.99 ± 0.11	0.90	21.3	21.2	21.0
1568	3:32:29.81	-27:47:19.60	20.96 ± 0.05	1.47	20.0	19.5	19.5
9133	3:32:29.82	-27:45:10.79	19.67 ± 0.02	1.29	18.4	17.9	18.2
2010	3:32:29.84	-27:51:05.93	20.33 ± 0.04	3.36	19.0	18.2	17.6
20134	3:32:29.85	-27:50:21.50	21.22 ± 0.09	0.90	20.5	20.4	20.3
9211	3:32:29.86	-27:43:54.91	21.60 ± 0.12	1.40	20.3	19.9	20.0
9153	3:32:29.86	-27:45:20.67	17.93 ± 0.01	1.03	17.3	17.0	17.1
962	3:32:29.88	-27:44:24.51	14.14 ± 0.00	0.40	15.0	14.7	14.8
2021	3:32:29.92	-27:50:55.35	21.72 ± 0.11	0.53	21.6	21.3	21.3
1578	3:32:29.93	-27:47:34.61	21.43 ± 0.07	0.79	20.8	21.1	20.6
9104	3:32:29.94	-27:44:54.06	21.22 ± 0.09	0.98	20.5	20.2	20.2
1596	3:32:29.94	-27:47:57.08	18.83 ± 0.01	0.38	18.9	18.5	18.5
20151	3:32:29.94	-27:50:32.03	20.84 ± 0.06	1.12	19.8	19.6	19.7

id	RA(J2000)	DEC(J2000)	K_s	z_{phot}	[3.6]	[4.5]	[5.8]
2052	3:32:29.96	-27:49:28.76	21.36 ± 0.09	2.70	19.9	19.4	18.7
9230	3:32:29.98	-27:44:04.94	14.48 ± 0.00	0.48	14.8	14.5	14.5
9209	3:32:30.02	-27:43:47.27	16.99 ± 0.01	0.93	16.3	16.2	16.1
1573	3:32:30.02	-27:47:26.79	18.97 ± 0.01	1.27	17.9	17.5	17.7
20142	3:32:30.04	-27:50:26.64	19.85 ± 0.02	1.01	18.8	18.6	18.6
9166	3:32:30.06	-27:45:23.55	18.43 ± 0.01	1.00	17.5	17.2	17.1
9174	3:32:30.07	-27:45:34.11	19.01 ± 0.01	0.81	18.5	18.7	18.3
2074	3:32:30.08	-27:49:47.63	21.24 ± 0.12	0.42	0.0	0.0	0.0
2022	3:32:30.09	-27:51:00.24	17.61 ± 0.01	0.70	17.1	17.1	16.8
9127	3:32:30.22	-27:45:04.62	19.00 ± 0.01	0.98	18.3	18.1	18.1
941	3:32:30.22	-27:45:53.08	21.46 ± 0.09	0.69	20.9	21.0	20.7
1567	3:32:30.22	-27:47:17.17	21.88 ± 0.12	1.48	20.8	20.3	20.2
20161	3:32:30.22	-27:50:37.18	21.41 ± 0.07	0.55	20.9	20.5	20.4
9158	3:32:30.24	-27:45:19.91	20.97 ± 0.05	0.51	20.8	20.5	20.5
20185	3:32:30.31	-27:48:52.42	20.35 ± 0.05	0.74	19.8	20.0	19.6
2072	3:32:30.31	-27:49:44.78	21.42 ± 0.10	0.78	20.6	20.6	20.4
1582	3:32:30.34	-27:47:39.28	21.69 ± 0.11	0.40	21.9	21.6	21.7
9156	3:32:30.35	-27:45:23.54	18.21 ± 0.01	1.32	17.4	17.0	17.3
9117	3:32:30.36	-27:45:01.14	20.09 ± 0.03	0.34	0.0	0.0	0.0
2023	3:32:30.39	-27:50:53.40	21.24 ± 0.06	0.69	20.6	20.7	20.4
9144	3:32:30.45	-27:45:13.74	21.70 ± 0.10	0.88	20.9	20.8	20.6
15103	3:32:30.46	-27:48:02.97	21.09 ± 0.06	0.40	21.2	20.8	20.7
15151	3:32:30.48	-27:46:47.15	21.83 ± 0.12	1.52	20.8	20.2	20.2
20120	3:32:30.48	-27:50:14.93	18.47 ± 0.01	0.61	17.9	17.9	17.7
20110	3:32:30.52	-27:50:04.40	19.23 ± 0.01	1.22	17.7	17.4	17.4
20166	3:32:30.52	-27:50:33.50	21.46 ± 0.09	1.28	20.2	19.8	19.8
967	3:32:30.54	-27:44:25.27	21.91 ± 0.17	0.84	20.9	21.0	20.7
1520	3:32:30.56	-27:48:36.42	20.57 ± 0.04	0.93	19.6	19.6	19.4
20126	3:32:30.57	-27:50:18.79	20.01 ± 0.03	0.99	19.2	18.9	19.0
9148	3:32:30.58	-27:45:18.27	17.63 ± 0.01	0.86	17.1	17.1	16.9
1585	3:32:30.67	-27:47:41.71	20.54 ± 0.04	0.22	0.0	0.0	0.0
2053	3:32:30.71	-27:49:28.77	20.28 ± 0.03	0.68	19.5	19.6	19.3
20137	3:32:30.71	-27:50:24.68	20.41 ± 0.06	0.41	20.4	20.0	20.0
15118	3:32:30.73	-27:46:17.12	19.24 ± 0.02	1.12	18.2	18.0	18.1
9204	3:32:30.75	-27:43:45.28	21.76 ± 0.12	1.15	21.1	20.9	20.8
914	3:32:30.76	-27:46:04.87	21.95 ± 0.15	0.60	21.5	21.4	21.4
15149	3:32:30.79	-27:46:37.44	21.54 ± 0.09	1.11	20.7	20.5	20.6
2011	3:32:30.82	-27:51:01.53	21.65 ± 0.12	0.52	21.2	21.1	20.9
15126	3:32:30.85	-27:46:21.62	18.65 ± 0.01	1.02	17.8	17.6	17.7
2056	3:32:30.85	-27:49:31.74	19.97 ± 0.03	0.92	19.0	18.9	18.7
1541	3:32:30.89	-27:46:49.35	19.17 ± 0.02	1.43	18.2	17.7	17.7
1510	3:32:30.92	-27:48:32.20	21.09 ± 0.06	1.44	19.9	19.4	19.4
1594	3:32:30.96	-27:47:54.16	21.75 ± 0.11	0.91	21.3	21.4	21.2
9147	3:32:30.97	-27:45:16.31	21.22 ± 0.07	0.93	20.4	20.4	20.3
986	3:32:30.98	-27:44:34.96	21.32 ± 0.08	1.09	20.5	20.3	20.4
96	3:32:31.04	-27:46:10.31	21.71 ± 0.16	0.95	21.1	20.9	20.9
15117	3:32:31.05	-27:46:15.14	21.57 ± 0.11	0.84	21.0	21.1	20.8
9176	3:32:31.09	-27:45:37.10	18.51 ± 0.01	0.50	18.7	18.5	18.4
1598	3:32:31.09	-27:47:58.39	21.72 ± 0.10	3.20	20.6	19.7	19.2
983	3:32:31.10	-27:44:33.42	20.98 ± 0.05	0.98	20.1	19.8	19.9
2094	3:32:31.11	-27:49:39.56	20.61 ± 0.03	1.68	18.8	18.0	17.7
1551	3:32:31.15	-27:47:02.69	21.86 ± 0.11	1.07	20.9	20.6	20.5
20178	3:32:31.17	-27:48:48.20	21.02 ± 0.09	0.59	20.2	20.1	20.1
9173	3:32:31.23	-27:45:32.62	19.32 ± 0.01	1.00	18.4	18.1	18.1
9185	3:32:31.23	-27:45:43.05	21.55 ± 0.08	0.86	20.6	20.6	20.3
1532	3:32:31.28	-27:48:20.19	20.32 ± 0.03	1.03	19.2	18.9	19.0
20188	3:32:31.30	-27:48:52.37	21.98 ± 0.19	2.20	20.6	20.1	19.6
15139	3:32:31.32	-27:46:33.12	21.57 ± 0.07	0.41	0.0	0.0	0.0
15150	3:32:31.32	-27:46:46.86	21.79 ± 0.08	1.19	20.5	20.1	20.1
9189	3:32:31.33	-27:45:44.60	20.64 ± 0.04	1.30	19.6	19.2	19.4
991	3:32:31.34	-27:44:19.02	19.44 ± 0.02	0.91	18.4	18.3	18.1
15136	3:32:31.35	-27:46:30.66	22.00 ± 0.11	0.33	21.9	21.7	21.8
1554	3:32:31.35	-27:47:06.56	21.30 ± 0.10	0.23	0.0	0.0	0.0
1571	3:32:31.35	-27:47:25.02	18.57 ± 0.01	0.81	18.2	18.2	18.0
925	3:32:31.39	-27:46:04.22	20.52 ± 0.05	3.07	19.2	18.5	17.9

id	RA(J2000)	DEC(J2000)	K_s	z_{phot}	[3.6]	[4.5]	[5.8]
2025	3:32:31.44	-27:50:47.50	21.79 ± 0.10	0.83	21.0	21.0	20.8
9114	3:32:31.46	-27:44:57.28	21.45 ± 0.09	1.07	20.6	20.3	20.4
1511	3:32:31.46	-27:48:30.42	21.14 ± 0.05	0.33	21.1	20.8	20.8
2045	3:32:31.46	-27:49:25.06	19.78 ± 0.03	1.53	18.5	17.8	17.6
15130	3:32:31.47	-27:46:22.92	18.95 ± 0.01	1.45	17.6	16.9	16.8
2070	3:32:31.48	-27:49:45.40	16.27 ± 0.00	0.51	16.4	16.1	16.0
9141	3:32:31.49	-27:45:13.73	21.43 ± 0.08	0.93	20.5	20.5	20.3
9199	3:32:31.51	-27:43:42.80	21.90 ± 0.14	1.30	20.5	20.1	20.2
9118	3:32:31.52	-27:44:59.64	21.80 ± 0.08	1.47	20.6	20.2	20.1
20186	3:32:31.52	-27:48:54.06	20.14 ± 0.05	2.08	18.6	17.8	17.2
9206	3:32:31.53	-27:43:50.86	21.09 ± 0.08	1.38	19.9	19.4	19.5
9101	3:32:31.55	-27:44:43.59	21.70 ± 0.11	3.73	20.6	19.8	19.3
1561	3:32:31.55	-27:47:11.36	21.51 ± 0.11	0.88	20.9	20.9	20.8
20143	3:32:31.56	-27:50:28.64	18.86 ± 0.01	1.43	17.5	16.9	16.8
92	3:32:31.57	-27:46:12.76	20.09 ± 0.04	0.81	19.5	19.6	19.3
2096	3:32:31.57	-27:49:56.92	21.41 ± 0.10	0.38	0.0	0.0	0.0
9178	3:32:31.59	-27:45:37.73	21.26 ± 0.10	0.38	21.2	21.0	21.0
20109	3:32:31.59	-27:50:04.56	19.03 ± 0.01	0.64	18.4	18.4	18.2
15116	3:32:31.61	-27:46:14.91	20.87 ± 0.09	0.33	21.3	20.9	20.9
1557	3:32:31.61	-27:47:07.99	21.84 ± 0.09	0.32	0.0	0.0	0.0
9140	3:32:31.62	-27:45:12.68	21.74 ± 0.13	0.93	21.1	21.1	21.0
9128	3:32:31.66	-27:45:04.83	20.63 ± 0.04	1.07	19.7	19.5	19.6
20128	3:32:31.68	-27:50:21.02	20.50 ± 0.03	0.70	19.1	19.0	18.6
2085	3:32:31.72	-27:49:54.28	19.88 ± 0.02	0.61	19.1	19.0	18.9
153	3:32:31.76	-27:48:39.40	20.59 ± 0.05	1.00	19.9	19.6	19.7
9236	3:32:31.77	-27:44:12.05	21.83 ± 0.13	0.55	21.5	21.4	21.2
159	3:32:31.78	-27:48:32.54	21.84 ± 0.12	3.47	20.6	19.8	19.2
20184	3:32:31.78	-27:48:51.31	19.42 ± 0.02	0.80	18.5	18.7	18.2
2092	3:32:31.82	-27:49:58.46	18.88 ± 0.01	0.95	17.8	17.6	17.4
9217	3:32:31.84	-27:43:56.31	19.56 ± 0.02	1.00	18.4	18.1	18.1
20130	3:32:31.84	-27:50:24.66	21.11 ± 0.07	1.48	20.1	19.7	19.6
2082	3:32:31.88	-27:49:50.16	21.65 ± 0.09	0.10	21.4	21.3	21.3
997	3:32:31.90	-27:44:44.95	20.04 ± 0.03	1.41	19.0	18.5	18.5
20111	3:32:31.91	-27:50:04.57	21.96 ± 0.13	1.26	20.8	20.5	20.6
20129	3:32:31.92	-27:50:21.20	20.00 ± 0.02	0.64	19.3	19.4	19.1
9163	3:32:32.04	-27:45:23.95	20.95 ± 0.06	0.32	21.2	20.8	20.9
9103	3:32:32.05	-27:44:51.75	18.42 ± 0.01	0.98	17.5	17.3	17.3
2090	3:32:32.13	-27:49:56.39	21.07 ± 0.07	0.99	20.1	19.8	19.9
2015	3:32:32.14	-27:51:05.50	18.88 ± 0.01	0.60	18.3	18.2	18.1
9207	3:32:32.15	-27:43:49.96	20.48 ± 0.04	0.98	19.6	19.4	19.4
9210	3:32:32.15	-27:43:55.56	20.82 ± 0.06	1.47	19.7	19.1	19.1
1539	3:32:32.17	-27:46:51.48	21.80 ± 0.10	2.96	19.9	19.1	18.4
9172	3:32:32.19	-27:45:34.85	17.26 ± 0.00	0.39	17.6	17.3	17.2
1524	3:32:32.19	-27:48:24.55	22.00 ± 0.12	0.30	0.0	0.0	0.0
20191	3:32:32.19	-27:48:57.17	20.61 ± 0.07	0.79	20.0	20.2	19.8
2030	3:32:32.24	-27:48:45.52	18.35 ± 0.01	0.58	17.9	17.9	17.7
20175	3:32:32.26	-27:50:44.75	21.75 ± 0.15	0.69	21.5	21.5	21.3
2083	3:32:32.27	-27:49:50.94	21.39 ± 0.10	0.64	20.7	20.8	20.5
1536	3:32:32.30	-27:46:15.14	20.34 ± 0.05	1.11	19.2	18.9	18.9
20124	3:32:32.32	-27:50:17.87	21.59 ± 0.09	0.91	20.6	20.7	20.4
9200	3:32:32.33	-27:43:43.65	20.59 ± 0.07	0.59	20.1	20.2	19.9
9155	3:32:32.33	-27:45:19.83	21.58 ± 0.11	0.93	21.2	21.1	21.0
20159	3:32:32.33	-27:50:37.06	20.93 ± 0.06	1.48	19.8	19.2	19.1
9203	3:32:32.34	-27:43:45.87	21.25 ± 0.07	1.02	20.2	20.0	20.1
1547	3:32:32.45	-27:46:56.45	21.91 ± 0.09	0.86	20.9	21.0	20.6
1542	3:32:32.47	-27:46:53.99	20.64 ± 0.03	0.98	19.4	19.1	19.1
20172	3:32:32.49	-27:50:43.95	21.00 ± 0.07	0.49	20.8	20.6	20.4
932	3:32:32.55	-27:45:59.81	20.69 ± 0.04	0.98	19.7	19.4	19.5
15138	3:32:32.56	-27:46:31.94	21.45 ± 0.09	0.37	0.0	0.0	0.0
1565	3:32:32.59	-27:47:05.72	20.86 ± 0.04	1.22	19.7	19.4	19.5
2026	3:32:32.59	-27:50:53.73	18.98 ± 0.01	0.68	18.4	18.5	18.2
20180	3:32:32.65	-27:48:48.80	20.57 ± 0.06	1.08	19.7	19.4	19.5
2066	3:32:32.68	-27:49:44.67	15.91 ± 0.00	0.50	15.6	15.4	15.3
20117	3:32:32.69	-27:50:11.22	17.23 ± 0.00	0.60	17.0	17.0	16.8
929	3:32:32.72	-27:45:47.37	17.61 ± 0.01	1.07	16.9	16.6	16.7

id	RA(J2000)	DEC(J2000)	K_s	z_{phot}	[3.6]	[4.5]	[5.8]
20193	3:32:32.73	-27:48:59.65	18.98 ± 0.01	0.74	18.2	18.3	17.9
9179	3:32:32.74	-27:45:38.69	19.10 ± 0.01	0.39	19.3	18.9	18.9
2048	3:32:32.74	-27:49:26.52	21.42 ± 0.10	0.81	20.7	20.9	20.6
2020	3:32:32.74	-27:51:02.42	17.41 ± 0.01	0.71	17.0	17.1	16.7
949	3:32:32.75	-27:44:15.86	20.32 ± 0.04	1.07	19.5	19.2	19.4
2027	3:32:32.77	-27:50:45.69	20.76 ± 0.05	0.70	19.9	20.0	19.7
9196	3:32:32.79	-27:43:38.92	21.34 ± 0.13	0.65	21.0	21.0	20.9
918	3:32:32.82	-27:46:07.70	16.88 ± 0.00	0.37	17.2	16.7	16.7
20123	3:32:32.83	-27:50:16.72	22.00 ± 0.11	3.64	20.9	20.1	19.6
9227	3:32:32.85	-27:44:05.95	21.61 ± 0.16	0.98	21.2	21.1	21.0
2018	3:32:32.90	-27:51:00.11	19.46 ± 0.02	1.53	18.1	17.4	17.1
9143	3:32:32.92	-27:45:14.95	19.47 ± 0.02	0.93	18.6	18.5	18.3
208	3:32:32.92	-27:51:07.73	19.80 ± 0.03	0.81	18.8	19.0	18.5
20187	3:32:32.93	-27:48:56.21	18.70 ± 0.01	0.88	17.8	17.8	17.6
20168	3:32:32.94	-27:50:40.58	20.39 ± 0.03	0.47	0.0	0.0	0.0
9181	3:32:32.96	-27:45:41.48	18.05 ± 0.01	0.40	18.3	17.9	17.9
9188	3:32:32.97	-27:45:45.58	17.02 ± 0.00	0.39	17.2	16.9	16.9
987	3:32:33.01	-27:44:36.73	17.39 ± 0.00	0.71	17.1	17.2	16.9
20146	3:32:33.01	-27:50:30.01	17.42 ± 0.00	0.71	16.6	16.6	16.2
935	3:32:33.02	-27:45:47.33	17.63 ± 0.00	0.81	17.2	17.3	16.9
915	3:32:33.02	-27:46:08.75	18.59 ± 0.01	0.39	18.8	18.5	18.5
148	3:32:33.03	-27:48:31.11	21.68 ± 0.16	0.10	0.0	0.0	0.0
1516	3:32:33.03	-27:48:29.57	20.81 ± 0.06	0.81	20.4	20.5	20.3
1480	3:32:33.04	-27:47:31.05	19.80 ± 0.04	0.96	19.2	19.1	18.9
1599	3:32:33.05	-27:47:59.47	21.85 ± 0.13	0.98	0.0	0.0	0.0
14131	3:32:33.05	-27:48:07.70	19.74 ± 0.03	0.99	18.6	18.4	18.4
1515	3:32:33.08	-27:48:30.96	21.36 ± 0.10	1.28	20.7	20.4	20.4
2054	3:32:33.08	-27:49:30.10	21.88 ± 0.14	0.50	0.0	0.0	0.0
20170	3:32:33.08	-27:50:42.67	20.15 ± 0.06	2.05	19.3	18.8	18.3
202	3:32:33.08	-27:51:11.30	19.95 ± 0.04	0.59	19.4	19.5	19.3
1412	3:32:33.10	-27:48:35.41	21.79 ± 0.17	0.79	21.0	21.2	20.8
988	3:32:33.14	-27:44:31.79	21.79 ± 0.16	0.58	0.0	0.0	0.0
9162	3:32:33.16	-27:45:22.59	21.83 ± 0.10	1.31	20.6	20.1	20.1
948	3:32:33.17	-27:44:15.19	19.72 ± 0.01	0.38	19.6	19.3	19.3
1525	3:32:33.19	-27:48:34.40	21.01 ± 0.10	0.93	20.6	20.6	20.5
20196	3:32:33.21	-27:48:58.69	21.91 ± 0.13	2.78	20.5	19.9	19.2
2038	3:32:33.21	-27:49:20.97	19.79 ± 0.02	0.53	19.4	19.2	19.0
20165	3:32:33.34	-27:50:40.58	21.48 ± 0.08	1.48	20.3	19.8	19.7
20164	3:32:33.35	-27:50:39.15	21.70 ± 0.11	2.02	20.3	19.8	19.3
950	3:32:33.36	-27:44:15.47	21.74 ± 0.11	1.10	20.6	20.4	20.5
9224	3:32:33.39	-27:43:54.47	21.97 ± 0.13	0.89	21.1	21.1	21.0
9110	3:32:33.39	-27:44:55.76	21.39 ± 0.08	1.32	20.2	19.9	20.0
942	3:32:33.40	-27:43:49.19	17.80 ± 0.01	0.45	18.0	17.7	17.7
951	3:32:33.42	-27:44:16.92	21.68 ± 0.09	0.75	21.1	21.3	20.9
996	3:32:33.44	-27:44:41.02	21.50 ± 0.10	0.60	21.2	21.2	21.1
1433	3:32:33.44	-27:46:50.33	20.77 ± 0.07	0.86	20.1	20.2	19.9
20162	3:32:33.44	-27:50:37.30	21.93 ± 0.13	1.22	20.7	20.4	20.6
924	3:32:33.45	-27:46:02.46	20.27 ± 0.04	1.07	19.2	18.9	19.0
927	3:32:33.46	-27:45:57.47	21.99 ± 0.16	0.93	21.7	21.7	21.5
9223	3:32:33.47	-27:44:04.96	21.39 ± 0.07	0.93	20.6	20.6	20.4
1461	3:32:33.47	-27:47:12.34	21.17 ± 0.06	0.96	19.9	19.9	19.8
973	3:32:33.48	-27:44:30.45	20.03 ± 0.03	0.42	20.3	20.1	20.1
2078	3:32:33.48	-27:49:47.74	21.55 ± 0.09	1.36	20.3	19.8	19.9
14165	3:32:33.53	-27:46:23.06	18.73 ± 0.01	0.10	18.8	18.8	18.9
9190	3:32:33.54	-27:45:47.44	20.90 ± 0.05	1.32	19.4	18.9	19.0
20144	3:32:33.59	-27:50:28.17	21.99 ± 0.16	0.53	22.0	21.7	21.7
14106	3:32:33.67	-27:47:51.07	20.54 ± 0.04	1.70	19.2	18.5	18.3
974	3:32:33.70	-27:44:30.76	21.96 ± 0.18	1.46	20.7	20.1	20.2
9130	3:32:33.74	-27:45:07.49	20.30 ± 0.04	1.31	19.3	18.8	18.9
14100	3:32:33.75	-27:47:44.36	21.26 ± 0.07	1.42	20.2	19.7	19.8
14137	3:32:33.75	-27:48:16.27	20.64 ± 0.06	0.61	20.3	20.3	20.2
955	3:32:33.78	-27:44:17.67	19.99 ± 0.03	1.21	19.0	18.7	18.8
9233	3:32:33.82	-27:44:10.12	17.98 ± 0.00	0.76	17.2	17.4	17.0
2095	3:32:33.82	-27:49:58.73	21.75 ± 0.16	2.71	0.0	0.0	0.0
14104	3:32:33.83	-27:47:48.02	19.44 ± 0.02	0.51	19.1	18.9	18.7

id	RA(J2000)	DEC(J2000)	K_s	z_{phot}	[3.6]	[4.5]	[5.8]
20112	3:32:33.83	-27:50:05.16	21.41 ± 0.10	1.39	20.3	19.9	19.9
9149	3:32:33.84	-27:45:18.10	20.40 ± 0.03	1.24	18.9	18.4	18.3
9150	3:32:33.84	-27:45:20.44	21.21 ± 0.06	1.25	19.8	19.3	19.2
938	3:32:33.84	-27:46:00.20	19.12 ± 0.01	1.58	17.9	17.2	17.0
9195	3:32:33.86	-27:45:42.29	20.32 ± 0.04	1.03	19.4	19.2	19.2
9215	3:32:33.87	-27:43:57.62	19.30 ± 0.01	1.00	18.1	17.8	17.9
9175	3:32:33.89	-27:45:33.07	21.98 ± 0.10	1.38	20.9	20.4	20.5
14146	3:32:33.90	-27:46:16.75	21.79 ± 0.13	1.02	20.6	20.4	20.4
2059	3:32:33.94	-27:49:32.58	20.73 ± 0.06	0.36	20.6	20.3	20.4
998	3:32:33.97	-27:44:45.02	20.39 ± 0.04	0.37	0.0	0.0	0.0
958	3:32:34.00	-27:44:19.02	20.56 ± 0.04	1.02	19.7	19.4	19.5
20195	3:32:34.00	-27:48:59.72	21.24 ± 0.07	2.76	19.3	18.4	17.6
9237	3:32:34.01	-27:44:12.22	20.64 ± 0.04	1.00	19.7	19.4	19.4
981	3:32:34.03	-27:44:33.15	20.14 ± 0.02	0.57	19.9	19.6	19.6
14135	3:32:34.03	-27:48:14.61	20.77 ± 0.07	1.38	20.0	19.6	19.7
20115	3:32:34.05	-27:50:09.54	19.91 ± 0.03	0.75	19.4	19.6	19.2
20147	3:32:34.05	-27:50:28.79	19.39 ± 0.02	1.10	18.5	18.2	18.3
2065	3:32:34.07	-27:49:37.99	19.52 ± 0.02	0.89	18.5	18.4	18.2
20182	3:32:34.11	-27:48:49.77	21.30 ± 0.09	0.50	0.0	0.0	0.0
20202	3:32:34.11	-27:49:12.08	20.06 ± 0.04	1.49	19.0	18.4	18.4
1458	3:32:34.12	-27:47:12.09	18.44 ± 0.01	0.10	18.5	18.4	18.5
201	3:32:34.12	-27:51:11.56	21.29 ± 0.12	0.39	21.2	21.0	21.0
1498	3:32:34.14	-27:47:43.50	21.53 ± 0.08	2.14	20.5	20.0	19.6
20157	3:32:34.17	-27:50:33.68	21.80 ± 0.17	1.68	20.7	20.1	19.9
2024	3:32:34.17	-27:50:49.52	21.68 ± 0.10	0.57	21.3	21.1	21.1
940	3:32:34.18	-27:45:54.04	18.26 ± 0.01	0.38	18.6	18.4	18.4
20107	3:32:34.18	-27:50:02.90	21.85 ± 0.11	0.50	21.3	20.9	20.9
2036	3:32:34.26	-27:49:19.56	21.82 ± 0.12	0.98	20.9	20.7	20.8
2067	3:32:34.27	-27:49:40.36	21.75 ± 0.11	3.38	20.2	19.3	18.8
20169	3:32:34.29	-27:50:40.53	21.70 ± 0.10	1.81	20.7	20.2	20.0
9193	3:32:34.30	-27:45:49.12	20.56 ± 0.03	0.69	19.8	20.0	19.7
9214	3:32:34.35	-27:43:50.21	17.98 ± 0.01	0.79	17.5	17.8	17.3
928	3:32:34.36	-27:46:02.40	21.89 ± 0.17	0.49	0.0	0.0	0.0
20190	3:32:34.37	-27:48:55.89	21.65 ± 0.12	0.92	20.5	20.0	19.3
20104	3:32:34.39	-27:50:02.95	21.25 ± 0.09	1.22	19.9	19.4	19.3
946	3:32:34.44	-27:44:13.91	21.84 ± 0.11	0.81	21.2	21.4	21.0
1447	3:32:34.44	-27:46:59.49	20.04 ± 0.03	1.22	18.9	18.5	18.6
20105	3:32:34.47	-27:50:04.87	20.36 ± 0.04	0.48	0.0	0.0	0.0
9216	3:32:34.52	-27:43:59.71	21.83 ± 0.11	0.86	21.2	21.3	21.0
2031	3:32:34.53	-27:48:48.62	15.96 ± 0.00	0.52	16.0	15.8	15.7
9222	3:32:34.58	-27:44:04.65	20.32 ± 0.03	0.98	19.4	19.1	19.1
20106	3:32:34.58	-27:50:06.36	20.98 ± 0.07	0.98	20.1	19.9	19.9
20204	3:32:34.59	-27:49:10.26	21.72 ± 0.12	0.96	21.4	21.4	21.2
14155	3:32:34.60	-27:46:24.48	21.95 ± 0.11	1.23	21.0	20.7	20.8
9205	3:32:34.64	-27:43:47.33	20.98 ± 0.09	2.68	19.8	19.1	18.5
1469	3:32:34.64	-27:47:20.88	21.14 ± 0.06	1.22	19.9	19.6	19.7
9229	3:32:34.65	-27:44:08.11	18.86 ± 0.01	1.09	17.5	17.1	17.1
9202	3:32:34.68	-27:43:41.10	21.94 ± 0.15	0.76	21.4	21.4	21.1
1425	3:32:34.68	-27:46:44.43	21.02 ± 0.04	0.70	19.7	19.6	19.4
20132	3:32:34.70	-27:50:22.78	20.01 ± 0.04	1.30	18.7	18.2	18.4
1477	3:32:34.71	-27:47:28.22	21.91 ± 0.13	1.08	21.2	21.0	20.9
2081	3:32:34.73	-27:49:38.59	20.79 ± 0.06	0.99	19.8	19.5	19.6
1453	3:32:34.74	-27:47:07.59	20.84 ± 0.04	2.81	20.5	20.4	20.3
1411	3:32:34.81	-27:48:35.72	20.23 ± 0.03	1.12	19.1	18.8	18.9
20133	3:32:34.81	-27:50:24.84	19.71 ± 0.03	0.97	18.8	18.6	18.5
1471	3:32:34.82	-27:47:22.12	20.81 ± 0.05	0.10	0.0	0.0	0.0
20199	3:32:34.84	-27:48:55.55	21.91 ± 0.15	0.29	0.0	0.0	0.0
9122	3:32:34.85	-27:45:03.71	21.05 ± 0.06	0.36	21.0	20.6	20.6
14182	3:32:34.86	-27:46:40.49	19.44 ± 0.01	0.83	18.5	18.5	18.2
995	3:32:34.89	-27:44:40.60	19.89 ± 0.02	0.39	19.9	19.6	19.6
9121	3:32:34.91	-27:45:01.86	20.05 ± 0.03	0.79	19.5	19.6	19.3
9109	3:32:34.92	-27:44:55.00	21.96 ± 0.13	2.93	20.2	19.6	19.0
2097	3:32:34.97	-27:50:00.92	20.95 ± 0.07	0.65	20.6	20.8	20.5
9146	3:32:35.01	-27:45:15.56	21.47 ± 0.12	0.40	0.0	0.0	0.0
1419	3:32:35.03	-27:48:23.39	21.19 ± 0.06	2.47	19.8	19.2	18.5

id	RA(J2000)	DEC(J2000)	K_s	z_{phot}	[3.6]	[4.5]	[5.8]
20139	3:32:35.03	-27:50:23.77	21.08 ± 0.06	0.87	19.8	19.8	19.6
2058	3:32:35.04	-27:49:32.42	21.29 ± 0.10	0.53	21.3	20.8	20.8
926	3:32:35.07	-27:45:59.49	21.38 ± 0.10	0.98	20.4	20.2	20.3
14144	3:32:35.08	-27:46:15.54	20.55 ± 0.05	1.19	19.6	19.3	19.3
1429	3:32:35.09	-27:46:47.46	21.07 ± 0.05	2.70	19.3	18.6	17.8
2093	3:32:35.09	-27:49:58.40	20.05 ± 0.03	1.03	19.1	18.8	18.8
9234	3:32:35.11	-27:44:10.71	19.36 ± 0.02	1.46	18.0	17.4	17.4
20101	3:32:35.11	-27:49:53.35	21.51 ± 0.09	1.10	20.6	20.4	20.5
2076	3:32:35.12	-27:49:47.51	21.86 ± 0.11	0.89	20.8	20.7	20.6
20116	3:32:35.12	-27:50:08.81	21.89 ± 0.12	1.13	20.8	20.6	20.7
993	3:32:35.13	-27:44:39.55	19.75 ± 0.02	1.00	18.9	18.6	18.7
2077	3:32:35.13	-27:49:49.29	21.64 ± 0.09	0.65	0.0	0.0	0.0
9183	3:32:35.22	-27:45:41.97	21.13 ± 0.09	1.29	20.1	19.7	19.7
20113	3:32:35.26	-27:50:07.14	21.96 ± 0.14	0.52	21.4	21.2	21.1
2016	3:32:35.26	-27:51:04.65	19.68 ± 0.03	0.61	19.2	19.2	19.1
93	3:32:35.29	-27:46:12.14	21.53 ± 0.12	0.64	20.8	21.0	20.7
14184	3:32:35.31	-27:46:42.31	21.73 ± 0.08	0.93	20.9	20.9	20.7
2075	3:32:35.32	-27:49:39.97	20.89 ± 0.07	2.19	20.0	19.5	18.9
1467	3:32:35.33	-27:47:18.54	20.97 ± 0.04	0.75	20.3	20.3	20.1
956	3:32:35.34	-27:44:18.86	19.84 ± 0.03	1.10	19.0	18.8	18.8
20189	3:32:35.36	-27:48:54.55	21.49 ± 0.12	2.56	0.0	0.0	0.0
9138	3:32:35.37	-27:45:12.41	20.20 ± 0.04	1.36	19.3	18.8	18.9
20197	3:32:35.37	-27:49:04.68	21.43 ± 0.12	2.20	19.9	19.3	18.6
2039	3:32:35.37	-27:49:20.82	20.58 ± 0.04	0.79	19.8	19.9	19.6
14180	3:32:35.39	-27:46:39.36	20.90 ± 0.04	1.79	19.6	19.0	18.7
20167	3:32:35.42	-27:50:20.94	21.05 ± 0.06	1.19	19.9	19.6	19.7
957	3:32:35.45	-27:44:21.18	19.40 ± 0.01	0.98	18.6	18.4	18.4
14176	3:32:35.47	-27:46:36.88	21.09 ± 0.05	1.05	20.0	19.8	19.8
20100	3:32:35.47	-27:50:00.75	21.11 ± 0.07	0.67	20.6	20.7	20.4
934	3:32:35.48	-27:45:56.27	21.68 ± 0.10	0.38	0.0	0.0	0.0
14169	3:32:35.52	-27:46:26.01	18.47 ± 0.01	1.20	17.6	17.3	17.3
1472	3:32:35.52	-27:47:15.67	21.68 ± 0.09	0.12	0.0	0.0	0.0
9218	3:32:35.54	-27:43:57.20	20.68 ± 0.05	0.55	20.8	20.5	20.5
20141	3:32:35.57	-27:50:20.83	20.58 ± 0.04	1.88	18.8	18.1	17.7
989	3:32:35.58	-27:44:38.20	18.26 ± 0.01	0.38	18.6	18.2	18.2
20119	3:32:35.60	-27:50:12.60	21.73 ± 0.11	0.62	20.7	20.6	20.5
2071	3:32:35.61	-27:49:43.89	18.54 ± 0.01	0.61	18.1	18.1	17.9
14168	3:32:35.63	-27:46:32.76	20.07 ± 0.02	0.57	19.7	19.4	19.4
14105	3:32:35.66	-27:47:48.71	21.04 ± 0.07	1.75	20.4	19.8	19.6
14138	3:32:35.71	-27:48:15.57	21.97 ± 0.10	0.88	21.2	21.2	21.0
14181	3:32:35.72	-27:46:38.73	21.32 ± 0.07	1.42	19.9	19.3	19.2
20206	3:32:35.72	-27:49:16.09	19.89 ± 0.03	2.40	18.1	17.5	16.8
960	3:32:35.73	-27:44:19.98	20.78 ± 0.05	0.95	20.1	20.0	20.0
20203	3:32:35.75	-27:49:09.45	21.16 ± 0.07	2.03	19.6	18.9	18.4
978	3:32:35.76	-27:44:32.49	21.85 ± 0.16	0.33	0.0	0.0	0.0
14123	3:32:35.76	-27:47:58.84	17.37 ± 0.00	0.70	16.8	16.8	16.7
14153	3:32:35.78	-27:46:27.42	19.20 ± 0.01	0.93	18.3	18.3	18.1
1439	3:32:35.78	-27:46:55.04	21.37 ± 0.07	1.53	20.3	19.8	19.7
9192	3:32:35.80	-27:45:48.96	20.73 ± 0.06	0.86	20.3	20.4	20.1
1488	3:32:35.81	-27:47:34.73	20.20 ± 0.02	1.08	19.0	18.8	18.8
14167	3:32:35.83	-27:46:43.65	21.40 ± 0.07	1.61	20.3	19.9	19.7
1470	3:32:35.83	-27:47:18.73	20.44 ± 0.04	0.21	0.0	0.0	0.0
14140	3:32:35.93	-27:48:17.33	21.35 ± 0.07	2.26	20.3	19.8	19.3
2040	3:32:35.93	-27:49:20.27	21.89 ± 0.13	0.95	21.2	21.1	21.0
14128	3:32:35.94	-27:48:04.25	21.86 ± 0.09	1.98	20.3	19.6	19.1
20153	3:32:35.95	-27:50:32.53	21.99 ± 0.11	0.56	21.5	21.3	21.3
14134	3:32:35.97	-27:48:11.89	18.71 ± 0.01	0.39	18.6	18.2	18.2
2049	3:32:35.97	-27:49:26.10	19.74 ± 0.03	0.48	19.6	19.4	19.3
20176	3:32:35.98	-27:48:50.43	19.06 ± 0.01	1.06	18.0	17.8	17.7
1491	3:32:36.00	-27:47:25.63	21.97 ± 0.10	2.99	20.4	19.7	19.1
966	3:32:36.03	-27:44:23.78	19.36 ± 0.01	1.00	18.6	18.3	18.4
20108	3:32:36.04	-27:50:04.23	19.22 ± 0.01	1.42	17.8	17.1	17.1
9157	3:32:36.07	-27:45:19.68	21.29 ± 0.07	0.28	21.1	21.0	21.4
20152	3:32:36.12	-27:50:32.34	21.54 ± 0.09	1.58	20.3	19.7	19.5
14147	3:32:36.15	-27:46:17.58	19.49 ± 0.03	0.41	19.5	19.4	19.4

id	RA(J2000)	DEC(J2000)	K_s	z_{phot}	[3.6]	[4.5]	[5.8]
2042	3:32:36.16	-27:49:22.23	21.22 ± 0.07	0.69	20.6	20.5	20.4
20160	3:32:36.17	-27:50:36.94	19.61 ± 0.02	1.55	18.1	17.4	17.2
14163	3:32:36.18	-27:46:27.53	21.15 ± 0.05	1.52	19.9	19.2	19.2
9177	3:32:36.19	-27:45:36.51	19.36 ± 0.02	0.31	19.7	19.4	19.6
1443	3:32:36.19	-27:46:57.20	21.78 ± 0.12	1.53	20.9	20.3	20.1
2057	3:32:36.19	-27:49:32.01	17.01 ± 0.00	0.60	16.3	16.2	16.0
976	3:32:36.21	-27:44:30.70	20.66 ± 0.05	1.21	19.8	19.4	19.5
1492	3:32:36.22	-27:47:26.26	20.34 ± 0.04	1.60	19.4	18.8	18.7
1410	3:32:36.24	-27:48:34.25	20.40 ± 0.05	1.08	19.5	19.2	19.2
2043	3:32:36.25	-27:49:24.03	21.06 ± 0.07	1.29	19.8	19.5	19.7
14178	3:32:36.27	-27:46:38.40	21.96 ± 0.12	0.88	21.2	21.2	21.1
9160	3:32:36.29	-27:45:21.32	21.65 ± 0.11	1.47	20.4	19.9	19.9
1422	3:32:36.29	-27:48:20.04	21.93 ± 0.10	0.71	21.2	21.2	21.1
984	3:32:36.31	-27:44:34.53	21.40 ± 0.06	3.58	20.3	19.5	19.0
9228	3:32:36.34	-27:44:07.36	20.38 ± 0.06	0.40	20.6	20.4	20.4
937	3:32:36.34	-27:46:00.04	19.77 ± 0.02	0.98	18.8	18.4	18.4
9198	3:32:36.37	-27:45:43.19	18.43 ± 0.01	0.41	0.0	0.0	0.0
9182	3:32:36.38	-27:45:40.63	20.79 ± 0.07	1.02	20.1	19.9	20.0
142	3:32:36.39	-27:48:39.39	21.78 ± 0.12	0.65	21.0	20.9	20.8
14103	3:32:36.41	-27:47:47.06	20.60 ± 0.04	0.17	0.0	0.0	0.0
9197	3:32:36.43	-27:43:38.58	19.80 ± 0.06	1.12	18.9	18.7	18.8
9142	3:32:36.44	-27:45:10.98	21.98 ± 0.12	1.13	20.9	20.7	20.8
14109	3:32:36.44	-27:47:50.58	20.52 ± 0.04	0.31	20.4	20.3	20.4
14161	3:32:36.46	-27:46:31.50	19.46 ± 0.02	1.00	18.8	18.6	18.5
1441	3:32:36.46	-27:46:55.09	21.30 ± 0.06	0.96	20.4	20.3	20.1
1446	3:32:36.46	-27:46:58.30	21.42 ± 0.06	0.86	20.6	20.7	20.4
972	3:32:36.47	-27:44:28.69	21.97 ± 0.11	1.31	20.7	20.3	20.2
977	3:32:36.48	-27:44:31.91	20.69 ± 0.06	0.84	20.3	20.4	20.1
14156	3:32:36.50	-27:46:29.11	18.91 ± 0.01	0.86	18.2	18.2	17.9
20103	3:32:36.51	-27:50:06.12	18.73 ± 0.01	0.73	18.3	18.4	18.1
9191	3:32:36.56	-27:45:42.62	20.50 ± 0.04	0.67	19.9	20.1	19.8
91	3:32:36.56	-27:46:12.37	21.61 ± 0.11	0.11	0.0	0.0	0.0
20102	3:32:36.59	-27:50:03.51	19.55 ± 0.02	0.80	18.9	19.0	18.6
912	3:32:36.61	-27:46:10.12	20.34 ± 0.08	0.53	20.2	20.0	19.8
20150	3:32:36.61	-27:50:30.85	21.14 ± 0.09	0.82	20.6	20.6	20.4
9123	3:32:36.67	-27:45:01.79	20.12 ± 0.02	1.00	18.9	18.7	18.7
14160	3:32:36.67	-27:46:30.97	19.51 ± 0.01	0.69	18.8	18.9	18.6
2012	3:32:36.69	-27:51:02.69	21.02 ± 0.07	0.62	20.4	20.6	20.3
9113	3:32:36.70	-27:44:57.30	21.20 ± 0.07	2.67	0.0	0.0	0.0
9225	3:32:36.72	-27:44:06.41	18.53 ± 0.01	0.93	17.7	17.6	17.5
144	3:32:36.76	-27:48:43.62	21.18 ± 0.16	0.20	0.0	0.0	0.0
947	3:32:36.83	-27:44:14.36	21.13 ± 0.07	0.53	21.1	20.8	20.8
149	3:32:36.88	-27:48:32.24	21.84 ± 0.09	0.53	0.0	0.0	0.0
921	3:32:36.91	-27:46:02.74	21.27 ± 0.11	1.46	20.3	19.8	20.0
14162	3:32:36.92	-27:46:28.45	20.42 ± 0.03	1.40	19.1	18.5	18.6
20140	3:32:36.92	-27:50:24.68	21.28 ± 0.07	0.43	0.0	0.0	0.0
14145	3:32:36.97	-27:46:15.72	21.49 ± 0.10	0.90	20.7	20.7	20.6
20194	3:32:37.04	-27:48:57.42	21.19 ± 0.09	0.91	20.5	20.6	20.4
2033	3:32:37.05	-27:49:17.41	21.35 ± 0.07	1.10	20.2	19.9	19.9
959	3:32:37.07	-27:44:19.05	21.30 ± 0.07	3.87	19.0	17.7	16.6
14136	3:32:37.07	-27:48:14.45	21.75 ± 0.08	1.30	20.3	19.9	20.0
9220	3:32:37.09	-27:44:02.13	20.54 ± 0.04	0.93	19.6	19.6	19.4
14148	3:32:37.09	-27:46:17.11	20.89 ± 0.06	2.41	19.4	18.9	18.2
2068	3:32:37.10	-27:49:40.99	20.88 ± 0.05	1.36	19.6	19.2	19.4
1430	3:32:37.11	-27:46:46.97	21.94 ± 0.11	0.98	0.0	0.0	0.0
14126	3:32:37.11	-27:48:03.93	21.86 ± 0.12	0.30	21.7	21.7	21.7
1490	3:32:37.13	-27:47:35.71	21.04 ± 0.06	0.28	20.8	20.7	20.9
14158	3:32:37.15	-27:46:25.87	20.82 ± 0.04	0.92	19.5	19.3	19.1
944	3:32:37.18	-27:43:50.40	21.62 ± 0.13	3.76	20.2	19.4	18.7
1416	3:32:37.20	-27:48:33.72	20.11 ± 0.05	1.45	19.3	18.9	18.9
2055	3:32:37.20	-27:49:29.55	21.92 ± 0.16	1.17	21.1	20.7	20.8
919	3:32:37.21	-27:46:08.35	17.09 ± 0.01	1.00	16.6	16.3	16.4
2061	3:32:37.23	-27:49:35.34	21.28 ± 0.08	2.25	20.0	19.4	18.8
20114	3:32:37.29	-27:50:08.90	19.97 ± 0.03	1.01	18.8	18.5	18.5
931	3:32:37.31	-27:45:57.87	20.15 ± 0.03	1.04	18.9	18.6	18.6

id	RA(J2000)	DEC(J2000)	K_s	z_{phot}	[3.6]	[4.5]	[5.8]
1476	3:32:37.31	-27:47:29.10	16.70 ± 0.00	0.80	16.1	16.2	15.9
1426	3:32:37.37	-27:46:45.47	20.11 ± 0.02	1.62	18.9	18.2	18.0
20121	3:32:37.38	-27:50:13.54	20.45 ± 0.05	1.06	19.5	19.2	19.2
9111	3:32:37.40	-27:44:56.88	21.00 ± 0.06	0.22	20.9	20.9	21.0
9232	3:32:37.41	-27:44:06.93	18.94 ± 0.01	0.98	17.8	17.5	17.5
1495	3:32:37.42	-27:47:41.60	20.89 ± 0.04	1.03	20.1	19.9	19.8
2037	3:32:37.42	-27:49:20.09	21.51 ± 0.09	0.81	20.9	20.9	20.6
95	3:32:37.43	-27:46:12.33	21.26 ± 0.12	1.05	0.0	0.0	0.0
20138	3:32:37.44	-27:50:24.69	21.73 ± 0.14	1.20	20.7	20.4	20.4
2080	3:32:37.49	-27:49:36.48	21.94 ± 0.14	1.25	20.8	20.3	20.3
9167	3:32:37.50	-27:45:26.53	21.89 ± 0.09	0.86	20.9	21.0	20.8
2098	3:32:37.51	-27:49:59.80	20.99 ± 0.04	1.55	19.4	18.7	18.5
1414	3:32:37.53	-27:48:38.92	18.66 ± 0.01	0.76	18.3	18.3	18.1
9120	3:32:37.55	-27:45:01.95	20.69 ± 0.07	1.49	19.8	19.2	19.2
2050	3:32:37.58	-27:49:27.65	21.97 ± 0.13	3.37	20.7	20.0	19.5
20156	3:32:37.60	-27:50:35.60	19.08 ± 0.02	0.71	18.8	18.9	18.6
2046	3:32:37.62	-27:49:23.13	20.82 ± 0.05	1.41	19.5	19.0	19.1
954	3:32:37.63	-27:44:18.80	20.91 ± 0.07	0.79	20.4	20.7	20.2
1496	3:32:37.63	-27:47:43.96	19.49 ± 0.01	1.06	18.6	18.3	18.3
953	3:32:37.70	-27:44:16.17	19.95 ± 0.03	1.07	19.0	18.7	18.7
2069	3:32:37.71	-27:49:41.93	21.44 ± 0.07	1.20	20.2	19.9	20.1
9124	3:32:37.74	-27:45:05.38	20.06 ± 0.03	4.73	17.9	17.1	16.3
1452	3:32:37.75	-27:47:06.93	19.70 ± 0.02	0.49	19.5	19.2	19.1
2099	3:32:37.75	-27:50:00.63	19.11 ± 0.01	1.52	17.7	17.0	16.9
14121	3:32:37.76	-27:47:54.39	21.43 ± 0.06	0.64	20.6	20.8	20.5
2088	3:32:37.78	-27:49:55.40	20.93 ± 0.05	0.83	20.0	20.1	19.8
14125	3:32:37.85	-27:47:56.34	21.13 ± 0.07	2.62	19.8	19.3	18.6
14117	3:32:37.88	-27:47:50.97	20.48 ± 0.04	0.87	19.9	19.9	19.8
9168	3:32:37.89	-27:45:18.64	21.23 ± 0.06	0.93	20.3	20.3	20.2
9131	3:32:37.90	-27:45:07.97	21.17 ± 0.06	1.05	20.2	19.9	20.1
20177	3:32:37.90	-27:48:52.76	20.91 ± 0.07	0.11	20.9	20.9	21.1
20125	3:32:37.93	-27:50:18.15	20.91 ± 0.05	1.10	19.9	19.6	19.6
1436	3:32:37.97	-27:46:51.99	19.96 ± 0.03	0.71	19.6	19.6	19.5
9219	3:32:37.99	-27:44:03.81	19.36 ± 0.03	1.10	18.7	18.5	18.5
14157	3:32:38.04	-27:46:26.22	20.83 ± 0.04	1.51	19.3	18.7	18.6
2086	3:32:38.05	-27:49:54.61	21.54 ± 0.10	0.99	20.5	20.3	20.4
982	3:32:38.12	-27:44:32.77	18.13 ± 0.01	1.21	17.4	17.0	17.2
14108	3:32:38.12	-27:47:49.67	20.16 ± 0.02	1.72	18.7	18.1	17.8
94	3:32:38.13	-27:46:14.20	20.02 ± 0.06	1.00	19.2	19.0	19.1
20136	3:32:38.13	-27:50:22.02	21.74 ± 0.11	1.40	20.5	20.0	20.1
9139	3:32:38.16	-27:45:13.31	18.53 ± 0.01	0.94	17.6	17.4	17.4
2087	3:32:38.18	-27:49:57.40	19.52 ± 0.03	0.63	19.0	19.1	18.8
20181	3:32:38.23	-27:48:49.21	20.82 ± 0.09	0.51	0.0	0.0	0.0
9106	3:32:38.26	-27:44:55.05	18.27 ± 0.01	0.71	17.7	17.8	17.5
917	3:32:38.29	-27:46:04.12	20.55 ± 0.05	1.13	19.1	18.8	18.8
20131	3:32:38.31	-27:50:21.03	21.48 ± 0.13	3.31	20.5	19.8	19.2
20122	3:32:38.34	-27:50:13.43	20.21 ± 0.04	0.57	19.6	19.5	19.3
9187	3:32:38.35	-27:45:44.18	21.31 ± 0.12	1.13	20.2	19.9	20.0
20145	3:32:38.36	-27:50:28.83	18.95 ± 0.02	0.69	18.5	18.6	18.3
2014	3:32:38.36	-27:51:00.92	20.91 ± 0.08	3.23	19.8	19.0	18.5
923	3:32:38.41	-27:46:00.77	20.97 ± 0.11	1.07	20.5	20.2	20.4
14164	3:32:38.45	-27:46:31.90	18.57 ± 0.01	0.51	18.5	18.2	18.1
2062	3:32:38.47	-27:49:31.91	19.66 ± 0.02	0.74	18.9	19.0	18.6
952	3:32:38.48	-27:44:15.96	21.54 ± 0.13	0.62	21.0	21.0	20.8
1449	3:32:38.49	-27:47:02.44	18.07 ± 0.01	0.84	17.4	17.5	17.2
1474	3:32:38.51	-27:47:25.23	21.48 ± 0.07	0.18	0.0	0.0	0.0
1481	3:32:38.56	-27:47:30.35	21.67 ± 0.08	2.53	20.1	19.5	18.8
985	3:32:38.57	-27:44:34.25	21.72 ± 0.13	0.98	20.9	20.7	20.7
20118	3:32:38.57	-27:50:09.06	21.67 ± 0.14	1.14	20.8	20.5	20.5
9119	3:32:38.59	-27:44:59.97	20.41 ± 0.05	1.00	19.5	19.2	19.3
14173	3:32:38.60	-27:46:31.33	18.98 ± 0.01	0.56	18.7	18.6	18.5
9201	3:32:38.64	-27:43:43.47	20.70 ± 0.10	1.07	19.6	19.4	19.5
1459	3:32:38.64	-27:47:11.44	21.37 ± 0.06	1.06	20.4	20.2	20.2
1468	3:32:38.65	-27:47:18.17	21.86 ± 0.14	1.00	21.1	20.8	20.9
2034	3:32:38.67	-27:49:19.24	21.17 ± 0.11	0.74	20.8	20.9	20.6

id	RA(J2000)	DEC(J2000)	K_s	z_{phot}	[3.6]	[4.5]	[5.8]
20173	3:32:38.67	-27:50:46.91	18.81 ± 0.01	0.59	18.3	18.3	18.1
9235	3:32:38.70	-27:44:02.81	21.76 ± 0.17	0.88	21.0	21.0	20.9
1499	3:32:38.72	-27:47:44.03	20.85 ± 0.05	0.10	20.9	20.8	20.8
14133	3:32:38.76	-27:48:10.03	21.26 ± 0.07	0.50	20.8	20.6	20.5
9100	3:32:38.79	-27:44:48.91	18.15 ± 0.01	0.81	17.4	17.6	17.2
913	3:32:38.79	-27:46:03.51	21.52 ± 0.13	0.81	20.8	21.0	20.6
1464	3:32:38.79	-27:47:14.84	20.23 ± 0.03	1.57	19.2	18.7	18.5
1483	3:32:38.79	-27:47:32.33	18.32 ± 0.01	0.54	18.0	17.7	17.8
1431	3:32:38.80	-27:46:48.92	18.37 ± 0.01	0.60	17.9	17.8	17.7
20201	3:32:38.81	-27:49:09.27	19.66 ± 0.04	0.75	19.1	19.2	18.9
2051	3:32:38.82	-27:49:28.44	19.25 ± 0.02	0.79	18.4	18.6	18.2
2084	3:32:38.82	-27:49:56.28	16.52 ± 0.00	0.54	16.1	16.0	15.8
9208	3:32:38.86	-27:43:44.66	20.77 ± 0.08	1.09	19.8	19.6	19.6
20171	3:32:38.86	-27:50:45.03	18.01 ± 0.01	0.98	16.9	16.6	16.5
14159	3:32:38.89	-27:46:26.08	20.90 ± 0.04	0.29	20.8	20.8	20.8
20198	3:32:38.89	-27:49:06.17	21.99 ± 0.18	1.19	20.8	20.4	20.4
14141	3:32:38.92	-27:48:19.47	20.95 ± 0.05	0.51	0.0	0.0	0.0
9221	3:32:38.95	-27:44:03.26	21.91 ± 0.16	0.69	21.5	21.5	21.4
999	3:32:38.95	-27:44:46.03	19.86 ± 0.05	0.94	19.4	19.3	19.3
20155	3:32:38.95	-27:50:33.22	21.55 ± 0.14	1.03	20.2	19.9	19.8
968	3:32:38.96	-27:44:26.13	20.87 ± 0.08	0.69	20.2	20.4	20.1
2064	3:32:38.96	-27:49:37.10	21.13 ± 0.09	0.63	20.2	20.4	20.1
14170	3:32:38.98	-27:46:30.22	18.39 ± 0.01	0.53	18.3	18.1	18.1
9231	3:32:39.00	-27:44:08.77	21.98 ± 0.23	1.41	21.0	20.6	20.6
20192	3:32:39.03	-27:48:59.37	22.00 ± 0.19	0.20	0.0	0.0	0.0
994	3:32:39.04	-27:44:20.31	18.88 ± 0.03	0.39	0.0	0.0	0.0
992	3:32:39.05	-27:44:39.13	21.44 ± 0.14	2.79	19.8	19.2	18.5
14115	3:32:39.12	-27:47:51.45	21.10 ± 0.04	1.92	19.5	18.9	18.5
209	3:32:39.15	-27:51:04.86	21.57 ± 0.18	1.92	20.1	19.5	19.2
146	3:32:39.17	-27:48:32.33	21.18 ± 0.05	2.71	19.8	19.2	18.6
20183	3:32:39.17	-27:48:49.15	21.77 ± 0.29	1.41	21.0	20.6	20.6
2028	3:32:39.17	-27:48:44.46	16.23 ± 0.01	0.58	15.7	15.8	15.5
14127	3:32:39.22	-27:47:58.25	17.63 ± 0.00	0.70	17.0	17.0	16.8
14152	3:32:39.36	-27:46:23.30	21.82 ± 0.13	2.43	20.5	20.0	19.4
143	3:32:39.43	-27:48:38.94	20.70 ± 0.04	0.49	20.3	20.0	19.9
1456	3:32:39.65	-27:47:09.12	19.11 ± 0.01	1.03	18.0	17.8	17.9
14142	3:32:39.75	-27:46:11.29	19.58 ± 0.03	1.47	18.3	17.8	17.7
1437	3:32:39.81	-27:46:53.56	19.93 ± 0.03	1.01	18.9	18.6	18.6
1460	3:32:39.89	-27:47:14.94	18.83 ± 0.01	1.05	18.1	17.8	17.7
1493	3:32:39.89	-27:47:38.11	21.55 ± 0.08	0.92	20.5	20.5	20.4
14112	3:32:40.05	-27:47:51.56	21.93 ± 0.11	0.91	21.1	21.2	20.9
14124	3:32:40.06	-27:47:55.37	19.64 ± 0.02	1.44	18.7	18.2	18.2
1484	3:32:40.06	-27:47:31.90	21.98 ± 0.11	0.61	21.1	21.2	21.0
1451	3:32:40.09	-27:47:04.80	21.88 ± 0.09	1.61	20.6	20.0	19.8
1482	3:32:40.18	-27:47:30.64	21.40 ± 0.07	0.50	21.1	20.9	20.8
1485	3:32:40.22	-27:47:33.00	20.78 ± 0.04	1.01	20.0	19.9	19.8
14114	3:32:40.30	-27:47:52.52	21.98 ± 0.11	0.30*	0.0	0.0	0.0
1473	3:32:40.33	-27:47:22.73	20.78 ± 0.04	0.67	20.2	20.1	20.0
1417	3:32:40.33	-27:48:26.69	21.87 ± 0.11	0.40	0.0	0.0	0.0
14122	3:32:40.36	-27:47:59.39	21.05 ± 0.06	0.71	20.4	20.5	20.2
14113	3:32:40.42	-27:47:52.33	21.21 ± 0.07	0.59	20.4	20.4	20.2
145	3:32:40.65	-27:48:37.32	21.60 ± 0.12	3.29	20.3	19.6	19.1
1479	3:32:40.67	-27:47:30.88	18.19 ± 0.01	0.51	17.9	17.6	17.5
14107	3:32:40.75	-27:47:49.46	20.78 ± 0.06	1.74	19.7	19.1	18.7
1423	3:32:40.79	-27:46:15.62	17.64 ± 0.01	0.60	17.3	17.3	17.2
1454	3:32:40.88	-27:47:06.92	21.91 ± 0.10	0.51	21.6	21.3	21.3
1438	3:32:40.98	-27:46:55.13	20.70 ± 0.04	0.52	20.3	20.1	20.0
14139	3:32:40.99	-27:48:16.87	21.30 ± 0.07	1.62	20.4	19.9	19.8
14166	3:32:41.03	-27:46:31.43	21.71 ± 0.12	3.26	20.6	19.8	19.2
1489	3:32:41.12	-27:47:34.55	21.63 ± 0.10	0.89	20.9	20.9	20.7
14151	3:32:41.13	-27:46:18.02	21.85 ± 0.09	1.57	20.5	19.8	19.6
14143	3:32:41.32	-27:46:13.28	21.19 ± 0.07	0.78	20.2	20.4	19.9
1421	3:32:41.32	-27:48:21.18	21.48 ± 0.09	0.10	0.0	0.0	0.0
14101	3:32:41.40	-27:47:46.80	19.44 ± 0.02	0.38	19.4	19.2	19.2
1465	3:32:41.42	-27:47:17.22	17.61 ± 0.01	0.69	17.1	17.1	17.0

id	RA(J2000)	DEC(J2000)	K_s	z_{phot}	[3.6]	[4.5]	[5.8]
1434	3:32:41.43	-27:46:51.43	18.98 ± 0.01	0.50	18.7	18.5	18.4
14183	3:32:41.53	-27:46:40.31	21.39 ± 0.07	1.01	20.5	20.3	20.3
14111	3:32:41.56	-27:47:47.90	20.91 ± 0.05	0.57	20.5	20.4	20.2
14119	3:32:41.59	-27:47:57.22	21.57 ± 0.09	0.23	21.5	21.4	21.5
14110	3:32:41.67	-27:47:50.44	21.39 ± 0.07	0.71	20.6	20.7	20.4
1415	3:32:41.68	-27:48:29.65	21.37 ± 0.06	1.62	20.2	19.7	19.5
1440	3:32:41.69	-27:46:55.41	21.65 ± 0.07	1.75	20.0	19.3	19.1
1418	3:32:41.76	-27:48:24.98	21.87 ± 0.12	3.40	20.5	19.8	19.3
14149	3:32:41.77	-27:46:19.33	18.17 ± 0.01	0.31	18.1	17.9	18.0
1442	3:32:41.84	-27:46:57.06	20.91 ± 0.05	1.46	19.9	19.5	19.6
1435	3:32:41.88	-27:46:51.19	21.15 ± 0.06	0.78	20.4	20.4	20.2
14120	3:32:41.94	-27:47:57.28	18.47 ± 0.01	0.57	18.6	18.4	18.4
14154	3:32:42.27	-27:46:25.16	19.93 ± 0.03	1.19	19.1	18.8	18.8
14102	3:32:42.29	-27:47:46.00	18.67 ± 0.01	0.95	17.9	17.7	17.6
1424	3:32:42.31	-27:46:43.96	21.72 ± 0.09	1.73	20.2	19.6	19.2
1444	3:32:42.36	-27:46:57.03	21.93 ± 0.09	0.64	21.1	21.0	20.9
1455	3:32:42.38	-27:47:07.60	19.26 ± 0.01	1.08	18.0	17.8	17.8
1487	3:32:42.74	-27:47:33.85	20.45 ± 0.03	1.22	19.2	18.9	18.9
1448	3:32:42.78	-27:46:59.03	20.90 ± 0.04	1.09	20.1	19.9	19.9
1450	3:32:42.84	-27:47:02.56	21.96 ± 0.09	3.20	20.9	19.9	19.4
14132	3:32:42.88	-27:48:09.42	21.92 ± 0.08	2.90	20.5	19.9	19.4
1457	3:32:42.99	-27:47:09.63	21.31 ± 0.08	0.57	21.0	20.8	20.7
1432	3:32:43.00	-27:46:49.73	19.20 ± 0.01	0.91	18.1	18.1	17.9
141	3:32:43.19	-27:48:42.48	21.41 ± 0.12	0.83	20.8	20.9	20.6
14118	3:32:43.26	-27:47:56.08	17.87 ± 0.01	0.52	17.7	17.6	17.5
1427	3:32:43.33	-27:46:46.65	21.59 ± 0.11	3.18	19.8	18.8	18.0
1497	3:32:43.35	-27:47:43.55	21.31 ± 0.09	1.51	20.6	20.0	19.9
1462	3:32:43.46	-27:47:13.24	21.21 ± 0.09	0.99	20.4	20.1	20.2
14174	3:32:43.47	-27:46:34.08	19.37 ± 0.01	0.60	18.7	18.7	18.6
1466	3:32:43.58	-27:47:16.68	22.00 ± 0.12	2.81	21.7	21.6	21.5
1445	3:32:43.60	-27:46:58.93	20.43 ± 0.05	1.57	19.4	18.8	18.6
14129	3:32:43.60	-27:48:04.68	20.13 ± 0.02	0.80	19.3	19.3	19.1
1428	3:32:43.70	-27:46:46.29	21.61 ± 0.07	0.10	21.4	21.3	21.5
1463	3:32:43.96	-27:47:14.18	21.97 ± 0.18	1.29	21.1	20.8	21.0
14172	3:32:44.03	-27:46:34.81	21.00 ± 0.07	0.29	21.0	20.9	21.2
1478	3:32:44.20	-27:47:29.50	20.19 ± 0.03	1.41	18.9	18.5	18.4
1486	3:32:44.20	-27:47:33.51	19.10 ± 0.01	0.81	18.4	18.4	18.2
1475	3:32:44.35	-27:47:23.91	20.61 ± 0.05	0.89	19.8	19.7	19.5
14179	3:32:44.36	-27:46:38.66	21.24 ± 0.09	0.67	20.6	20.7	20.4
14175	3:32:44.44	-27:46:41.72	20.71 ± 0.07	0.53	0.0	0.0	0.0
1413	3:32:44.45	-27:48:19.13	17.51 ± 0.01	0.43	17.6	17.2	17.2
147	3:32:44.62	-27:48:36.17	21.26 ± 0.11	0.84	20.6	20.6	20.3
14171	3:32:44.65	-27:46:31.92	20.53 ± 0.06	0.92	19.5	19.4	19.3
14116	3:32:44.75	-27:47:53.06	21.26 ± 0.10	1.51	20.0	19.4	19.3

Bibliography

[1] Lifshitz E.M., 1946, Sov.Phys. JETP **10**, 116

[2] Longair M.S., 1998, *Galaxy Formation*, Springer-Verlag

[3] Peacock J.A., 1999, *Cosmological Physics*, Cambridge University Press

[4] Efstathiou G., Bond J.R., White S.D.M., 1992, MNRAS **258**, 1

[5] Perlmutter S. et al., 1999, ApJ **517**, 565

[6] Bennett C.L. et.al., 2003, ApJS **148**, 1

[7] Press W.H., Schechter P., 187, ApJ **187**, 425

[8] White S.D.M., Rees M.J., 1978, MNRAS **183**, 341

[9] White S.D.M., Frenk C.S., 1991, ApJ **379**, 52

[10] Ellis R.S., Smail I., Dressler A., Couch W.J., Oemler A. Jr., Butcher H., Sharples R.M., 1997, ApJ **483**, 582

[11] Elston R., Rieke G.H., Rieke M.J., 1988, ApJ **331**, L77

[12] Hawley S.L. et al., 2002, ApJ **123**, 3409

[13] Bressan A., Fagotto F., Bertelli G., Chiosi C., 1993, A&AS **100**, 647

[14] Binney J., Merrifield M., 1998, *Galactic Astronomy*, Princeton University Press

[15] Bruzual G. A., Charlot S., 1993, ApJ **405**, 538

[16] Dunlop J.S., Peacock J., Spinrad H., Dey A., Jiménez R., Stern D., Windhorst R., 1996, Nature **381**, 581

[17] Nolan L.A., Dunlop J.S., Jiménez R., 2001, MNRAS **323**, 385

[18] Puget J.-L., Abergel A, Bernard J.-P., Boulanger F., Burton W.B., Désert F.-X., Hartmann D., 1996, A&A **308**, L5

[19] Chandrasekhar S., 1960, *Radiative Transfer*, Dover Publications, New York

[20] Calzetti D., 2001, PASP **113**, 1449

[21] Seaton M.J., 1979, MNRAS **187**, 73

[22] Cardelli J.A., Clayton G.C., Mathis J.S., 1989, ApJ **345**, 245

[23] Schlegel D.J., Finkbeiner D.P., Davis M., 1998, ApJ **500**, 525

[24] Faber S. M., Wegner G., Burstein D., Davies R. L., Dressler A., Lynden-Bell D., Terlevich R. J., 1989, ApJS **69**, 763

[25] Fitzpatrick E.L., 1986, AJ **92**, 1068

[26] Prévot M.L., Lequeux J., Prévot L., Maurice E., Rocca-Volmerange B., 1984, A&A **132**, 389

[27] Calzetti D., Armus L., Bohlin R., Kinney A., Koornneef J., Storchi-Bergmann T., 2000, ApJ **533**, 682

[28] Steidel C.C., Adelberger K.L., Giavalisco M., Dickinson M., Pettini M., 1999, ApJ **519**, 1

[29] Baade W., 1958, *Stellar Populations*, O'Connell D.J.K., ed., 3

[30] Tinsley B.M., Gunn J.E., 1976, ApJ **203**, 52

[31] Bower R.G., Lucey J.R., Ellis R.S., 1992, MNRAS **254**, 589

[32] McCarthy P.J., Persson S.E., West S.C., 1992, ApJ **386**, 52

[33] Graham J.R., Dey A., 1996, ApJ **471**, 720

[34] Cimatti A. et al., 1999, A&A **352**, L45

[35] Cimatti A. et al., 2002, A&A **392**, 395

[36] Cimatti A. et al., 2002, A&A **381**, L68

[37] Daddi E. et al., 2002, A&A **384**, L1

[38] Scott S.E. et al., 2002, MNRAS **331**, 817

[39] Blain A.W., Chapman S.C., Smail I., Ivison R., 2004, ApJ **611**, 725

[40] Firth A.E. et al., 2002, MNRAS **332**, 617

[41] Kauffmann G., Charlot S., 1998, MNRAS **297**, L23

[42] Smail I., Owen F.N., Morrison G.E., Keel W.C., Ivison R.J., Ledlow M.J., 2002, ApJ **581**, 844

[43] Roche N.D., Almaini O., Dunlop J.S., Ivison R.J., Willott C.J., 2002, MNRAS **337**, 1282

[44] Miyazaki M. et al., 2003, PASJ **55**, 1079

[45] Yan L., Thompson D., 2003, ApJ **586**, 765

[46] Daddi E. et al., 2000, A&A **361**, 535

[47] Roche N.D., Dunlop J.S., Almaini O., MNRAS **346**, 803 (R03)

[48] Daddi E. et al., 2003, ApJ **588**, 50

[49] Overzier R.A., Röttgering H.J.A., Rengelink R.B., Wilman R.J., 2003, A&A **405**, 53

[50] Conselice C.J., Bershady M.A., Dickinson M., Papovich C., 2003, AJ **126**, 1183

[51] Sérsic J.L., 1968, *Atlas de galaxias australes*, Observatorio Astronómico de Córdoba

[52] de Vaucouleurs G., 1948, Ann. Astrophys. **11**, 247

[53] Stiavelli M., Treu T., 2000, in *Galaxy Disks and Disks Galaxies*, ASP Conference Series, Funes J.G., Corsini E.M., eds.

[54] Moriondo G., Cimatti A., Daddi E., 2000, A&A **364**, 26

[55] Moustakas L.A. et al., 2004, ApJ **600**, L131

[56] Yan L., Thompson D., Soifer B.T., 2004, ApJ **127**, 1274

[57] Pozzetti L., Mannucci F., 2000, MNRAS **317**, L17

[58] Cimatti A. et al., 2003, A&A **412**, L1

[59] Tinsley B.M., 1980, ApJ **241**, 41

[60] Bruzual A.G., Kron R.G., 1980, ApJ **241**, 25

[61] Pozzetti L., Bruzual A.G., Zamorani G., 1996, MNRAS **281**, 953

[62] Kauffmann G., White S. D. M., Guiderdoni B., MNRAS **264**, 201

[63] Cole S., Aragón Salamanca A., Frenk C.S., Navarro J.F., Zepf S.E., 1994, MNRAS **271**, 781

[64] Somerville R.S., Primack J.R., MNRAS **310**, 1087

[65] Marzke R.O., Geller M.J., Huchra J.P., Corwin H.G., 1994, AJ **108**, 437

[66] Kochanek C.S. et al., 2001, ApJ **560**, 566

[67] Cimatti A. et al., 2002, A&A **391**, L1

[68] Fontana A. et al., 1999, MNRAS **310**, L27

[69] Somerville R.S. et al., 2004, ApJ **600**, L135

[70] Mobasher B. et al., 2004, 2004, ApJ **600**, L167

[71] Somerville R.S., Primack J.R., Faber S.M., 2001, MNRAS **320**, 504

[72] Daddi E., Cimatti A., Renzini A., 2000, A&A **362**, L45

[73] Devriendt J.E.G., Guiderdoni B., 2000, A&A **363**, 851

[74] Somerville R., 2004, Proceedings of the ESO/USM/MPE Workshop on *Multi-wavelength Mapping of Galaxy Formation and Evolution*, eds. R. Bender and A. Renzini

[75] Baugh C.M. et al., 2004, MNRAS submitted (astro-ph/0406069)

[76] Granato G.L., de Zotti G., Silva L., Bressan A., Danese L., 2004, ApJ **600**, 580

[77] Balland C., Devriendt J.E.G., Silk J., 2003, MNRAS **343**, 107

[78] Dickinson M. et al., 2000, ApJ **531**, 624

[79] Totani T., Yoshii Y., Iwamuro F., Maihara T., Motohara K., 2001, ApJ **558**, L87

[80] Franx M. et al., 2003, ApJ **587**, L79

[81] McLure R.J., Kukula M.J., Dunlop J.S., Baum S.A., O'Dea C.P., Hughes D.H., 1999, MNRAS **308**, 377

[82] Spinrad H., Dey A., Stern D., Dunlop J., Peacock J., Jiménez R., Windhorst R., 1997, ApJ **484**, 581

[83] Dunlop J.S., 1999, in *The Most Distant Radio Galaxies*, Best P.N., Röttgering H.J.A., Lenhert M.D., eds., 14

[84] Willott C.J., Rawlings S., Blundell K.M., 2001, MNRAS **324**, 1

[85] Cimatti A., Villani D., Pozzetti L., di Serego Alighieri S., 2000, MNRAS **318**, 453

[86] Best P.N., Lenhert M.D., Miley G.K., Röttgering H.J.A., 2003, MNRAS **343**, 1

[87] van der Kruit P.C., 1973, A&A **29**, 263

[88] Hélou G., Bicay M.D., 1993, ApJ **415**, 93

[89] Yan L. et al., 2004, ApJS **154**, 75

[90] Cimatti A., Andreani P., Röttgering H.J.A., Tilanus R., 1998, Nature **392**, 895

[91] Dey A., Graham J.R., Ivison R.J., Smail I., Wright G.S., Liu M.C., 1999, ApJ **519**, 610

[92] Ivison R.J. et al., 2002, MNRAS **337**, 1

[93] Wehner E.H., Barger A.J., Kneib J.-P., 2002, ApJ *577*, L83

[94] Webb T.M.A., Brodwin M., Eales S., Lilly S.J., 2004, ApJ **605**, 645

[95] Frayer D.T., Reddy N.A., Armus L., Blain A.W., Scoville N.Z., Smail I., 2004, AJ **127**, 728

[96] Mushotzky R.F., Cowie L.L., Barger A.J., Arnaud K.A., 2000, Nature **404**, 459

[97] Lehmann I. et al., 2001, A&A **371**, 833

[98] Cowie L.L. et al., 2001, ApJ **551**, L9

[99] Alexander D.M., Vignali C., Bauer F.E., Brandt W.N., Hornschemeier A.E., Garmire G.P., Schneider D.P., 2002, AJ **123**, 1149

[100] Franceschini A., Fadda D., Cesarsky C.J., Elbaz D., Flores H., Granato G.L., 2002, ApJ **568**, 470

[101] Mainieri V. et al., 2002, A&A **393**, 425

[102] Brusa M., Comastri A., Daddi E., Cimatti A., Mignoli M., Pozzetti L., 2002, ApJ **581**, L89

[103] Stevens J.A., Page M.J., Ivison R.J., Smail I., Lehmann I., Hasinger G., Szokoly G., 2003, MNRAS **342**, 249

[104] Giavalisco M. et al., 2004, ApJ **600**, L93 m E

[105] Bertin E., Arnouts S., 1996, A&A **117**, 393

[106] Bertin E., *SExtractor v2.1.3 user's guide*, Institut d'Astrophysique & Observatoire de Paris

[107] Baum W.A., 1962, IAU Symposium **15**, 390

[108] Connolly A.J., Csabai I., Szalay A.S., Koo D.C., Kron R.G., Munn J.A., 1995, AJ **110**, 2655

[109] Bolzonella M., Miralles J.-M., Pelló R., 2000, A&A **363**, 476

[110] Bruzual A. G., Charlot S., 1993, ApJ **405**, 538

[111] Coleman G.D., Wu C.-C., Weedman D.W., 1980, ApJS **43**, 393

[112] Allen C.W., 1976, in *Astrophysical Quantities*, University of London eds., Athlone

[113] Bouchet P., Lequeux J., Maurice E., Prévot L., Prévot-Burnichon M.L., 1985, A&A **149**, 330

[114] Benítez N., 2000, ApJ **536**, 571

[115] Loredo T., 1992, *The Promise of Bayesian Inference for Astrophysics*, in *Statistical Challenges in Modern Astronomy*, Feigelson E.D., Babu G.J., eds., Springer-Verlag, New York

[116] Willott C.J., Rawlings S., Jarvis M.J., Blundell K.M., 2003, MNRAS **339**, 173

[117] Poggianti B.M., 1997, A&AS **122**, 399

[118] Cole S. et al., 2001, MNRAS **326**, 255

[119] Saracco P. et al. 2004, A&A **420**, 125

[120] Bruzual G., Charlot S., 2003, MNRAS **344**, 1000

[121] Somerville R. S., Lee K., Ferguson H. C., Gardner J. P., Moustakas L. A., Giavalisco M., 2004, ApJ **600**, L171

[122] Bolzonella M., Pelló R., Maccagni D., 2002, A&A **395**, 443

[123] Dunlop J.S., 2001, in *FIRSED2000, New Astronomy Reviews* **45**, van Bemmel I.M., Wilkes B., Barthel P., ed., Elsevier, 609

[124] Aretxaga I., Hughes D.H., Chapin E.L., Gaztañaga E., Dunlop J.S., Ivison R.J., 2003, MNRAS **342**, 759

[125] Chapman S.C., Blain A.W., Ivison R.J., Smail I.R., 2003, Nature **422**, 695

[126] Stanway E.R., Bunker A.J., McMahon R.G., 2003, MNRAS **342**, 439

[127] Bouwens R.J. et al., 2003, ApJ **595**, 589

[128] Bremer M.N., Lenhert M.D., Waddington I., Hardcastle M.J., Boyce P.J., Phillipps S., 2004, MNRAS **347**, L7

[129] Dickinson M. et al., 2004, ApJ **600**, L99

[130] Mainieri V., 2003, PhD thesis, Univ. Roma Tre

[131] Szokoly G.P. et al., 2004, ApJS accepted (astro-ph/0312324)

[132] Vanzella E. et al., 2004, A&A submitted (astro-ph/0406591)

[133] Le Fèvre O. et al., 2004, A&A submitted, (astro-ph/0403628)

[134] Drory N., Bender R., Feulner G., Hopp U., Maraston C., Snigula J., Hill G. J., 2003, ApJ **595**, 698

[135] Kodama T. et al., 2004, MNRAS **350**, 1005

[136] Glazebrook K. et al., 2004, Nature **430**, 181

[137] Drory N., Bender R., Feulner G., Hopp U., Maraston C., Snigula J., Hill G.J., 2004, ApJ **608**, 742

[138] Fontana A. et al., 2004, A&A **424**, 23

[139] Dickinson M., Papovich C., Ferguson H., Budavári T., 2003, ApJ **587**, 25

[140] Fontana A. et al., 2003, ApJ **594**, L9

[141] Rudnick G. et al., 2003, ApJ **599**, 847

[142] Franx M. et al., 2003, ApJ **587**, L79

[143] Bell E.F., McIntosh D.H., Katz N., Weinberg M.D., 2003, ApJS **149**, 289

[144] Heavens A., Panter B., Jiménez R., Dunlop J., 2004, Nature **428**, 625

[145] Mo H.J., Jing Y.P, White S.D.M., 1997, MNRAS **284**, 189

[146] Fazio G. G. et al., 2004, to appear in the ApJ Supp. Spitzer issue (astro-ph/0405616)

[147] Wilson G. et al., 2004, to appear in the ApJ Supp. Spitzer issue (astro-ph/0405612)

[148] Yan H. et al., 2004, ApJ accepted (astro-ph/0408070)

[149] Takamiya M., 1999, ApJS **122**, 109

[150] Hubble E.P., 1936, *The Realm of the Nebulae*, Yale University Press, New Haven

[151] de Vaucouleurs G., 1974, *The Formation and Dynamics of Galaxies*, D. Reidel Publishing Company, Dordrecht

[152] Sandage A.R., 1975, in Stars and Stellar systems - Galaxies and the Universe, Sandage et al. eds., University of Chicago Press, Chicago

[153] Caon N., Capaccioli M., D'Onofrio M., 1993, MNRAS **265**, 1013

[154] Conselice C.J., Bershady M.A., Jangren A., 2000, ApJ **529**, 886

[155] Ravindranath S. et al., 2004, ApJ **604**, L9

[156] Conselice C., Blackburne J.A., Papovich C., 2004, ApJ accepted (astro-ph/0405001)

[157] Trujillo I. et al., 2004, ApJ **604**, 521

[158] McLure R.J., Dunlop J.S., Kukula M.J., 2000, MNRAS **318**, 693

[159] Press W.H. et al., 1989, *Numerical Recipes - The Art of Scientific Computing*, Cambridge University Press

[160] Dressler A. et al., 1997, ApJ **490**, 577

[161] Kodama T., Smail I., 2001, MNRAS **326**, 637

[162] Butcher H.R., Oemler G., 1978, ApJ **219**, 18

Index

4000Å break, 9

age-dust degeneracy, 12, 41

Bayesian statistics, 40
BPZ, 40
bulge fraction, 111, 114

Calzetti, reddening law, 11, 48
CDM (cold dark matter), 2, 3, 24, 60, 91
  Λ, 3
  standard (S), 2
clustering, 17
CM diagram, 7
colour excess, 10
correlation length, 17
cosmic variance, 19, 28, 71, 87

dark matter haloes, 3, 58–60, 69, 91, 93, 94, 105
de Vaucouleurs law, 19, 106
disc-bulge decomposition, 111

e-correction, 49, 56
Einstein-de Sitter model, 15
ERGs
  $L > L^*$ progenitors , 56
  $z > 4$ candidates, 61
  clustering, 17, 67
  definition, 7
  far-IR, 28
  Hubble diagram, 46
  LF, 53
  morphology, 19
  number counts, 76
  radio, 27
  redshift distribution, 44, 81
  spectra, 20
  X-rays, 29, 67
EROs
  definition, 6
extinction, 10

frequentist statistics, 40

GOODS, 32, 33
  CDFS deep ISAAC field, 34

half-light radius, 118
HDM (hot dark matter), 1
HEROs, 26, 61
Hubble diagram, 32, 46, 83
HUDF (Hubble Ultradeep Field), 33, 63, 74
HYPERZ, 39
  primary solution, 40
  secondary solution, 40

initial mass function
    Salpeter, 92
    top-heavy, 26
IRAC (Infrared Array Camera), 33, 72, 100

Jeans instability, 1

K_s-selected galaxies
    Hubble diagram, 83
    IR magnitudes, 100
    LF, 85
    morphology, 106
    number counts, 76
    redshift distribution, 81
    stellar mass, 91
k-correction, 11, 49, 88
    morphological, 108, 114
K20 survey, 15
Kauffmann & Charlot test, 24

LF (luminosity function), 24, 32, 53, 85
Lyman-break galaxies, 61

mass-to-light ratio, 60, 91, 107
maximum likelihood, 39, 111
mergers, 107, 114
MS (main sequence), 7

passive evolution, 12
peculiar galaxies, 106
PLE (pure luminosity evolution), 23
Pozzetti & Mannucci plot, 22
PSF (point-spread function), 107, 111, 112

radiative transfer, 10
radio galaxies, 14, 15, 18, 27, 48, 83
reddening, 10, 39
redshift desert, 20

Sérsic index, 19, 106, 111
SED (spectral energy distribution), 7
stellar populations
    AGB, 6, 7
    MS, 7
    RGB, 7
    WD, 8

ULIRGs (ultra-luminous infrared galaxies), 28

Acknowledgements II

Based on observations made with the Advanced Camera for Surveys and the Near Infrared Camera and Multi Object Spectrometer on board the Hubble Space Telescope operated by NASA/ESA and with the Infrared Spectrometer and Array Camera on the 'Antu' Very Large Telescope operated by the European Southern Observatory in Cerro Paranal, Chile, which form part of the publicly available GOODS datasets. We kindly thank the GOODS teams for providing reduced data products.

I also want to acknowledge funding from a POE-network studentship and the Overseas Research Scheme Award (ORS/2001014037).